Abbildende magnetische Mikrospektroskopie

Habilitationsschrift

zur Erlangung des akademischen Grades

Dr. rer. nat. habil.

vorgelegt der

Mathematisch-Naturwissenschaftlich-Technischen Fakultät
der Martin-Luther-Universität Halle-Wittenberg

von Herrn Dr. rer. nat. **Wolfgang Kuch**

geb. am 07. Januar 1964 in Boston, U.S.A.

Gutachter:

1. Prof. Dr. J. Kirschner, MPI für Mikrostrukturphysik, Halle

2. Prof. Dr. M. Donath, Westfälische Wilhelms-Universität Münster

3. Prof. Dr. H.-J. Elmers, Johannes-Gutenberg-Universität Mainz

Halle (Saale), verteidigt am 10.06.2002, Probevorlesung am 22.10.2002

Inhaltsverzeichnis

Kapitel 1

Einleitung

1.1 Magnetische Schichtsysteme

Grundlagenforschung und industrielle Entwicklung auf dem Gebiet des Magnetismus dünner Filme haben in den vergangenen zehn Jahren einen beispiellosen Aufschwung erlebt. Dies ist in erheblichem Ausmaß auf die Anwendung von Magnetowiderstandseffekten in magnetischen Sensoren und Festplattenleseköpfen zurückzuführen. 1988 entdeckten parallel zueinander die Arbeitsgruppen um Peter Grünberg in Jülich [1] und Albert Fert in Orsay [2], dass sich die elektrische Leitfähigkeit von magnetischen Schichtsystemen, in denen ultradünne magnetische Filme durch nichtmagnetische Zwischenschichten getrennt sind, stark mit der relativen Orientierung der Magnetisierungsrichtungen zueinander ändert. Dieser Effekt wurde unter dem Namen Riesenmagnetowiderstandseffekt (GMR, giant magnetoresistance) bekannt. Eine schematische Erläuterung zeigt Fig. 1.1. Der elektrische Widerstand durch ein Schichtsystem aus mindestens zwei ferromagnetischen Schichten, die durch eine nichtmagnetische Zwischenschicht getrennt sind, ist deutlich niedriger, wenn beide Schichten in die gleiche Richtung magnetisiert sind, als wenn ihre Magnetisierungsrichtungen entgegengesetzt ausgerichtet sind. Es war sofort klar, dass diese Entdeckung für Sensorikanwendungen von großem Interesse sein würde. Da die für den Effekt nötige Dicke der Schichten nur wenige Atomlagen beträgt, war dies auch für Anwendungen in der magnetischen Datenspeicherung höchst interessant. Durch einen massiven Einsatz von Forschungs- und Entwicklungsressourcen weltweit—hervorzuheben ist hier die Gruppe um
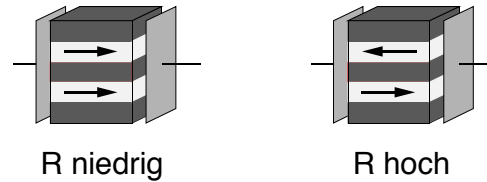
Abbildung 1.1: Schematische Darstellung des Riesen-Magnetowiderstands in ultradünnen magnetischen Schichtsystemen. Eine deutliche elektrische Widerstandsänderung tritt auf, wenn die Magnetisierungsrichtung in zwei ultradünnen magnetischen Schichten relativ zueinander geändert wird. Der Unterschied zwischen R_{low} und R_{high} kann bei Raumtemperatur einige zehn Prozent betragen.

Stuart Parkin im IBM Forschungszentrum Almaden in San Jose [3]—wurde mit Hochdruck sowohl an den Grundlagen des Effekts als auch an der Optimierung und Integration in bestehende Technologien gearbeitet. In weniger als zehn Jahren nach der Veröffentlichung des neuen Effekts war die Marktreife für die ersten kommerziell erhältlichen Produkte erzielt worden — ein neuer Rekord! Abb. 1.2 zeigt als Beispiel ein Riesenmagnetowiderstandselement in einem IBM Festplattenlesekopf, der seit 1997 in kommerziell erhältlichen Festplattenlaufwerken eingesetzt wird. Mittlerweile werden alle IBM Festplatten standardmäßig mit solchen Köpfen ausgestattet. Im oberen Bild ist der Halter des Kopfs und an dessem vorderen Ende der Gleiter zu erkennen, der beim Betrieb dicht über der Festplattenoberfläche schwebt. Der eigentliche Schreib-/Lesekopf ist ein winziges Plättchen, das auf der Stirnseite des Gleiters sitzt, wie mit einem Kreis und Pfeil in Abb. 1.2 angedeutet. Im mittleren Bild ist dieser Kopf vergrößert dargestellt. Während der Schreibkopf mit Spule und Joch auf der Oberseite deutlich hervortritt, ist der eigentliche Lesekopf nur ein kleines, in die Schichtstruktur des Aufbaus integriertes Plättchen. Er ist unten in Abb. 1.2 vereinfacht gezeichnet. Als funktionelle Elemente enthält er zwei ultradünne magnetische Schichten, von denen eine, die hartmagnetische Schicht, eine konstante Magnetisierungsrichtung beibehält. Die zweite, weichmagnetische Schicht, ändert im Streufeld der magnetischen Datenbits auf der Festplatte ihre Magnetisierungsrichtung. Eine Möglichkeit, die Magnetisierungsrichtung der harten Schicht festzuhalten, ist die Kopplung zu einer antiferromagnetischen Schicht [4]. Eine solche Situation ist in Abb. 1.2 unten schematisch dargestellt, bei der die obere der beiden magnetischen Schichten die weiche Schicht darstellt.

weichmagnetische Schicht

hartmagnetische Schicht

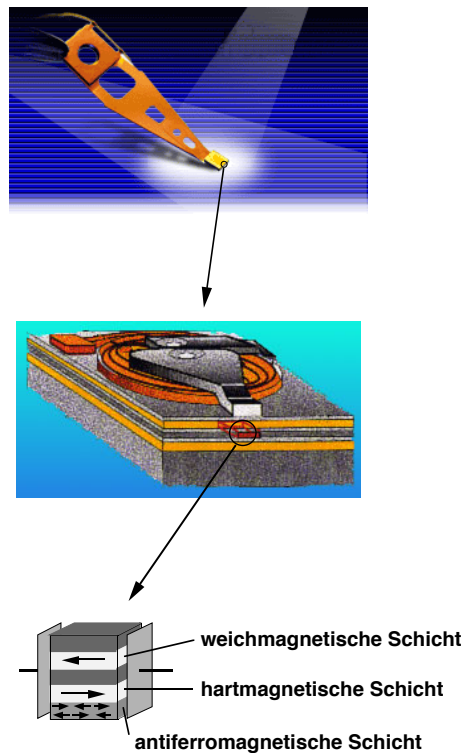antiferromagnetische Schicht

Abbildung 1.2: Aufbau eines Schreib-/Lesekopfs von Computerfestplatten. Oben: Träger und Gleiter. Mitte: Der eigentliche Schreib-/Lesekopf, der sich auf der Stirnseite des Gleiters befindet (Quelle: IBM). Unten: Vereinfachende schematische Darstellung des Lesesensors, der in die Stirnseite des Schreib-/Lesekopfs integriert ist. Funktionelle Elemente sind zwei magnetische Schichten, von denen eine, in der Abbildung die obere, ihre Magnetisierungsrichtung im Streufeld der Datenbits von der Festplatte ändert, während die andere durch den Kontakt mit einer antiferromagnetischen Schicht ihre Magnetisierungsrichtung beibehält.

Durch die höhere Sensitivität der den Riesenmagnetowiderstand ausnützenden Elemente gegenüber herkömmlichen Sensoren war es möglich, mit niedrigeren magnetischen Streufeldern auszukommen und die Speicherdichte entsprechend zu steigern. Weitere Anwendungen des Riesenmagnetowiderstandseffekts sind berührungsfreie Winkelsensoren, die zum Beispiel im Automobilbau zum Einsatz kommen [5]. Ein anderes Feld von geplanten Anwendungen nutzt aus, dass man die in Abb. 1.1 gezeigten Widerstandswerte R_{low} und R_{high} mit den Zuständen „0" und „1" eines Datenbits identifizieren kann. Da eine einmal eingestellte Magnetisierung der weichen Schicht auch ohne Stromversorgung erhalten bleibt, bieten solche Elemente die Möglichkeit, Ar-

beitsspeicherchips zu realisieren, deren Information nach Abschalten des Geräts erhalten wäre. Dazu müssten miniaturisierte Riesenmagnetowiderstandselemente in einer Matrix angeordnet werden [6]. Für solche Datenspeicher (MRAM, magnetic random access memory) laufen bereits Entwicklungsarbeiten in mehreren Unternehmen. Noch nicht ganz so weit fortgeschritten ist die Entwicklung der sogenannten Magnetoelektronik. Darunter versteht man die Integration von magnetischen Schichten in Halbleiterstrukturen. Die zugrunde liegende Idee ist, in elektronischen Bauteilen nicht nur die elektrische Ladung der Elektronen, sondern auch deren Spin auszunutzen [7]. Denkbar wären zum Beispiel magnetisch umprogrammierbare Logikschaltungen oder magnetisch gesteuerte Transistoren. Ein Vorteil von metallischen Magnetfilmen gegenüber Halbleitern ist die größere Schnelligkeit und niedrigere Dissipation, die prinzipiell eine stärkere Miniaturisierung ermöglicht.

Allen diesen gegenwärtigen und zukünftigen Anwendungen gemeinsam ist das bereits in Abb. 1.1 vereinfacht dargestellte Prinzip, nämlich das Vorhandensein von mindestens zwei magnetischen Schichten, deren relative Magnetisierungsänderung Magnetowiderstandseffekte hervorruft. Notwendig dazu ist die unabhängige Kontrolle der Magnetisierungen beider Schichten, die die Kenntnis und Beherrschung des Kopplungsmechanismus durch die dazwischenliegende nichtmagnetische Schicht mit einschließt. Gleichzeitig wird die Größe solcher Elemente weiter stark abnehmen, um mit der gegenwärtig genutzten Halbleitertechnik konkurrenzfähig zu sein. Zur Untersuchung solcher Elemente ist folglich eine Technik gefordert, die einerseits in der Lage ist, mit einer mikroskopischen Ortsauflösung Vorgänge zu untersuchen, die aufgrund der verkleinerten Abmessungen eine Rolle spielen, andererseits aber vermag, die magnetischen Eigenschaften der verschiedenen magnetischen Schichten getrennt zu untersuchen. Genau diese Vorraussetzungen erfüllt die Photoelektronen-Emissionsmikroskopie (PEEM) in Verbindung mit dem zirkularen magnetischen Dichroismus in der Röntgenabsorption (XMCD, x-ray magnetic circular dichroism). In XMCD werden Übergänge aus atomaren Rumpfniveaus angeregt, um die Spinpolarisation der unbesetzen Zustände an der Fermikante zu untersuchen. Wegen der Elementselektivität dieser Methode können verschiedene magnetische Schichten, die unterschiedliche Elemente enthalten, separat untersucht werden. Durch die Verwendung eines PEEMs zur Detektion der Röntgenabsorption wird diese Information mikroskopisch ortsaufgelöst gewonnen. Damit ist es

zum Beispiel möglich, die magnetische Domänenstruktur in einem wie in Abb. 1.1 gezeigten Mehrschichtsystem für beide magnetische Schichten getrennt abzubilden.

Darüberhinaus bietet XMCD auch quantitative Informationen über die atomaren magnetischen Momente. Durch Verwendung von Summenregeln können die Momente getrennt nach Spin- und Bahnanteil quantitativ erfasst werden. Auch diese Größen lassen sich ortsaufgelöst bestimmen, indem das PEEM nicht nur zur Abbildung von Domänenmustern, sondern zum Aufnehmen kompletter ortsaufgelöster Absorptionsspektren verwendet wird. Dies wird hier als „Abbildende magnetische Mikrospektroskopie" bezeichnet. Im Folgenden wird dargelegt, welche Schwierigkeiten dabei auftreten und wie man sie bewältigen kann. Zunächst wird in den beiden nächsten Abschnitten eine Einführung in die zugrundeliegenden Techniken XMCD und PEEM gegeben. Kap. 2 befasst sich mit der Durchführung der Experimente und der Auswertung der Daten. Verweise auf ausgewählte Ergebnisse im Anhang und deren Diskussion ist der Inhalt von Kap. 3. Zuletzt wird in Kap. 4 ein Ausblick über die in diesem Gebiet in naher Zukunft zu erwartenden methodischen Neuheiten und Verbesserungen gegeben.

1.2 Magnetischer Zirkulardichroismus in der Röntgenabsorption

„Dichroismus" kommt aus dem Griechischen und bedeutet „Zweifarbigkeit". Unter „Magnetischem Dichroismus" versteht man allgemein die Abhängigkeit spektroskopischer Eigenschaften von der Magnetisierung der Probe. Diese können genau dann auftreten, wenn durch die Magnetisierung die Symmetrie des Experiments erniedrigt wird [8]. In der winkelaufgelösten Photoelektronenspektroskopie ist die Symmetrie des Experiments durch die Einfallsrichtung und Polarisation der anregenden Strahlung sowie durch die Richtung der detektierten Photoelektronen relativ zur Probe gegeben. Eine Änderung der Photoelektronenspektren bei einfacher Ummagnetisierung der Probe, d.h. Änderung der Magnetisierungsrichtung um 180°, lässt sich am einfachsten mit zirkular polarisierter Strahlung erreichen. Man spricht dann von „Zirkulardichroismus". Magnetischer Zirkulardichroismus in der Valenzband-Photoelektronenspektroskopie wurde in den vergangen Jahren als Untersuchungsmethode zur Bestimmung der elektronischen Struktur magnetischer Metalle etabliert [9–11], und liefert eine Vielzahl von Informationen über magnetische Proben [12]. Wegen der doppelten Energiemonochromatisierung sowohl der anre-

genden Strahlung als auch der detektierten Photoelektronen jedoch ist die Elektronenintensität, die bei der Verwendung von Photoelektronenspektroskopie zur abbildenden magnetischen Mikrospektroskopie zur Verfügung stehen würde, relativ gering.

In der Röntgen*absorptions*spektroskopie ist zur Detektion des Signals keine Energiemonochromatisierung von Elektronen notwendig, was den Einsatz zur abbildenden magnetischen Mikrospektroskopie vereinfacht. Hier ist die Symmetrie des Experiments durch die Richtung und Polarisation der einfallenden Strahlung relativ zur Probe gegeben. Ein Zirkulardichroismus bei Magnetisierungsumkehr kann auftreten, wenn der Helizitätsvektor der anregenden Strahlung eine Komponente entlang der Magnetisierungsachse besitzt. Seit seiner experimentellen Entdeckung 1987 [13] hat sich der magnetische Zirkulardichroismus in der Röntgenabsorption (XMCD) zu einer verbreiteten Standardmethode zur Untersuchung von dünnen magnetischen Schichten entwickelt. Die Gründe dafür liegen zum einen in der bereits im vorigen Abschnitt erwähnten Elementselektivität, die Untersuchungen von komplizierteren Schichtstrukturen ermöglicht. Zusätzlichen Auftrieb erhielt die Methode, als 1992 und 1993 die sogenannten Summenregeln veröffentlicht wurden [14, 15]. Diese Summenregeln geben an, wie durch Auswertung der Absorptionsspektren das magnetische Moment, getrennt nach Spin- und Bahnanteil, quantitativ ermittelt werden kann. Ein weiterer Grund für die Verbreitung von XMCD liegt in der steigenden Verfügbarkeit von monochromatisiertem Röntgenlicht in Form von Synchrotronstrahlung. Die gemessenen Effekte sind groß, und das eigentliche Experiment, wenn das Synchrotron und ein entsprechendes Strahlrohr bereits vorhanden sind, lässt sich verhältnismäßig einfach durchführen. Die Absorption der einfallenden Röntgenstrahlung an einer Probe kann im einfachsten Fall bereits über den abfließenden Probenstrom gemessen werden. So ist es nicht verwunderlich, dass eine Literaturrecherche im Juli 2001 914 Zitate für „x-ray magnetic circular dichroism" ergab, wovon alleine 690 aus den Jahren seit 1995 stammten [16]!

1.2.1   Röntgenabsorptionsspektroskopie

Der XMCD-Effekt beruht auf dem Abfragen der Spin- und Bahnpolarisation der unbesetzten Valenzbandzustände dicht über der Fermikante durch elektronische Übergänge aus Rumpfniveaus. Die Intensität der Absorption von Photonen der Energie $\hbar\omega$ durch Anregung elektronischer

Übergänge wird durch Fermis Goldene Regel beschrieben:

$$I(\hbar\omega) \propto \sum_{i,f} \int\limits_{\mathrm{BZ}} d^3k \; M_{fi}^2 \; \delta\left(E_f(\mathbf{k}) - E_i(\mathbf{k}) - \hbar\omega\right) \; \mathcal{F}(E_i(\mathbf{k})) \; \left[1 - \mathcal{F}(E_f(\mathbf{k}))\right]. \tag{1.1}$$

Dabei wurde der Impulsübertrag durch das Photon vernachlässigt. Die Summe läuft über alle Anfangs- und Endzustände i und f, das Integral über die gesamte Brillouinzone. Die Deltafunktion gibt die Energieerhaltung bei der Absorption wieder, und die Fermifunktion $\mathcal{F}$ trägt der Tatsache Rechnung, dass Übergänge von besetzten Anfangszuständen i in unbesetzte Endzustände f angeregt werden. Das Übergangsmatrixelement M_{fi}^2 lautet in Dipolnäherung $|\langle f \,|\mathbf{A} \cdot \mathbf{p}|\, i\rangle|^2$. Die Polarisation der anregenden Röntgenstrahlung ist dabei im elektrischen Feldvektor $\mathbf{A}$ enthalten, wobei die Verwendung von zirkularer Polarisation im allgemeinen zu spinpolarisiertern Übergängen führt, wie im nachfolgenden Abschnitt 1.2.2 erläutert.

Lässt man diese Polarisationseffekte zunächst außer acht, so beschreibt die doppelte Summe über i und f in Gleichung 1.1 nach Ausführung der Integration über die Brillouinzone eine Faltung der besetzten Zustandsdichte unterhalb der Fermienergie E_F mit der unbesetzten Zu-
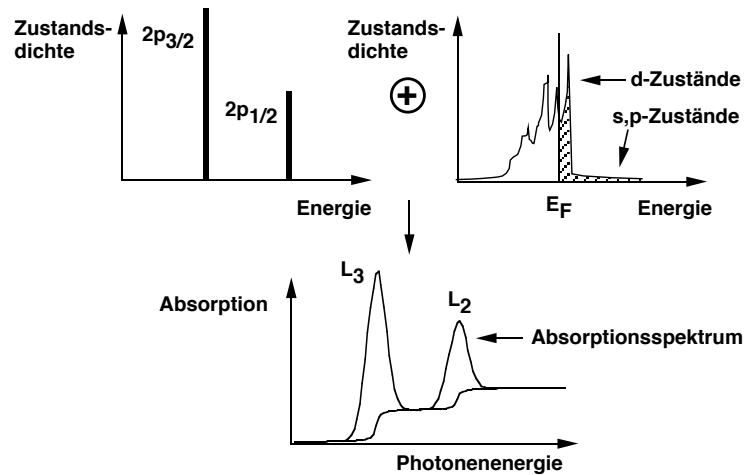
Abbildung 1.3: Schematische Erklärung der Entstehung eines Röntgenabsorptiosnspektrums im Bereich der $2p \to 3d$-Übergänge. Das unten gezeigte Absorptionsspektrum enststeht als Faltung der besetzten Zustandsdichte der $2p$-Rumpfzustände (links oben) und der unbesetzten Zustandsdichte oberhalb der Fermienergie E_F (rechts oben, schraffiert). Der Beitrag der d-Zustände führt zu charakteristischen Peaks im Absorptionsspektrum, der der s, p-Zustände zu einem Untergrund, der üblicherweise durch Stufenfunktionen angenähert und abgezogen wird.

standsdichte oberhalb E_F. Dies ist schematisch in Abb. 1.3 dargestellt. Hier wird am Beispiel von $2p \rightarrow 3d$-Übergängen die Entstehung eines Röntgenabsorptionsspektrums gezeigt. Links oben ist die Zustandsdichte der $2p_{1/2}$ und $2p_{3/2}$ Rumpfniveaus schematisch durch Deltafunktionen dargestellt, deren Höhe die Besetzung mit 2 bzw. 4 Elektronen wiedergibt. Wichtig ist dabei die energetische Trennung zwischen $2p_{1/2}$- und $2p_{3/2}$-Zuständen von typischerweise 10–15 eV durch die Spin-Bahn-Kopplung. Rechts oben ist eine schematische Zustandsdichte der Valenzbänder um den Bereich der Fermikante E_F abgebildet. Die für Übergänge aus Rumpfniveaus verfügbaren unbesetzten Zustände oberhalb E_F sind schraffiert gekennzeichnet. Bei einem Scan der Photonenenergie beobachtet man eine starke Absorption genau dann, wenn die Photonenenergie dem energetischen Abstand einer hohen besetzten Rumpfniveauzustandsdichte und einer hohen unbesetzten Valenzelektronen-Zustandsdichte entspricht. Die untere Graphik in Abb. 1.3 zeigt die Faltung dieser beiden Zustandsdichten, wobei auch noch eine Verbreiterung durch die experimentelle Energieauflösung in Betracht gezogen wurde. Die beiden Peaks stammen dabei von Übergängen von $2p_{3/2}$- und $2p_{1/2}$-Elektronen in unbesetzte $3d$-Zustände, die ein scharfes Maximum direkt oberhalb der Fermikante aufweisen. Die übliche Nomenklatur dabei ist, die durch $2p_{1/2} \rightarrow 3d$-Übergänge erzeugte Absorptionskante mit L_2, die durch $2p_{3/2} \rightarrow 3d$-Übergänge erzeugte Kante mit L_3 zu bezeichnen. Der stufenartige Untergrund im Absorptionsspektrum ist die Folge von Übergängen in s, p-artige Zustände, die energetisch breiter verteilt sind. Da die interessierenden unbesetzten Zustände die $3d$-Zustände sind, weil diese den Hauptanteil der magnetischen Momente in den Übergangsmetallen ausmachen, wird der Beitrag der s, p-Elektronen üblicherweise durch Stufenfunktionen angenähert und abgezogen, wie im unteren Bild von Abb. 1.3 angedeutet.

1.2.2 Magnetischer Zirkulardichroismus als Folge spinpolarisierter Übergänge

Wenn nun zirkular polarisierte Röntgenstrahlung für die Röntgenabsorptionsspektroskopie verwendet wird, so sind auch die elektronischen Übergänge polarisiert, sowohl was den Spin als auch das Bahnmoment betrifft. Dies wird in Abb. 1.4 erläutert. Am unteren Ende sind die $2p_{3/2}$- und $2p_{1/2}$-Zustände, aufgeteilt nach den Quantenzahlen m_j, dargestellt. Während es für $m_j = -3/2$ und $m_j = +3/2$ jeweils nur eine Kombination von $m_\ell + m_S = m_j$ gibt, kann man sich $m_j = +1/2$

$|m_\ell, m_S\rangle$

3d

$|{-2},{-1/2}\rangle$ $|{-2},1/2\rangle$ $|{-1},{-1/2}\rangle$ $|{-1},1/2\rangle$ $|0,{-1/2}\rangle$ $|0,1/2\rangle$ $|1,{-1/2}\rangle$ $|1,1/2\rangle$ $|2,{-1/2}\rangle$ $|2,1/2\rangle$

rechts-zirkular:

$\Delta m_\ell = +1$

$\Delta m_S = 0$

| 7.5% | 2.5% | 15% | 15% | 15% | 45% | 10% | 15% | 15% | 60% |

$|m_\ell, m_S\rangle$

$|{-1},{-1/2}\rangle$ $|{-1},1/2\rangle, |0,{-1/2}\rangle$ $|0,1/2\rangle, |1,{-1/2}\rangle$ $|1,1/2\rangle$ $|{-1},1/2\rangle, |0,{-1/2}\rangle$ $|0,1/2\rangle, |1,{-1/2}\rangle$

$m_j = {-3/2}$ $-1/2$ $1/2$ $3/2$ $-1/2$ $1/2$

$2p_{3/2}$ $2p_{1/2}$

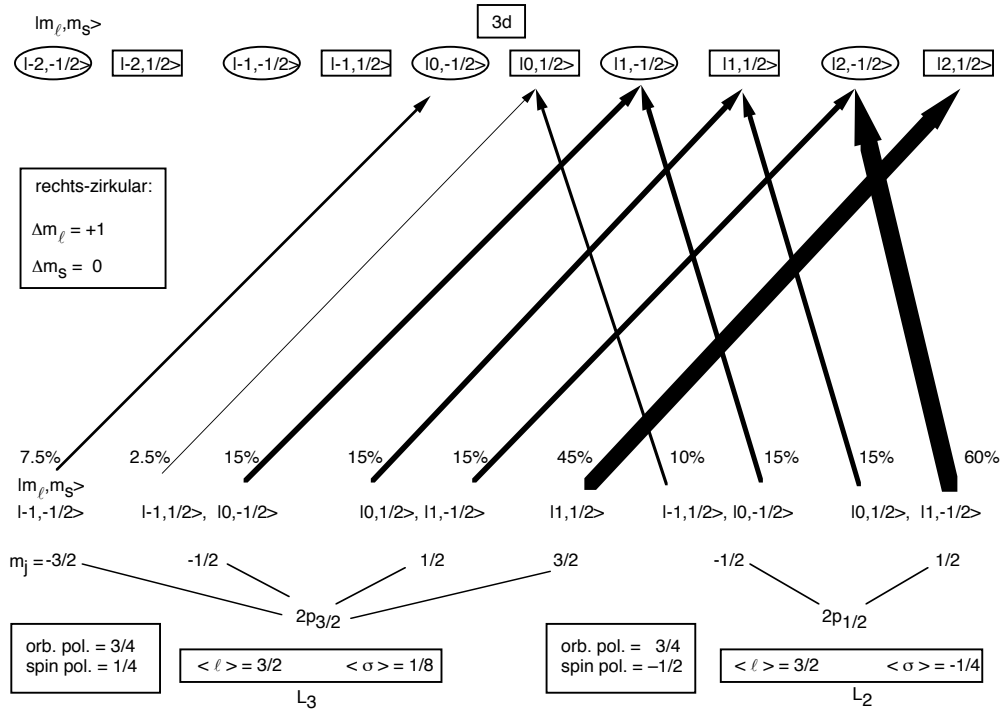| orb. pol. = 3/4 spin pol. = 1/4 | $\langle \ell \rangle = 3/2$ $\langle \sigma \rangle = 1/8$ | orb. pol. = 3/4 spin pol. = −1/2 | $\langle \ell \rangle = 3/2$ $\langle \sigma \rangle = -1/4$ |

L_3 L_2

Abbildung 1.4: Aufteilung der $2p \rightarrow 3d$-Übergänge bei Anregung mit rechts zirkular polarisiertem Licht nach Quantenzahlen $|m_\ell, m_S\rangle$. Die Übergänge müssen die Bedingungen $\Delta m_S = 0$ und $\Delta m_\ell = +1$ erfüllen. Die Übergangswahrscheinlichkeiten, die sich aus den entsprechenden Drehimpuls-Matrixelementen ergeben, sind durch die unterschiedlichen Pfeilstärken angedeutet und zusätzlich in Prozent, getrennt nach $2p_{3/2}$- und $2p_{3/2}$-Anfangszuständen, angegeben. Man erhält eine Polarisation der Übergänge sowohl bezüglich des Spins („spin pol.") als auch des Bahndrehimpulses („orb. pol.").

als Kombination von $m_\ell = 1$, $m_S = -1/2$ und $m_\ell = 0$, $m_S = +1/2$ vorstellen. Analoges gilt für $m_j = -1/2$. In Abb. 1.4 sind alle diese Kombinationen von m_ℓ und m_S aufgeführt. Am oberen Ende der Abbildung sind die entsprechenden $|m_\ell, m_S\rangle$-Kombinationen der $3d$-Zustände aufgelistet. Der Übersichtlichkeit wegen wurde hier auf eine Sortierung nach m_j verzichtet. Übergänge mit rechts zirkular polarisiertem Licht sind nun durch die Bedingungen $\Delta m_S = 0$ und $\Delta m_\ell = +1$ gekennzeichnet, d.h. die Spinquantenzahl ändert sich nicht, während die Bahnquantenzahl um eins zunimmt. Letzteres ist die direkte Konsequenz der Bahndrehimpulserhaltung bei der Absorption eines zirkular polarisierten Lichtquants, für die bei rechts-zirkularer Polarisation $m_\ell = +1$ gilt. Die für diese Bedingungen möglichen Übergänge sind in Abb. 1.4 durch Pfeile gekennzeichnet. Die Übergangswahrscheinlichkeit der einzelnen Übergänge erhält man aus den

entsprechenden Drehimpuls-Matrixelementen [17]. Gemäß den Koeffizienten für die Drehimpuls-addition, den Clebsch-Gordon-Koeffizienten, verhalten sich die aufsummierten Wahrscheinlich-keiten der Übergänge für m_ℓ von $1 \to 2$: $0 \to 1$: $-1 \to 0$ wie $60 : 30 : 10$. Die resultierenden Übergangswahrscheinlichkeiten der einzelnen Übergänge, getrennt nach Übergängen von $2p_{3/2}$- und $2p_{3/2}$-Zuständen, sind in Abb. 1.4 angegeben und durch unterschiedliche Dicke der Pfeile graphisch kenntlich gemacht. Aus diesen Übergangswahrscheinlichkeiten läßt sich direkt die Spinpolarisation der Übergänge ablesen, indem man den Erwartungswert der Spinquantenzahl der erreichten Endzustände errechnet. Zur einfacheren Unterscheidung sind $3d$-Zustände mit $m_S = +1/2$ durch ein rechteckiges Symbol, solche mit $m_S = -1/2$ durch eine Ellipse gekenn-zeichnet. Betrachtet man zunächst nur Übergänge aus $2p_{1/2}$ Niveaus, so erreicht man mit 75% der Übergänge $3d$-Zustände mit $m_S = -1/2$ und nur mit 25% der Übergänge Zustände mit $m_S = +1/2$. Der Erwartungswert des Spinoperators ist daher $< \sigma >= -1/4$, was einer Spin-polarisation von $-1/2$ entspricht. Analog erhält man von den Übergängen aus $2p_{3/2}$-Zuständen einen Erwartungswert $\langle \sigma \rangle = +1/8$ bzw. eine Spinpolarisation von $+1/4$. Für links zirkular pola-risiertes Licht sind alle oben gemachten Betrachtungen identisch bei umgekehrtem Vorzeichen. Wichtig ist die energetische Trennung von $2p_{1/2}$- und $2p_{3/2}$-Anfangszuständen, da sich sonst die Gesamtspinpolarisation zu Null mitteln würde. Weitere Subniveauaufspaltungen sind für die prinzipielle Beschreibung des XMCD und der Summenregeln nicht wichtig, so dass alle anderen Energieniveaus als jeweils entartet betrachtet werden können.

Mit diesen spinpolarisierten Übergängen wird nun die Spinpolarisation der unbesetzten $3d$-Zustände geprüft. Die Spinpolarisation der Übergänge hängt dabei von der Helizität der anre-genden Strahlung, also der Lichtpolarisation ab, während die Spinpolarisation der unbesetzten $3d$-Zustände von der Magnetisierungsrichtung in der Probe bestimmt wird. Wenn beide Spinpo-larisationen übereinstimmen, erhält man eine hohe Zahl von möglichen Übergängen, also eine hohe Absorption. Dreht man entweder die Magnetisierungsrichtung oder die Lichthelizität um, so stimmt die Polarisation der unbesetzten Zustände nicht mehr mit der durch die Zirkularität des Lichts bevorzugten Polarisationsrichtung der Übergänge überein, so dass man eine geringere Absorption erhält. Da das Vorzeichen der Spinpolarisation für Übergänge von $2p_{1/2}$- und $2p_{3/2}$-Elektronen entgegengesetzt ist, resultiert auch das umgekehrte Verhalten für die beiden Linien.
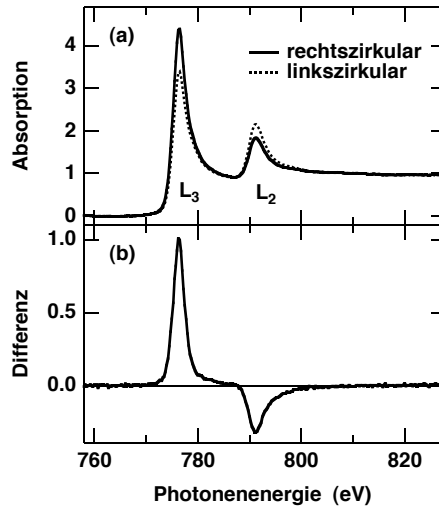
Abbildung 1.5: Beispiel eines XMCD-Spektrums. (a): Absorptionsspektren eines dünnen Co-Films auf Cu(001) für rechts-zirkular (durchgezogen) und linkszirkular (gestrichelt) polarisierte Röntgenstrahlung. Man erkennt den magnetischen Dichroismus als Unterschied in der Absorption an den Co-L_3- und L_2-Kanten. (b): Differenz der beiden Absoptionsspektren. Aufgrund der entgegengesetzten Spinpolarisation von $2p_{3/2} \rightarrow 3d$- und $2p_{1/2} \rightarrow 3d$-Übergängen ist das Vorzeichen des Dichroismus an der L_3- und der L_2-Kante entgegengesetzt.

Schematisch dargestellt ist dies in Abb. 1.5. Die obere Kurve zeigt Absorptionsspektren an der Co-$L_{2,3}$-Kante eines dünnen Co-Films auf Cu(001) für rechts- bzw. linkspolarisiertes Licht. Für eine feststehende Magnetisierungsrichtung der Probe ist je nach Lichthelizität entweder die Absorption an der L_3- oder der L_2-Kante gegenüber einer nichtmagnetischen Probe erhöht oder erniedrigt. In Abb. 1.5 (b) ist die Differenz aus den beiden Absorptionsspektren dargestellt. Sie zeigt den Dichroismus an den Absorptionsmaxima, der an den beiden Kanten ein umgekehrtes Vorzeichen hat.

1.2.3 Die Summenregeln

Außer der eben besprochenen Spinpolarisation sind $2p \rightarrow 3d$-Übergänge auch bezüglich der Drehimpulsquantenzahl, also des Bahnmoments, polarisiert. Aus Abb. 1.4 entnimmt man als Erwartungswert für m_ℓ $\langle \ell \rangle = 3/2$, sowohl für $2p_{3/2} \rightarrow 3d$- als auch für $2p_{3/2} \rightarrow 3d$-Übergänge. Bezogen auf $\ell = 2$ für $3d$-Zustände bedeutet dies eine Bahnmomentpolarisation von 3/4. Im Gegensatz zur Spinpolarisation tritt die Bahnmomentpolarisation jedoch mit gleichem Vorzei-

chen an der L_3- und der L_2-Kante auf. Analog zu den obigen Betrachtungen kann man mit diesen Übergängen also auch die Bahnpolarisation der unbesetzten $3d$-Zustände prüfen. Schematisch ist dies in Abb. 1.6 dargestellt. Abb. 1.6 (a) zeigt den Fall einer hypothetischen Probe, deren magnetisches Moment ausschließlich durch Spinpolarisation der Valenzzustände hervorgerufen ist, während die Bahnmomentpolarisation, also das Bahnmoment μ_L Null ist. Durch die Spinpolarisation der Übergänge wird die Spinpolarisation der Valenzzustände, also das Spinmoment μ_S, gemessen. Wie oben beschrieben, ergibt sich ein umgekehrtes Vorzeichen an der L_2- und der L_3-Kante. Die Drehimpulspolarisation der Übergänge ist hier irrelevant. Berücksichtigt man, dass Übergänge aus $2p_{1/2}$-Zuständen eine doppelt so hohe Spinpolarisation wie Übergänge aus $2p_{3/2}$-Zuständen haben, aber nur halb so viele Elektronen zur Verfügung stehen, so erhält man die in Abb. 1.6 (a) schematisch dargestellte Situation mit gleich hohen Dichroismuspeaks umgekehrten Vorzeichens an der L_3- und L_2-Kante.

Im mittleren Graph, Abb. 1.6 (b), ist der hypothetische Fall einer Probe dargestellt, deren magnetisches Moment ausschließlich aus einem Bahnmoment besteht, bei der also keine Spinpolarisation der unbesetzten Valenzzustände, sondern nur eine Bahnmomentpolarisation vorliegt. Da die Bahnmomentpolarisation der Übergänge an der L_2- und der L_3-Kante mit demselben Vorzeichen auftritt, ergibt sich ein Differenzspektrum wie in Abb. 1.6 (b) gezeigt. Durch die identische Bahnmomentpolarisation, aber unterschiedliche Besetzungszahlen von $2p_{1/2}$ und $2p_{3/2}$ ergibt sich hier ein doppelt so großer Peak an der L_3-Kante als an der L_2-Kante.

In Wirklichkeit wird eine Probe sowohl ein Spin- als auch ein Bahnmoment besitzen, wobei in Festkörpern das Spinmoment sehr viel größer ist. Das gemessene Differenzspektrum wird also eine lineare Kombination aus den in (a) und (b) gezeigten hypothetischen Fällen sein. Dies ist in Abb. 1.6 (c) schematisch dargestellt. Ein Beispiel einer realen Probe wurde bereits in Abb. 1.5 gezeigt. Für die Summenregeln wird nun ausgenutzt, dass die in Abb. 1.6 (a) und (b) gezeigten Grenzfälle eine linear unabhängige Basis für das gemessene Spektrum in (c) bilden. Durch Auswertung der unter den Differenzpeaks an der L_2- und der L_3-Kante liegenden Flächen und Berücksichtigung der aus Abb. 1.4 erhaltenen Spin- und Drehimpulspolarisation der Übergänge kann man also eindeutig die Beiträge von Spin- und Bahnmoment zum magnetischen Moment trennen und quantitativ bestimmen [14,15]. Bezeichnet man wie in Abb. 1.6 (c) die Fläche unter

dem L_3-Differenzpeak mit A und die Fläche unter dem L_2-Differenzpeak mit B, wobei in Abb. 1.6 (c) B negativ wäre, so erhält man unter Berücksichtigung der Spin- und Bahnpolarisation der einzelnen Übergänge sowie der Besetzungszahlen für die Spin- und Bahnmomente μ_S und μ_L

$$\mu_S = -\frac{1}{C}\left(A - 2B\right)\mu_B \qquad (1.2)$$

$$\mu_L = -\frac{2}{3C}\left(A + B\right)\mu_B. \qquad (1.3)$$

Diese Gleichungen werden als erste und zweite Summenregel bezeichnet. Den Proportionalitätsfaktor C müsste man im Prinzip aus einer Messung einer Referenzprobe mit bekannten Momenten bestimmen. Gebräuchlicher ist es aber, zur Bestimmung dieses Faktors den Zusammenhang zwischen der helizitätsgemittelten Gesamtfläche unter der Absorptionskurve und der Zahl der
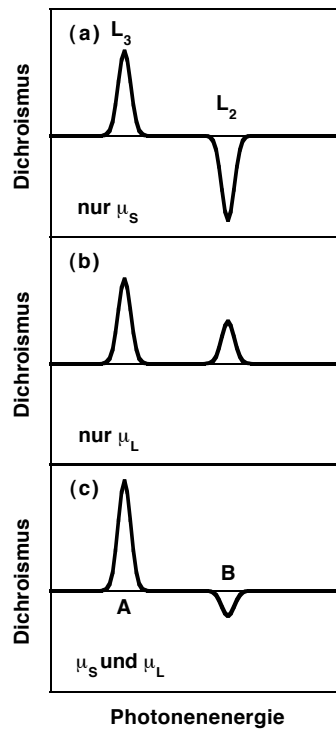

Abbildung 1.6: Graphische Erklärung der XMCD-Summenregeln. Dargestellt ist die Zerlegung eines gemessenen Differenzspektrums (c) in die Anteile, die vom Spinmoment μ_S (a) und dem Bahnmoment μ_L (b) der Probe hervorgerufen werden. Da die Spektren in (a) und (b) eine linear unabhängige Basis bilden, ist diese Zerlegung eindeutig.

Löcher im Valenzband n_h heranzuziehen. Dies wird manchmal auch als „Nullte Summenregel"
bezeichnet:

$$n_h = \frac{1}{C} \left(I(L_2) + I(L_3) \right). \tag{1.4}$$

Hierbei sind $I(L_2)$ und $I(L_3)$ die Flächen unter den L_2- und L_3-Peaks in der Absorptionskurve,
nachdem der von Übergängen in s, p-artige Zustände hervorgerufene Untergrund wie in Abb.
1.3 gezeigt abgezogen wurde.

Der Herleitung der Summenregeln liegen einige vereinfachende Annahmen zugrunde. So
wurden Übergänge zwischen Zuständen von freien Atomen angenommen, eine völlige energe-
tische Trennung zwischen $2p_{1/2}$- und $2p_{3/2}$-Zuständen vorausgesetzt sowie Vielteilcheneffekte
vernachlässigt. Zur Gültigkeit der Summenregeln sind bereits zahlreiche Untersuchungen durch-
geführt worden. Es scheint sich aber herauszustellen, dass trotz der vereinfachenden Annahmen
zumindest für die $3d$-Übergangsmetalle sinnvolle Werte für Spin- und Bahnmomente erhalten
werden [18–22]. Insgesamt kann man sagen, dass sich das Potenzial von XMCD zur elements-
elektiven Bestimmung von magnetischen Momenten in der breiten Verwendung zeigt, die diese
Methode erfährt.

1.3 Photoelektronen-Emissionsmikroskopie

1.3.1 Geschichte

Das Photoelektronen-Emissionsmikroskop (PEEM) gehört zu den ältesten Elektronenmikrosko-
pen, die realisiert wurden [23, 24]. Das Wort „Photoelektron" im Namen ist dabei historisch be-
dingt und für den hier beschriebenen Einsatz mit Synchrotronstrahlung sogar etwas irreführend.
Es stammt von den bei Anregung mit Quecksilberdampflampen knapp oberhalb des Vakuum-
niveaus emittierten Photoelektronen, mit denen PEEM über lange Zeit und in verschiedenen
Anwendungsbereichen betrieben wurde. Wegen des in Schwellenphotoemission hohen Austritts-
arbeitskontrasts zwischen verschieden orientierten Kristalliten fand PEEM zunächst eine Ver-
wendung in der Metallurgie [25]. Nach dem Aufkommen der Ultrahochvakuumtechnologie und
der Entwicklung entsprechender Mikroskope [26, 27] wurde PEEM mit großem Erfolg in zahlrei-
chen Studien von Oberflächen und Oberflächenreaktionen eingesetzt [28–31]. Eine Modifikation,

bei der die Anregung durch Elektronen erfolgt, die über einen magnetostatischen Strahlteiler in den Strahlengang eingelenkt werden, stellt das LEEM (low energy electron microscope) dar, das zusätzliche Information über die Morphologie und Struktur der Oberfläche liefert [32,33].

Mit der Zunahme der Zahl von Synchrotronstrahlungsquellen und der damit verbundenen Verfügbarkeit von durchstimmbarer monochromatischer Ultraviolett- und Röntgenstrahlung wurde bald das Potenzial von PEEM als Mikroskopiemethode in Verbindung mit Röntgenabsorptionsspektroskopie offenbar [34]. Bei dieser Anwendung wird das Bild nicht, wie der Name Photoelektronen-Emissionsmikroskopie vermuten lassen würde, von Photoelektronen, sondern überwiegend von niederenergetischen Sekundärelektronen erzeugt. Da die Zahl der emittierten Sekundärelektronen, wie in Abschnitt 1.2.1 beschrieben, von der Stärke der Röntgenabsorption durch Rumpfniveauübergänge abhängt, ist der Vorteil bei der Verwendung von Synchrotronstrahlung ein Elementkontrast, der es erlaubt, die mikroskopische Verteilung unterschiedlicher Elemente auf einer Probe abzubilden [35–37].

Bei Anregung mit zirkular polarisierter Röntgenstrahlung erhält man zusätzlich noch den Vorteil eines rein magnetischen Kontrasts. Dabei wird ausgenützt, dass die Absorption an elementspezifischen Absorptionskanten wegen des in Abschnitt 1.2.2 beschriebenen magnetischen Zirkulardichroismus von der relativen Orientierung der Magnetisierung bezüglich der Lichteinfallsrichtung abhängt. Damit wurden in den letzten Jahren erfolgreich Untersuchungen magnetischer Domänen in dünnen Filmen und mikrostrukturierten Proben durchgeführt [38–46].

Bei diesen Untersuchungen muss PEEM allerdings mit einer Vielzahl von anderen magnetischen Mikroskopiemethoden konkurrieren, die zum Teil Vorteile bezüglich der Ortsauflösung oder der Unempfindlichkeit gegenüber äußeren Magnetfeldern aufweisen. Einen guten Überblick über magnetische Mikroskopie findet man in Ref. [47]. Die eigentliche Stärke von PEEM zur magnetischen Domänenabbildung liegt jedoch in der Elementselektivität von XMCD, die diesen Mechanismus einzigartig macht. Damit ist es möglich, in einer aus verschiedenen magnetischen Schichten bestehenden Probe diese Schichten separat abzubilden, sofern sie verschiedene Elemente enthalten. Ein Beispiel ist in Abb. 1.7 gezeigt. Dort werden magnetische Domänenbilder von einem Dreilagensystem gezeigt, bestehend aus 15 atomaren Monolagen (ML) Ni und 3 ML
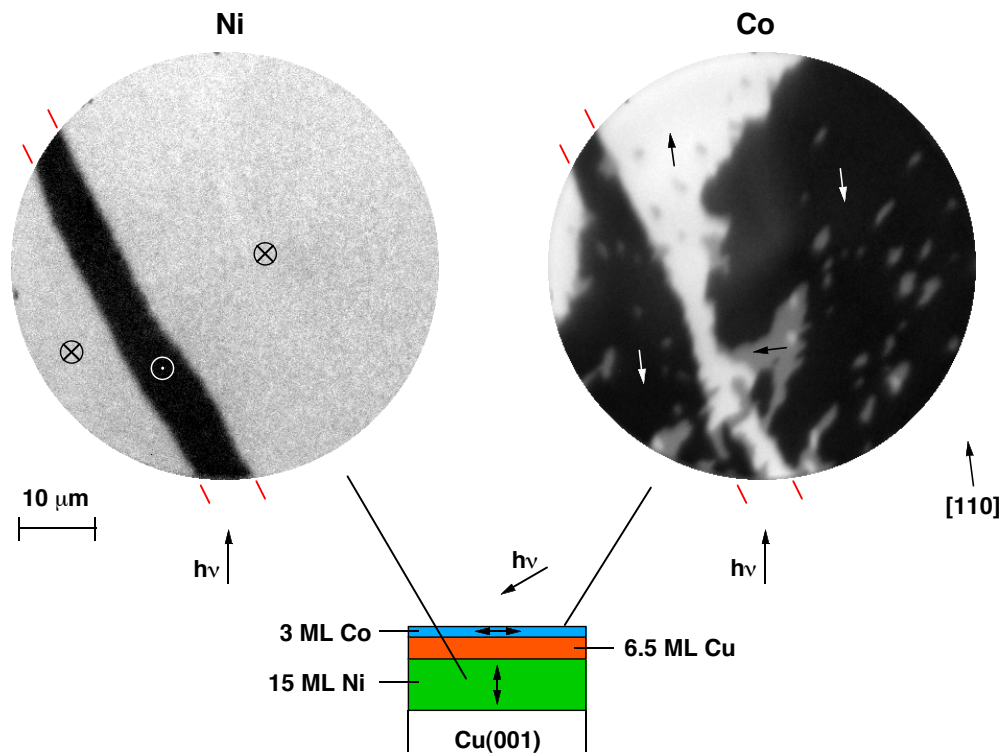
Abbildung 1.7: Beispiel einer elementaufgelösten Domänenabbildung mit PEEM. Dargestellt sind lagen-aufgelöste Domänenbilder einer 3 ML Co/6.5 ML Cu/15 ML Ni/Cu(001)-Probe. Links: Das Domänenbild, aufgenommen an der Ni L_3-Kante, gibt die Domänen der Ni-Schicht wieder. Aufgrund von magnetischen Anisotropien ist die Magnetisierung hier senkrecht zur Filmebene, wie im Bild angedeutet. Rechts: Das Domänenbild, aufgenommen an der Co L_3-Kante, gibt die Domänen der Co-Schicht wieder. Die Magnetisierung ist hier entlang der vier kristallographischen ⟨110⟩-Richtungen in der Filmebene, wie durch Pfeile angedeutet. Trotz der orthogonalen Ausrichtung von Ni- und Co-Magnetisierung erkennt man eine gewisse Korrelation zwischen den Domänenmustern. Zur Verdeutlichung markieren kleine Striche am Rand der Bilder identische Positionen.

Co, die durch 6.5 ML nichtmagnetisches Cu voneinander getrennt sind. Alle drei Schichten wurden durch Molekularstrahlepitaxie auf einer Cu(001)-Einkristalloberfläche aufgewachsen, und das ohne Einwirkung eines äußeren Magnetfelds entstandene Domänenmuster abgebildet. Das linke Bild zeigt die magnetischen Domänen der Ni-Schicht, das rechte Bild die Domänen der Co-Schicht an exakt derselben Stelle der Probe. Die beiden magnetischen Schichten sind durch indi-rekte Austauschwechselwirkung [48, 49] über die Cu-Schicht nur schwach gekoppelt. Da Ni und Co auf Cu(001) eine unterschiedliche Vorzugsrichtung der Magnetisierung aufweisen, stellt sich

im Fall schwacher Kopplung eine nichtkollineare Konfiguration ein [45, 46]: Während die Magnetisierung der Co-Schicht entlang kristallographischer ⟨110⟩-Richtungen in der Filmebene liegt, ist die Ni-Schicht senkrecht zur Filmebene magnetisiert. Dies ist schematisch in Abb. 1.7 unten dargestellt. Die links abgebildeten Domänen der Ni-Schicht zeigen das für senkrecht magnetisierte Filme typische Streifenmuster [47]. Durch die Bildung von abwechselnd auf- und abwärts magnetisierten Domänen kann nämlich die im Falle senkrechter Magnetisierung ungünstige Streufeldenergie erniedrigt werden [50, 51]. Im Domänenbild der Co-Schicht auf der rechten Seite erkennt man deutlich mehr verschiedene Domänen, die entlang einer der vier ⟨110⟩-Richtungen in der Filmebene magnetisiert sind. Für diese orthogonale Magnetisierungsausrichtung der beiden magnetischen Schichten zueinander würde man nicht notwendigerweise mit einer Korrelation zwischen den beiden Domänenmustern rechnen. Es ist jedoch eine gewisse Korrelation in den Domänenbildern zu erkennen. Um dies zu verdeutlichen, sind an beiden Bildern jeweils am Rand Striche angebracht, die identische Positionen markieren. Man sieht deutlich, dass sich über beinahe der Hälfte der Domänenwände der Ni-Schicht auch Domänenwände in der Co-Schicht befinden. Die wahrscheinlichste Erklärung für diese Korrelation sind magnetische Streufelder von den Domänenwänden, die in der unmittelbaren Nähe der Domänenwände so stark werden können, dass sie mit einer anderen magnetischen Schicht wechselwirken. Solche mikromagnetischen Kopplungseffekte sind für Anwendungen von magnetischen Mehrschichtsystemen von großer Bedeutung. Deren Erforschung ist daher von höchstem grundlegendem und anwendungsbezogenem Interesse. Hier kann die elementaufgelöste Domänenabbildung mit PEEM wichtige Beiträge leisten. Untersuchungen wie die in Abb. 1.7 gezeigten stehen an vorderster Front der aktuellen Forschung auf diesem Gebiet.

Eine relativ neue Entwicklung ist auch die magnetische Abbildung mit linear polarisierter Röntgenstrahlung. Dabei wird die durch die Magnetisierung hervorgerufene räumliche Anisotropie der Ladungsverteilung ausgenützt. Da im Gegensatz zur zirkularen Lichtpolarisation bei der linearen Polarisation keine Richtung, sondern nur ein Achse ausgezeichnet ist, kann dieser Mechanismus verwendet werden, um die Spinachse in kollinearen Antiferromagneten experimentell zu bestimmen. Es wurde gezeigt, dass dieser Mechanismus in oxidischen Proben wie zum Beispiel NiO zu einem messbaren Effekt führt [52]. Nachfolgend wurde damit mit Hilfe von PEEM erfolg-

reich eine Abbildung von Domänen in antiferromagnetischem NiO [53, 54] und LaFeO$_3$ [55, 56] durchgeführt.

In allen eben erwähnten Untersuchungen wird zur Abbildung ausgenutzt, dass sich bei einer bestimmten Energie im Absorptionsspektrum der gewünschte Kontrast einstellt. Der Oberbegriff für diese Art von mikroskopischer Abbildung ist „Spektromikroskopie", womit eine Mikroskopiemethode gemeint ist, die spektroskopische Eigenschaften zur Kontrastbildung ausnutzt. In der vorliegenden Arbeit wird nun die Erweiterung zur vollständigen Fusion von Spektroskopie und Mikroskopie aufgezeigt. Wie bereits am Ende von Kapitel 1.1 erwähnt, ist es prinzipiell möglich, die in XMCD-Spektren enthaltene Information mit Hilfe eines PEEM auch räumlich aufgelöst zu messen. Dazu ist es nötig, nicht nur bei den Photonenenergien, bei denen der Kontrasteffekt maximal ist, Bilder aufzunehmen, sondern eine Energieserie von Bildern zu erstellen, bei denen die Bilddatensätze dann als komplette Energiespektren vorliegen. Damit existiert zu jedem Bildpunkt ein komplettes XMCD-Absorptionsspektrum. Dies wird hier „Abbildende Mikrospektroskopie" genannt. Der Begriff „Mikrospektroskopie" bezeichnete bis dato üblicherweise Untersuchungen, bei denen Spektroskopie an einer mikroskopisch kleinen Stelle der Probe durchgeführt wird. Im Grenzfall der in dieser Arbeit beschriebenen Verknüpfung von spektroskopischer und mikroskopischer Information verliert die Unterscheidung zwischen „Spektromikroskopie" und „Mikrospektroskopie" ihren Sinn, weil in diesem Fall beide Begriffe dasselbe meinen. Zur Bezeichnung wurde hier der Begriff „Abbildende Mikrospektroskopie" gewählt.

Die im Folgenden gezeigten Beispiele befassen sich mit XMCD-Spektroskopie, d.h. mit zirkular polarisierter Röntgenstrahlung. Prinzipiell ließe sich alles Angeführte genauso auf den Fall der Anregung mit linearer Polarisation übertragen. Ein Vorteil bei der Verwendung von zirkularer Polarisation liegt aber in den in Abschnitt 1.2.3 beschriebenen Summenregeln, die es erlauben, aus XMCD-Spektren die Spin- und Bahnmomente elementaufgelöst quantitativ zu bestimmen. Ähnliche Summenregeln wurden für lineare Polarisation bisher noch nicht formuliert.

1.3.2 Prinzip

In einem PEEM wird die Elektronenintensitätsverteilung an der Probenoberfläche auf einem Leuchtschirm vergrößert abgebildet. Dies geschieht durch eine parallel abbildende Elektronen-
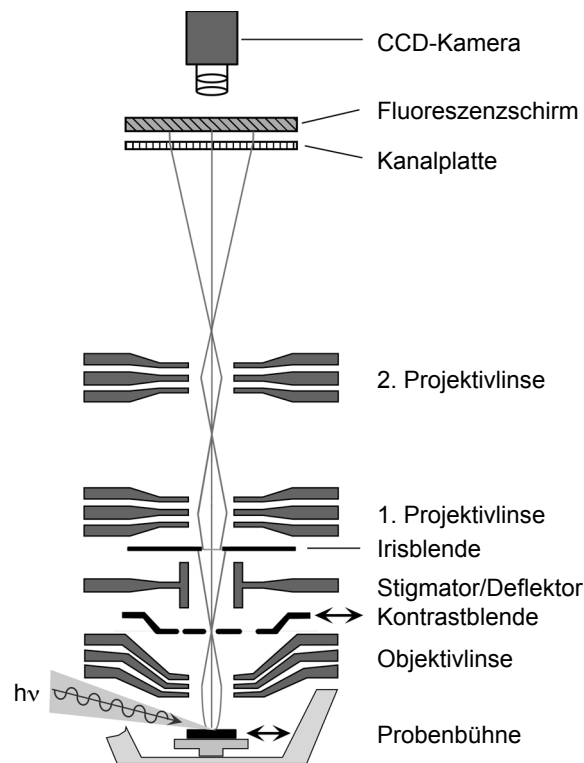
Abbildung 1.8: Schematische Darstellung des verwendeten elektrostatischen PEEMs. Von der nach Anregung mit $h\nu$ an der Probenoberfläche vorhandenen Elektronenintensitätsverteilung wird mit der Objektivlinse ein Zwischenbild am Ort der Irisblende erzeugt. Dieses Bild wird mit einer zweistufigen Projektionsoptik nachvergrößert und auf einem Fluoreszenzschirm sichtbar gemacht.

optik. In Abb. 1.8 ist schematisch der Aufbau des hier verwendeten PEEMs gezeigt. Es handelt sich dabei um eine nur leicht modifizierte Version eines kommerziell erhältlichen elektrostatischen Instruments [57]. Die ausschließliche Verwendung von elektrostatischen Elektronenlinsen hat gegenüber magnetostatischen Linsen den Vorteil, dass bei der Untersuchung von magnetischen Proben diese nicht durch magnetische Streufelder von der Elektronenoptik beeinflußt werden können.

In Abb. 1.8 zeigt die Probenseite des Mikroskops nach unten. Die anregende Röntgentstrahlung fällt in der Zeichnung von links auf die Probe, wie mit „$h\nu$" angedeutet. Der Einfallswinkel beträgt dabei konstruktionsbedingt 30° zur Probenoberfläche, was bei der späteren Diskussion der Ergebnisse bei der Anwendung der Summenregeln hinsichtlich von Sättigungseffekten

berücksichtigt werden muss. Die eigentliche Abbildung der Probenoberfläche in die Ebene, an der sich die Irisblende befindet, wird durch eine beschleunigende dreiteilige Kathodenlinse als Objektivlinse bewerkstelligt. Die Elektronen von der Probe werden dabei in einem elektrischen Feld von 10–15 kV von der Probe weg beschleunigt. Die Probe ist somit selbst Teil der Objektivoptik, was gewisse Anforderungen bezüglich der Ebenheit der Oberfläche stellt.

In der Brennebene der Objektivlinse befindet sich die sogenannte Kontrastblende. Da die für die Abbildung verwendeten Elektronen keinen wohldefinierten Startwinkel und keine scharfe Startenergie besitzen, ist die Kontrastblende zur Beschränkung chromatischer Bildfehler und zur Erzielung einer guten Auflösung nötig. Dies wird durch Winkel- und Energieselektion der Elektronen in der Brennebene durch eine kreisförmige Blende von 30–150 μm Durchmesser erreicht. In dem hier beschriebenen Instrument befinden sich mehrere Blenden verschiedenen Durchmessers auf einem Blendenträger, die durch Verschieben in zwei Richtungen in der Brennebene ausgewählt und justiert werden können. Dabei geht eine bessere Ortsauflösung zu Lasten einer hohen Intensität und umgekehrt.

Der Stigmator/Deflektor besteht aus einer Oktupollinse, mit der eine unter Umständen vorhandene Verkippung der Probe sowie ein axialer Astigmatismus aufgrund von Linsenfehlern ausgeglichen werden können. Mit der Irisblende kann das Gesichtsfeld zur Unterdrückung von Streuelektronen eingeschränkt werden. Das in der Bildebene entstandene Bild wird weiterhin mit Hilfe von zwei Projektivlinsen nachvergrößert und auf die Rückseite der Kanalplatte projiziert. Die Kanalplatte selbst ist ein ortsempfindlicher Elektronenvervielfacher, der die für die Sichtbarkeit auf dem Fluoreszenzschirm nötige Elektronenintensität liefert. Das dort entstandene Bild wird schließlich von einer außerhalb der Vakuumapparatur befindlichen CCD-Kamera aufgenommen und an einen Computer weitergeleitet.

Mit dem hier beschriebenen PEEM wurden in Schwellenphotoemission Auflösungen von 20 nm erzielt [58]. Bei Anregung mit Synchrotronstrahlung ist jedoch der chromatische Bildfehler durch die breitere energetische Verteilung der zur Abbildung verwendeten Elektronen deutlich größer, was sich nachteilhaft auf die Auflösung auswirkt. Die normalerweise erzielte Auflösung bei Anregung mit Röntgenstrahlung ist daher um etwa eine Größenordnung schlechter als in Schwellenphotoemission. Beim Einsatz eines PEEMs zur abbildenden Mikrospektroskopie ist es

außerdem wichtig, ausreichend Intensität zur Abbildung zur Verfügung zu haben, damit sich die Messzeiten zur Aufnahme der großen Menge an Energie-/Ortsdaten in vernünftigen Grenzen halten. Für die hier beschriebenen Messungen wurde als Kompromiss eine Ortsauflösung von 500 nm gewählt.

Kapitel 2

Von der magnetischen Domänenabbildung zur abbildenden Mikrospektroskopie

Messungen der Röntgenabsorption sind im Prinzip mit relativ geringem experimentellem Aufwand durchzuführen. Da die Zahl der ausgelösten Elektronen der Stärke der Absorption proportional ist, kann der abfließende Probenstrom zur Messung der Absorption verwendet werden. Die Informationstiefe ist dabei durch die Austrittstiefe der Elektronen bestimmt, die durch die mittlere freie Weglänge der inelastisch gestreuten Sekundärelektronen dominiert wird. Typische Werte für die Tiefe, bei der das Signal auf $1/e$ abgefallen ist, liegen bei den $3d$-Übergangsmetallen um etwa 2 nm [59]. Im einfachsten Fall reicht bereits ein empfindliches Strommessgerät, um so die Absorption der einfallenden Strahlung als Funktion der Photonenenergie zu bestimmen. Voraussetzung für quantitative Messungen ist lediglich die entsprechende Genauigkeit und Stabilität. Darüber hinaus ist es zusätzlich nötig, die Intensität der einfallenden Strahlung zu kennen. Für magnetische Dichroismusmessungen ist dies um so wichtiger, da hier das eigentliche magnetische Messergebnis als kleine Differenz von großen Signalen vorliegt. Bei der quantitativen Auswertung mit den in Abschnitt 1.2.3 beschriebenen Summenregeln wird zudem das Differenzspektrum über die Energiebereiche der L_3- und L_2-Absorptionskanten integriert. Da-

bei kann ein kleiner experimenteller Artefakt, der die Lage der Nulllinie leicht verfälscht, einen gravierenden Einfluß auf das Ergebnis haben. Um die Summenregeln vernünftig anwenden zu können, muss daher sorgfältig und unter konstanten Bedingungen der Probenstrom und das Signal eines Intensitätsmonitors gemessen werden. Hier muss berücksichtigt werden, dass bei Verwendung von Synchrotronstrahlung die einfallende Intensität auch zeitlichen Schwankungen, zum Beispiel durch die Abnahme des Elektronenstroms im Speicherring oder durch Strahllageschwankungen, unterworfen ist. Magnetfelder am Ort der Probe können ebenfalls einen Einfluss auf das gemessene Probenstromsignal haben, da es dadurch zum Wiedereintritt eines Teils der emittierten Elektronen kommen kann, der dann über die Probenstrommessung nicht erfasst wird.

All das eben gesagte gilt natürlich in gleichem Maße auch für die Durchführung von abbildender XMCD-Mikrospektroskopie. Zusätzlich müssen hier noch die folgenden, für die abbildende Mikrospektroskopie spezifischen Erfordernisse beachtet werden: Die Normierung auf die lokale einfallende Intensität, das eventuelle Vorhandensein einer Energiedispersion über den Bildbereich, sowie die erhöhten Anforderungen an die Stabilität der Abbildung und die Linearität des Bildaufnahmesystems. Im folgenden Abschnitt wird kurz beschrieben, wie sich diese Effekte auswirken, und was man tun kann, um deren Einfluss möglichst gering zu halten.

2.1   Experimentelle Erfordernisse

Der gravierendste Unterschied zwischen abbildender XMCD-Mikrospektroskopie und gewöhnlicher, räumlich mittelnder XMCD-Spektroskopie liegt in der Normierung auf die einfallende Intensität. Bei integrierenden XMCD-Messungen trägt die gesamte auf der Probe einfallende Intensität zum gemessenen Signal bei, egal wie groß der Messfleck auf der Probe ist. Es ist daher relativ leicht, die Intensität der einfallenden Strahlung zu bestimmen. Dazu wird üblicherweise der Photostrom eines Strahlmonitors verwendet. Dieser kann entweder ein im Strahlengang befindliches Netz aus Gold oder einem anderen inerten Material sein, oder ein optisches Element des Strahlrohrs selbst, das elektrisch isoliert aufgehängt ist. Da bei beiden Messungen, sowohl der Messung der Absorption auf der Probe als auch der Bestimmung der Intensität der einfallenden Strahlung über den gesamten Photonenstrahl integriert wird, kann die Normierung durch einfache Division des Probensignals und des Monitorsignals erfolgen. Anders bei der abbil-

denden Mikrospektroskopie: Da hier das Probensignal ortsaufgelöst gemessen wird, müsste zur Normierung gleichzeitig die Intensität der einfallenden Strahlung ebenso ortsaufgelöst gemessen werden. Dies ist allerdings nicht ohne weiteres möglich.

Das Ziel ist es daher, das Experiment so durchzuführen, dass die einfallende Intensität an jeder Stelle des Bilds für alle Photonenenergien und Helizitäten immer proportional zur integrierten Intensität des einfallenden Röntgenstrahls ist. In diesem Fall, wenn also die laterale räumliche Verteilung der einfallenden Intensität konstant wäre, könnte man durch Normierung auf das integrale Monitorsignal die Energieabhängigkeit und den zeitlichen Verlauf des Photonenflusses herauskorrigieren. Die Unterschiede im lokalen Photonenfluss, die bei dieser Normierung natürlich nicht erfasst werden, können dann über die Intensität der lokalen helizitätsgemittelten XMCD-Mikrospektren ermittelt werden.

Das Problem bei der Verwendung von Synchrotronstrahlung ist, dass bei den in Synchrotronstrahlungsquellen der dritten Generation verwendeten Insertion Devices die Intensitätsverteilung im Photonenstrahl energieabhängig ist. Abb. 2.1 zeigt schematisch das Prinzip eines solchen Insertion Devices, eines sogenannten Undulators. Die Elektronen im Speicherring werden durch eine periodische Anordnung von Permanentmagneten auf eine wellenförmige Bahn gezwungen. Die an jedem Wellenbauch emittierte elektromagnetische Strahlung überlagert sich kohärent.
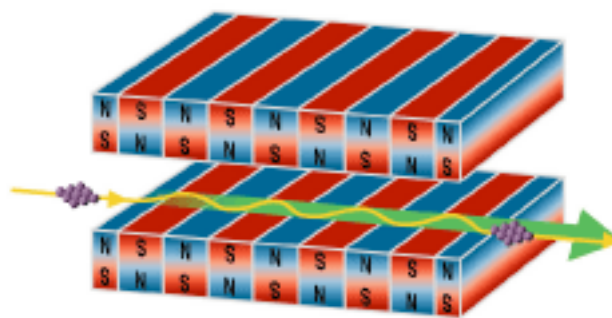

Abbildung 2.1: Schematische Darstellung eines Undulators zur Erzeugung von hochbrillanter Synchrotronstrahlung. Elektronenpakete werden durch periodische Anordnung von Permanentmagneten auf eine wellenförmige Bahn gezwungen. Die Emission von elektromagnetischer Strahlung von jedem der Wellenbäuche verstärkt sich bei bestimmten Photonenenergien kohärent. (Quelle: SPring-8).

Bei bestimmten Photonenenergien, den sogenannten Undulatorharmonischen, führt dies zu einer Verstärkung der Intensität. Durch Verstellung des vertikalen Abstands zwischen unterer und oberer Magnetträgerleiste, des sogenannten Undulatorgaps, kann die Stärke der Magnetfelder am Ort des Elektronenstrahls und somit die energetische Lage der Undulatorharmonischen verändert werden.

Die in den folgenden Kapiteln beschriebenen Messungen wurden an der Synchrotronstrahlungsquelle SPring-8 in Japan durchgeführt. Durch die Auslegung des Elektronenspeicherrings auf hohe Energien—bei SPring-8 sind es 8 GeV Elektronenenergie—besteht ein Undulator für weiche Röntgenstrahlung aus relativ wenigen und dafür langen Magnetfeldperioden [60]. Die resultierende Harmonische ist daher vergleichsweise breitbandig. Bei Synchrotronstrahlungsquellen, die speziell für weiche Röntgenstrahlung ausgelegt sind, erhält man durch die höhere Zahl von Perioden im Undulator eine entsprechend höhere Intensität, aber auch eine schmalbandigere Energieverteilung. Abb. 2.2 zeigt das gemessene Energiespektrum des verwendeten Undulators bei SPring-8. Die Komplikation für Mikrospektroskopie liegt darin, dass sich über das Energiespektrum der Undulatorharmonischen die laterale Verteilung der Intensität im Photonenstrahl
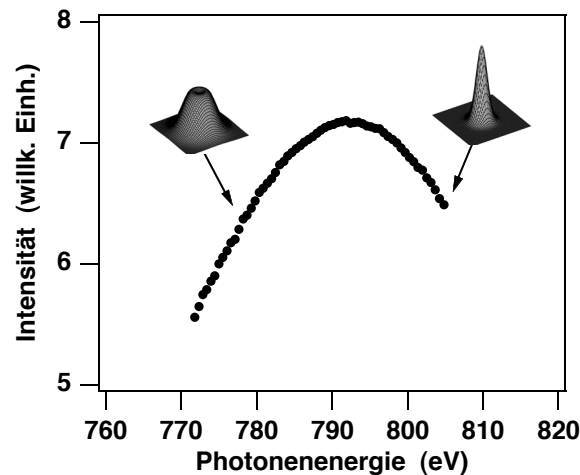

Abbildung 2.2: Die Messkurve zeigt ein typisches gemessenes Intensitätsspektrum der Undulatorharmonischen des BL25SU-Undulators bei SPring-8. Die beiden dreidimensionalen Plots stellen schematisch und übertrieben die unterschiedliche laterale Intensitätsverteilung auf der höher- und niederenergetischen Seite der Harmonischen dar. Dies ist eines der Hauptprobleme bei der Normierung des lokalen Photonenflusses in abbildender Mikrospektroskopie.

ändert. Dies ist in Abb. 2.2 schematisch übertrieben mit Hilfe der beiden dreidimensionalen Plots dargestellt. Auf der höherenergetischen Seite der Harmonischen, in Abb. 2.2 rechts, ist die Intensität stärker in der Mitte des Lichtflecks konzentriert, während auf der niederenergetischen Seite mehr Intensität auch außerhalb der Mitte vorliegt. Bei einem Energiescan über die Undulatorharmonische verschiebt sich also die Intensitätsverteilung über das Bildfeld, ohne dass dies aus dem integralen Monitorsignal erkennbar wäre.

Im Experiment muss man versuchen, diesen Effekt zu minimieren, indem man zum einen den Lichtfleck möglichst mittig zu dem vom Mikroskop abgebildeten Bildfeld justiert. Dort ist der Unterschied bei Variation der Photonenenergie am geringsten. Zum anderen muss man versuchen, den im Intensitätsmonitor gemessenen integralen Photonenfluss möglichst gut an das Bildfeld anzupassen. Dazu wird die beleuchtete Fläche auf der Probe durch geeignete Blenden im Strahlrohr soweit reduziert, dass außerhalb des Bildfelds möglichst wenig Photonenfluss auf die Probe trifft. Damit erreicht man, dass der vom Monitor gemessene integrale Photonenfluss des Lichtstrahls dem über das Bildfeld gemittelten Photonenfluss nahe kommt und nicht durch außerhalb des Bildfelds liegende energieabhängige Intensitätsverteilung zusätzlich verfälscht wird. Durch sorgfältige Durchführung dieser beiden Maßnahmen konnte bei den in den nachfolgenden Kapiteln vorgestellten Messungen der durch die Energieabhängigkeit der Photonenflussverteilung hervorgerufene Fehler auf unter 7% reduziert werden. Im Falle von schmalbandigeren Harmonischen kommt man aber nicht umhin, zusätzlich zur Photonenenergie des Monochromators auch die Position der Undulatorharmonischen durch synchrones Bewegen des Undulatorgaps zu verändern, um so relativ zum Energiemaximum der Undulatorharmonischen immer an derselben Stelle zu messen.

Abb. 2.3 zeigt den Einfluss dieser energieabhängigen Intensitätsverteilung auf XMCD-Mikrospektren am Beispiel eines $3 \times 3 \ \mu\text{m}^2$ großen Bildpunkts eines dünnen Eisenfilms. In Bild (a) sind gemessene Rohdaten der Fe-$L_{2,3}$-Absorption vor der Normierung dargestellt. Absorptionsspektren für positive Lichthelizität sind als durchgezogene Linien, Spektren für negative Helizität als gestrichelte Linien gezeichnet. Das zugehörige Monitorsignal, das den integralen Photonenfluss als Funktion der Photonenenergie wiedergibt, ist in Bild (b) abgebildet. Dieses Monitorsignal ist für alle Mikrospektren identisch. Man erkennt, dass die einfallende Intensität für negative
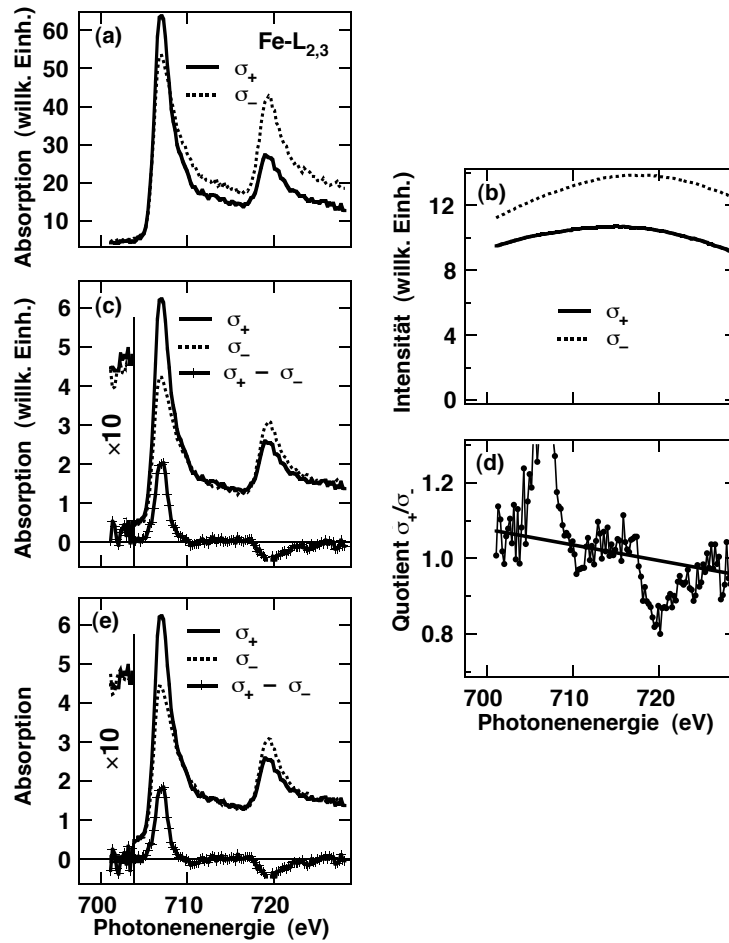
Abbildung 2.3: Beispiel für den Einfluss der energieabhängigen lateralen Intensitätsverteilung auf XMCD-Mikrospektren und dessen Korrektur. Gezeigt sind XMCD-Mikrospektren an der Fe-$L_{2,3}$-Kante eines $3 \times 3\ \mu m^2$ großen Bildpunkts von 10 ML Fe/6 ML Co/Cu(001). Absorptionsspektren für positive Lichthelizität sind als durchgezogene Linien, Spektren für negative Helizität als gestrichelte Linien gezeichnet. (a): gemessene Rohdaten ohne Normierung. (b): Monitorsignal, gibt integralen Photonenfluss als Funktion der Photonenenergie wieder. (c): Absorptionsspektren nach Normierung auf Monitorsignal. Am unteren Bildrand ist das Differenzspektrum dargestellt. Unterhalb von 704 eV Photonenenergie sind die Spektren um einen Faktor 10 vergrößert wiedergegeben. (d): Quotient aus den beiden Absorptionsspektren aus (c). Die gerade Linie zeigt das Ergebnis eines linearen Fits an diese Daten, wobei die Peakregionen der Fe-Absorptionspeaks beim Fit ausgenommen wurden. Im Idealfall sollte diese Linie bei 1.0 verlaufen. Abweichungen davon sind das Resultat der unterschiedlichen lokalen Energieabhängigkeit der Intensitätsverteilung bei positiver und negativer Helizität, das im integralen Monitorsignal nicht enthalten ist. (e): Spektren aus (c), nachdem die Kurve für negative Helizität mit der Geraden aus (d) multipliziert wurde. Das entsprechende Differenzspektrum ist am unteren Bildrand abgebildet. Unterhalb von 704 eV Photonenenergie sind die Spektren wieder um einen Faktor 10 vergrößert dargestellt. Im Vergleich zu (c) erkennt man hier die bessere Übereinstimmung der Spektren in der Vorkantenregion. (Aus [61].)

Helizität um etwa 20–25% höher ist als die für positive Helizität. Das liegt daran, dass für die unterschiedlichen Helizitäten verschiedene, hintereinander angeordnete Undulatoren verwendet wurden. Dabei befand sich der für negative Helizität verwendete Undulator näher an der Lochblende, die den Lichtstrahl in das Strahlrohr ausblendet. Man erkennt auch, dass trotz nominell identischer Einstellung der beiden Undulatoren eine Energieverschiebung des Maximums der Undulatorharmonischen um etwa 4 eV zwischen den beiden Helizitäten auftrat.

Bild (c) zeigt die Daten aus (a) nach der Normierung auf dieses Monitorsignal. Am unteren Bildrand ist das zugehörige Differenzspektrum dargestellt. Unterhalb von 704 eV Photonenenergie sind die Spektren um einen Faktor 10 vergrößert wiedergegeben, um die Übereinstimmung der Spektren in der Vorkantenregion besser beurteilen zu können. Die Linien bei etwa 4.5 auf der y-Achse sind dabei die vergrößerten Absorptionsspektren. Man erkennt, dass die beiden Spektren nicht genau deckungsgleich sind, wie man das in der Vorkantenregion eigentlich erwartet. Das Signal für positive Helizität liegt etwas höher als das für negative Helizität. Dies ist der Einfluss der oben beschriebenen Energieabhängigkeit der lateralen Intensitätsverteilung, der nach Optimierung von Ausleuchtung und Mittigkeit des Bildfelds noch als kleiner Resteffekt in den Spektren zu sehen ist.

Zur Korrektur wurde die folgende Prozedur verwendet: Zunächst wurde der Quotient aus den beiden Absorptionsspektren von Bild (c) gebildet. Dieser ist in Bild (d) dargestellt, in dem das Verhältnis von Absorption bei positiver Helizität zu Absorption bei negativer Helizität gezeigt wird. Anschließend wurde daran numerisch eine Gerade angepasst, wobei die beiden Peakregionen der Fe-Absorptionspeaks bei der Anpassung ausgenommen wurden. Die gerade Linie in Bild (d) ist das Ergebnis einer solchen Anpassung. Im Idealfall sollte diese Linie horizontal bei 1.0 verlaufen. Abweichungen davon sind das Resultat der unterschiedlichen lokalen Energieabhängigkeit der Intensitätsverteilung bei positiver und negativer Helizität. Für den gezeigten Bildpunkt betragen diese Abweichungen +7% am niederenergetischen Ende und −2% am hochenergetischen Ende des Spektrums. Zur Korrektur wurde schließlich die Kurve für negative Helizität aus Bild (c) mit dieser Geraden multipliziert. Die entsprechend korrigierten Absorptionsspektren samt zugehörigem Differenzspektrum sind in Bild (e) dargestellt. Unterhalb von 704 eV Photonenenergie sind die Spektren wieder um einen Faktor 10 vergrößert abgebildet. Im Vergleich

zu (c) erkennt man jetzt die völlige Übereinstimmung der Spektren in der Vorkantenregion. Solange die Abweichungen wie hier nur wenige Prozent betragen, kann der Effekt als linear in der Energie angenommen und wie beschrieben korrigiert werden, ohne dass es zu merklichen Veränderungen der nachfolgenden Auswertung mit den Summenregeln kommt. Bei höheren Abweichungen muss man versuchen, die Justage des Strahlrohrs zu verbessern, oder das Bildfeld und die Ausleuchtung auf der Probe weiter zu reduzieren.

Bei einem verbreiteten Typ von Strahlrohroptik wird der Austrittsspalt mit einem Refokussierspiegel auf die Probe abgebildet. Mit der Größe des Austrittsspalts stellt man bei lateral integrierenden Messungen die gewünschte Energieauflösung ein, wobei eine geringere Auflösung zu einer höheren Intensität und umgekehrt führt. Im Bild des Austrittsspalts liegt dabei senkrecht zum Spalt die vom Monochromator erzeugte Energiedispersion vor. Ein Öffnen des Spalts hat zur Folge, dass der Lichtfleck auf der Probe und gleichzeitig der Bereich der durch den Spalt selektierten Photonenenergien größer wird. Im Fall von räumlich mittelnden Messungen ist dies genau der gewünschte Effekt. Bei abbildenden Messungen dagegen bestimmt bei einer solchen Refokussieroptik nicht mehr die Spaltgröße die lokale Energieauflösung, sondern die laterale Auflösung der Abbildung, die in der Regel deutlich kleiner ist. Eine Veränderung der Spaltgröße führt daher lediglich zu einer Vergrößerung des Beleuchtungsflecks, aber nicht zu einer Änderung der Auflösung oder zu einer Erhöhung der Photonenflussdichte. Dies kann zum Beispiel zu der im vorigen Abschnitt erwähnten Reduktion des Lichtflecks auf der Probe verwendet werden. Die wichtige Implikation für Mikrospektroskopie ist aber, dass über den Bereich des Lichtflecks ständig eine Photonenenergiedispersion vorliegt. Der Gradient dieser Dispersion ist dabei durch die am Monochromator eingestellte Strahlrohroptik bestimmt. Besonders bei großen Bildfeldern und scharfen Absorptionslinien kann sich dies durchaus bei der Auswertung bemerkbar machen, und muss entsprechend korrigiert werden. In den in den nachfolgenden Kapiteln vorgestellten Messungen betrug dieser Gradient etwa 0.25 meV/μm. Da aber in Zusammenhang mit einem großen Bildfeld nur die relativ breite Eisenabsorptionskante verwendet wurde, und bei der schärferen Nickelabsorptionskante ein kleineres Bildfeld gewählt wurde, konnte ohne Korrektur ausgekommen werden.

Weitere zu testende Punkte vor der Aufnahme von Mikrospektren betreffen die Stabilität

der Bilderzeugung und die Linearität des Bildwandlersystems. Besonders für hochauflösende Mikrospektroskopie ist es wichtig, dass die Abbildung nicht durch unterschiedliche Elektronenintensität beeinflusst wird, wie es zum Beispiel durch Raumladungseffekte geschehen kann. Für metallische Proben und abgeschirmte Keramikbauteile stellt dies jedoch normalerweise kein Problem dar. Ein typisches Bildwandlersystem besteht aus mehreren Komponenten wie Kanalplatten, Fluoreszenz-Leuchtschirm und Videokamera, deren Linearität zunächst überprüft werden muss. Ein berühmtes Beispiel für Nichtlinearitäten im Zusammenhang mit der Verwendung eines Bildwandlersystems zur Detektion von ortsintegrierenden Photoelektronenspektren ist die Veröffentlichung der „Multi-atom resonant photoemission" [62], die später in dieser Form als Artefakt, hervorgerufen durch krasse Nichtlinearitäten des Detektors, widerrufen werden musste [63]. Beides, sowohl die Stabilität der Abbildung gegenüber unterschiedlichen Intensitäten als auch die Linearität des Detektorsystems lassen sich durch gezielte Variation der einfallenden Primärintensität relativ leicht testen. Im vorliegenden Fall wurden bei den verwendeten Einstellungen keinerlei Abweichungen vom idealen Verhalten gefunden. Lediglich bei sehr hohen Spannungen der Kanalplatten, die für die Mikrospektroskopiemessungen vermieden wurden, wurde ein langsamer zeitlicher Abfall des Verstärkungsfaktors um etwa 10% beobachtet, der vermutlich auf Erwärmung durch den Dunkelstrom zurückzuführen ist.

2.2 Datenauswertung

Nachdem der durch den Unterschied von lokaler Photonenflussdichte und integralem Monitorsignal verbleibende Fehler wie im vorangegangenen Abschnitt beschrieben korrigiert ist, könnte die eigentliche Auswertung der Mikrospektren mit den in Abschnitt 1.2.3 beschriebenen Summenregeln wie in der Literatur [19,64,65] beschrieben durchgeführt werden. Der Hauptunterschied zwischen herkömmlicher XMCD-Spektroskopie und abbildender XMCD-Mikrospektroskopie ist jedoch, dass es in der abbildenden Mikrospektroskopie in der Regel um die Auswertung von vielen zehntausend XMCD-Spektren, nämlich der aller Bildpunkte in einem Mikroskopiebild geht. Es ist daher zwingend notwendig, die Auswertung zu automatisieren. Dazu wird ein Verfahren benötigt, das zum einen schnell genug ist, eine pixelweise Bildauswertung mit den Summenregeln in einer vernünftigen Zeit zu bewältigen, und zum anderen robust genug funktioniert, um

auch mit eventuell verrauschten Differenzspektren einzelner Bildpunkte fertig zu werden. Ein Verfahren, dass diesen beiden Anforderungen gewachsen ist, wird im nachfolgenden beschrieben.

Man nutzt dabei aus, dass sich die spektrale Form der einzelnen Absorptionspeaks über einen mikroskopischen Bildausschnitt meistens nicht ändert. Die Information über die magnetischen Momente ist in der relativen Höhe der L_3- und L_2-Absorptionspeaks bei unterschiedlicher Helizität enthalten. Die Auswertung von XMCD-Spektren mit den Summenregeln zielt normalerweise darauf ab, zwei Zahlenwerte als Ergebnis zu erhalten, nämlich die magnetischen Spin- und Bahnmomente. Gleichungen 1.2 und 1.3 geben an, wie sich diese zwei Größen aus den zwei Flächen A und B ergeben, die man aus der Integration über die L_3- und L_2-Absorptionskante im Differenzspektrum erhält. Unter der Annahme jeweils konstanter spektraler Form der Differenzpeaks an den beiden Kanten sind diese Flächen proportional zur Höhe der Peaks. Um den Fehler in der Bestimmung der Höhe der Differenzpeaks klein zu halten, ist es günstig, statt einiger weniger Datenpunkte am Peakmaximum die Information des gesamten Energiespektrums heranzuziehen, indem man die Peaks durch eine geeignete Kurve anpasst. Im Idealfall sind füer diese Anpassung lediglich zwei freie Parameter nötig. Die Zahl der freien Parameter entspricht dabei den zwei Freiheitsgraden des Endergebnisses, nämlich Spin- und Bahnmoment. Anstatt die Peakform durch mathematische Kurven anzunähern, bei denen dann letztendlich sowieso alle Parameter ausser der Höhe konstant gehalten werden, ist es einfacher, aus den vorhandenen experimentellen Daten eine Musterkurve zu generieren, und diese an die Differenzspektren der einzelnen Bildpunkte anzupassen. Mit diesem Verfahren, das im Folgenden an einem Beispiel anschaulich erläutert wird, ist es möglich, große Mengen an XMCD-Spektren mit gleicher Kurvenform der Einzelpeaks verlässlich automatisch auszuwerten.

Zunächst muss dazu eine Musterkurve generiert werden. Um eine möglichst gute Statistik zu erhalten, bietet es sich an, räumlich über eine große Domäne im Bild zu mitteln, oder aber, falls sich die Magnetisierung über den ganzen Bildausschnitt nicht zu Null mittelt, die Intensität über das ganze Bild zu integrieren. Dadurch erhält man ein einzelnes XMCD-Spektrum, das man „von Hand" auswerten kann. Diese Auswertung beinhaltet die in Abschnitt 1.2.3 beschriebene Integration über das Differenzsignal an den L_3- und L_2-Kanten, sowie die Normierung auf die Gesamtintensität mittels Gleichung 1.4. Abb. 2.4 (a) zeigt als Beispiel Eisen-Absorptionsspektren,
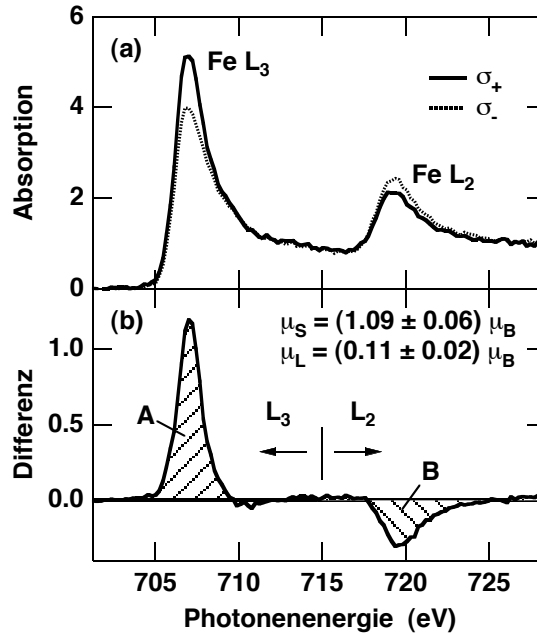
Abbildung 2.4: (a): Gemitteltes Absorptionsspektrum der Eisen-$L_{2,3}$-Kante einer 1.2 ML Ni/0–14 ML Fe/6 ML Co/Cu(001)-Probe für positive Helizität (durchgezogene Linie) und negative Helizität (gepunktete Linie). (b): Differenz der beiden Spektren aus (a) als Musterspektrum zur Anpassung an XMCD-Spektren einzelner Bildpunkte. Dazu wird die Kurve bei 715 eV Photonenenergie in zwei Segmente geteilt, die für die Anpassung unabhängig voneinander skaliert werden. Das Ergebnis der Summenregel-Auswertung des Musterspektrums für das Spinmoment (μ_S) und das Orbitalmoment (μ_L) von Eisen ist in (b) angegeben. Die dabei in Glg. 1.2 und 1.3 verwendeten Flächen unter den Differenzpeaks A und B sind durch Schraffuren gekennzeichnet.

die durch Mittelung über 5644 Bildpunkte von einer 1.2 ML Ni/Fe/6 ML Co-Dreilagenschicht erhalten wurden. Die Eisenschichtdicke stieg dabei über den Bildbereich von 0 bis 14 ML linear an. Das Spektrum für positive Helizität ist als durchgezogene Linie, das für negative Helizität als gepunktete Linie dargestellt. Das Differenzsignal aus dieser Mittelung bildet nun die Musterkurve. Sie ist in Abb. 2.4 (b) abgebildet. Die Flächen A und B unter den Differenzpeaks der Fe-L_3- und Fe-L_2-Absorptionsmaxima, die in Gleichungen 1.2 und 1.3 verwendet werden, sind schraffiert dargestellt. Die Summenregel-Auswertung dieser Spektren ergibt als Spinmoment $\mu_S = (1.09 \pm 0.06)\ \mu_B$, als Bahnmoment $\mu_L = (0.11 \pm 0.02)\ \mu_B$ [66]. Für die Anpassung der Differenzkurve aus Abb. 2.4 (b) an die Differenzspektren der einzelnen Bildpunkte wird sie bei einer Energie unterhalb des L_2-Peaks, im vorliegenden Beispiel bei 715 eV, in zwei Teile

geteilt, die dann bei der Anpassung jeweils mit einem eigenen Faktor skaliert werden, um die Differenzkurven der einzelnen Bildpunkte wiederzugeben.
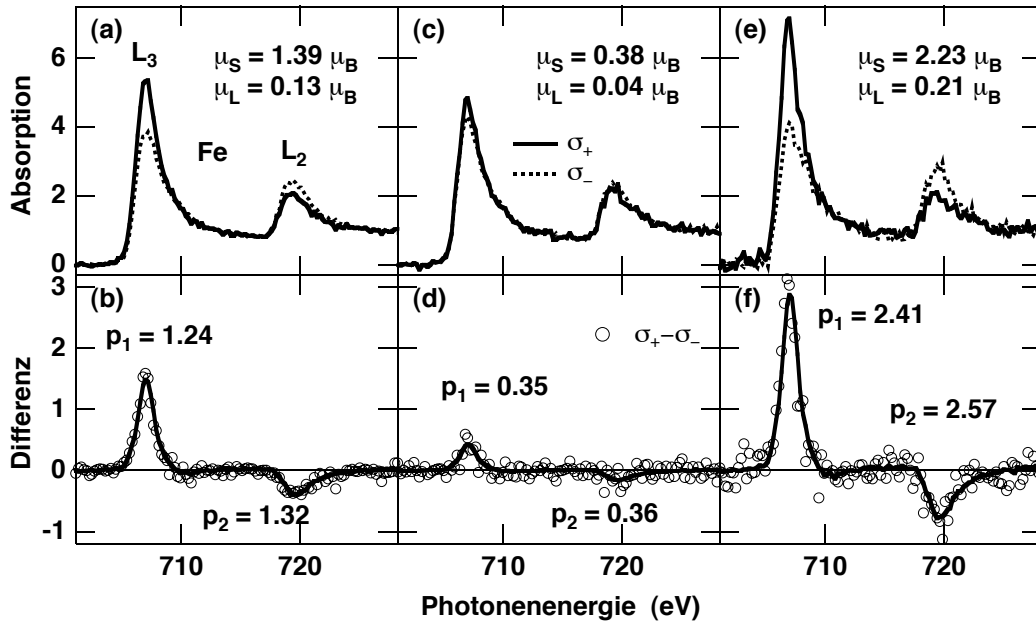

Abbildung 2.5: Beispiel für die automatische Summenregel-Auswertung mit Hilfe des Musterfits. (a), (c), (e): Absorptionsspektren einzelner $3 \times 3 \ \mu m^2$-Bildpunkte für positive Helizität (durchgezogene Linien) und negative Helizität (gestrichelte Linien). Die Probe war 1.2 ML Ni/Fe/6 ML Co/Cu(001), mit Fe-Schichtdicken von 10 ML (a), 5 ML (c) und 2 ML (e). (b), (d), (f): Differenz der Spektren aus (a), (c) und (e) (offene Kreise). Die durchgezogenen Linien sind Segmente der Muster-Differenzkurve aus Abb. 2.4 (b), die an der L_3-Kante mit p_1, an der L_2-Kante mit p_2 skaliert wurden, um die Differenzspektren der einzelnen Bildpunkte anzupassen. Das Spinmoment μ_S und das Orbitalmoment μ_L der einzelnen Bildpunkte, berechnet nach Gleichungen 2.1 und 2.2 aus p_1, p_2 und den Momenten des Musterspektrums sind in (a), (c) und (e) angegeben.

Abb. 2.5 zeigt als Beispiel drei Eisen-XMCD-Spektren einer 1.2 ML Ni/Fe/6 ML Co-Drei-lagenschicht auf Cu(001). Die Spektren stammen von einzelnen Bildpunkten des zu Abb. 2.4 gehörenden XMCD-Datensatzes und entsprechen jeweils $3 \times 3 \ \mu m^2$ Fläche auf der Probe. Die Eisenschichtdicke an den entsprechenden Bildpunkten betrug, von links nach rechts, 10, 5 und 2 ML. Diese Schichtdicken wurden für das vorliegende Beispiel gewählt, um möglichst verschiedene magnetische Momente im Eisen vorliegen zu haben. Die drastische Änderung des atomaren magnetischen Moments in diesen Eisenschichten als Funktion der Schichtdicke ist eine Folge des Zusammenhangs zwischen Struktur und Magnetismus, der in dünnen Eisenfilmen auf fcc-

Substraten besonders ausgeprägt ist. Dies wird ausführlicher in Abschnitt 3.1 diskutiert.

In der oberen Reihe von Abb. 2.5 sind jeweils die Absorptionsspektren der einzelnen Pixel für positive Helizität (durchgezogene Linien) und negative Helizität (gestrichelte Linien) abgebildet. Die zugehörigen Differenzspektren sind in der unteren Reihe mit offenen Kreisen wiedergegeben. Die durchgezogenen Linien in den Differenzspektren stellen die Ergebnisse der Anpassungen mit der in Abb. 2.4 (b) abgebildeten Musterkurve dar. Sie ergeben sich aus den zwei unabhängig skalierten Segmenten der Musterkurve. Anpassparameter sind die beiden Skalierungsfaktoren p_1 und p_2, die man braucht, um die Musterkurve an ein Differenzspektrum eines Bildpunkts anzupassen. Die jeweils verwendeten Werte für p_1 (Skalierung an der L_3-Kante) und p_2 (Skalierung an der L_2-Kante) sind in Abb. 2.5 (b), (d) und (f) angegeben. Mit diesen beiden Werten kann man das Ergebnis der Summenregel-Auswertung der Musterkurve auf die einzelnen Bildpunkte umrechnen. Aus Gleichungen 1.2 und 1.3 erhält man:

$$\mu_{S,P} \;=\; C_M/C_P \left[p_1 \left(\frac{1}{3}\,\mu_{S,M} \;+\; \mu_{L,M} \right) + p_2 \left(\frac{2}{3}\,\mu_{S,M} - \mu_{L,M} \right) \right] \tag{2.1}$$

$$\mu_{L,P} \;=\; C_M/C_P \left[p_1 \left(\frac{2}{9}\,\mu_{S,M} + \frac{2}{3}\,\mu_{L,M} \right) + p_2 \left(-\frac{2}{9}\,\mu_{S,M} + \frac{1}{3}\,\mu_{L,M} \right) \right]. \tag{2.2}$$

Dabei bezeichnen Indizes P die Momente der einzelnen Bildpunkte, Indizes M die Momente des Musterspektrums. Der Korrekturfaktor C_M/C_P berücksichtigt Änderungen in der helizitätsgemittelten Gesamtintensität der Absorptionsspektren bei der Bestimmung des Proportionalitätsfaktors C nach Gleichung 1.4. Die mit diesen Gleichungen berechneten Spin- und Bahnmomente $\mu_{S,P}$ und $\mu_{L,P}$ der drei im Beispiel gezeigten Bildpunkte sind in Abb. 2.5 (a), (c) und (e) angegeben.

Die Vorteile dieser Methode der Anpassung an eine Musterkurve sind eine einfache numerische Anpassung ohne komplizierte Formelberechnung, was hilft, die Verarbeitungszeiten niedrig zu halten, und ein stabiles Verhalten selbst bei verrauschten und kleinen Differenzsignalen. Das Ergebnis stellt eine Mittelung über die einzelnen Datenpunkte in den Differenzspektren dar, wobei automatisch eine stärkere Wichtung der Punkte an den Absorptionsmaxima stattfindet; Punkte weit ausserhalb der Absorptionsmaxima spielen bei dieser Anpassung keine Rolle. Es sollte jedoch vor Anwendung an mehreren Stellen im Bild geprüft werden, ob die Voraussetzung für die Anwendbarkeit dieser Methode, nämlich die konstante Kurvenform der Absorptionspeaks

über den gesamten Bildbereich, gegeben ist.

Kapitel 3

Ausgewählte Ergebnisse

3.1 Magnetische Phasen in fcc-Eisenfilmen

Bereits bei Betrachtung von Abb. 2.5 des vorigen Kapitels konnte man eine Vorstellung davon bekommen, wie unterschiedlich das magnetische Moment von ultradünnen Eisenfilmen auf einem Cu(001)-Substrat je nach Schichtdicke sein kann. Dies liegt an den unterschiedlichen strukturellen und magnetischen Phasen, die diese Filme annehmen. Von besonderem Interesse ist dabei eine Phase, bei der das Eisen in fcc-Form vorliegt und nichtferromagnetisches Verhalten zeigt. Abgesehen von grundlagenorientierten Fragen zur Spinstruktur in einer solchen nichtferromagnetischen fcc-artigen Eisenschicht ist sie auch hinsichtlich der magnetischen Kopplung von benachbarten ferromagnetischen Schichten interessant. In diesem Abschnitt werden Untersuchungen von Eisenfilmen, die sich zwischen ferromagnetischen Kobalt- und Nickelschichten befinden, mit abbildender XMCD-Mikrospektroskopie vorgestellt. Um die verschiedenen Phasen des Eisens zu erhalten, wurde das Dreilagensystem aus Ni/Fe/Co bei Raumtemperatur epitaktisch auf Cu(001) aufgewachsen. Der Einsatz von abbildender Mikrospektroskopie erlaubt es, die Filme mit keilförmigem Schichtdickenprofil aufzubringen und so innerhalb eines Bilds die komplette Schichtdickenabhängigkeit von Spin- und Bahnmoment zu untersuchen. Wegen der Elementselektivität von XMCD ist es darüberhinaus möglich, die Magnetisierungsrichtungen in den ferromagnetischen Nickel- und Kobaltschichten zu bestimmen, um so Information über die magnetische Zwischenschichtkopplung durch die Eisenschicht hindurch zu erhalten.

3.1.1   Fe/Cu(001)

Die Gitterkonstante von Kupfer bietet die Möglichkeit, Eisen in Form von ultradünnen Filmen auf Kupfersubstraten in der fcc-Modifikation herzustellen [67], die im Volumen nur bei Temperaturen oberhalb von 1183 K existiert. Erste systematische Kerr-Effekt-Messungen der Schichtdickenabhängigkeit von Fe/Cu(001) zeigten einen diskontinuierlichen Verlauf des Sättigungssignals mit der Schichtdicke [68], der schnell das Interesse vieler Forschergruppen auf dieses System und den Zusammenhang zwischen Struktur und Magnetismus in ultradünnen Eisenfilmen lenkte. Abb. 3.1 zeigt schematisch die Schichtdickenabhängigkeit des magnetischen Moments von Fe/Cu(001). Man kann drei Schichtdickenbereiche unterscheiden, die in Abb. 3.1 mit I, II und III bezeichnet sind. In Phase I und III steigt das Moment linear mit der Schichtdicke an, was auf eine durchgehend ferromagnetische Schicht hindeutet. In Phase II hingegen findet man ein konstantes Moment, das etwa dem von 2 ML Eisen aus Phase I entspricht. Hier trägt also ein signifikanter Teil des Films nicht zum Ferromagnetismus bei.
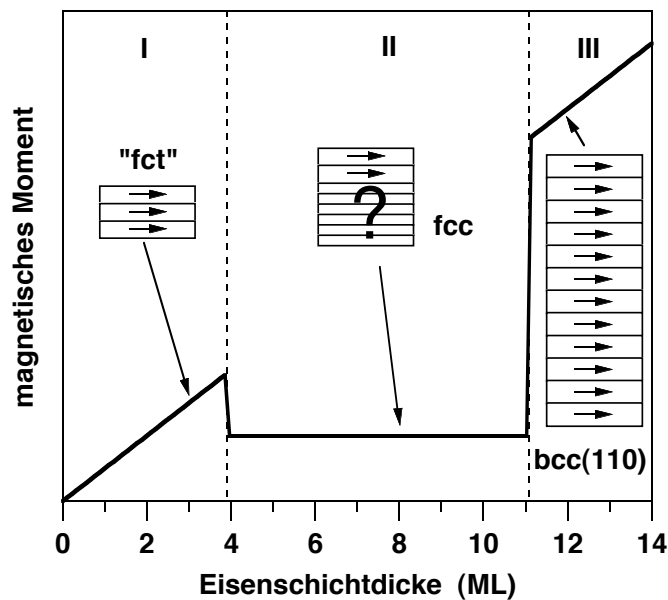

Abbildung 3.1: Schematische Darstellung des magnetischen Moments und der verschiedenen Phasen von Fe/Cu(001) als Funktion der Schichtdicke. Der lineare Anstieg des Moments in Phase I und III deutet auf eine durchgehend ferromagnetische Schicht hin, während in Phase II ein signifikanter Teil des Films nicht zum Ferromagnetismus beiträgt.

Nachfolgende Strukturuntersuchungen ergaben, dass in Phase II zwischen etwa 4 und 11 ML Schichtdicke die inneren Atomlagen des Films in einer fcc-artigen Struktur mit gegenüber dem Cu-Substrat reduzierten vertikalen Lagenabständen vorliegen [69, 70]. Das ferromagnetische Moment wird den obersten Atomlagen zugeschrieben [71, 73], die einen größeren vertikalen Lagenabstand aufweisen [69]. Bei etwa 11 ML Schichtdicke findet eine Transformation zu einer (110)-orientierten bcc-Struktur statt (Phase III), die nicht mehr pseudomorph zum Substrat ist [74–76]. Hier sind die einzelnen Atomlagen dichter gepackt und daher vertikal noch weiter expandiert. Die magnetischen Eigenschaften entsprechen weitgehend denen von Eisen in Volumenproben. Die geometrische Struktur von Filmen in Phase I ist deutlich komplizierter. Zu einem gegenüber Kupfer durch tetragonale Verzerrung expandierten vertikalen Lagenabstand kommt noch eine Korrugation von Atomreihen in der Ebene [77–79]. Neueste Rastertunnelmikroskopieuntersuchungen deuten sogar darauf hin, dass es sich dabei nicht um eine durch tetragonale Verzerrung modifizierte fcc-Struktur handelt, sondern dass diese Phase mit einer tetragonal verzerrten bcc-Struktur beschrieben werden muss [80].

In Abb. 3.1 ist die Struktur der drei Phasen schematisch durch den unterschiedlichen vertikalen Lagenabstand illustriert. Die zum Ferromagnetismus beitragenden Atomlagen sind durch Pfeile gekennzeichnet. Ungeklärt ist bisher die magnetische Konfiguration der inneren, nichtferromagnetischen Lagen in Phase II, die in Abb. 3.1 durch ein Fragezeichen markiert sind. Es wurden schon relativ früh erste experimentelle Hinweise auf eine antiferromagnetische Ordnung in diesen Lagen publiziert [71, 81], wobei sich jedoch die Ordnungstemperaturen signifikant voneinander unterschieden (70 K in Ref. [81], 200 K in Ref. [71]). In den meisten Theorien wird eine antiferromagnetische Konfiguration mit einer zweilagenweisen antiferromagnetischen Ausrichtung der Spins bevorzugt [82–84]. Neueste Experimente deuten auf eine inkommensurable antiferromagnetische Spindichtewelle unterhalb von 200 K hin, bei der nichtkollineare Magnetisierungsrichtungen der einzelnen Lagen auftreten [86].

Dieselbe Abfolge der drei Phasen wurde auch auf anderen Substraten gefunden, so zum beispiel auf $Cu_{90}Au_{10}$(001) [87], das eine um 1.5% größere Gitterkonstante als Kupfer aufweist, sowie auf epitaktischem Co/Cu(001) [88–93]. Sogar in aufgesputterten Multilagensystemen aus Fe/Ni und Fe/$Ni_{81}Fe_{19}$ auf MgO(001)-Substraten, die ähnliche laterale Gitterparameter aufwei-

sen, konnten in den Eisenschichten diese drei Phasen beobachtet werden [94, 95].

Zum offensichtlichem Zusammenhang zwischen Struktur und Magnetismus wurden Theorien herangezogen, die auf der Volumenabhängigkeit der jeweils energetisch günstigsten magnetischen Konfiguration von fcc-Eisen basieren [96–98]. In diesen Berechnungen liegt die Gitterkonstante von Kupfer in einem Bereich, in dem eine sensible Abhängigkeit der magnetischen Phase vom Atomvolumen besteht.

3.1.2   Mikrospektroskopie an Ni/Fe/Co/Cu(001)

Im vorliegenden Beispiel dient die Mikrospektroskopie dazu, durch Verwendung von keilförmigen Schichten möglichst effektiv und genau mittels XMCD die Schichtdickenabhängigkeit der magnetischen Momente zu bestimmen. Die Filme wurden dazu wie in Abb. 3.2 schematisch dargestellt als gekreuzte Doppelkeile aufgebracht. Dazu wurde bei den entsprechenden Verdampfungsschritten eine spaltförmige Blende von $0.5 \times 2\,\mathrm{mm}^2$ in 1 mm Abstand vor die Probenoberfläche gesetzt. Periodisches Vor- und Zurückdrehen der Probe entlang der Blendenlängsrichtung während des Aufdampfens führt zu einem keilförmigen Profil der aufgedampften Struktur rechts und links von einem Plateau. Führt man diese Prozedur für zwei orthogonale Azimuthwinkel der Probe durch, so erhält man die in Abb. 3.2 dargestellte Struktur. Je nach überstrichenem Drehwinkel während der Aufdampfung sind die Anstiegsflanken zwischen 100 und 400 μm breit. Abbildende
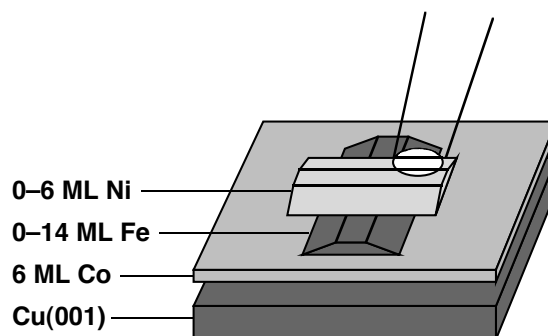

Abbildung 3.2: Schematische Darstellung der gekreuzten Doppelkeile von Nickel und Eisen auf einem kontinuierlichen Kobaltfilm auf Cu(001). Die nachfolgenden Messungen wurden in dem durch den Kreis hervorgehobenen Bereich durchgeführt, in dem sich orthogonal zueinander sowohl die Nickel- als auch die Eisenschichtdicke ändert.

XMCD-Mikrospektroskopie an solch einem gekreuzten Doppelkeil liefert mit einem Bild die gesamte Abhängigkeit der magnetischen Momente von zwei Schichtdicken. Da für diese Messungen keine besondere Ortsauflösung nötig ist, arbeitet man in dem sogenannten Übersichtsmodus des Instruments, bei dem die Objektivlinsenspannung auf etwa 100 V abgesenkt wird. Damit kann man Gesichtsfelder von über 0.5 mm erhalten.

Abb. 3.3 zeigt das Ergebnis der bildpunktweisen Summenregelauswertung für das Spinmoment im Eisen in einem Bereich im Doppelkeil, in dem sowohl der Beginn des Eisenkeils als auch des Nickelkeils enthalten ist. Die Eisenschichtdicke ist an der oberen Achse angegeben, die Nickelschichtdicke an der rechten Achse. Um Domänen zu vermeiden, wurde die Probe vorher in einem externen Magnetfeld von 500 Oe gesättigt. Die drei Phasen von Eisen, wie sie im vorhergehenden Abschnitt besprochen wurden, sind auch im Ni/Fe/Co-Dreilagensystem deutlich zu erkennen. Sie sind in Abb. 3.3 entsprechend gekennzeichnet. Mit ansteigender Nickelschichtdicke erkennt man innerhalb von Phase II einen Bereich in der Umgebung von 5.5 ML Eisenschichtdicke, in dem das Eisenspinmoment gegenüber dem Rest der Phase II nochmal deutlich erniedrigt ist. Dieser Bereich ist mit IIa gekennzeichnet, zur Unterscheidung von Phase IIb bei höheren Fe-Schichtdicken. In Abb. 3.3 (b) sind Linienprofile des Eisenspinmoments als Funktion der Eisenschichtdicke wiedergegeben. Man erkennt auch hier deutlich die in Abb. 3.1 schematisch dargestellten drei Phasen. Man beachte, dass im Unterschied zu Abb. 3.1 hier allerdings nicht das gesamte magnetische Moment des Films, sondern das Spinmoment pro Atom aufgetragen ist.

Die quantitative Auswertung des Spinmoments in den drei Phasen liefert wertvolle Information über die jeweils vorliegende magnetische Spinkonfiguration [66]. So ist zum Beispiel das in Abb. 3.1 gezeigte einfache Modell von Phase II nicht mit dem hier gemessenen Spinmoment vereinbar, da man sonst einen abfallenden Verlauf mit der Eisenschichtdicke beobachten müsste. Der relativ hohe Wert von 0.7 μ_B weist auf ferromagnetische oberste Lagen des Eisenfilms hin. Zur Erklärung der Schichtdickenabhängigkeit des Fe-Spinmoments muss man Rauhigkeiten, die zu Fluktuationen der lokalen Schichtdicke führen, und die sich daraus ergebenden Frustrationen berücksichtigen [66]. Nichtkollineare Spinkonfigurationen [86] oder ferromagnetische bcc-Keime, die schon bei Eisenschichtdicken von 7 ML beobachtet wurden [75, 99], können außerdem eine
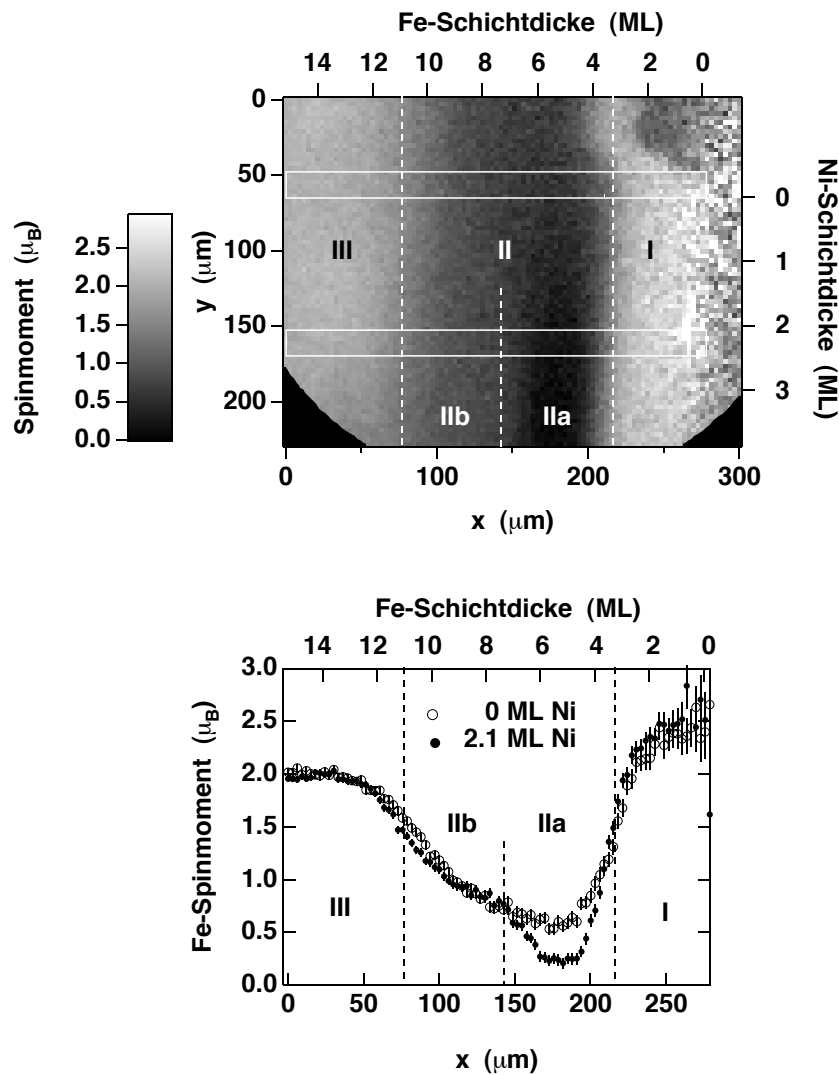
Abbildung 3.3: Ergebnis der abbildenden Mikrospektroskopie des Ni/Fe-Doppelkeils auf 6 ML Co/Cu(001). (a): Grautondarstellung des Fe-Spinmoments pro Atom. Weiße Rechtecke markieren die Position der in (b) gezeigten Linienprofile. Die drei in Abschnitt 3.1.1 vorgestellten Phasen sind gut zu erkennen und mit I, II und III gekennzeichnet. Bei Bedeckung mit Ni kann man in Phase II zwei verschiedene Unterphasen IIa und IIb unterscheiden. (b): Linienprofile entlang des Fe-Keils außerhalb des Ni-Keils (offene Kreise) und bei 2.1 ML Ni-Schichtdicke (ausgefüllte Kreise). (Aus Ref. [66].)

Rolle spielen.

Besonders interessant ist der Abfall des Spinmoments in Phase IIa auf fast Null. Eigene elementaufgelöste Abbildungen an der Ni- und Co-L_3-Kante ergaben nämlich, dass in genau diesem Bereich die Magnetisierung im Ni antiparallel zu der im Co steht [66]. Das gemessene reduzierte

Spinmoment könnte somit durch eine teilweise Kompensation von induziertem Ferromagnetismus im Eisenfilm an den beiden Grenzflächen herrühren. Die antiferromagnetische Kopplung von Ni und Co über die Eisenschicht bei genau dieser Schichtdicke könnte durch die elektronischen Zustände im Potenzialtopf des Eisenfilms hervorgerufen sein [100,101]. Dies nennt man die oszillatorische indirekte Austauschkopplung, die bei der Kopplung über paramagnetische und antiferromagnetische Schichten auftreten kann, und Oszillationen im Vorzeichen der Kopplung mit einer Periode von mehreren atomaren Monolagen aufweist [48]. Bei der Kopplung über antiferromagnetische Schichten geringer Rauhigkeit kann auch eine durch die antiferromagnetische Spindichtewelle hervorgerufene Oszillation überlagert sein [102].

Im vorliegenden System wird nur bei einer Schichtdicke antiferromagnetische Kopplung beobachtet. Dies kann daran liegen, dass der Schichtdickenbereich der Phase II zu gering ist, um mehr als eine Oszillationsperiode zu beinhalten. Durch weitergehende Experimente mit vorsätzlich verschlechterten Vakuumbedingungen konnte der Schichtdickenbereich von Phase II erweitert werden. Tatsächlich konnte in diesem Fall dann eine weitere Stelle bei etwa 11 ML Eisenschichtdicke beobachtet werden, die man als antiferromagnetische Kopplung interpretieren kann [66]. Die sich ergebende Periode von etwa 5.5 ML stimmt mit den üblicherweise bei paramagnetischen fcc-Metallen beobachteten Kopplungsperioden überein [48], während der Interpretation einer inkommensurablen antiferromagnetischen Spindichtewelle von 2.7 ML Periode aus Ref. [86] zufolge eine kürzere Kopplungsperiode beobachtet werden müsste.

Weitere Information über den Magnetismus in der Eisenschicht erhält man aus dem Bahnmoment. Analog zu Abb. 3.3 zeigt Abb. 3.4 das Verhältnis von orbitalem Moment zu Spinmoment. Sättigungseffekte, die auftreten wenn die Eindringtiefe der Röntgenstrahlen an den Absorptionskanten in eine vergleichbare Größenordnung wie die Elektronenaustrittstiefe kommt [59], wurden wie in Ref. [66] beschrieben korrigiert. Aus dem orbitalen Moment kann man zum einen Information über die Dimensionalität der Filme erhalten. Messungen haben gezeigt, dass in zweidimensionalen Systemen das orbitale Moment gegenüber Volumenproben relativ zum Spinmoment erhöht ist [65,103]. Aus Abb. 3.4 sieht man allerdings, dass in Phase II keine nennenswerte Erhöhung des relativen orbitalen Moments zu beobachten ist. Dies würde folglich einer Interpretation von zweidimensionalem Ferromagnetismus an den beiden Grenzflächen mit
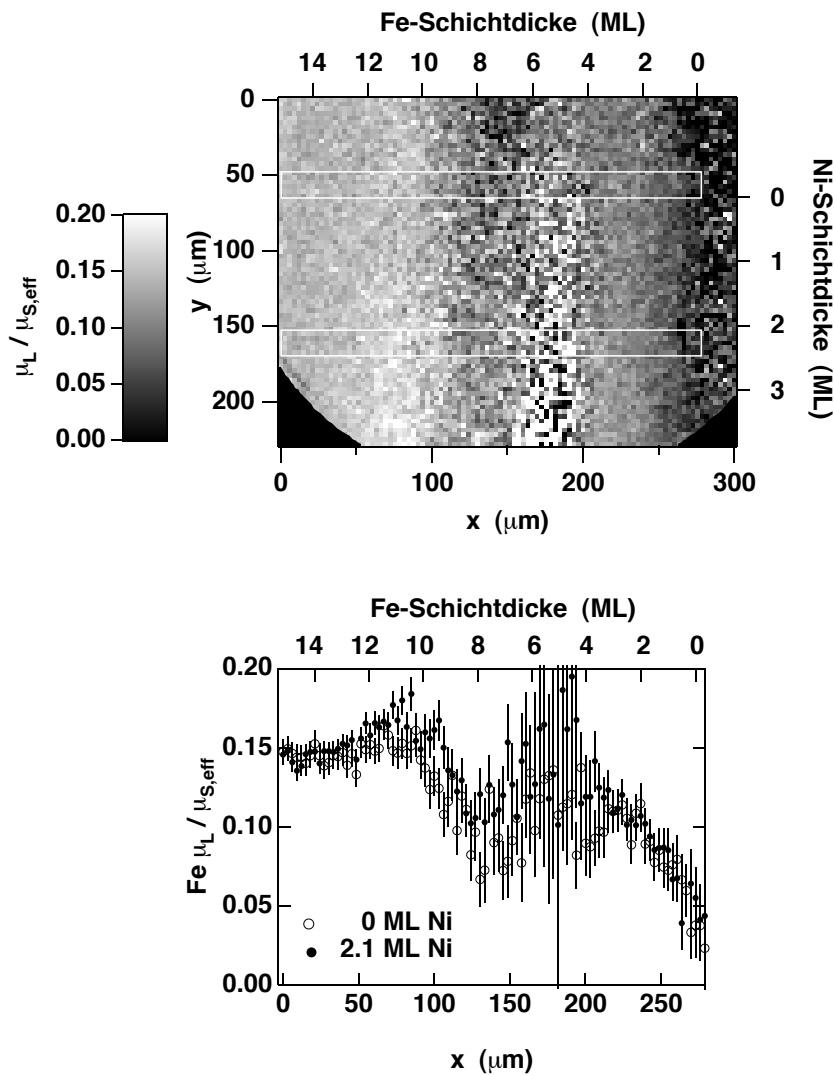
Abbildung 3.4: Ergebnis der abbildenden Mikrospektroskopie des Ni/Fe-Doppelkeils auf 6 ML Co/Cu(001). (a): Grautondarstellung des Verhältnisses von orbitalem Moment zu Spinmoment der Eisenschicht an derselben Stelle wie in Abb. 3.3. Weiße Rechtecke markieren die Position der in (b) gezeigten Linienprofile. (b): Linienprofile entlang des Fe-Keils außerhalb des Ni-Keils (offene Kreise) und bei 2.1 ML Ni-Schichtdicke (ausgefüllte Kreise). Bei kleinen Eisenschichtdicken ist ein kontinuierlicher Anstieg des relativen orbitalen Moments mit der Schichtdicke zu erkennen.

paramagnetischen Lagen dazwischen widersprechen, und auf eine Reduktion des Ferromagnetischen Moments durch antiferromagnetische Ordnung hinweisen. Zum anderen liefert das orbitale Moment, wie im nachfolgenden Abschnitt noch genauer diskutiert wird, Information über die elementaufgelöste magnetische Anisotropie. Diese gibt an, welche magnetische Vorzugsachse in

der jeweiligen Schicht existiert. Das orbitale Moment ist größer, wenn die Magnetisierung mit dieser Vorzugsachse übereinstimmt, als wenn sie senkrecht dazu steht [104–107]. Im vorliegenden Beispiel ist die Probe in der Filmebene magnetisiert. Dies ist eine Folge der starken magnetischen Anisotropie der 6 ML Kobalt. Aus Abb. 3.4 sieht man, dass das relative orbitale Moment in Phase III höher ist als in Phase I und II. Dies stimmt sehr gut mit dieser Interpretation überein, wenn man annimmt, dass die magnetische Vorzugsachsen des Eisenfilms dieselben sind wie in Fe/Cu(001). Dort ist nämlich die Magnetisierung in Phase I und II senkrecht zur Filmebene, in Phase III in der Filmebene [68, 71, 74]. In der vorliegenden Probe wäre also die Magnetisierung in Phase III entlang der Vorzugsachse der Eisenschicht, in Phase I und II nicht. Dies könnte der Grund für die Erhöhung des relativen orbitalen Moments in Phase III sein.

In diesem Abschnitt wurde abbildende Mikrospektroskopie verwendet, um die magnetischen Momente in der Eisenschicht in einem Ni/Fe/Co-Dreischichtsystem auf Cu(001) zu untersuchen. Spin- und Bahnmoment in den drei verschiedenen strukturellen und magnetischen Phasen konnte so bestimmt und als zweidimensionaler Plot der Schichtdickenabhängigkeit von der Eisen- und Nickelschichtdicke dargestellt werden. Im Bereich antiferromagnetischer Kopplung zwischen der Nickel- und der Kobaltschicht zeigen sich charakteristische Änderungen im Fe-Spinmoment. Im Bahnmoment spiegelt sich im wesentlichen die elementaufgelöste magnetische Anisotropie der Fe-Schicht wieder.

3.2 Spinreorientierungsübergänge in Co/Ni-Doppellagen

Die Kontrolle über die leichte magnetische Richtung von magnetischen dünnen Filmen ist für viele Anwendungen von großer Bedeutung. Sie wird beschrieben durch das Minimum der magnetischen Anisotropieenergie. Diese gibt an, welche Energie nötig ist, um die Magnetisierung einer Probe in einer bestimmten Richtung zu halten [67, 108]. Die Berechnung der Anisotropieenergie und die Vorhersage der leichten Richtung stellt eine Herausforderung an die Theorie dar, da diese Energien im Bereich von einigen μeV/Atom liegen, die sich in der Berechnung als Differenz der gesamten elektronischen Energie von etlichen eV/Atom für unterschiedliche Magnetisierungsrichtungen ergeben [109–111]. Wie im vorigen Abschnitt bereits erwähnt, kann der Zusammenhang zwischen der magnetischen Anisotropieenergie und dem orbitalen Moment
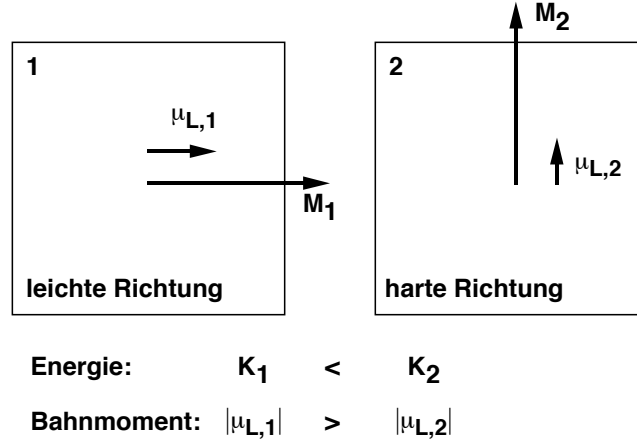
Abbildung 3.5: Schematische Darstellung des Zusammenhangs zwischen magnetischer Anisotropieenergie und Bahnmoment. In Bild 1 ist eine Probe entlang einer leichten Richtung magnetisiert, in Bild 2 entlang einer harten Richtung. Der Absolutwert des Bahnmoments μ_L ist höher, wenn die Magnetisierung in die energetisch begünstigtere Richtung zeigt (1).

ausgenutzt werden, um mit XMCD elementaufgelöst Anisotropien zu untersuchen. Dieser Zusammenhang wurde 1989 von Bruno in die folgende quantitative Form gebracht [104]:

$$\Delta K = -\frac{\xi}{4} \frac{G}{H} \frac{\Delta \mu_L}{\mu_B}. \qquad (3.1)$$

Dabei ist ΔK die Energiedifferenz zwischen zwei Magnetisierungsrichtungen und $\Delta \mu_L$ die damit verbundene Änderung des orbitalen Moments. ξ ist der Spin-Bahn-Kopplungsparameter, der zum Beispiel für Ni etwa 50 bis 100 meV beträgt [9,112], und μ_B das Bohrsche Magneton. G/H ist ein dimensionsloser Faktor, der sich aus zwei verschiedenen Integralen über die elektronische Zustandsdichte G und H errechnet [104]. Eine grobe Abschätzung für die $3d$-Übergangsmetalle ergibt $G/H = 0.2$ [106]. Das negative Vorzeichen in Gleichung 3.1 bedeutet, dass für eine Magnetisierung entlang einer leichteren Richtung, also mit niedrigerer Anisotropieenergie K, ein höheres Bahnmoment μ_L erwartet wird. Dies ist in Abb. 3.5 schematisch dargestellt. Eine Probe ist im Fall 1 entlang einer leichten Richtung magnetisiert, im Fall 2 entlang einer harten Richtung. Die Magnetisierung in der harten Richtung kann zum Beispiel durch ein äußeres Feld erfolgen, durch das die nötige Anisotropieenergie $K_2 - K_1$ aufgebracht wird. Das Bahnmoment μ_L ist parallel zur Richtung der Magnetisierung, sofern diese entlang einer Symmetrierichtung des

Kristalls verläuft [113]. Der Absolutwert des Bahnmoments ist höher, wenn die Magnetisierung in eine energetisch begünstigtere Richtung zeigt.

Experimentell wurde dieser Zusammenhang zwischen magnetischer Anisotropie und der Anisotropie des Bahnmoments von verschiedenen Gruppen mit Messungen an Co/Au(111) [106], Co/Pt-Vielfachschichten [114], Co/Ni/Cu(001) [115] und Ni/Pt-Vielfachschichten [116] bestätigt, allerdings mit verschiedenen Proportionalitätskonstanten G/H aus Gleichung 3.1. Es wurde später von van der Laan ausgeführt, dass Gleichung 3.1 nur im Fall eines vollständig gefüllten Majoritätsbands gültig ist [107]. Für das im folgenden betrachtete Ni ist dies jedoch annähernd der Fall.

Im nun folgenden Beispiel wurde der Spinreorientierungsübergang zwischen einer Magnetisierung senkrecht zur Filmebene („out-of-plane") und einer Magnetisierung in der Filmebene („in-plane") mit abbildender magnetischer Mikrospektroskopie untersucht. Als Probe diente dabei ein Co/Ni-Doppelkeil auf Cu(001), ähnlich wie in Abb. 3.2 schematisch gezeigt. Einzelne Co- und Ni-Filme auf Cu(001) haben eine unterschiedliche Vorzugsrichtung der Magnetisierung: Während Co/Cu(001) immer in der Ebene magnetisiert ist [117, 118], zeigt Ni/Cu(001) in einem weiten Schichtdickenbereich eine senkrechte Magnetisierung [119–121]. In Co/Ni-Doppelschichten erwartet man daher für große Co- und kleine Ni-Schichtdicken eine Magnetisierung in der Ebene, während die Magnetisierung für kleine Co- und große Ni-Schichtdicken senkrecht zur Filmebene sein sollte.

Abb. 3.6 zeigt die pixelweise Auswertung mit den Summenregeln eines gekreuzten Co/Ni-Doppelkeils auf Cu(001). Verschiedene Grautöne geben das auf die Lichteinfallsrichtung projizierte Spinmoment der Ni-Schicht wieder, wie in der Legende unterhalb des Bilds dargestellt. Die Ni-Schichtdicke steigt von links nach rechts an, wie an der oberen Achse angegeben, die Co-Schichtdicke von unten nach oben, wie an der rechten Achse angegeben. Die Lichteinfallsrichtung verläuft von unten nach oben, wobei der Winkel zur Probenoberfläche 30° betrug. Das Bild setzt sich aus $76\,800$ Einzelspektren zusammen, von denen jedes die spektrale Information von 370×370 nm^2 der Probenoberfläche repräsentiert. Jedes XMCD-Spektrum wiederum enthält Messpunkte bei 105 verschiedenen Photonenenergien für jede Helizität, so dass Abb. 3.6 die Information von insgesamt mehr als 16 Millionen Datenpunkten enthält!
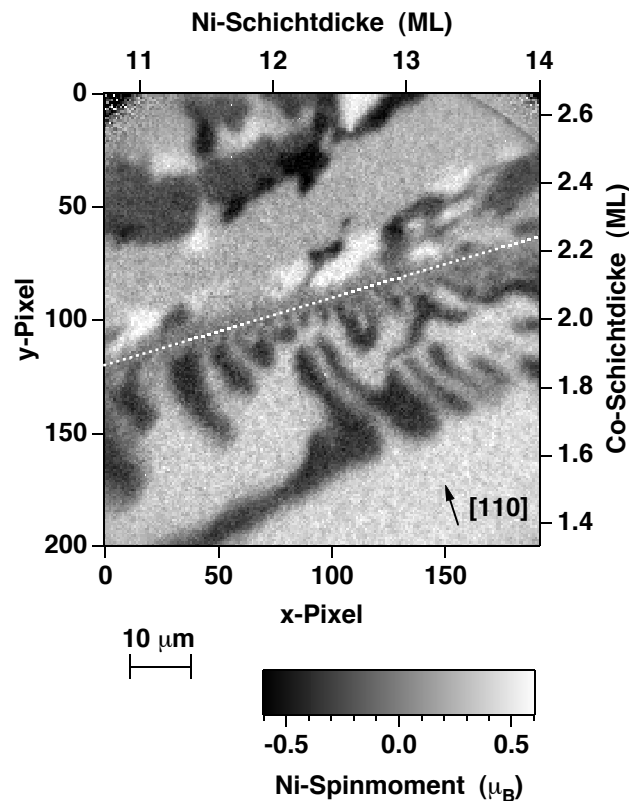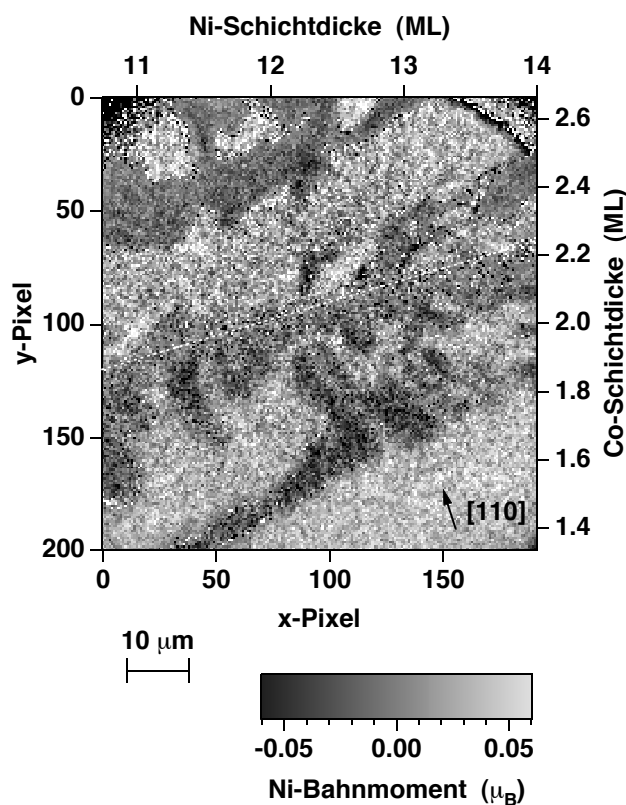
Abbildung 3.6: Ergebnis der abbildenden Mikrospektroskopie an einem Co/Ni-Doppelkeil auf Cu(001). Gezeigt ist die Projektion des Ni-Spinmoments auf die Lichteinfallsrichtung (von unten nach oben, 30° zur Probenoberfläche) als Grautondarstellung, wie in der Legende erklärt. Die Ni-Schichtdicke steigt von links nach rechts an (obere Achse), die Co-Schichtdicke von unten nach oben (rechte Achse). Das Bild setzt sich aus der Auswertung von 76 800 Einzelspektren von jeweils 370×370 nm^2 der Probenoberfläche zusammen. Die gestrichelte weiße Linie markiert die Position eines Spinreorientierungsübergangs, der eine Region mit Magnetisierung in der Filmebene (oberhalb) von einer Region mit senkrechter Magnetisierung (unterhalb) trennt.

Im unteren Teil des Bilds erkennt man magnetische Domänen zweier verschiedener Helligkeitsstufen, deren Grauwerte einem auf die Lichteinfallsrichtung projiziertem Spinmoment von plus und minus $0.3\,\mu_B$ entsprechen. In diesem Bereich der Probe liegt out-of-plane-Magnetisierung vor. Berücksichtigt man die geometrische Projektion der beiden entgegengesetzten Magnetisierungsrichtungen senkrecht zur Filmebene auf die Lichteinfallsrichtung, entspricht dies einem Absolutwert des Spinmoments von $0.6\,\mu_B$, also in etwa dem Volumenwert von Nickel. Oberhalb der gestrichelten Linie findet man Domänen mit vier verschiedenen Grauwerten. Diese können

den Projektionen des Spinmoments entlang der vier in der Ebene liegenden kristallographischen $\langle 110 \rangle$-Richtungen auf die Lichteinfallsrichtung zugeordnet werden, wobei sich als Absolutwert wieder 0.6 μ_B ergibt. In diesem Bereich der Probe liegt also in-plane-Magnetisierung vor. Die gestrichelte weiße Linie markiert folglich die Position eines Spinreorientierungsübergangs zwischen in-plane- und out-of-plane-Magnetisierung. Aus der Neigung dieser Linie folgt, dass schichtdickenabhängige Übergänge von in-plane nach out-of-plane also sowohl für größer werdende Ni-Schichtdicke als auch für kleiner werdende Co-Schichtdicke auftreten.

Abbildung 3.7: Ergebnis der abbildenden Mikrospektroskopie an einem Co/Ni-Doppelkeil auf Cu(001). Gezeigt ist die Projektion des Ni-Bahnmoments auf die Lichteinfallsrichtung an derselben Stelle der Probe wie in Abb. 3.6. Die Grautonskala ist in der Legende angegeben.

Abb. 3.7 zeigt die zugehörige mikrospektroskopische Auswertung nach dem Ni-Bahnmoment. Verschiedene Graustufen entsprechen hier verschiedenen Größen der Projektion des lokalen Bahnmoments auf die Lichteinfallsrichtung, wie in der Legende dargestellt. Deutlich sind dieselben Domänen wie in Abb. 3.6 zu erkennen. Das Bild ist jedoch stärker verrauscht als Abb.

3.6. Dies ist eine Folge der Anwendung der Summenregeln: zur Berechnung des Spinmoments werden die Flächen unter dem Dichroismusspektrum an der L_2- und L_3-Kante addiert, während sie zur Berechnung des Bahnmoments subtrahiert werden (sh. Abschnitt 1.2.3).
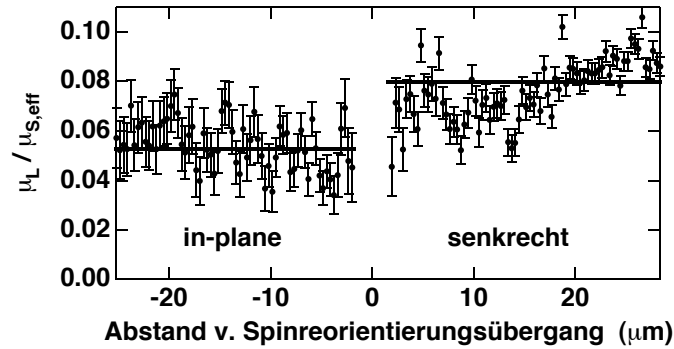

Abbildung 3.8: Verhältnis von Bahn- zu Spinmoment im Nickel als Funktion des Abstands vom Spinreorientierungsübergang aus Abb. 3.6 und 3.7. Jeder Datenpunkt stellt die Mittelung über 192 Bildpunkte von 370×370 nm^2 entlang von Linien parallel zum Spinreorientierungsübergang dar. Die horizontalen Balken geben den Mittelwert für die beiden Regionen mit senkrechter Magnetisierung (rechts) und mit Magnetisierung in der Filmebene (links) an. Man erkennt, dass das Bahnmoment in der senkrecht magnetisierten Region signifikant höher ist als in der in-plane-Region.

Die Interpretation des Bahnmoments bezüglich magnetischer Anisotropien muss unabhängig von der jeweiligen Magnetisierungsrichtung in den einzelnen Domänen erfolgen. Dies wird erreicht, indem man das Verhältnis von Bahn- zu Spinmoment μ_L/μ_S bildet. Dabei kürzen sich die geometrischen Faktoren heraus. Bei Betrachtung von Abb. 3.7 wird jedoch klar, dass das Rauschen der einzelnen 370×370 nm^2-Bildpunkte im vorliegenden Beispiel eine pixelweise Interpretation von μ_L/μ_S nicht zulässt. Es ist jedoch möglich, durch eine räumliche Mittelung über eine gewisse Anzahl von Bildpunkten die Statistik auf Kosten der lateralen Auflösung zu verbessern. Das Ergebnis einer solchen Mittelung ist in Abb. 3.8 gezeigt. Aufgetragen ist das Verhältnis von Bahn- zu Spinmoment μ_L/μ_S als Funktion des Abstands zum Spinreorientierungsübergang, der weißen gestrichelten Linie in Abb. 3.6. Dazu wurden jeweils die 192 Bildpunkte entlang einer einen Bildpunkt breiten Linie parallel zum Spinreorientierungsübergang gemittelt. Die linke Seite von Abb. 3.8 entspricht dabei dem oberen Teil von Abb. 3.6 und 3.7 (in-plane-Magnetisierung), die rechte Seite dem unteren Teil (out-of-plane-Magnetisierung). In

der Mitte fehlen ein paar Datenpunkte; diese weisen wegen der verschwindenden Projektion des Spinmoments direkt am Spinreorientierungsübergang und der damit einhergehenden Division durch Null einen weit größeren Fehlerbalken auf.

Man erkennt beiderseits des Spinreorientierungsübergangs einen annähernd konstanten Wert des Verhältnisses von Bahn- zu Spinmoment, der auf der out-of-plane Seite deutlich höher ist als auf der in-plane Seite. Die horizontalen Linien markieren den jeweiligen Mittelwert. Das Bahnmoment im Nickel ist also im Bereich der senkrechten Magnetisierung um fast 0.03 Spinmomente höher als im Bereich, in dem die Magnetisierung in der Filmebene liegt. Dieser Unterschied wird dem in diesem Abschnitt eingangs erwähnten Zusammenhang zwischen der Anisotropie des orbitalen Moments und der magnetischen Anisotropie zugeschrieben. Im Falle von Co/Ni/Cu(001)-Doppelschichten muss man folglich annehmen, dass die Anisotropie der Ni-Schicht wie im Falle ohne Co-Deckschicht eine senkrechte Anisotropie aufweist, also eine senkrechte Magnetisierungsrichtung energetisch begünstigt. In der Summe der Anisotropieenergien beider Schichten wird ab einer bestimmten Co-Schichtdicke aber die in-plane-Anisotropie der Co-Schicht überwiegen. Da die beiden ultradünnen Schichten durch direkte Austauschwechselwirkung magnetisch fest miteinander gekoppelt sind, wird in diesem Fall die gemeinsame leichte Richtung der Magnetisierung in der Ebene sein. Die Größe des Ni-Bahnmoments spiegelt aber elementaufgelöst nur die Anisotropie der Ni-Schicht wieder, und wird daher im Fall der durch Co erzwungenen in-plane-Magnetisierung, die dann ja aus Sicht der Ni-Schicht entlang einer harten Richtung ist, geringer sein als im Fall der out-of-plane-Magnetisierung.

Mit Hilfe von Gleichung 3.1 kann dies zu einer Abschätzung der magnetischen Anisotropieenergie des Nickelfilms ausgenutzt werden. Setzt man für die Proportionalitätskonstante $\xi G/4H$ den für Ni in Ni/Pt-Vielfachschichten experimentell bestimmten Wert von 2.6 meV [116] ein, so erhält man eine Ni-Anisotropieenergie von 47 μeV/Atom. Berücksichtigt man die mit der Proportionalitätskonstanten verbundenen Unsicherheiten, so liegt dieser Wert durchaus genau im Bereich der erwarteten Energien. Ein Literaturwert für die Anisotropieenergie der inneren Lagen von Ni-Filmen auf Cu(001) beträgt 34 μeV/Atom [122]. Der etwas höhere Wert von 47 μeV/Atom läßt sich leicht erklären, wenn man berücksichtigt, dass die XMCD-Messung ein über die Elektronenaustrittstiefe gemitteltes Signal liefert, und die Nickelatome direkt an der

Co/Ni-Grenzfläche einen hohen Beitrag zur senkrechten Anisotropie liefern [123].

In diesem Beispiel der Co/Ni-Doppelschichten auf Cu(001) wurde magnetische abbildende Mikrospektroskopie für eine elementaufgelöste mikroskopische Untersuchung der magnetischen Momente in der Nähe eines Spinreorientierungsübergangs der leichten magnetischen Richtung verwendet. Während die gemessenen Projektionen der Ni-Spinmomente einen konstanten Absolutwert des Spinmoments beiderseits des Spinreorientierungsübergangs ergeben, ist der Absolutwert der lokalen Bahnmomente im Bereich der Magnetisierung in der Filmebene erniedrigt. Diese Erniedrigung des Bahnmoments wird durch die magnetische Anisotropie hervorgerufen, die zu einer Anisotropie des Bahnmoments führt. Diese Korrelation von Bahnmoment und magnetischer Anisotropieenergie erweitert das Potenzial der abbildenden magnetischen Mikrospektroskopie um mikroskopisch aufgelöste elementselektive Messungen der magnetischen Anisotropie. Solche Messungen der lokalen magnetischen Anisotropie sind besonders zur Untersuchung mikromagnetischer Effekte wichtig. Messungen des Bahnmoments in mikrostrukturierten Proben oder in der Nähe von Domänenwänden, in denen sich die Magnetisierung kontinuierlich über eine harte Richtung hinweg ändert, könnten die nötige Information für verbesserte mikromagnetische Rechnungen liefern und das allgemeine Verständnis der damit verbundenen Effekte verbessern.

Kapitel 4

Ausblick

Die vollständige Kombination von PEEM und XMCD erlaubt es, mit einem vertretbaren experimentellen Aufwand elementaufgelöste magnetische abbildende Mikrospektroskopie durchzuführen. Das PEEM wird dabei als parallel arbeitender ortsaufgelöster Detektor für den lokalen Absorptionsquerschnitt weicher Röntgenstrahlung benutzt. Damit ist es möglich, für jeden Bildpunkt einer mikroskopischen Abbildung die volle spektroskopische Information der XMCD-Spektroskopie zu erhalten, sofern einige experimentelle Voraussetzungen bezüglich Gleichmäßigkeit der Beleuchtung des Gesichtsfelds, Normierung auf den Photonenfluss sowie Linearität und Stabilität des Bildwandlersystems erfüllt sind. Bei einer Auswertung solcher Datensätze nach den Summenregeln [14, 15] kann die erhaltene Information in Form von Graustufenbildern der magnetischen Momente, separiert nach Spin- und Bahnanteil und projiziert auf die Lichteinfallsrichtung, dargestellt werden. In Fällen, in denen keine spezielle Ortsauflösung nötig ist, kann diese Methode zur schnellen Untersuchung von Schichtdickenabhängigkeiten verwendet werden, indem keilförmige Filme mit geeigneten Abmessungen präpariert werden. Dies wurde am Beispiel von ultradünnen Ni/Fe/Co-Schichten auf Cu(001) gezeigt, wobei die Nickel- und Eisenschichten als gekreuzte Doppelkeile auf Co/Cu(001) aufgebracht wurden.

Diese Methode erlaubt aber auch, mit höherer Auflösung mikromagnetische Phänomene zu untersuchen. Das Beispiel der abbildenden Mikrospektroskopie an Spinreorientierungsübergängen in Co/Ni/Cu(001)-Doppelschichten zeigte, dass es möglich ist, damit sogar elementselektiv Aussagen über lokale magnetische Anisotropien machen zu können. Verbesserungen in der Bildinten-

sität durch Erhöhung der Photonenflussdichte und der Effizienz des Detektionssystems werden dazu beitragen, das Rauschen im ausgewerteten Signal weiter zu verringern und so zu einer mikroskopischen Abbildung von Anisotropieeffekten zu gelangen. Eine höhere Intensität kann auch genutzt werden, die für abbildende Mikrospektroskopie erreichbare Ortsauflösung zu verbessern, ohne die Messzeit über Gebühr zu verlängern.

Eine höhere Ortsauflösung wird auch durch den Einsatz von neuen Instrumenten mit aberrationskorrigierenden Optiken [124] erwartet. Da in diesen Mikroskopen eine Korrekturoptik die Abbildungsfehler ausgleicht, wird es möglich sein, mit sehr viel größeren Kontrastblenden zu arbeiten, was neben der verbesserten Auflösung vor allem eine signifikant höhere Intensität bedeutet. Neue Strahlrohre an den Synchrotronstrahlungsquellen, die ein schnelles Umschalten der Polarisation von hochbrillanter Strahlung erlauben [125], werden die Genauigkeit von Dichroismusmessungen noch weiter erhöhen und den Einfluss von Strahllageschwankungen und Drifts im experimentellen Aufbau auf die Spektren verringern.

Der Einsatz von Energiefiltern zur Energieselektion der bei der Abbildung verwendeten Elektronen [126–129] wird zum einen ein weites Feld von Dichroismuseffekten, die nicht in der Absorption der Strahlung, sondern in der Photoemission der ausgeschlagenen Elektronen auftreten [130], für die abbildende Spektroskopie öffnen. Zum anderen kann in diesem Fall eine Einstellung der Abbildungsoptik, die nicht des Realraumbild sondern das Elektronenbeugungsbild auf den Detektor abbildet, verwendet werden, um Photoelektronenbeugungsexperimente [131–133] mit XMCD-Messungen zu verbinden. Dabei kann zum Beispiel die Kontrastblende verwendet werden, um spezielle Beugungsspots für die Realraumabbildung zu selektieren, und so eine strukturelle Selektivität in der abbildenden magnetischen Mikrospektroskopie zu erreichen.

Die Einbeziehung der Zeitstruktur der anregenden Synchrotronstrahlung [134] schließlich kann dazu verwendet werden, mit XMCD-PEEM dynamische magnetische Effekte stroboskopisch zeitaufgelöst sowohl mikroskopisch abzubilden als auch zu spektroskopieren. Denkbar sind hier zum Beispiel Momentaufnahmen der mikroskopischen Verteilung von Spin- und Bahnmomenten im Verlauf von reversiblen dynamischen Ummagnetisierungsvorgängen.

Literaturverzeichnis

[1] G. Binasch, P. Grünberg, F. Saurenbach und W. Zinn, Phys. Rev. B **39**, 4828 (1989).

[2] M. N. Baibich, J. M. Broto, A. Fert, F. Nguyen Van Dau, F. Petroff, P. Etienne, G. Creuzet, A. Friederich und J. Chazelas, Phys. Rev. Lett. **61**, 2472 (1988).

[3] S. S. P. Parkin, N. More und K. P. Roche, Phys. Rev. Lett. **64**, 2304 (1990).

[4] C. H. Tsang, R. E. Fontana, Jr., T. Lin, D. E. Heim, B. A. Gurney und M. L. Williams, IBM J. Res. Develop. **42**, 103 (1998).

[5] S. Mengel, „Technologieanalyse Magnetismus, Band 2: XMR-Technologien", VDI Technologiezentrum Physikalische Technologien, Düsseldorf (1997).

[6] J.-G. Zhu, Y. Zheng und G. A. Prinz, J. Appl. Phys. **87**, 6668 (2000).

[7] G. A. Prinz, J. Magn. Magn. Mater. **200**, 57 (1999).

[8] W. Kuch und C. M. Schneider, Rep. Prog. Phys. **64**, 147 (2001).

[9] W. Kuch, A. Dittschar, K. Meinel, M. Zharnikov, C. M. Schneider, J. Kirschner, J. Henk und R. Feder, Phys. Rev. B **53**, 11621 (1996).

[10] W. Kuch, M. Zharnikov, A. Dittschar, K. Meinel, C. M. Schneider, J. Kirschner, J. Henk und R. Feder, J. Appl. Phys. **79**, 6426 (1996).

[11] W. Kuch, A. Dittschar, M. Salvietti, M.-T. Lin, M. Zharnikov, C. M. Schneider, J. Camarero, J. J. de Miguel, R. Miranda und J. Kirschner, Phys. Rev. B **57**, 5340 (1998).

[12] W. Kuch, A. Dittschar, M.-T. Lin, M. Salvietti, M. Zharnikov, C. M. Schneider, J. Kirschner, J. Camarero, J. J. de Miguel und R. Miranda, J. Magn. Magn. Mater. **170**, L13 (1997).

[13] G. Schütz, W. Wagner, W. Wilhelm, P. Kienle, R. Zeller, R. Frahm und G. Materlik, Phys. Rev. Lett. **58**, 737 (1987).

[14] B. T. Thole, P. Carra, F. Sette und G. van der Laan, Phys. Rev. Lett. **68**, 1943 (1992).

[15] P. Carra, B. T. Thole, M. Altarelli und X. Wang, Phys. Rev. Lett. **70**, 694 (1993).

[16] Datenbank: INSPEC 1969–Mai 2001, Stichwortsuche mit „AND"-Verknüpfung.

[17] H. Ebert, Rep. Prog. Phys. **59**, 1665 (1996).

[18] Y. U. Idzerda, C. T. Chen, H.-J. Lin, H. Tjeng und G. Meigs, Physica B **208-209**, 746 (1995).

[19] C. T. Chen, Y. U. Idzerda, H.-J. Lin, N. V. Smith, G. Meigs, E. Chaban, G. H. Ho, E. Pellegrin und F. Sette, Phys. Rev. Lett. **75**, 152 (1995).

[20] J. Vogel und M. Sacchi, Phys. Rev. B **49**, 3230 (1994).

[21] X. Le Cann, C. Boeglin, B. Carrière und K. Hricovini, Phys. Rev. B **54**, 373 (1996).

[22] J. Hunter Dunn, D. Arvanitis und N. Mårtensson, Phys. Rev. B **54**, R11157 (1996).

[23] E. Brüche, Z. Phys. **86**, 448 (1933).

[24] J. Pohl, Zeitschr. f. techn. Physik **12**, 579 (1934).

[25] G. Möllenstedt und F. Lenz, in: „Advances in Electronics and Electron Physics", Ed.: L. Marton, Academic Press, London (1963).

[26] H. Bethke und M. Klaua, Ultramicroscopy **11**, 207 (1983).

[27] W. Engel, M. E. Kordesch, H. H. Rotermund, S. Kubala und A. von Oertzen, Ultramicroscopy **36**, 148 (1991).

[28] M. E. Kordesch, W. Engel, G. J. Lapeyre, E. Zeitler und A. M. Bradshaw, App. Phys. A **49**, 399 (1989).

[29] M. Mundschau, M. E. Kordesch, B. Rausenberger, W. Engel, A. M. Bradshaw und E. Zeitler, Surf. Sci. **227**, 246 (1990).

[30] H. H. Rotermund, S. Nettesheim, A. von Oertzen und G. Ertl, Surf. Sci. **275**, L645 (1992).

[31] S. Nettesheim, A. von Oertzen, H. H. Rotermund und G. Ertl, J. Chem. Phys. **98**, 9977 (1993).

[32] W. Telieps und E. Bauer, Ultramicroscopy **17**, 57 (1985).

[33] E. Bauer, Rep. Prog. Phys. **57**, 895 (1994).

[34] B. P. Tonner und G. R. Harp, Rev. Sci. Instrum. **59**, 853 (1988).

[35] B. P. Tonner, D. Dunham, T. Droubay, J. Kikuma, J. Denlinger, E. Rotenberg und A. Warwick, J. Electron Spectrosc. Relat. Phenom. **75**, 309 (1995).

[36] J. Stöhr und S. Anders, IBM J. Res. Develop. **44**, 535 (2000).

[37] Ch. Ziethen, O. Schmidt, G. K. L. Marx, G. Schönhense, R. Frömter, J. Gilles, J. Kirschner, C. M. Schneider und O. Gröning, J. Electron Spectrosc. Relat. Phenom. **107**, 261 (2000).

[38] J. Stöhr, Y. Wu, M. G. Samant, B. B. Hermsmeier, G. Harp, S. Koranda, D. Dunham und B. P. Tonner, Science **259**, 658 (1993).

[39] W. Swiech, G. H. Fecher, Ch. Ziethen, O. Schmidt, G. Schönhense, K. Grzelakowski, C. M. Schneider, R. Frömter, H. P. Oepen und J. Kirschner, J. Electron Spectrosc. Relat. Phenom. **84**, 171 (1997).

[40] C. M. Schneider, J. Magn. Magn. Mater. **175**, 160 (1997).

[41] F. U. Hillebrecht, D. Spanke, J. Dresselhaus und V. Solinus, J. Electron Spectrosc. Relat. Phenom. **84**, 189 (1997).

[42] W. Kuch, R. Frömter, J. Gilles, D. Hartmann, Ch. Ziethen, C. M. Schneider, G. Schönhense, W. Swiech und J. Kirschner, Surf. Rev. Lett. **5**, 1241 (1998).

[43] S. Imada, S. Ueda, R.-J. Jung, Y. Saitoh, M. Kotsugi, W. Kuch, J. Gilles, S. S. Kang, F. Offi, J. Kirschner, H. Daimon, T. Kimura, J. Yanagisawa, K. Gamo und S. Suga, Jpn. J. Appl. Phys. **39**, L585 (2000).

[44] L. Thomas, J. Lüning, A. Scholl, F. Nolting, S. Anders, J. Stöhr und S. S. P. Parkin, Phys. Rev. Lett. **84**, 3452 (2000).

[45] W. Kuch, X. Gao und J. Kirschner, submitted to Phys. Rev. B.

[46] W. Kuch, J. Gilles, X. Gao und J. Kirschner, submitted to J. Magn. Magn. Mater.

[47] A. Hubert und R. Schäfer, „Magnetic Domains", Springer, Berlin (1998).

[48] „Ultrathin magnetic structures", Vol. 2, Chap. 2, Ed.: B. Heinrich und J. A. C. Bland, Springer, Berlin (1994).

[49] M. D. Stiles, J. Magn. Magn. Mater. **200**, 322 (1999).

[50] B. Kaplan und G. A. Gehring, J. Magn. Magn. Mater. **128**, 111 (1993).

[51] A. B. Kashuba und V. L. Pokrovsky, Phys. Rev. B **48**, 10335 (1993).

[52] D. Alders, L. H. Tjeng, F. C. Voogt, T. Hibma, G. A. Sawatzky, C. T. Chen, J. Vogel, M. Sacchi und S. Iacobucci, Phys. Rev. B **57**, 11623 (1998).

[53] J. Stöhr, A. Scholl, T. J. Regan, S. Anders, J. Lüning, M. R. Scheinfein, H. A. Padmore und R. L. White, Phys. Rev. Lett. **83**, 1862 (1999).

[54] H. Ohldag, A. Scholl, F. Nolting, S. Anders, F. U. Hillebrecht und J. Stöhr, Phys. Rev. Lett. **86**, 2878 (2001).

[55] A. Scholl, J. Stöhr, J. Lüning, J. W. Seo, J. Fompeyrine, H. Siegwart, J.-P. Locquet, F. Nolting, S. Anders, E. E. Fullerton, M. R. Scheinfein und H. A. Padmore, Science **287**, 1014 (2000).

[56] F. Nolting, A. Scholl, J. Stöhr, J. W. Seo, J. Fompeyrine, H. Siegwart, J.-P. Locquet, S. Anders, J. Lüning, E. E. Fullerton, M. F. Toney, M. R. Scheinfein und H. A. Padmore, Nature **405**, 767 (2000).

[57] Focus IS-PEEM, Omicron, Taunusstein.

[58] Omicron Newsletter IV/1997.

[59] R. Nakajima, J. Stöhr und Y. U. Idzerda, Phys. Rev. B **59**, 6421 (1999).

[60] Y. Saitoh, T. Nakatani, T. Matsushita, T. Miyahara, M. Fujisawa, K. Soda, T. Muro, S. Ueda, H. Harada, A. Sekiyama, S. Imada, H. Daimon und S. Suga, J. Synchrotron Rad. **5**, 542 (1998).

[61] W. Kuch, J. Gilles, F. Offi, S. S. Kang, S. Imada, S. Suga und J. Kirschner, Surf. Sci. **480**, 153 (2001).

[62] A. Kay, E. Arenholz, S. Mun, F. J. García de Abajo, C. S. Fadley, R. Denecke, Z. Hussain und M. A. Van Hove, Science **281**, 679 (1998).

[63] A. W. Kay, F. J. Garcia de Abajo, S.-H. Yang, E. Arenholz, B. S. Mun, N. Mannella, Z. Hussain, M. A. Van Hove und C. S. Fadley, Phys. Rev. B **63**, 115119 (2001).

[64] J. Stöhr, J. Electron Spectrosc. Relat. Phenom. **75**, 253 (1995).

[65] W. Kuch, M. Salvietti, Xingyu Gao, M.-T. Lin, M. Klaua, J. Barthel, C. V. Mohan und J. Kirschner, Phys. Rev. B **58**, 8556 (1998).

[66] W. Kuch, J. Gilles, F. Offi, S. S. Kang, S. Imada, S. Suga und J. Kirschner, J. Electron Spectrosc. Relat. Phenom. **109**, 249 (2000).

[67] U. Gradmann, in *Handbook of Magnetic Materials*, edited by K. H. J. Buschow, Elsevier, Amsterdam (1993).

[68] J. Thomassen, F. May, B. Feldmann, M. Wuttig und H. Ibach, Phys. Rev. Lett. **69**, 3831 (1992).

[69] P. Bayer, S. Müller, P. Schmailzl und K. Heinz, Phys. Rev. B **48**, 17611 (1993).

[70] S. Müller, P. Bayer, A. Kinne, P. Schmailzl und K. Heinz, Surf. Sci. **322**, 21 (1995).

[71] Dongqi Li, M. Freitag, J. Pearson, Z. Q. Qiu und S. D. Bader, Phys. Rev. Lett. **72**, 3112 (1994).

[72] Th. Detzel, M. Vonbank, M. Donath und V. Dose, J. Magn. Magn. Mater. **147**, L1 (1995).

[73] M. Straub, R. Vollmer und J. Kirschner, Phys. Rev. Lett. **77**, 743 (1996).

[74] M. Wuttig, B. Feldmann, J. Thomassen, F. May, H. Zillgen, A. Brodde, H. Hannemann und H. Neddermayer, Surf. Sci. **291**, 14 (1993).

[75] J. Giergiel, J. Kirschner, J. Landgraf, J. Shen und J. Woltersdorf, Surf. Sci. **310**, 1 (1994).

[76] J. Giergiel, J. Shen, J. Woltersdorf, A. Kirilyuk und J. Kirschner, Phys. Rev. B **52**, 8528 (1995).

[77] S. Müller, P. Bayer, C. Reischl, K. Heinz, B. Feldmann, H. Zillgen und M. Wuttig, Phys. Rev. Lett. **74**, 765 (1995).

[78] K. Heinz, S. Müller und P. Bayer, Surf. Sci. **337**, 215 (1995).

[79] S. Müller, P. Bayer, A. Kinne, C. Reischl, R. Metzler und K. Heinz, Surf. Sci. **331**–**333**, 723 (1995).

[80] A. Biedermann, R. Tscheließnig, M. Schmid und P. Varga, Phys. Rev. Lett. **87**, 086103 (2001).

[81] R. D. Ellerbrock, A. Fuest, A. Schatz, W. Keune und R. A. Brand, Phys. Rev. Lett. **74**, 3053 (1995).

[82] R. Lorenz und J. Hafner, Phys. Rev. B **54**, 15937 (1996).

[83] L. Szunyogh, B. Újfalussy und P. Weinberger, Phys. Rev. B **55**, 14392 (1997).

[84] T. Asada und S. Blügel, J. Magn. Magn. Mater. **177-181**, 1233 (1998).

[85] V. Popescu, H. Ebert, L. Szunyogh, P. Weinberger und M. Donath, Phys. Rev. B **61**, 15241 (2000).

[86] D. Qian, X. F. Jin, J. Barthel, M. Klaua und J. Kirschner, Phys. Rev. Lett. **87**, 227204 (2001).

[87] S. S. Kang, W. Kuch und J. Kirschner, Phys. Rev. B **63**, 024401 (2001).

[88] W. L. O'Brien und B. P. Tonner, Surf. Sci. **334**, 10 (1995).

[89] W. L. O'Brien und B. P. Tonner, Phys. Rev. B **52**, 15332 (1995).

[90] E. J. Escorcia-Aparicio, R. K. Kawakami und Z. Q. Qiu, Phys. Rev. B **54**, 4155 (1996).

[91] R. K. Kawakami, E. J. Escorcia-Aparicio und Z. Q. Qiu, J. Appl. Phys. **79**, 4532 (1996).

[92] D. Schmitz, C. Charton, A. Scholl, C. Carbone und W. Eberhardt, Phys. Rev. B, 59, 4327 (1999).

[93] W. Kuch, J. Gilles, S. S. Kang, F. Offi, J. Kirschner, S. Imada und S. Suga, J. Appl. Phys. **87**, 5747 (2000).

[94] W. Kuch und S. S. P. Parkin, Europhys. Lett. **37**, 465 (1997).

[95] W. Kuch und S. S. P. Parkin, J. Magn. Magn. Mater. **184**, 127 (1998).

[96] C. S. Wang, B. M. Klein und H. Krakauer, Phys. Rev. Lett. **54**, 1852 (1985).

[97] V. L. Moruzzi, P. M. Marcus, K. Schwarz und P. Mohn, Phys. Rev. B **34**, 1784 (1986).

[98] Y. Zhou, W. Zhang, L. Zhong, X. Nie und D.-S. Wang, J. Magn. Magn. Mater. **167**, 136 (1997).

[99] A. Biedermann, M. Schmid und P. Varga, Phys. Rev. Lett. **86**, 464 (2001).

[100] P. Bruno und C. Chappert, Phys. Rev. Lett. **67**, 1602 (1991).

[101] P. Bruno, Phys. Rev. B **52**, 411 (1995).

[102] J. Unguris, R. J. Celotta und D. T. Pierce, Phys. Rev. Lett. **69**, 1125 (1992).

[103] M. Tischer, O. Hjortstam, D. Arvanitis, J. Hunter Dunn, F. May, K. Baberschke, J. Trygg, J. M. Wills, B. Johansson und O. Eriksson, Phys. Rev. Lett. **75**, 1602 (1995).

[104] P. Bruno, Phys. Rev. B **39**, 865 (1989).

[105] J. Stöhr und H. König, Phys. Rev. Lett. **75**, 3748 (1995).

[106] D. Weller, J. Stöhr, R. Nakajima, A. Carl, M. G. Samant, C. Chappert, R. Mégy, P. Beauvillain, P. Veillet und G. A. Held, Phys. Rev. Lett. **75**, 3752 (1995).

[107] G. van der Laan, J. Phys.: Cond. Matt. **10**, 3239 (1998).

[108] H. Fritzsche, J. Kohlhepp, H. J. Elmers und U. Gradmann, Phys. Rev. B **49**, 15665 (1994).

[109] G. H. O. Daalderop, P. J. Kelly und M. F. M. Schuurmans, Phys. Rev. B **41**, 11919 (1990).

[110] D.-S. Wang, R. Wu und A. J. Freeman, Phys. Rev. Lett. **70**, 869 (1993).

[111] A. Lessard, T. H. Moos und W. Hübner, Phys. Rev. B **56**, 2594 (1997).

[112] A. R. Mackintosh und O. K. Anderson, in: „Electrons at The Fermi Surface", Ed.:M. Springford, Cambridge University Press, Cambridge (1980).

[113] G. van der Laan und H. A. Dürr, Physica B **248**, 121 (1998).

[114] H. A. Dürr und G. van der Laan, J. Appl. Phys. **81**, 5355 (1997).

[115] H. A. Dürr, G. Y. Guo, G. van der Laan, J. Lee, G. Lauhoff und J. A. C. Bland, Science **277**, 213 (1997).

[116] F. Wilhelm, P. Poulopoulos, P. Srivastava, H. Wende, M. Farle, K. Baberschke, M. Angelakeris, N. K. Flevaris, W. Grange, J.-P. Kappler, G. Ghiringhelli und N. B. Brookes, Phys. Rev. B **61**, 8647 (2000).

[117] P. Krams, F. Lauks, R. L. Stamps, B. Hillebrands und G. Güntherodt, Phys. Rev. Lett. **69**, 3674 (1992).

[118] M. Kowalewski, C. M. Schneider und B. Heinrich, Phys. Rev. B **47**, 8748 (1993).

[119] F. Huang, M. T. Kief, G. J. Mankey und R. F. Willis, Phys. Rev. B **49**, 3962 (1994).

[120] W. L. O'Brien und B. P. Tonner, Phys. Rev. B **49**, 15370 (1994).

[121] B. Schulz und K. Baberschke, Phys. Rev. B **50**, 13467 (1994).

[122] M. Farle, B. Mirwald-Schulz, A. N. Anisimov, W. Platow und K. Baberschke, Phys. Rev. B **55**, 3708 (1997).

[123] W. Kuch, J. Gilles, S. S. Kang, S. Imada, S. Suga und J. Kirschner, Phys. Rev. B **62**, 3824 (2000).

[124] R. Fink, M. R. Weiss, E. Umbach, D. Preikszas, H. Rose, R. Spehr, P. Hartel, W. Engel, R. Degenhardt, R. Wichtendahl, H. Kuhlenbeck, W. Erlebach, K. Ihmann, R. Schlögl, H.-J. Freund, A. M. Bradshaw, G. Lilienkamp, T. Schmidt, E. Bauer und G. Benner, J. Electron Spectrosc. Relat. Phenom. **84**, 231 (1997).

[125] M. R. Weiss, R. Follath, K. J. S. Sawhney, F. Senf, J. Bahrdt, W. Frentrup, A. Gaupp, S. Sasaki, M. Scheer, H.-C. Mertins, D. Abramsohn, F. Schäfers, W. Kuch und W. Mahler, Nucl. Instr. and Meth. A **467-468**, 449 (2001).

[126] D. W. Turner, I. R. Plummer und H. Q. Porter, Rev. Sci. Instrum. **59**, 45 (1988).

[127] G. K. L. Marx, V. Gerheim und G. Schönhense, J. Electron Spectrosc. Relat. Phenom. **84**, 251 (1997).

[128] Y. Sakai, M. Kato, S. Masuda, Y. Harada und T. Ichinokawa, Surf. Rev. Lett. **5**, 1199 (1998).

[129] T. Schmidt, S. Heun, J. Slezak, J. Diaz, K. C. Prince, G. Lilienkamp und E. Bauer, Surf. Rev. Lett. **5**, 1287 (1998).

[130] G. Rossi, G. Panaccione, F. Sirotti und N. A. Cherepkov, Phys. Rev. B **55**, 11483 (1997).

[131] C. S. Fadley, in *Core-Level Spectroscopy in Condensed Systems*, edited by J. Kanamori und A. Kotani, Springer, Berlin (1988).

[132] C. S. Fadley, Surf. Sci. Rep. **19**, 231 (1993).

[133] H. Daimon, T. Nakatani, S. Imada, S. Suga, Y. Kagoshima und T. Miyahara, Rev. Sci. Instrum. **66**, 1510 (1995).

[134] M. Bonfim, G. Ghiringhelli, F. Montaigne, S. Pizzini, N. B. Brookes, F. Petroff, J. Vogel, J. Camarero und A. Fontaine, Phys. Rev. Lett. **86**, 3646 (2001).

Kapitel 6

Originalveröffentlichungen

Die nachfolgend wiedergegebenen Originalveröffentlichungen enthalten umfangreiche Details zu den Messungen, weitere Ergebnisse sowie ausführliche Diskussionen. Im einzelnen werden in den angefügten Publikationen 6.1–6.6 die folgenden Schwerpunkte behandelt: 6.1 zeigt den Einsatz des Photoemissionsmikroskops zur elementaufgelösten Abbildung von magnetischen Domänen in gekoppelten magnetischen Mehrschichtsystemen. Die hier untersuchten Proben sind dünne Ni-Filme auf Co-Mikrostrukturen und austauschgekoppelte Co/Cr/Fe-Dreilagensysteme. In 6.2 wird ein Überblick über spektromikroskopische und mikrospektroskopische Methoden gegeben und deren Vor- und Nachteile für den möglichen Einsatz zur abbildenden magnetischen Mikrospektroskopie beleuchtet. XMCD-PEEM-Mikrospektroskopie wird als am aussichtsreichsten identifiziert, und die Methode erläutert. Details der experimentellen Durchführung und die Überwindung der für Mikrospektroskopie spezifischen Schwierigkeiten werden in 6.3 erläutert. Dort wird auch die automatische Auswerteprozedur beschrieben. Ein Beispiel für abbildende magnetische Mikrospektroskopie findet man in 6.4 Dort werden die Spin- und Bahnmomente einer dünnen Eisenschicht auf Co/Cu(001) abgebildet. 6.5 und 6.6 schließlich enthalten die in Kapitel 3 bereits kurz vorgestellten Ergebnisse über die magnetischen Phasen von ultradünnen fcc-Eisenfilmen in Ni/Fe(Co/Cu(001) (6.5) und der magnetischen abbildenden Mikrospektroskopie am Spinreorientierungsübergang in Co/Ni-Doppellagen auf Cu(001) (6.6). In beiden Veröffentlichungen ist jeweils eine umfangreiche Diskussion enthalten, die über das in Kapitel 3 kurz angerissene weit hinausgeht.

Die Referenzen der einzelnen Originalveröffentlichungen sind:

6.1 W. Kuch, R. Frömter, J. Gilles, D. Hartmann, Ch. Ziethen, C. M. Schneider, G. Schönhen-
se, W. Swiech und J. Kirschner, „Element-selective magnetic imaging in exchange-coupled
systems by magnetic photoemission microscopy", Surface Review and Letters **5**, 1241
(1998). (Copyright (1998) by the World Scientific Publishing Company.)

6.2 W. Kuch, „Imaging Magnetic Microspectroscopy", zur Veröffentlichung eingeladen in „Ma-
gnetic Microscopy of Nanostructures", herausgegeben von H.-P. Oepen und H. Hopster,
Springer-Verlag, Berlin (vorr. 2003).

6.3 W. Kuch, J. Gilles, F. Offi, S. S. Kang, S. Imada, S. Suga und J. Kirschner, „Element-
selective mapping of magnetic moments in ultrathin magnetic films using a photoemission
microscope", Surface Science **480**, 153 (2001). (Mit Erlaubnis von Elsevier Science, Copy-
right (2001).)

6.4 W. Kuch, J. Gilles, S. S. Kang, F. Offi, J. Kirschner, S. Imada und S. Suga, „Quantitative
x-ray magnetic circular dichroism microspectroscopy of Fe/Co/Cu(001) using a photo-
emission microscope", Journal of Applied Physics **87**, 5747 (2000). (Copyright (2000) by
the American Institute of Physics.)

6.5 W. Kuch, J. Gilles, F. Offi, S. S. Kang, S. Imada, S. Suga und J. Kirschner, „Imaging
microspectroscopy of Ni/Fe/Co/Cu(001) using a photoemission microscope", Journal of
Electron Spectroscopy and Related Phenomena **109**, 249 (2000). (Mit Erlaubnis von El-
sevier Science, Copyright (2000).)

6.6 W. Kuch, J. Gilles, S. S. Kang, S. Imada, S. Suga und J. Kirschner, „Magnetic-circular-
dichroism microspectroscopy at the spin reorientation transition in Ni(001) films", Physical
Review B **62**, 3824 (2000). (Copyright (2000) by the American Physical Society.)

ELEMENT-SELECTIVE MAGNETIC IMAGING IN EXCHANGE-COUPLED SYSTEMS BY MAGNETIC PHOTOEMISSION MICROSCOPY

W. KUCH, R. FRÖMTER, J. GILLES and D. HARTMANN

Max-Planck-Institut für Mikrostrukturphysik, Weinberg 2,
D-06120 Halle, Germany

CH. ZIETHEN, C. M. SCHNEIDER* and G. SCHÖNHENSE

Institut für Physik, Johannes Gutenberg-Universität Mainz, Staudingerweg 7,
D-55099 Mainz, Germany

W. SWIECH

Materials Research Laboratory, University of Illinois at Urbana-Champaign,
Urbana, IL 61801, USA

J. KIRSCHNER

Max-Planck-Institut für Mikrostrukturphysik, Weinberg 2,
D-06120 Halle, Germany

We have used a photoemission microscope to obtain element-resolved magnetic contrast in stacked magnetic thin film systems. Magnetic information is thereby provided by X-ray magnetic circular dichroism. Elemental sensitivity, which is crucial for studying magnetic coupling phenomena in systems with several different layers, is achieved by tuning the energy of the illuminating photons to atomic absorption edges. We present measurements of a Ni-coated Co micropattern on Cu(001), and a wedged Co/Cr/Fe(001) sample. In the former sample the Ni magnetization is seen to follow the magnetization of the Co pattern, thereby changing from an out-of-plane easy axis in areas without underlying Co to in-plane on top of the Co microstructures. In the latter a reversal of the exchange coupling of the Co layer to the Fe magnetization is observed when the Cr layer thickness exceeds approximately two monolayers. A small net magnetic moment is also observed in the Cr spacer layer, which follows in sign the Co magnetization at the reversal of the exchange coupling. This finding is discussed in terms of interface roughness or interdiffusion.

The recent interest in magnetic coupling phenomena of ultrathin films has been nourished both by fundamental questions and by the prospect of commercial applications. On the fundamental side the striving for basic knowledge of the magnetic exchange coupling[1] of two magnetic layers across a nonmagnetic spacer layer and its dependence on the thicknesses and compositions of the film has challenged experimentalists[2–7] as well as theoreticians.[8–12]

Technologically such systems have attracted considerable attention since the discovery of the connection of the magnetic exchange coupling with large changes in the electrical resistance.[13–15] This so-called giant magnetoresistance (GMR) effect offers a huge potential for applications, primarily in data storage.[16] Devices based on the GMR effect for reading magnetic information from a storage disk allow a hitherto unattainable reduction in size, and thus promise

---

*Present address: Institut für Festkörper and Werkstofforschung, Postfach 27 00 16, D-01171 Dresden, Germany

to keep pace with the fast increase in areal storage density.[17] Arrays of magnetoresistive submicrometer devices are being developed for random access memory application.[18] In each case the magnetic and resistive properties of the commercially interesting devices are tailored to meet specific requirements by combining a variety of functional layers, which act as seed, buffer, lead, spacer, or pinning layers. For the study of such systems, the size of which is reaching down into the micromagnetics regime, the requirement of probing magnetic information with both spatial *and* elemental resolution becomes obvious. Combining photoelectron emission microscopy (PEEM) with excitation by circularly polarized soft X-ray synchrotron radiation (X-PEEM), tuned to atomic absorption edges, can offer the desired spatially and elementally resolved magnetic information.[19,20] Magnetic contrast is thereby provided by X-ray magnetic circular dichroism (XMCD).[21–23] XMCD is the difference in absorption cross section upon helicity reversal, and depends on the relative orientation of local sample magnetization and incident light. The absorption of X-ray photons manifests itself in the emission of electrons, which are imaged by the PEEM. The exponential attenuation length of the probed electrons is thereby about 20 Å in the case of $3d$ metals.[24] Scanning the photon energy across an absorption edge and recording total electron yield spectra with the PEEM allows one even to extract quantitative information about magnetic properties with spatial resolution by applying so-called sum rules, which have been proposed for the analysis of XMCD absorption spectra.[25]

In this contribution we describe the application of a newly designed photoemission microscope (Focus IS-PEEM, with a routinely achieved resolution in threshold photoemission that is better than 30 nm) to demonstrate the versatility of this approach for the element-selective study of magnetic coupling phenomena of micropatterned structures and buried layers. By examining the magnetic domain structure of a Ni-coated artificially microstructured Co ultrathin film on Cu(001), we will show how the elemental resolution helps to obtain magnetic information also from subsurface layers, as long as the thickness of the cap layers does not exceed a few times the probing depth. A common means of conveniently studying the thickness dependence of thin film properties is to image their spatial distribution on wedge-shaped samples. We will present an investigation of the magnetic exchange coupling between a Co ultrathin film and an Fe(001) substrate across a wedged Cr interlayer. The elemental sensitivity and the ability to access also buried layers allows one not only to image the magnetization direction in the top magnetic Co layer with respect to the Fe substrate, but also the residual net magnetic signal of the Cr spacer layer.

A schematic setup of the photoelectron emission microscope is shown in Fig. 1. A more detailed description of the instrument has already been published elsewhere,[20] so here only a brief description is given. The instrument is a three-lens electrostatic straight optical axis microscope with an integral sample stage and a variable contrast aperture. An electrostatic octupole stigmator in the back focal plane of the objective lens allows correction of astigmatism and alignment of the optical axis in any rotational direction. The image is magnified by a
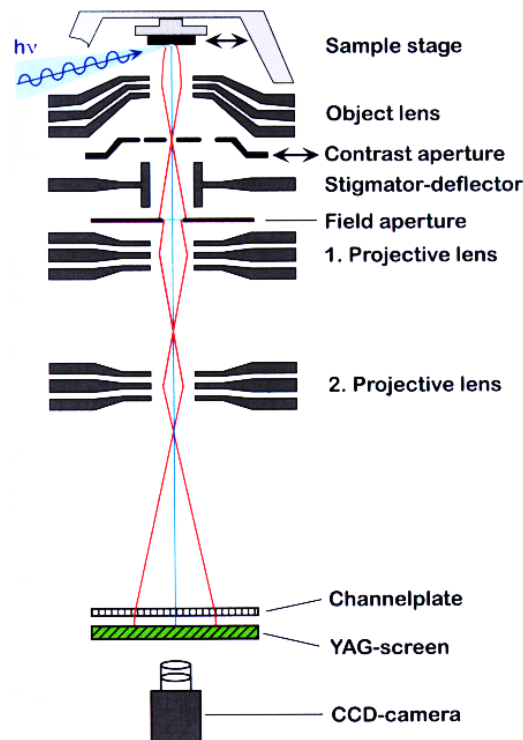

Fig. 1. Schematic setup of the photoelectron emission microscope (Focus IS-PEEM) with an integral sample stage and a variable contrast aperture.

two-stage projective lens system, intensified by a multichannel plate, and converted into visible light by means of a scintillator crystal. The image is then computer-recorded with 16-bit intensity resolution with a Peltier-cooled slow scan CCD camera. Constrast apertures with different diameters can be selected *in situ* by x–y movement of a multiaperture mount. For the measurements presented here a 200 μm diameter aperture was used. Experiments were performed at the beamline PM 3 at the Berlin synchrotron radiation source (BESSY), and at the beamline ID 12B of the European Synchrotron Radiation Facility (ESRF) in Grenoble. At BESSY light emitted from a bending magnet was accepted 0.3 mrad above and below the storage ring orbit, resulting in an estimated degree of circular polarization of about 40% at photon energies between 800 and 1000 eV.[26] At the ESRF the helicity of the helical undulator of the beamline was switched to deliver right and left circularly polarized light of more than 85% polarization.[27] The light was incident with an angle of 25° to the sample surface, thus allowing the imaging of both magnetization components for in-plane and perpendicular magnetization. The element-resolved magnetic contrst is achieved by subtracting images recorded for both helicities of the exciting light at the L_3 absorption edges of Cr, Fe, Co and Ni at photon energies of 575, 707, 779 and 855 eV, respectively. To correct for imperfections of the imaging system and suppress the topographical and work function contrast, asymmetry images are reported, which result from normalizing this difference by the sum. Film preparation and image acquision were performed in a vacuum better than 5×10^{-8} Pa.

Figure 2(a) shows a sketch of the micropatterned epitaxial sample. Fifteen monolayers (ML) of Co were electron-beam-evaporated through a copper grid mask comprising an array of 8×8 μm^2 square apertures with 12 μm period located about 100 μm in front of a clean Cu(001) substrate surface. This resulted in the Co micropattern as schematically depicted. The azimuthal orientation of the Co squares with respect to the crystallographic orientation of the Cu substrate and the direction of light incidence is indicated in Fig. 2(b). After removal of the grid, the Co structures were coated with 8 ML of Ni. Both deposition steps were done at room temperature, with evaporation rates of about 0.7 ML/min (Co) and

0.2 ML/min (Ni). To illustrate better the influence of the Co structures on the magnetic behavior of the Ni film, the images presented in Fig. 2 have been recorded at the edge of the mask, which leaves an area free of Co on the right hand side of the images.
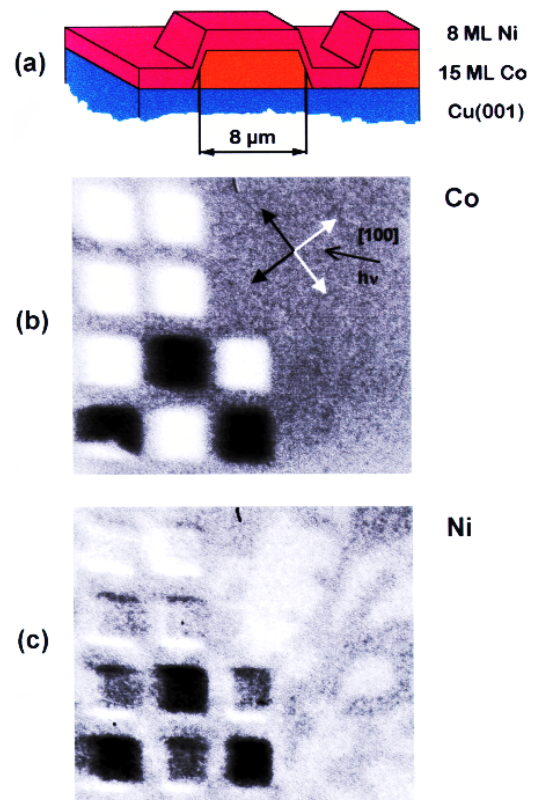

Fig. 2. (a) Sketch of the micropatterned epitaxial Ni/Co film. An array of 15-ML-thick 8×8 μm^2 Co squares with a 12 μm period on top of Cu(001) is coated with 8 ML of Ni. (b) Element-specific asymmetry image of the micropatterned Ni/Co film, recorded at the Co L_3 edge. Co squares are present only on the left hand side of the image. Different gray shades correspond to different projections of the magnetization direction onto the direction of the incoming light. The arrows suggest possible in-plane orientations of the Co magnetization. (c) Same as (b), but recorded at the Ni L_3 edge. Rounded out-of-plane domains are observed off the Co squares; on top of the Co squares the Ni magnetization follows that of the Co and is in-plane. The inset shows the geometry of the experiment. Because of the oblique incidence angle both in-plane and out-of-plane magnetization directions contribution to the magnetic contrast.

Figures 2(b) and 2(c) show a typical domain structure of this film in the as-grown state at the Co and Ni L_3 edges, respectively. The images were taken at BESSY at room temperature. The settings of the microscope were chosen to give a spatial resolution of about 500 nm; the monochromator exit slit was set to 200 μm, corresponding to a resolving power of about 200. This resulted in an exposure time of 10 min for each helicity. The spatially resolved asymmetry in the total electron emission intensity, which is a measure for the magnetization component in direction of the light incidence, is reproduced in Figs. 2(b) and 2(c) in a gray scale. Dark areas have a positive magnetization component in the direction of the incident light, bright areas a negative. Figure 2(b) shows the image taken at the Co L_3 edge, i.e seen through the Ni layer. Only three different gray scale levels are present in this image. The intermediate gray level outside the Co squares corresponds to zero asymmetry; bright and dark areas on the Co structures represent two opposite projections of the magnetization onto the direction of light incidence.

In films with a fourfold in-plane rotational symmetry one would expect four equivalent easy axes of in-plane magnetization. In epitaxial Co films on Cu(001) the easy axis was found to be along the substrate [110] azimuth.[28] In our experiment the substrate was aligned with its in-plane [100] crystallographic direction in the direction of the incident X-rays. A spontaneous magnetization of the Co squares along the four ⟨110⟩ directions would thus result in equal projections of either two of these easy axes along the light incidence. This would lead to the observation of only two different asymmetries in the experiment. The experimental finding is thus compatible with the Co structures magnetized in one of these fourfold crystallographic axes, which are indicated by two white and two black arrows in Fig. 2(b).

Another explanation for the appearance of only two different asymmetries in the present case could be the presence of a uniaxial in-plane anisotropy, aligning the magnetization along one principal axis. Such a uniaxial anisotropy could be induced, for example, by atomic steps in the substrate due to a miscut.[29] In the demagnetized state this would result in only two (opposite) directions of the magnetization, leading also to the observed gray tones. To unequivocally determine the direction of magne-

tization one would have to rotate the sample *in situ* around its azimuth. This is, unfortunately, not possible with the instrument in the present state. Work is in progress, however, to provide such a sample azimuthal rotation inside the microscope for future studies.

Figure 2(c) shows the asymmetry image recorded at the same spot of the sample at the Ni L_3 edge. The direction of light incidence is the same as in Fig. 2(b). The magnetic contrast at the positions of the underlying Co squares resembles the contrast observed at the Co L_3 edge. The bright and dark contrast right at the lower and upper edges of the squares, respectively, are an artifact due to a slight vertical sample drifft between the acquisition of the two images for opposite light helicity. In the Ni image additional domains are also observed in the region outside the Co structures, where the 8 ML Ni film sits directly on the Cu substrate. These domains exhibit a rounded shape, and a lower asymmetry difference between dark and bright. It is known that in ultrathin Ni films on Cu(001) the easy axis of magnetization turns from in-plane to perpendicular with increasing Ni thickness between 7 and 10 ML, and again to in-plane between 56 and 75 ML.[30,31] The Ni thickness of the first spin reorientation transition further varies slightly for different substrate temperatures during Ni deposition.[32] From the thickness of the Ni film, the rounded shape of the domains (which is indicative of a perpendicular magnetization), the knowledge from the literature, and our own investigations of Ni/Cu(001), we conclude that the Ni magnetization in the regions outside the Co squares is perpendicular to the film plane. On the Co squares the Ni magnetization is ferromagnetically aligned with the Co magnetization, which, due to the strong magnetostatic shape anisotropy of 15 ML Co, lies in the film plane. The inset of Fig. 2(c) shows the geometry of the light incidence in the present measurements. As already mentioned, both in-plane and out-of-plane magnetization directions contribute to the magnetic signal. Because of the incidence angle of 25° to the sample surface the projection of the magnetization onto the light helicity is lower in the case of perpendicular magnetization, which leads to the lower asymmetry difference between oppositely magnetized domains outside the Co squares. We therefore conclude from the images shown in Fig. 2 that the film undergoes a spin reorientation

transition from perpendicular to in-plane induced by the underlying Co.

It should be noted that the gray scales for the magnetic contrast in Figs. 2(b) and 2(c) are not identical, but are scaled to show the full range of resulting asymmetry values present in each image. Since raw images acquired at the maximum of the Ni L_3 absorption were used to calculate the asymmetry, and no background correction was performed, the tail of the energetically lower-lying Co $L_{2,3}$ absorption contributes to the Ni image, and induces the artifactual offset of the Ni asymmetry on top of the Co squares with respect to the area beside the Co squares, as is seen in Fig. 2(c). Although the Co signal is attenuated upon transmission through the Ni overlayer, it exhibits in the present case still the better signal-to-noise ratio at identical exposure time, because of the smaller XMCD asymmetry of Ni compared to Co.

The random pattern of dark and bright Co squares indicates that there is little or no interaction between different squares. Horizontally patterned films appear technologically promising, because of the additional control of magnetic properties by the design of the pattern.[33] With decreasing separation between the structures of such patterns, magnetic interactions between neighboring structures become increasingly important. Further work is in progress to image significantly smaller patterns with improved lateral resolution, and to study their properties and lateral interaction.

Figure 3(a) is a sketch of the Co/Cr/Fe sample used to study the magnetic exchange coupling between Fe and Co across a Cr spacer layer. On an Fe(001) whisker (300 μm width) a Cr wedge with a slope of ≈ 8 ML/mm was deposited by positioning a mask 0.7 mm in front of the sample and rocking the joint mask sample assembly by $\pm 17°$ during evaporation. After deposition of the Cr wedge it was completely covered with 5 ML Co. Both deposition steps were done at 500 K, with evaporation rates of about 0.1 ML/min (Cr) and 0.5 ML/min (Co). Figures 3(b)–3(d) show asymmetry images recorded at the ESRF at room temperature from the same area of the sample but with the photon energy turned to the Fe, Co and Cr L_3 edges, respectively. In these images the light was incident from the left, along the wedge gradient. The settings of the
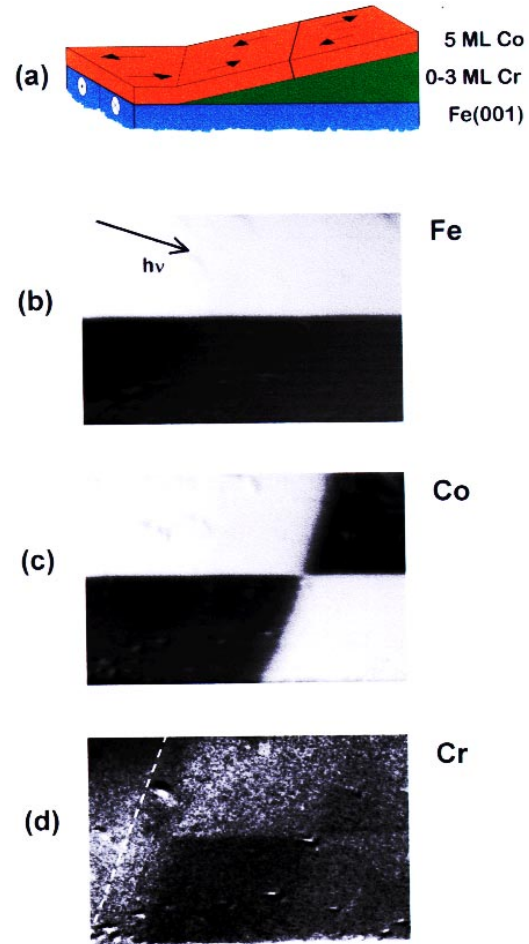

Fig. 3. (a) Sketch of the wedge-shaped Co/Cr layer on an Fe(001) whisker. A 0–3 ML Cr wedge is covered with 5 ML Co. Arrows indicate the direction of magnetization in the substrate and in the Co overlayers as found from the element-resolved magnetic domain images (b)–(d). (b) Element-specific asymmetry image recorded at the Fe L_3 edge. The Fe substrate exhibits a simple domain configuration of two oppositely magnetized domains aligned parallel to the whisker. (c) Element-specific asymmetry image recorded at the Co L_3 edge. The orientation of the Cr wedge is tilted by 19° with respect to the Fe whisker; the Cr thickness increases from left to right. The Co magnetization follows that of the Fe substrate up to a Cr coverage of ≈ 2 ML; at higher Cr film thicknesses antiferromagnetic coupling is observed. (d) Element-specific asymmetry image recorded at the Cr L_3 edge. The onset of the Cr wedge is indicated by the white broken line. The Cr magnetization follows that of the Co cover layer, except at the very lowest Cr coverages (≤ 0.3 ML), where the Cr magnetization is opposite to that of Fe and Co.

photoemission microscope were adjusted to enable the imaging of a relatively large area of the sample. This is achieved by using low extraction fields ($\approx$ 200 V, survey mode). A lateral resolution of about 1 μm and a field of view of more than 700 μm are the consequences. The exposure time for all of these images was only about 5 min for each helicity, thanks to the high brightness of the insertion device.

Figure 3(b) shows the asymmetry at the Fe L_3 edge, representing the Fe substrate magnetization seen through the Cr and Co layers. It consists of two oppositely magnetized domains aligned alongside the whisker, which is parallel to the horizontal edges of the image. The magnetization of these domains is indicated on the left hand edge of the sketch in Fig. 3(a). Bright areas correspond to a magnetization orientation opposite to the direction of the incident light, and dark areas to a magnetization along the light incidence. Such a simple domain configuration is often encountered in Fe whiskers, and is very convenient for imaging magnetic coupling in wedge-shaped overlayers.[6,7,34]

In Fig. 3(c) the corresponding image acquired at the Co L_3 edge is reproduced. The orientation of the Cr wedge is such that it increases from upper left to lower right, with a tilt angle of 19° with respect to the Fe whisker, as indicated schematically in Fig. 3(a). The highest Cr thickness in the lower right hand corner is about 3 ML. Comparing panels (b) and (c), one sees that at low Cr thickness the Co magnetization follows that of the Fe substrate, i.e the Co is coupled ferromagnetically to the Fe. For Cr thicknesses above $\approx$ 2 ML the magnetic contrast in the Co image is reversed with respect to the Fe image; Co hence displays an antiferromagnetic coupling to the Fe substrate at these Cr thicknesses. At the transition from ferromagnetic to antiferromagnetic coupling at 2 ML Cr coverage, a small region with an intermediate gray scale contrast is observed. This could be due to a simultaneous presence of ferromagnetic and antiferromagnetic coupling in that region, or to a biquadratic coupling behavior, which would result in a 90° rotation of the Co magnetization.[36] From the present measurements we cannot distinguish between these two possibilities.

The bottommost panel [Fig. 3(d)] shows the image recorded at the Cr L_3 edge. As mentioned before, a particular advantage of the technique lies in the combination of element selectivity and access to

buried layers. This makes it possible to study the residual ferromagnetic ordering of the Cr wedge, induced by the adjacent Fe and Co magnetic layers. Figures 3(d) shows that there is indeed a net ferromagnetic moment also in the Cr layer. The onset of the Cr wedge is indicated by the white broken line. Left of that line no Cr was deposited. The Cr magnetization follows that of the Co cover layer, with a darker constrast on the bottom half at the center of the image, and a darker area also on the upper right hand side. Only at the lowest Cr coverages below $\approx$ 0.3 ML, just right of the broken line, does the Cr magnetization seem to be opposite to that of Fe and Co. We observe a similar behavior on submonolayer Cr wedges on Fe(001) without additional overlayers, in the cases where the Cr is deposited at room temperature or slightly elevated temperatures. The temperature dependence of this effect points towards an important role of the Fe/Cr interface, and will be discussed in a forthcoming publication.[37] At this point we would like to emphasize again that elemental selectivity is an absolutely necessary prerequisite for studying the coupling behavior of submonolayer coverages on a ferromagnetic surface.

The Cr thickness where the antiferromagnetic exchange coupling is first observed (2 ML in Co/Cr/Fe) is lower than that of Fe/Cr/Fe (4–5 ML).[6,34] Whereas the period of the oscillation in the interlayer exchange coupling depends only on the nonferromagnetic interlayer material, different magnetic layers may influence the phase.[5,12] The difference in the Cr switching thickness could thus be attributed to a phase shift in the oscillations in the exchange coupling due to the different matching of the electronic states of Co to Cr compared to Fe and Cr. A significant influence of the amount of interface intermixing on the occurrence of the antiferromagnetic interlayer coupling[35] may also play a role.

The asymmetry contrast at the Cr L_3 edge [Fig. 3(d)] is only between 0.2 and 0.5% compared to about 20% at the Fe or Co L_3 edges [Figs. 3(b) and 3(c), respectively]. This indicates that the total net moment of the Cr layer is much lower than the Fe or Co moments. Furthermore, the contrast is significantly weaker in the region of antiferromagnetic exchange coupling compared to the region of ferromagnetic alignment between Fe and Co. On the right hand side of Fig. 3(d) the domain boundary between the upper and lower Fe domains is hardly discernible

in the Cr signal. If we assume that the apparent ferromagnetic moment in the Cr is primarily induced at the interfaces, the parallel alignment in the region of ferromagnetic exchange coupling points towards a net ferromagnetic contribution at both the Fe/Cr and Co/Cr interfaces. Assuming further that no change in these interface contributions occurs at the Cr thickness at which the exchange coupling changes from ferromagnetic to antiferromagnetic, the two interface contributions would tend to cancel out in the antiferromagnetically coupled region. This would explain the drop in asymmetry contrast above 2 ML Cr thickness. The residual Cr magnetism above 2 ML is oriented along the Co magnetization direction. In the above argumentation this leads to the conclusion that the Co/Cr interface contribution outweighs the Fe/Cr contribution to the Cr net moment. This could be attributed to interface roughness, which probably is higher between Cr and Co because of different roughness at the upper and lower Cr interfaces in the film growth at 500 K.[38] We note that due to the limited probing depth the Co/Cr interface has a somewhat higher weight in the images than the Fe/Cr interface; at 2 ML Cr thickness, however, this leaves only a less than 15% difference between the two interfaces, and the drop in asymmetry connected the effect of different weight alone should be much bigger.

In conclusion, we have demonstrated in this contribution how magnetic domain imaging using circularly polarized synchrotron radiation with a PEEM can be used to study magnetic coupling in a laterally resolved way. A specific feature of this approach is the selective mapping of buried layers and microstructures. The magnetic behavior of an array of Co microstructures coated with a perpendicularly magnetized Ni film was imaged. The interlayer exchange coupling between Co and Fe across Cr was investigated by imaging a wedged Co/Cr/Fe sample. By tuning the photon energy to the Co L_3 absorption edge the sign of the exchange coupling could be determined, which was found to change from ferromagnetic to antiferromagnetic at 2 ML Cr thickness. Besides, it was possible to detect a ferromagnetic signal from the Cr spacer layer. This signal follows the Co magnetization except for Cr coverages below ≈ 0.3 ML. The smaller Cr asymmetry in the region of antiferromagnetic coupling at Cr thickness between 2 and 3 ML compared to Cr below 2 ML

suggests that the observed Cr ferromagnetism is due to ferromagnetic coupling at the interfaces. Future work will be devoted to clarifying the role of interface quality and its dependence on growth temperature in the interface coupling of Cr to ferromagnetic materials.

Acknowledgments

References

1. P. Grünberg, R. Schreiber, Y. Pang, M. B. Brodsky and H. Sowers, *Phys. Rev. Lett.* **57**, 2442 (1986).
2. S. S. P. Parkin, N. More and K. P. Roche, *Phys. Rev. Lett.* **64**, 2304 (1990); S. S. P. Parkin, *Phys. Rev. Lett.* **67**, 3598 (1991).
3. A. Cebollada, R. Miranda, C. M. Schneider, P. Schuster and J. Kirschner, *J. Magn. Magn. Mater.* **102**, 25 (1991).
4. P. J. H. Bloemen, M. T. Johnson, M. T. H. van de Vost, R. Coehoorn, J. J. de Vries, R. Jungblut, J. aan de Stegge, A. Reinders and W. J. M. de Jonge, *Phys. Rev. Lett.* **72**, 764 (1994).
5. M. T. Johnson, M. T. H. van de Vorst, P. J. H. Bloemen, R. Coehoorn, A. Reinders, J. aan de Stegge and R. Jungblut, *Phys. Rev. Lett.* **75**, 4686 (1995).
6. J. Unguris, R. J. Celotta and D. T. Pierce, *Phys. Rev. Lett.* **67**, 140 (1991).
7. J Unguris, R. J. Celotta and D. T. Pierce, *Phys. Rev. Lett.* **79**, 2734 (1997).
8. D. Edwards and J. Mathon, *J. Magn. Magn. Mater.* **93**, 85 (1991); J. Mathon, M. Villeret, A Umerski, R. B. Muniz, J. d'Albuquerque e Castro, and D. M. Edwards, *Phys. Rev.* **B56**, 11797 (1997).
9. M. D. Stiles, *Phys. Rev.* **B48**, 7238 (1993).
10. P. Bruno, *Phys. Rev.* **B52**, 411 (1995).
11. P. B. Allen, *Solid State Commun.* **102**, 127 (1997), and references therein.
12. J. Kudrnovský, V. Drchal, R. Coehoorn, M. Šob and P. Weinberger, *Phys. Rev. Lett.* **78**, 358 (1997).
13. M. N. Baibich, J. M. Broto, A. Fert, F. Nguyen van Dau, F. Petroff, P. Eitenne, G. Creuzet, A Friederich and J. Chazelas, *Phys. Rev. Lett.* **61**, 2472 (1988).
14. G. Binasch, P. Grünberg, F. Saurenbach and W. Zinn, *Phys. Rev.* **B39**, 4828 (1989).

15. S. S. P. Parkin, R. Bhadra and K. P. Roche, *Phys. Rev. Lett.* **66**, 2152 (1991).

16. J. A. Brug, T. C. Anthony and J. H. Nickel, *MRS Bulletin*, Sept. 1996, p. 23.

17. J. L. Simonds, *Physics Today*, Apr. 1995, p. 26.

18. G. J. Gallagher, J. H. Kaufman, S. S. P. Parkin and R. E. Scheuerlein, US-Patent No. 5640343.

19. J. Stöhr, Y. Wu, M. G. Samant, B. B. Hermsmeier, G. Harp, S. Koranda, D. Dunham and B. P. Tonner, *Science* **259**, 658 (1993).

20. W. Swiech, G. H. Fecher, C. Ziethen, O. Schmidt, G. Schönhense, K. Grzelakowski, C. M. Schneider, R. Frömter, H. P. Oepen and J. Kirschner, *J. Electron Spectr. Rel. Phen.* **84**, 171 (1997); C. M. Schneider, *J. Magn. Magn. Mater.* **175**, 160 (1997).

21. G. Schütz, W. Wagner, W. Wilhelm, R. Kienle, R. Zeller, R. Frahm and G. Materlik, *Phys. Rev. Lett.* **58**, 737 (1987).

22. C. T. Chen. Y. U. Idzerda, H.-J. Lin, N. V. Smith, G. Meigs, E. Chaban, G. H. Ho, E. Pellegrin and F. Sette, *Phys. Rev. Lett.* **75**, 152 (1995).

23. J. Stöhr, *J. Electron Spectr. Rel. Phen.* **75**, 253 (1995).

24. W. L. O'Brien and B. P. Tonner, *Phys Rev.* **B50**, 2963 (1994).

25. B. T. Thole, P. Carra, F. Sette and G. van der Laan, *Phys. Rev. Lett.* **68**, 1943 (1992); P. Carra, B. T. Thole, M. Altarelli and X. Wang, *ibid.* **70**, 694 (1993).

26. W. Kuch, M. Salvietti, Xingyu Gao, M.-T. Lin, M. Klaua, J. Barthel, Ch. V. Mohan and J. Kirschner, *Phys. Rev. B*, in print.

27. M. Drescher, G. Snell, U. Kleineberg, H.-J. Stock, N. Müller, U. Heinzmann and N. B. Brookes, *Rev. Sci. Instrum.* **68**, 1939 (1997).

28. C. M. Schneider, P. Bressler, P. Schuster, J. Kirschner, J. J. de Miguel, R. Miranda and S. Ferrer, *Vacuum* **41**, 503 (1990); C. M. Schneider, A. K. Schmid, P. Schuster, H. P. Oepen and J. Kirschner, in *Magnetism and Structure in Systems of Reduced Dimension*, eds. R. F. C. Farrow *et al.* (Plenum, New York, 1993).

29. A. Berger, U. Linke and H. P. Oepen, *Phys. Rev. Lett.* **68**, 839 (1992); H. P. Oepen, A. Berger, C. M. Schneider, T. Reul and J. Kirschner, *J. Magn. Magn. Mater.* **121**, 490 (1993).

30. W. L. O'Brien and B. P. Tonner, *Phys. Rev.* **B49**, 15370 (1994).

31. B. Schulz and K. Baberschke, *Phys. Rev.* **B50**, 13467 (1994).

32. M. Zheng, J. Shen, Ph. Ohresser, Ch. V. Mohan, J. Barthel and J. Kirschner, to be published.

33. C. Mathieu, C. Hartmann. M. Bauer, O. Buettner, S. Riedling, B. Roos, S. O. Demokritov, B. Hillebrands, B. Bartenlian, C. Cappert, D. Decanini, F. Rosseaux, E. Cambril, A. Müller, B. Hoffmann and U. Hartmann, *Appl. Phys. Lett.* **70**, 2912 (1997).

34. C. M. Schneider, K. Meinel, J. Kirschner, M. Neuber, V. Wilde, M. Grunze, K. Holldak, Z. Celinski and F. Baudelet, *J. Magn. Magn. Mater.* **162**, 7 (1996).

35. M. Freyss, D. Stoeffler and H. Dreyssé, *Phys. Rev.* **B56**, 6047 (1997).

36. M. Rührig, R. Schäfer, A. Hubert, R. Mosler, J. A. Wolf, S. Demokritov and P. Grünberg, *Phys. Stat. Sol. (a)* **125**, 635 (1991).

37. C. M. Schneider, R. Frömter, Ch. Ziethen, W. Swiech, W. Kuch, J. Gilles, M. Seider, G. Schönhense and J. Kirschner, to be published.

38. B. Heinrich, J. F. Cochran, D. Venus, K. Totland, C. M. Schneider and K. Myrtle, *J. Magn. Magn. Mater.* **156**, 215 (1996).

1 Imaging Magnetic Microspectroscopy

WOLFGANG KUCH

Max-Planck-Institut für Mikrostrukturphysik, Weinberg 2, D-06120 Halle, Germany

There are several well established techniques for spectroscopy of magnetic films and surfaces that are commonly employed when information about electronic states, binding properties, or element-resolved magnetic properties is required. The reduction in lateral size that goes along with the soaring extend to which magnetic elements and devices are used or planned to be used in technological applications in magnetic sensors, data storage, or magnetoelectronics, demands for magnetic spectroscopic information on a microscopic lateral lengthscale. Thus the combination of magnetic spectroscopy and microscopy into what is commonly termed microspectroscopy or spectromicroscopy would be ideal for the study of small magnetic structures.

This chapter explains the combination of photoelectron emission microscopy (PEEM) and x-ray magnetic circular dichroism (XMCD) in absorption for imaging XMCD-PEEM microspectroscopy. In a PEEM, an electrostatic electron optics creates a magnified image of the secondary electron intensity distribution at the sample surface. When excited by soft x-rays, the image intensity can thus be regarded as a local electron yield probe of x-ray absorption. In XMCD, the measurement of the total electron yield of the sample is frequently used to determine the x-ray absorption as a function of photon energy and helicity of the circularly polarized radiation. Scanning consequently the photon energy and recording PEEM images at each photon energy step for both helicities results in a microspectroscopic data set which allows to extract the full information that is usually obtained from XMCD spectra for each single pixel of the images. Of particular interest is thereby the application of the so-called sum rules to extract the effective spin moment and the orbital moment, projected onto the direction of incoming light. This chapter starts with a short overview of magnetic microspectroscopy techniques in comparison to XMCD-PEEM microspectroscopy. The basics of the underlying spectroscopic and microscopic methods is shortly explained in Sec. 1.2. Important experimental aspects inherent to XMCD-PEEM microspectroscopy are discussed in Sec. 1.3. Finally in Sec. 1.4 two recent examples of application of XMCD-PEEM microspectroscopy are presented, in which the method has proven beneficial for the study of interesting issues in the field of ultrathin magnetic films.

2

1.1
Microspectroscopy and Spectromicroscopy – an Overview

The terms "microspectroscopy" and "spectromicroscopy" both refer to techniques which combine spectroscopy and microscopy. "Spectromicroscopy" is commonly used to describe microscopic imaging techniques in which the image contrast is due to spectroscopic details. The acquired images are then related to a certain energy of either electrons or photons. "Microspectroscopy", on the other hand, is primarily used to describe techniques in which spectroscopic information is obtained from a small area on a sample. In terms of the dependence of delivered information, spectromicroscopy is thus a technique that yields data as a function of the two space coordinates for a certain value of the energy coordinate, whereas microspectroscopy delivers data as a function of energy for a fixed pair of values of the space coordinates. The consequent extension of both spectromicroscopy and microspectroscopy would be to get the full spectroscopic *and* spatial information in the same measurement, that is, data are obtained as a function of all three variables, namely the two space coordinates and energy. In that limit "spectromicroscopy" and "microspectroscopy" become identical. The topic of this contribution is the combination of x-ray magnetic circular dichroism (XMCD) and photoelectron emission microscopy (PEEM) for the measurement of such a three-dimensional data set. It may be considered as either full-image microspectroscopy or full-energy spectromicroscopy, where we (arbitrarily) have chosen the former name, and thus will refer to it as microspectroscopy. In all cases the extension to full-image microspectroscopy, or imaging microspectroscopy, represents a considerably higher experimental effort, and it will be only practical if the gain in information is worth it.

In this section a short overview over some microspectroscopic and spectromicroscopic techniques used for the investigation of magnetic samples is given, and the use of XMCD-PEEM as an ideal imaging microspectroscopic technique is motivated. A more comprehensive overview over spectromicroscopic techniques also for non-magnetic applications can be found in Ref. [1.1].

1.1.1
Scanning techniques

In microscopy one can generally distinguish between scanning techniques and techniques that use parallel imaging. We will start with the scanning techniques.

A scanning technique that is commonly employed at most synchrotron light sources and can be used for magnetic microspectroscopy is scanning x-ray microscopy (SXM). The incident x-ray radiation from the synchrotron is focused by an appropriate x-ray optics, for example by Fresnel zone plates, into a small spot on the sample. Depending on the photon energy range spot sizes smaller than 200 nm have been achieved [1.2, 3]. In plain microscopy applications the sample is

3

scanned, and the transmitted x-rays generate the microscopic image. With only minor modifications such set-ups can easily be used for spectromicroscopy or microspectroscopy. For magnetic microspectroscopy in the simplest case the dependence of the transmitted, absorbed or reflected x-ray intensity on photon energy is recorded. Magnetic contrast is obtained from the dependence of the x-ray absorption cross section at elemental absorption edges on magnetization direction, when circular polarization is used (see section 1.2.1). Another variant includes electron spectroscopy, where emitted electrons of a certain kinetic energy are detected [1.4]. Here magnetic contrast can be obtained from magnetic dichroism in photoelectron spectroscopy [1.5]. Since the magnetic contrast is higher in absorption, only this has been used for magnetic imaging [1.6, 7]. The advantage of scanning x-ray microscopy is that the microscopy component of the technique is completely in the excitation path, so that on the detection path standard spectrometers can be used to provide the spectroscopy component. The energy resolution for electron detection can thus be chosen to be the same as in plain photoelectron or Auger electron spectroscopy. For imaging microspectroscopy, however, the disadvantage, as in all scanning techniques, is that the time needed for a complete scan of both the sample position and the energy can be quite long.

Another scanning spectromicroscopic technique for imaging magnetic properties is spin-polarized scanning tunneling microscopy, in which the spin-dependence in electron tunneling spectroscopy is used as contrast mechanism (see chapter 10). The bias voltage between a magnetic tip and the sample is set to an energy at which the dependence of the tunnel current on the direction of sample magnetization is maximized [1.8, 9]. Without changing the experimental set-up also microspectroscopy can be performed. For this the tip position is kept fixed, and the bias voltage is scanned. In principle also imaging scanning tunneling microspectroscopy is possible. In most cases, however, the microspectroscopic information is only needed to find the best energy for obtaining magnetic domain images.

For the imaging of magnetic domains also laser scanning Kerr microscopy has been used [1.10]. The magneto-optical Kerr effect using visible light is a commonly employed method to measure magnetization curves. The spectroscopic variant, Kerr spectroscopy, where the wavelength of the exciting laser light is scanned, is used for the characterization of electronic properties [1.11]. No reports exist, however, of imaging scanning Kerr microspectroscopy measurements.

As mentioned before, the disadvantage of all scanning techniques for imaging microspectroscopy in general is that three parameters, namely two space coordinates *and* the energy, need to be scanned step by step, which can make it a rather lengthy undertaking. In most cases consequently the relation between effort and benefit is not favoring imaging scanning microspectroscopy.

1.1.2
Imaging techniques

Parallel imaging techniques have the advantage over scanning techniques that for imaging microspectroscopy only the energy needs to be scanned, while at each

4

energy step a complete image is acquired. Parallel imaging techniques may thus be accelerated to achieve feasible measuring times even for full image microspectroscopy. The individual images are equivalent to two-dimensional sets of data points, which are acquired in parallel. Parallel imaging of magnetic spectroscopic information is based either on magneto-optical effects or on magneto-dichroic effects in electron spectroscopy after optical excitation.

An example for magneto-optical effects [1.12] is the magneto-optical Kerr effect using visible light, as already mentioned in the previous section. In the microscopic variant optical microscopy is used to convert the magneto-optical information into a domain image of the sample [1.10]. The plus in information that would result from the combination off Kerr microscopy with wavelength scanning Kerr spectroscopy, however, seems not worth the effort, since no imaging Kerr microspectroscopy has been reported in literature up to now.

This is different in the range of soft x-rays, where elemental core level absorption edges are accessed. The optical constants vary strongly in the vicinity of these edges, and depend on the magnetization of the sample. The absorption of circularly polarized x-rays at the absorption edges depends on the relative orientation between light helicity and magnetization direction. This mechanism, which will be presented in the following section, is named x-ray magnetic circular dichroism (XMCD) in absorption, and is the first choice for obtaining magnetic contrast in imaging. It has been demonstrated, though, that in principle also magnetic circular dichroism in angle-resolved photoemission can be used to obtain magnetic contrast in photoelectron spectromicroscopy. Images obtained in an imaging hemispherical electron analyzer from Fe $3p$ photoelectrons after off-resonant excitation with circular polarization exhibited a weak magnetic contrast [1.13]. In a more recent paper even magnetic contrast using unpolarized light from an x-ray tube and magnetic dichroism in Fe $2p$ photoemission was claimed [1.14]. The signal to noise ratio, however, is significantly worse in the photoemission case compared to images obtained in the same instrument using XMCD in absorption to generate magnetic contrast [1.15, 16].

Two ways can generally be used to image the local x-ray absorption: either by imaging of photons, or by imaging of emitted electrons. Imaging of the transmitted photons has been successfully performed for magnetic spectromicroscopic domain imaging in a transmission x-ray microscope [1.17]. The sample is thereby prepared such that its total thickness allows transmission of soft x-rays, and a zone plate based x-ray optics is used to create the image of the transmitted beam. The drawback for microspectroscopy with photon imaging techniques in general are problems due to the energy dependence of the focal length of x-ray optics, in particular of zone plates. The magnification and focusing of the resulting image thus varies during a photon energy scan, which leads to a significant blurring of the image if no correction for example by a sophisticated image processing software is performed.

In that respect the imaging of the distribution of emitted electron intensity for microspectroscopic purposes is clearly easier. Since just the x-ray absorption needs

5

to be detected as a function of photon energy, no explicit energy filtering of the electrons is necessary, and the high intensity secondary electrons may be used. X-ray optics, if any, is used only for the illumination of the imaged area of the sample. Different types of electron optics have been employed successfully for XMCD based spectromicroscopic imaging of magnetic domains, all of which are classified under the name electron emission microscopy. While in most of the more recent work fully electrostatic photoelectron emission microscopes (PEEMs) (see section 1.2.2) were used [1.18-23], also an imaging hemispherical electron analyzer [1.15, 16], and in Ref. [1.24] a low energy electron microscope (LEEM, [1.25, 26]) have been employed. Fig. 1.1 shows an example of a domain image taken with a PEEM. It shows a lithographic triangular microstructure of 30 nm thick polycrystalline Co. Different grayscale contrast represents different directions of magnetization, where bright means pointing up, dark pointing down, and
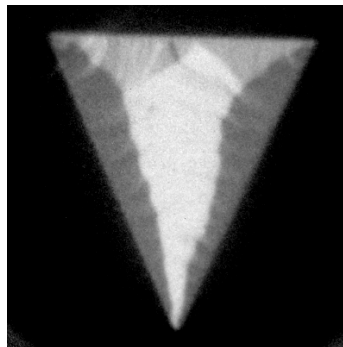
Fig. 1.1: Magnetic domain image of a triangular microstructure of 30 nm thick polycrystalline Co on Si using a PEEM and XMCD. Field of view 40×40 μm^2. [1.27]

intermediate gray indicates a horizontal magnetization direction [1.27].

The advantage of extending XMCD based spectromicroscopy with electron detection to imaging microspectroscopy are obvious: Experimentally it is quite straightforward, if some aspects as outlined in section 1.3 are considered. XMCD is a widely used and comparably well understood spectroscopic technique, so there is a significant gain in quantitative information from full-image microspectroscopy compared to the acquisition of spectromicroscopic images; this will be discussed in section 1.2.1. Finally due to the availability of high flux insertion device beamlines at third generation synchrotron radiation light sources the time required for recording three-dimensional data sets for imaging microspectroscopy is approaching feasibility while still maintaining reasonable spatial resolution. This will be demonstrated by selected examples in section 1.4.

A further advantage of x-ray absorption based spectromicroscopy is that by using linearly polarized x-rays a magnetic-dichroic signal can be obtained even

6

from oxidic antiferromagnets [1.28, 29]. The use of this x-ray linear magnetic dichroism for the imaging of antiferromagnetic domains is outlined in chapter 2.

In the remainder of this chapter PEEM is assumed as the electron emission microscopy technique for magnetic x-ray absorption spectroscopy. This is due to the existing work in this field, however, most of what is said is identically valid also for any other type of electron emission microscopy.

1.2
Basics

1.2.1
X-ray Magnetic Circular Dichroism

Since its experimental discovery [1.30], magnetic circular dichroism in soft x-ray absorption has developed into a widely used technique for the element-specific characterization of magnetic films and multilayers. This is in part due to the so-called sum rules that have been proposed to deduce quantitative magnetic information from XMCD spectra [1.31, 32]. Other reasons for the widespread use of XMCD are: the magnetism-related changes in absorption cross section are quite large, there are several synchrotron radiation light sources around the world providing x-rays of tunable wavelength, and it is comparatively easy to measure x-ray absorption from the total photoelectron yield, where only the sample current has to be detected.

This section is aimed to provide the reader who is not familiar with XMCD spectroscopy with the basic ideas in order to follow the remainder of the chapter. More comprehensive introductions can be found elsewhere [1.12, 22, 33-36].

7
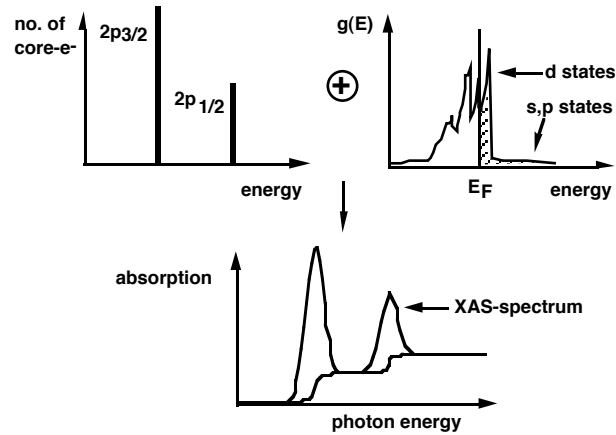
Fig. 1.2: Schematic explanation of x-ray absorption spectroscopy (XAS). The absorption spectrum shown in the bottom panel results from the convolution of the occupied density of states of the core levels (upper left) and the unoccupied density of states *g(E)* of the valence states (upper right, shaded area). The contribution from *s,p* states is usually approximated and subtracted in the form of a step function (bottom panel).

   We will restrict ourselves to the $L_{2,3}$ absorption edges of $3d$ transition metals, i.e., the onset of excitation of transitions of $2p$ core electrons to empty states above the Fermi level. Let us for the moment consider absorption in a paramagnet. An explanation of x-ray absorption spectroscopy in a one-electron description is shown in Fig. 1.2. The left upper panel shows a schematic representation of the occupied density of states of the $2p$ core levels. The important point here is that because of spin-orbit interaction the $2p$ states are energetically split into the clearly separated $2p_{1/2}$ and $2p_{3/2}$ levels. Any further splitting into sublevels is not important here. Absorption of x-rays by the excitation of electronic transitions from the $2p$ states is determined by the occupied density of states of the $2p$ core electrons, and the unoccupied density of states available for these transitions above the Fermi energy (E_F). The latter is schematically shown in the upper right panel, where the shaded area represents the unoccupied states. The contribution from states of predominantly s,p character is represented by a flat energy dependence, whereas d states are shown as sharp peaks at about E_F. The resulting absorption spectrum is obtained from the convolution of the occupied density of states of the left upper panel and the unoccupied density of states of the right upper panel. Finite experimental photon energy resolution has to be taken into account by an additional convolution with a Gaussian. A typical $L_{2,3}$ absorption spectrum is shown in the bottom panel of Fig. 1.2. It is seen that the absorption signal related to transitions into empty $3d$ states shows up as two peaks at the energetic positions of the $2p_{1/2}$ and $2p_{3/2}$ states, whereas the unoccupied s,p states give rise to a step-like background. Since the magnetic moment of the $3d$ transition metals is mainly governed by $3d$ valence electrons, the latter is usually subtracted as a

8

step-function with relative step heights of 2:1 [1.37], according to the occupation
of the $2p_{3/2}$ and $2p_{1/2}$ core states, as shown in the bottom panel of Fig. 1.2.
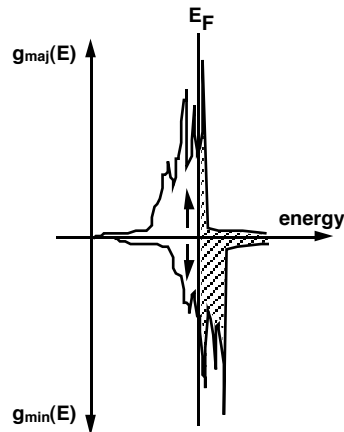
Fig. 1.3: Schematic representation of density of states of a ferromagnetic metal. Shown are the spin
resolved density of states for majority electrons $g_{maj}(E)$ in the positive y direction, and the spin re-
solved density of states for minority electrons $g_{min}(E)$ in the negative y direction. The shaded areas
are unoccupied density of states above the Fermi energy E_F available for $2p{\to}3d$ transitions.

If $2p{\to}3d$ transitions are excited by circularly polarized radiation, these transi-
tions exhibit a spin polarization because of selection rules [1.38]. In other words,
for a certain light helicity more electrons of one spin direction with respect to the
direction of the incoming light are excited into the unoccupied $3d$ states than of
the other spin direction. In a paramagnet this does not lead to a change in absorp-
tion intensity, since the number of unoccupied states is equal for both spin direc-
tions. In a ferromagnet, however, the density of unoccupied states is different for
electrons of spin parallel or antiparallel to the magnetization direction, leading to a
spin magnetic moment defined by the difference in occupation. This is explained
in Fig. 1.3. It shows a schematic representation of the spin resolved density of
states, separated into density of states of majority spin electrons on the top, and
density of states of majority spin electrons on the bottom. If magnetization and
light incidence are aligned with each other to some degree, there are consequently
more possible transitions for one direction of light helicity than for the other. This
leads to a difference in absorption for opposite light helicity. In a dichroism spec-
trum, calculated as the difference between absorption spectra for opposite helicity, a
non-zero difference will show up at the energy positions of the peaks related to
transitions from the $2p_{3/2}$ and $2p_{1/2}$ levels into the empty $3d$-like states. Since the
spin polarization of $2p_{3/2}{\to}3d$ transitions has an opposite sign than the that of the
spin polarization of $2p_{1/2}{\to}3d$ transitions [1.12, 35], the dichroism at the L_3 and
L_2 edge will have opposite sign, i.e., the difference curve will show peaks of
opposite sign at the energy positions of the L_3 and the L_2 edge. This is

9

schematically shown for the (hypothetical) case of a material with only a spin moment μ_S in the top panel of Fig. 1.4. There the difference curve between absorption spectra taken with opposite helicity of the circularly polarized light is depicted, which exhibits a positive peak at the L_3 edge, a negative peak at the L_2 edge, and zero elsewhere. The spin-polarization of $2p_{1/2} \rightarrow 3d$ transitions is twice as large as the spin polarization of $2p_{3/2} \rightarrow 3d$ transitions, whereas the absorption at the L_3 edge is twice as high as at the L_2 edge because of core hole occupation (cf. Fig. 1.2). Both together leads to an equal size of the dichroism at the two edges, as schematically plotted in the topmost panel of Fig. 1.4.

$2p \rightarrow 3d$ transitions excited by circularly polarized radiation are not only spin polarized, but also show an orbital polarization. This is a direct consequence of the absorption of a circularly polarized photon with angular momentum $\Delta m = \pm 1$ [1.12, 35]. Both the $2p_{1/2} \rightarrow 3d$ and $2p_{3/2} \rightarrow 3d$ transitions show the same sign and same magnitude of orbital polarization. If a sample possesses a non-zero orbital magnetic moment this means that the unoccupied states (and also the occupied states) have a non-zero net angular momentum. Let us consider the (hypothetical) case of a metal with only an orbital moment and no spin moment. In that case there will be again a non-zero dichroism at the L_3 and L_2 edges, but this time with an equal sign at the two edges. Because of the different number of $2p_{1/2}$ and $2p_{3/2}$ electrons the resulting dichroism at the L_3 edge is twice as large as at the L_2 edge (middle panel of Fig. 1.4).

A real sample will have both spin and orbital magnetic moments. The two extreme cases shown in the top and center panel of Fig. 1.4 define an orthonormal basis for the measured XMCD spectrum from a real sample (bottom panel of Fig. 1.4), which will be a superposition of both. The experimental spectrum can thus be decomposed unambiguously into its spin and orbital basis functions. This is what is done by the so-called sum rules [1.31, 32].

It has to be mentioned that what is extracted as the "spin moment" from the sum rules is an effective spin moment $\mu_{S,eff}$ [1.32], which includes the actual spin magnetic moment μ_S, plus a contribution from the magnetic dipole term $7/2\ T_Z$. The latter is zero in the bulk of cubic crystals, but can be of the same order as the orbital moment in ultrathin films [1.39].

Although the derivation of the sum-rules was done under simplifying assumptions, and there has been some dispute about their applicability [1.34, 37, 40-43], they seem to yield reasonable results for the $3d$ transition metals [1.34, 37, 44-46]. Together with the element-selectivity of x-ray absorption spectroscopy at core level absorption edges they provide a quite powerful tool for the quantitative investigation of magnetic materials.

10
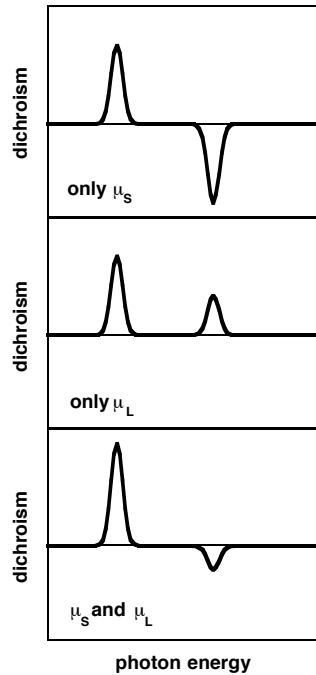
Fig. 1.4: Schematic explanation of sum rule analysis of XMCD spectra to obtain spin and orbital moments. Shown is the decomposition of an XMCD spectrum (bottom) into its components resulting from spin moment μ_S (top) and orbital moment μ_L (center).

1.2.2
Photoelectron Emission Microscopy

Photoelectron emission microscopy (PEEM) belongs to the parallel imaging electron microscopies. The name "photoelectron" is due to its use in metallurgy in early years, where threshold excitation of photoelectrons at the vacuum level by illumination with Hg discharge lamps was used for the acquisition of work function contrast images [1.47]. For excitation with higher photon energies, which will be considered in this chapter, low energy secondary electrons are dominant in the imaging process. We nevertheless stick to the name PEEM, although in that case "secondary electron emission microscope" would be more correct.

After the introduction of ultrahigh-vacuum compatible instruments [1.48, 49], PEEM has been used for the study of surfaces and surface reactions [1.50-53]. Including a magnetic electron beam splitter allowed the excitation by low energy electrons (LEEM, low energy electron microscopy [1.25, 54]), which yields additional information about the surface structure and morphology. The availability of synchrotron light sources for excitation with x-rays of tunable

11

energy opened a new field of application of PEEMs [1.55], in which resonant x-ray absorption at elemental core levels is used to image the distribution of different elements at the sample surface.

In a PEEM, in contrast to transmission electron microscopy, the electrons that are used for the imaging do not have a well defined energy and momentum. To get a sharp image it is therefore necessary to limit the range of electron energies and emission angles. In a PEEM this is done by passing the accelerated electrons through a pinhole aperture, the so-called contrast aperture. A higher lateral resolution is thereby achieved at the expense of intensity, and vice versa.
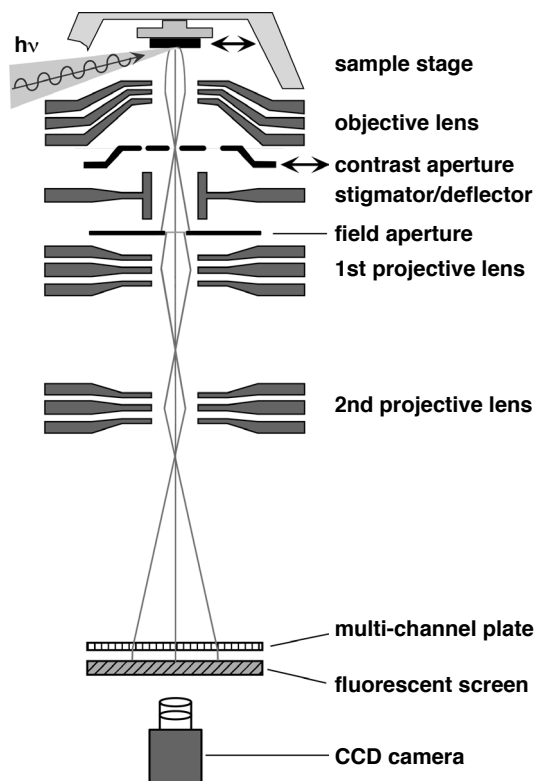
Fig. 1.5: Schematic set up of a photoelectron emission microscope (PEEM). Electrostatic electron lenses create an image of the electrons emitted at the sample surface at a fluorescent screen. (From Ref. [1.21]).

Fig. 1.5 shows the schematic set-up of an electrostatic PEEM [1.21]. The principle of other electrostatic PEEMs is similar, so that the main points can be explained on this type. In Fig. 1.5 the sample is shown at the top. It is illuminated by synchrotron radiation under a grazing angle to the sample surface, which is 30° in the present example. The sample is kept on ground potential, and

12

electrons are accelerated towards the objective lens, an electrostatic tetrode lens. Typical acceleration voltages are 10–20 kV. The contrast aperture is located in the back focal plane of the objective lens. It selects only those electrons for imaging that originate from a certain range of emission angles. The size and lateral position of this aperture can be changed by moving a slider assembly carrying several apertures of different diameter. In an alternative design the contrast aperture is located at the back focal plane of the first projective lens [1.23]. Astigmatism and small misalignments of the optical axis, caused for example by a misalignment of the sample, can be corrected by an electrostatic octupole stigmator and deflector. A variable field aperture in the image plane of the objective lens allows to limit the field of view and to suppress stray electrons. Two electrostatic projective lenses transfer the image onto an imaging unit, which in our example consists of an electron multichannel multiplier and a fluorescent screen on the vacuum side, and of a charge coupled device (CCD) camera with a conventional lens optics outside the vacuum chamber. Alternative approaches use a glass fiber coupling between screen and CCD camera [1.23].

Top resolutions of down to 20 nm in PEEM imaging using topographic or elemental contrast in threshold photoemission [1.56] and for excitation with synchrotron radiation [1.23, 57] have been reported. Even better resolution can be achieved in the LEEM mode, using magnetic objective lenses [1.25, 26, 58]. Presently attempts are underway to push the resolution to below 5 nm by aberration correction [1.59]. In XMCD-PEEM magnetic microspectroscopy, however, intensity is a critical issue. To achieve reasonable acquisition times for the measurement of a complete microscopic and spectroscopic data set, lateral resolution will typically be selected to be a few hundred nanometers in practical microspectroscopy applications.

1.3
About doing XMCD-PEEM microspectroscopy

When employing magnetic dichroism effects for the spectroscopy of magnetic materials, the magnetic information is obtained from changes in the spectra that occur either upon changing the magnetization state of the sample, or the polarization properties of the exciting radiation. This usually involves the measurement of relatively small differences between large signals, and imposes high experimental requirements with respect to signal reproducibility, stability, and flux normalization. The additional imaging step in microspectroscopy is certainly not facilitating the fulfillment of these requirements. In the following, some of the crucial obstacles and their solutions specific for XMCD-PEEM microspectroscopy will be discussed.

13

1.3.1
Experiment

Let us first consider effects related to the incident radiation. The normalization to the flux of the incoming beam is not straightforward in microspectroscopy, in contrast to conventional absorption spectroscopy. In the latter usually the photo yield from a suitable optical element in the beamline or from a specially designed flux monitor is recorded simultaneously to the sample signal. Since the entire photon beam is contributing to both the monitor signal and the signal from the sample, normalization is achieved by simply dividing one by the other. In imaging microspectroscopy, however, the *local* photon flux density is important, not the *integral* flux. It can not be directly measured, and may locally deviate significantly from the integral monitor flux signal. The cause of such deviations may be the radiation characteristics of the insertion devices used in third generation synchrotron light sources, and beamline x-ray optics. An inhomogeneous distribution of the photon intensity within the imaged area on the sample invalidates the normalization to a conventional beam monitor. The fact that the intensity distribution of undulators depends also on the relative photon energy with respect to the maximum of the undulator harmonics complicates matters further. Although in principle these effects can not be avoided, it is possible from the experimental side to reduce the discrepancy between the local flux density and the integral flux measured by the monitor as much as possible, as described in the following. If the remaining error is below a few percent it can be approximately corrected out in the course of data analysis, as will be explained in more detail in section 1.3.2.

To get a better correlation between the local and integral photon flux it is important that the illuminated area on the sample be not much bigger than what is imaged in microspectroscopy. All the flux outside the field of view adds an irrelevant contribution to the monitor signal. Should the typical light spot of a certain beamline be too big, suitable apertures or beam blockers may be inserted upstream from where the monitor signal is measured. Good positions are close to image planes of the light spot, since sharp cutting edges are achieved there. In beamline optics where the light spot is an image of the exit slit, reducing the exit slit width also reduces the illuminated area. Attention should be also paid to the adjustment of the imaged area to the center of the undulator radiation. A significant reduction of photon energy dependent effects can be achieved when the movement of the insertion device gap can be synchronized with the scanning of the grating of the monochromator. In this way a constant relative energy position with respect to the undulator harmonic, for example the maximum, can be maintained, and the flux distribution on the sample should be energy independent.

An important issue for those beamline optics where the light spot is an image of the exit slit is local energy resolution. In such beamlines the monochromator energy dispersion at the position of the exit slit is imaged onto the sample surface. As a consequence the local resolution does not change when the slit size is varied.

14

The more serious implication for microspectroscopy is that there is also a photon energy dispersion across the image in this case. The monochromator mode of operation should therefore be selected to have the least possible dispersion. If the energy dispersion across the image is still too big compared to the width of the spectral features of the sample, which may be the case for low magnification applications, this shift in energy across the image has to be considered in data analysis of the microspectra.

Especially for high resolution microspectroscopy image stability during an energy scan is important. In the case of absorption measurements of XMCD, where the photon energy is scanned, only such effects on image stability are left that are related to electron intensity, as for example space charges, or to the energy of the electrons used for imaging. For metallic samples and sufficiently high photon energies, such as the L-edges of transition metals where the scan range is small compared to the absolute energy, image stability is usually not a problem.

A point that is normally not given closer attention in microscopy, but which becomes essential in quantitative microspectroscopy, is the linearity of the image detection system. A typical detection system may consist of several components as for example multichannel electron multiplier, fluorescence screen, and CCD camera. Although it is desirable to reach intensities as high as possible to get short exposure and scan times, it may be sometimes necessary to sacrifice some output signal in order to operate in the linear range of the image detection system. This range can be determined beforehand by manipulating the incident beam flux in a controlled way and comparing image intensity and flux monitor signal.

1.3.2
Data analysis

In principle data analysis in microspectroscopy could follow the same procedures as already established for data analysis in conventional spectroscopy. The main difference, however, is that in imaging microspectroscopy there are *many* spectra, for example as many as there are pixels in the image. Data analysis for extracting the important parameters from this large number of spectra should therefore meet the following two requirements: it should be quick, and it should be automatic. In this section a method will be described that allows the automatic analysis of XMCD microspectra to extract spin and orbital magnetic moments by means of sum rules.

To explain the procedure, the example of XMCD-PEEM microspectroscopy from a bilayer of 10 atomic monolayers (ML) Fe and 6 ML Co on a Cu(001) single crystal surface will be examined [1.60]. A typical single pixel spectrum corresponding to 3×3 μm^2 area of the sample is shown in Fig. 1.6 (a). Depicted are the raw pixel intensity data for incident light of positive (solid line) and negative helicity (dotted line). The two peaks correspond to the Fe L_3 and L_2 absorption maxima. Circularly polarized x-rays of opposite helicity were provided by one of the two helical undulators of beamline BL25SU of SPring-8, Japan. After hav-

15

ing set the two undulators to opposite helicity, helicity reversal was realized by using only one undulator and fully opening the other.
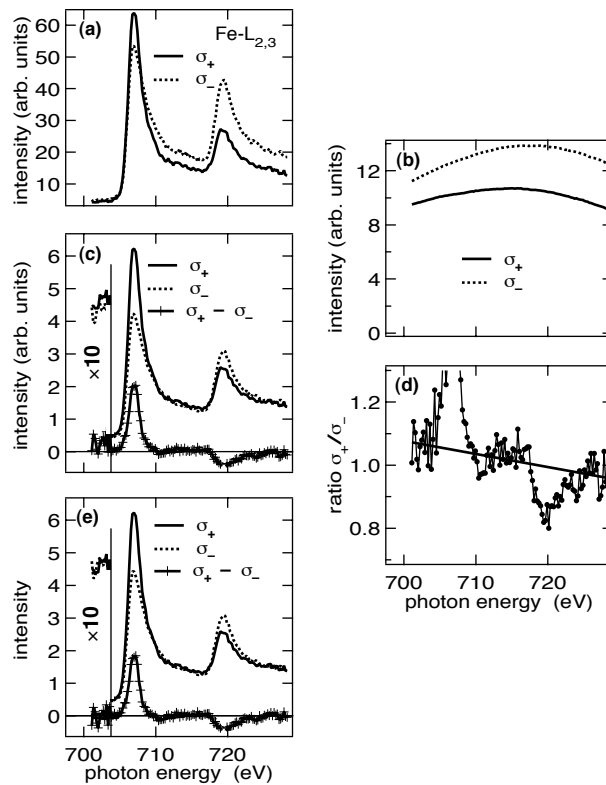

Fig. 1.6: Correction of single pixel XMCD data. As an example raw pixel intensity spectra for opposite helicity from a 3×3 mm² pixel of 10 ML Fe/6 ML Co/Cu(001) are shown in panel (**a**). Curves for positive and negative helicity are shown as solid and dotted lines, respectively. (**b**): integral photon flux as measured from the photo yield of the last mirror. (**c**): data from (**a**), corrected by the flux (**b**). The difference of the two curves is shown at the bottom. (**d**): ratio of the two spectra of (**c**). The straight line is a linear fit to the data disregarding the peak regions. (**e**): spectra from (**c**) after multiplying the curve for negative helicity by the straight line of (**d**). Also shown is the difference curve. The pre-edge region for photon energies below 704 eV is shown scaled by a factor of 10 in intensity in panels (**c**) and (**e**) for better visualization of the alignment of the spectra. (From Ref. [1.60].)

The integral monitor signal taken simultaneously with the spectra of Fig. 1.6 (a) is shown in Fig. 1.6 (b). It was obtained from the photo yield of the last optical element, a gold coated refocussing mirror. The intensity for negative helicity, which was provided by the downstream undulator, is about 20–25% higher than that of the upstream undulator because of the shorter distance between source and pinhole aperture. It is also seen that the energetic position of the maxima of the

16

harmonics are slightly different, with the maximum for negative helicity being about 4 eV higher in energy.
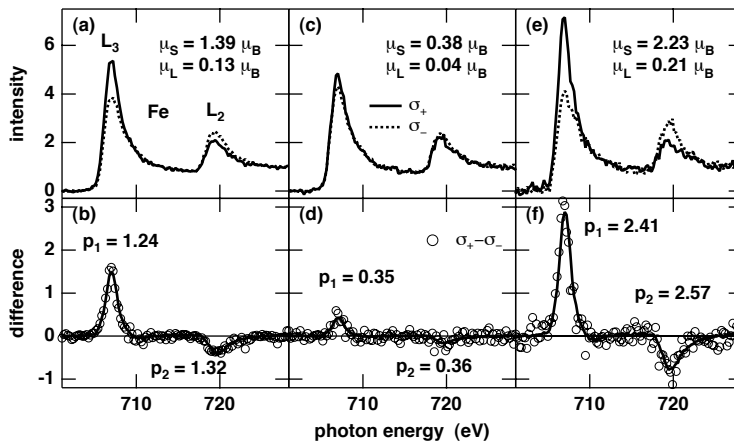
Fig. 1.7: Example for the sum rule analysis of single pixel spectra. (**a**), (**c**), (**e**): single pixel absorption spectra for positive (solid lines) and negative helicity (dotted lines) from 1.2 ML Ni/Fe/6 ML Co/Cu(001) films for three different Fe thicknesses ((**a**) 10 ML, (**b**) 5 ML, (**c**) 2 ML). (**b**), (**d**), (**f**): difference between spectra for opposite helicity of panels (**a**), (**c**), and (**e**) (open symbols). The solid lines in (**b**), (**d**), and (**f**) are portions of a template difference curve, obtained from averaging over a larger area, scaled by the fit parameters p_1 and p_2 at the L_3 and L_2 edges, respectively, to match the single pixel data. The spin and orbital moments, calculated from p_1, p_2, and the spin and orbital moments of the template spectrum, are listed in panels (**a**), (**c**), and (**e**). (From Ref. [1.60].)

Fig. 1.6 (c) shows the spectra of panel (a) after normalization to the integral photon flux of panel (b). At the bottom the difference between the two spectra is presented, showing the magnetic circular dichroism at the Fe L_3 and L_2 absorption edges. The leftmost part of the figure at photon energies below 704 eV is shown magnified by a factor of 10 in intensity. In that part of the spectra no differences between the spectra for opposite light helicity due to magnetic circular dichroism are expected. The small residual differences seen in Fig. 1.6 (c) in that region are thus caused by discrepancies between the integral photon flux of panel (b) and the unknown local photon flux at the position in the image from where the spectra were taken. They amount to roughly 5% of the pre-edge intensity. This is better seen from the ratio of the two curves of panel (c) plotted in Fig. 1.6 (d). Outside the absorption peaks the ratio between absorption of x-rays with positive and negative helicity should be one. The deviation from one clearly depends on photon energy, being greater on the left hand side. This can be understood from the shift of the maximum of the undulator harmonics seen in Fig. 1.6 (b). The resulting energy relative to the respective maximum of the undulator harmonic is consequently different for the two helicities, which leads to a different intensity distribu-

17

tion in the light spot. Closer to the maximum of the undulator harmonics the intensity distribution in the light spot is more centered. From Fig. 1.6 (b) it is seen that the maximum of the undulator harmonics for positive helicity was at slightly lower energies than for negative helicity. The local intensity for positive helicity in the center of the illuminated area is consequently higher at the low energy side of the spectra, since here the energy distance to the maximum is smaller than for negative helicity.

For the correction of this effect, a linear energy dependence is assumed. It is obtained from a fit of a straight line to Fig. 1.6 (d), excluding the peak regions exhibiting the magnetic dichroism from the fit. The line shown in Fig. 1.6 (d) is the result of such a fit. This line is used to correct the single pixel spectra. In the example of Fig. 1.6 this correction amounts to +7.0% at the left hand side, and −3.8% at the right hand side. The corrected spectra and the corresponding difference curve are shown in Fig. 1.6 (e). Again the region below 704 eV photon energy is shown magnified by a factor of 10 in intensity. Compared to the magnified part of Fig. 1.6 (c), it is seen that now the spectra overlap perfectly also in the pre-edge region. This procedure is done individually for each pixel of the image. Although it may seem exaggerated to correct such small discrepancies that would not even be visible in the plots without magnification of the vertical scale, they can have a larger influence on the integral of the difference curve, leading to significant errors in the result of the sum-rule analysis.

As mentioned before, sum-rule analysis of the corrected single pixel data has to be performed automatically. A problem thereby is that the data can be sometimes rather noisy, especially at positions where the dichroism is small. In most cases when the sum-rules are applied the goal is only to extract two numbers, namely the spin and orbital moments. In the following a method is described that makes use of the fact that usually the line shape of the helicity-averaged absorption spectrum does not change across a microscopic image. In that case, the full spectral information of the single-pixel spectra can be reduced to two parameters of interest by a simple fit procedure, thereby improving statistics.

For this procedure, first a template XMCD spectrum with a sufficiently good statistics for sum-rule analysis is generated by averaging many single-pixel spectra over a larger area. This averaged spectrum can be analyzed as described in section 1.2.1. The resulting difference curve between the two spectra for opposite helicity is then cut into two parts at an energy between the L_3 and L_2 edges, such that the two parts represent the dichroism of the L_3 and L_2 absorption edges. All the single pixel spectra are first corrected for local photon flux effects as described above, then normalized to an edge jump of one, and finally fit by the two parts of the template difference curve. The only two fit parameters in that fit are the two scaling factors needed to reproduce the single pixel difference curve by the two parts of the template difference curve. An example is shown in Fig. 1.7. It shows corrected Fe $L_{2,3}$ absorption spectra of three different of 3×3 μm^2 pixels, obtained from 1.2 ML Ni/x ML Fe/6 ML Co films on Cu(001) for different Fe layer thicknesses x [1.60]. The results obtained from that sample will be discussed in section 1.4.1. The three

18

pixels presented in Fig. 1.7 have been selected to show very different Fe magnetic moments. In the top row (panels (a), (c), and (e)) the single pixel absorption spectra for positive (solid line) and negative helicity (dotted line) are shown. The bottom panels (b), (d), and (f) show the corresponding single pixel difference curves as open symbols. Please note the different vertical scale in the top and bottom panels. The solid lines in panels (b), (d), and (f) are the result of template fits as described above. The corresponding scaling factors for the dichroism at the L_3 and L_2 edge, p_1 and p_2, respectively, are also given. The solid line is, in other words, identical to the difference curve of the template spectrum, scaled by p_1 at the L_3 edge, and by p_2 at the L_2 edge. The analysis of the template spectrum resulted in a spin moment of 1.1 μ_B and an orbital moment of 0.1 μ_B [1.60]. From these moments and the knowledge of p_1 and p_2 it is straightforward to calculate the spin and orbital moments for each of the single pixel fit results. For the three pixels presented in Fig. 1.7 the resulting Fe moments are listed in the upper panels.

By this template fit procedure, stable fits are obtained even for noisy single pixel data and small dichroism. The scatter of individual data points in the difference spectrum is averaged out in an elegant way. Furthermore, the position of the zero line is maintained, and data points far outside the absorption edges are not considered in the fit. It should, however, be checked at several positions of the image that the prerequisite for the fit, namely the constant shape of the helicity averaged absorption spectrum, is fulfilled.

1.4
Specific examples

We will now discuss two specific examples where the application of XMCD-PEEM microspectroscopy has proven beneficial for the study of the involved physical phenomena.

1.4.1
Ultrathin fcc Fe films

An interesting system for quantitative analysis of magnetic moments from microspectroscopy are ultrathin epitaxial Fe films. In these films the interplay between structural and magnetic properties leads to a variety of different structural and magnetic phases. Whereas bulk Fe exists only in the bcc structure at temperatures up to 1184 K, an fcc-like phase of Fe can be stabilized at room temperature when grown epitaxially on substrates with suitable surface lattice dimensions [1.61-71]. Room-temperature grown films of Fe on Cu(001) single crystal surfaces are known to exhibit three structurally and magnetically different phases depending on film thickness. For thicknesses below ≈4 atomic monolayers (ML) a fully ferromagnetic tetragonally expanded fcc-like structure is present (phase I) [1.62, 63]. In the thickness range between 4 and 11 ML, a second phase (II), a relaxed fcc structure,

19

is found, in which one observes a non-ferromagnetic behavior of the inner film layers [1.64-66]. For thicknesses above ≈11 ML a third phase appears, a ferromagnetic (011) oriented bcc phase (III) [1.67-69]. The magnetic behavior of these three phases is linked to the structure by the atomic volume. For different atomic volumes different magnetic ground states are theoretically predicted [1.72-74].
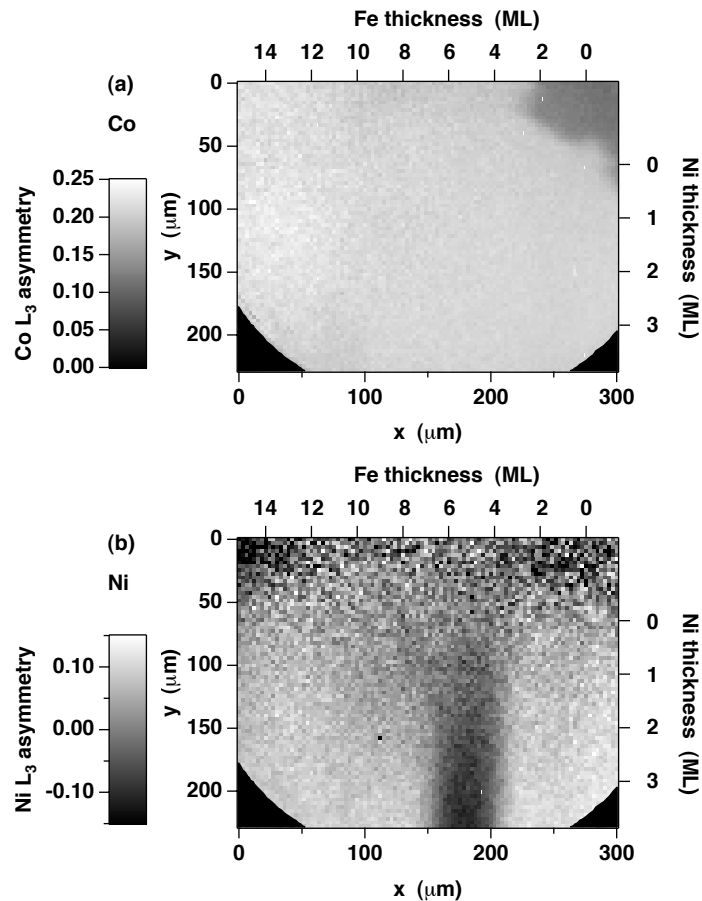
Fig. 1.8: Co (**a**) and Ni (**b**) asymmetry images of 0–4 ML Ni/0–14 ML Fe/ 6 ML Co/Cu(001). Ni and Fe thicknesses are indicated at the right and top axes, respectively. Different levels of gray correspond to different values of the magnetic asymmetry, as explained in the legend. Note that the grayscale in panel (**b**) is symmetric around zero, in contrast to panel (**a**). The Ni magnetization is antiparallel to the Co magnetization around 5 ML Fe thickness. (From Ref. [1.79].)

Especially the second phase of fcc Fe, where a large fraction of the film is non-ferromagnetic, has attracted a lot of interest. An antiferromagnetic coupling between ferromagnetic layers, separated by phase II fcc Fe, has been concluded from

20

the measurements of magnetization loops of Co/Fe/Co/Cu(001) [1.75, 76], and
Ni/Fe and $Ni_{81}Fe_{19}$/Fe multilayers [1.77, 78]. While total magnetization meas-
urements of stacks of multiple magnetic layers can give only indirect evidence
about the magnetic configuration, XMCD-PEEM microspectroscopy can provide
element-resolved quantitative information. In this section measurements of a
Ni/Fe/Co/Cu(001) sample are presented [1.79], in which microspectroscopy at the
Fe $L_{2,3}$ edges was used for determining the magnetic moments of the Fe layer.
Element resolved imaging of the Co underlayer and Ni overlayer revealed the pres-
ence of antiferromagnetic interlayer coupling.

To study the thickness dependence by microspectroscopy, the Fe and Ni layers
were shaped into 255 μm wide crossed wedges. They were prepared by placing a
slit aperture of 0.5 mm width 1 mm in front of the sample, and rocking the sam-
ple-slit assembly by ±7.5° about the long axis of the aperture during deposition.
The thickness of the continuous Co underlayer was 6 ML, the Fe thickness 0–14
ML, and the Ni thickness 0–6 ML. Low magnification settings of the PEEM
enabled imaging of a complete wedge.

Fig. 1.8 shows magnetic images of the Co and Ni layers at the onset of the
crossed Ni and Fe wedges. The complete Fe wedge of 0–14 ML Fe is within the
imaged area. The Fe thickness increases from right to left as indicated at the upper
axis. The imaged part of the Ni wedge corresponds to 0–4 ML thickness increas-
ing from top to bottom, as indicated at the right axis. The Fe thickness is such
that all three phases as mentioned above are present within this wedge. The upper
panel of Fig. 1.8 shows the magnetic asymmetry of the Co layer. It shows a nearly
uniform bright contrast. It corresponds to a magnetization direction along the
direction of the external field which was applied after the deposition of the Co layer
and again after completion of the complete trilayer. The lower panel shows the
contrast obtained at the Ni L_3 edge. Note that here the grayscale is defined
symmetrically around zero, in contrast to panel (a). In a stripe located at Fe
thicknesses between 5.0 and 6.5 ML a negative (dark) Ni asymmetry is found,
while the rest of the image exhibits an approximately uniform positive (bright)
contrast. A negative asymmetry corresponds to an antiparallel orientation of the Ni
layer magnetization at this position with respect to the Co layer magnetization.
The Fe layer consequently mediates an antiferromagnetic interlayer coupling
between the Co and Ni layers at this particular Fe thickness.

We will now turn our attention to the laterally resolved quantitative evaluation
of the Fe magnetic moments at exactly same region of the sample by XMCD-
PEEM microspectroscopy. The result of a pixel-by-pixel sum-rule analysis is
shown in the upper panel of Fig. 1.9. A total of 121 images for each helicity were
recorded as a function of photon energy in the interval between 701 and 728 eV,
similar to the spectra shown in Fig. 1.3. The size of a single pixel is 3×3 $μm^2$,
the exposure time was 10 s per image. Different levels of gray correspond to differ-
ent values of the Fe effective spin moment, as explained in the legend. In the upper
part of the image at zero or low Ni coverages the three different phases of Fe as
introduced above are recognized by their distinctly different spin moments. They

21

are labeled I, II, and III. Phase I extends up to an Fe thickness of approximately 3.5 ML, and shows high spin moments of up to 2.5 μ_B. Phase II between approximately 3.5 and 11 ML is characterized by a low spin moment, whereas phase III again shows increasing spin moments up to 2.0 μ_B at Fe thicknesses above 11 ML. These numbers can be seen more easily from a linescan along the Fe wedge. The open symbols in Fig. 1.9 (b) represent a horizontal linescan obtained from a 7 pixel vertical average of the uncovered Fe/6 ML Co/Cu(001) sample in the region as indicated by the upper white rectangle in panel (a). For increasing thickness of the Ni top layer differences in phase II Fe moment are observed. The solid symbols of Fig. 1.9 (b) show a linescan at around 2.1 ML Ni thickness (lower rectangle in panel (a)). From this linescan and also from the image plot of the Fe spin moments in panel (a) a further reduction of the Fe moment in phase II between about 4 and 7 ML compared to the uncovered Fe layer is observed. This region is labeled IIa, to distinguish from the rest of phase II where no change as a function of Ni overlayer thickness occurs (region IIb).

The observed Fe moments in phase I and III agree rather well with what is expected and known from literature [1.46, 80]. The interesting behavior occurs in phase II. There is some dispute in the literature as to the origin and location of the remaining moment of about 0.7–1.0 μ_B in phase II of the uncovered Fe/Co/Cu(001) sample. While from oxygen adsorption [1.75, 76] and XMCD experiments [1.81, 82] it had been concluded that the surface is not ferromagnetically ordered, and the ferromagnetism consequently had been attributed to the Co/Fe interface, other XMCD experiments [1.80] as well as measurements of photoelectron diffraction in magnetic dichroism [1.83] and spin-resolved valence band photoemission [1.84] provided evidence for the presence of a ferromagnetic layer on top of non-ferromagnetic underlayers, plus possibly ferromagnetism at the Fe/Co interface. The result from XMCD-PEEM microspectroscopy has to be interpreted as the exponentially depth averaged signal of all Fe monolayers in the film. A constant amount of ferromagnetic Fe at both interfaces plus non-ferromagnetic Fe in between would lead to a decreasing apparent magnetic moment with increasing Fe film thickness. This is not what is observed in the experiment (cf. Fig. 1.9). The situation is therefore probably more complicated. Layerwise or bilayerwise antiferromagnetic ordering of Fe moments [1.85-88], frustrations at interface steps or non-collinear moments [1.89] may have to be considered, possibly supported by further theoretical calculations.

By comparing Fig. 1.8 and Fig. 1.9 it becomes evident that region IIa with the extremely low Fe moment corresponds to the region of antiferromagnetic coupling between Ni and Co. Assuming ferromagnetic interface layers at both interfaces, this lowering of Fe moments could be explained by the strong direct coupling to the neighboring magnetic layers. In the case of antiferromagnetic alignment of Co and Ni, the Fe layers at both interfaces should be aligned oppositely to each other leading to lower apparent moments as compared to the parallel alignment in region IIb. The question remains why without Ni overlayer no such decrease of the Fe moment by antiparallel alignment of the ferromagnetic Fe surface layer to the

22

Co layer (and thus also to the Fe interface layer) is observed at the same Fe thickness. The reason could be some different influence of interface roughness and roughness-related magnetic frustrations in Fe/Co with and without Ni overlayer. There is also the possibility that without Ni, a 90° orientation of the Fe surface layer around 5.5 ML Fe thickness is present as the result of such competing frustrations, similar to the mechanisms leading to 90° interlayer exchange coupling [1.90, 91].

In the present example of Ni/Fe/Co trilayers XMCD-PEEM microspectroscopy was used for the thickness dependent study of Fe moments. The effective spin moments of Fe in the three structural phases could be obtained from images show-
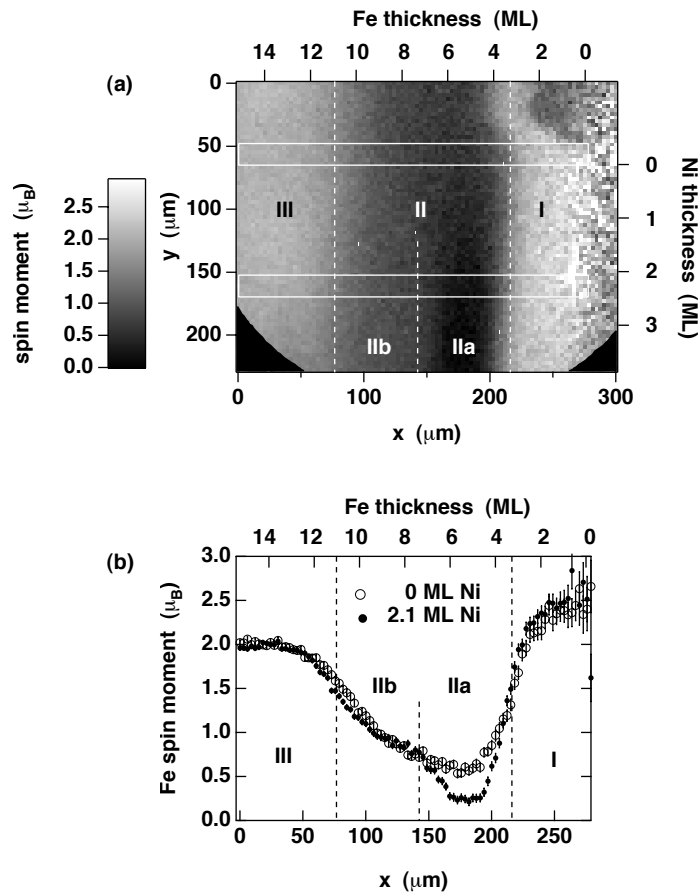
Fig. 1.9: (**a**) Result of a pixel-by-pixel sum-rule analysis for the Fe effective spin moment $\mu_{S,eff}$. Different values of $\mu_{S,eff}$ are represented by different levels of gray, as explained in the legend. The imaged region of the crossed Ni/Fe double wedge is exactly the same as in Fig. 1.8. Ni and Fe thicknesses are indicated at the right and top axes, respectively. Regions with different values of $\mu_{S,eff}$ are separated by dashed vertical lines and labeled I through III, IIa, and IIb. Horizontal line scans of $\mu_{S,eff}$ at the positions indicated by white rectangles in (**a**) are shown in (**b**). (From Ref. [1.79].)

23

ing the moments in a two-dimensional plot as a function of both Ni and Fe thicknesses. Characteristic changes connected with antiferromagnetic interlayer exchange coupling across the Fe layer could be observed. For this purpose no special lateral resolution is required. In that case microspectroscopy is just used as a very efficient way of parallel acquisition of a great number of XMCD spectra of crossed double wedges, designed at lengthscales that are convenient for imaging with respect to intensity and lateral resolution. In the next section, an example of microspectroscopy with higher resolution is presented in which spin and orbital magnetic moments within magnetic domains are determined.

1.4.2
Spin-reorientation transition in Co/Ni bilayers

The control of the easy axis of magnetization is important for many applications in which magnetic ultrathin films are used. The direction of the easy axis is described by the angle dependent part of the free energy, the so-called magnetic anisotropy energy (MAE). Minimization of the MAE with respect to the magnetization direc-
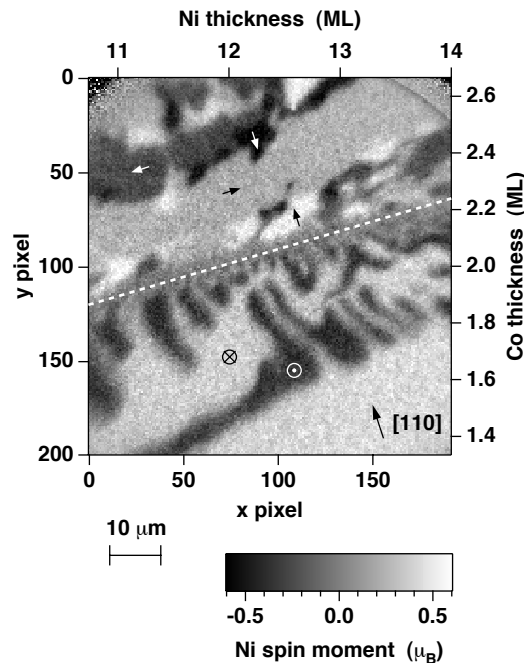
Fig. 1.10: Map of Ni spin moment projections onto the light incidence direction (from bottom to top, with an angle of 30° to the sample surface), resulting from the pixel-by-pixel sum-rule analysis of 76800 single-pixel XMCD microspectra of a Co/Ni/Cu(001) crossed double-wedge sample. The Ni thickness is indicated at the top axis, the Co thickness at the right axis. The grayscale to magnetic moment conversion is given in the legend at the bottom. At the white dotted line a spin-reorientation transition between in-plane magnetization (top) and out-of-plane magnetization (bottom) occurs. The magnetization directions are indicated by arrows in some domains. (From Ref. [1.93].)

24

tion yields the easy axis of magnetization. The MAE is directly related to the anisotropy of the orbital magnetic moment [1.92]: The orbital moment should be higher for a direction of magnetization preferred by the MAE. This can be used to measure the angle dependence of the MAE in an element-selective and laterally resolved way by mapping the orbital magnetic moment by XMCD-PEEM micro-spectroscopy.

In the example presented in this section, Co/Ni epitaxial bilayers on Cu(001) have been investigated [1.93]. They were shaped into wedges of 255 μm width, rotated by 90° to each other, similar to the wedges described in the previous section. Co and Ni single films on Cu(001) exhibit a different behavior with respect to the easy axis of magnetization: whereas Co/Cu(001) is magnetized always in the film plane ("in-plane") [1.94, 95], Ni/Cu(001) shows a perpendicular magnetization ("out-of-plane") over a wide range of thicknesses [1.96-99]. In Co/Ni bilayers, in-plane magnetization is therefore expected for high Co thicknesses and small Ni thicknesses, whereas out-of-plane magnetization should be present for small Co thicknesses and high Ni thicknesses.

Fig. 1.10 shows the result of a pixel-by-pixel sum-rule analysis of the Ni spin moments of a region in a Ni/Co/Cu(001) crossed double wedge. The Ni thickness increases in the displayed area from 10.7 to 14 ML from left to right, as indicated at the top axis, and the Co thickness increases from 1.35 to 2.65 ML from bottom
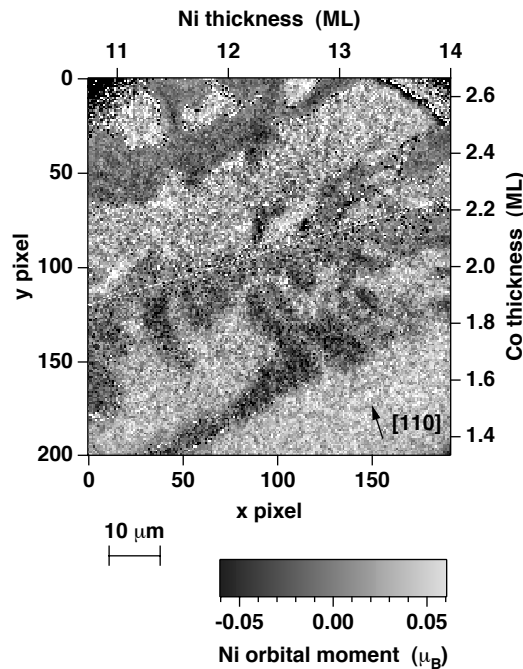
Fig. 1.11: As in Fig. 1.10, but for the Ni orbital moment μ_L. Different projections onto the direction of the incoming light are represented by different grayscales, as defined in the legend. (From Ref. [1.93].)

25

to top, as indicated at the right hand axis. The image was obtained from 76800 single pixel XMCD spectra of 370×370 nm^2 size each. The resolution of the PEEM was adjusted to 500 nm, which resulted in 30 s exposure time per photon energy step. A total of 105 images for each helicity between 845 and 890 eV photon energy have been acquired, using variable photon energy step spacings of 0.26 eV near the L_3 peak, 0.34 eV near the L_2 peak, 0.65 eV before the L_3 peak and in between the L_3 and L_2 peaks, and 1.4 eV in the post-L_2 region. Unlike the previous example this sample was not magnetized by an external field before imaging. The resulting moments include therefore the cosine of the angle between the helicity of the incoming light and the local magnetization direction, which is different in the different domains of the as-grown domain structure. The microspectroscopic analysis thus does not yield the absolute moments, but a projection on the direction of incoming light, which in the present example was from bottom to top of Fig. 1.10, with an angle of 60° to the surface normal. Note that the grayscale used to represent the Ni spin moment projections is symmetric around zero.

Inspection of the domain pattern of Fig. 1.10 reveals two qualitatively different regions, separated by the dotted line. In the upper part of the image four different shades of gray are recognized, namely black, dark gray, light gray, and white. In the lower part only two different shades of gray are found, and the domains are more rounded. Quantitative analysis of the values of $\mu_{S,\mathrm{eff}}$ for Ni in the single domains leads to the result that in the upper part of the image the magnetization direction is in-plane, oriented along the four <110> crystallographic directions, as indicated by arrows. Since the light incidence azimuth was deliberately rotated out of the crystal symmetry axes, each of these four directions results in a different grayscale representation. In the lower part of the image the magnetization is out-of-plane, either parallel of antiparallel to the surface normal. The resulting absolute value of the Ni effective spin moment is 0.65 μ_B, constant over the entire image [1.93].

At the dotted line of Fig. 1.10 a spin reorientation transition between in-plane and out-of-plane magnetization occurs, either by varying the Ni thickness, or by varying the Co thickness. From the position and slope of that line conclusions about the relative MAEs of the Co and Ni layers can be drawn [1.93]. The domain pattern on the out-of-plane side of the spin reorientation line is related to the spin-reorientation transition: As the spin reorientation line is approached, more and more oppositely magnetized out-of-plane domains are formed. This can be explained by the competition between the magnetostatic energy on the one hand, and the energy cost for creating domain walls on the other hand. Closely spaced alternatingly up and down magnetized out-of-plane domains have a lower magnetostatic energy than a single out-of-plane domain due to partial flux closure [1.100]. The formation of domains, on the other hand, requires the creation of additional domain walls of a certain domain wall energy. Since in domain walls between two out-of-plane domains an in-plane component of the magnetization is present, this domain wall energy is directly related to the MAE of the system. Close to the

26

spin-reorientation transition the domain wall energy is consequently low, so that the formation of many small domains can be energetically favorable [1.101].

Fig. 1.11 shows the result of the pixel-by-pixel sum-rule analysis for the Ni orbital moments of the same region of the sample as Fig. 1.10. The same domain pattern is recognized, although the noise in the image is higher. The higher noise is a consequence from the application of the sum-rules, where for the evaluation of the spin moment the peak areas of the L_2 and L_3 dichroism are added, whereas for the orbital moment they are subtracted [1.31]. The interesting quantity for the interpretation of the orbital moment, independent of magnetization direction, is the ratio of orbital to spin moment, $\mu_L/\mu_{S,eff}$. From the statistics of Fig. 1.11 it is clear that for the present 370×370 nm^2 pixel resolution a pixelwise interpretation of orbital moments would yield too big an error. To improve statistics in $\mu_L/\mu_{S,eff}$, the information from several pixels has to be averaged. The result of an averaging of pixels with a common distance from the spin reorientation line is shown in Fig. 1.12. Here the orbital to spin moment ratio $\mu_L/\mu_{S,eff}$ is plotted as a function of the distance from the spin reorientation line. The left hand side of Fig. 1.12 corresponds to the in-plane region of the image, the right hand side to the out-of-plane region. Each data point contains information of 192 pixels along a line parallel to the spin reorientation transition. The horizontal solid lines in Fig. 1.12 mark the average on both sides.
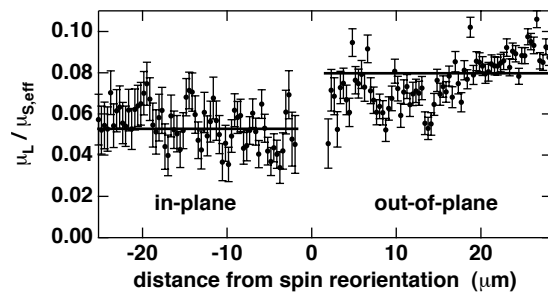
Fig. 1.12: Orbital to spin moment ratio $\mu_L/\mu_{S,eff}$ as a function of the distance from the spin reorientation line. Each data point is an average of 192 points along a line parallel to the spin reorientation transition in Fig. 1.10. Solid lines mark the average $\mu_L/\mu_{S,eff}$ ratio in the in-plane region (left) and in the out-of-plane region (right). (From Ref. [1.93].)

Although there is still considerable scatter, the orbital moment in the out-of-plane region is seen to be distinctly higher than in the in-plane region by nearly 0.03 $\mu_{S,eff}$. This is interpreted in terms of the above mentioned connection between the anisotropy of the orbital moment and the magnetic anisotropy energy. In the present example of Co/Ni/Cu(001) the MAE of the Ni layer alone is favoring an out-of-plane easy axis in the whole range of thicknesses considered here [1.93]. The observed in-plane magnetization is thus exclusively due to a stronger in-plane

27

anisotropy of the Co layer, which overcompensates the out-of-plane anisotropy of the Ni layer. The rigid magnetic exchange coupling between the two magnetic layers leads to a common easy axis of the bilayer, which results from energy minimization of the summed MAE contributions of both layers. That means that in the upper part of the images the magnetization direction of the Ni layer is along the Ni hard in-plane direction, and in the lower part along the Ni easy out-of-plane direction. The Ni orbital moment is thus higher for a magnetization direction along the easy axis, and lower for a magnetization direction along the hard axis.

Estimates for the size of the MAE can be made from the difference in orbital moment. A simplified theoretical description of the relation between the difference in orbital moment and the difference in MAE for two different magnetization directions resulted in a proportionality between both [1.92]. The proportionality factor, however, depends on some integrals over density of states in the valence bands [1.92], and may vary strongly between different samples, or even as a function of film thickness. In the present example the change in orbital moment is 0.027 $\mu_{S,eff}$, or 0.018 μ_B. A proportionality constant between $\Delta\mu_L$ and MAE has been determined experimentally for Ni in Ni/Pt multilayers by independent measurements of both the orbital moments and the magnetic anisotropy [1.102]. Assuming that the same proportionality constant is valid for the present Co/Ni bilayers, an MAE of +(47±10) μeV/atom is obtained. In spite of the uncertainties connected to the use of the proportionality constant of a different sample, this value very well makes sense, if we remember that XMCD measures the exponentially depth weighted average within the probing depth of the orbital magnetic moment, and thus of the MAE. A literature value for the MAE of the inner layers of Ni/Cu(001) is +34 μeV/atom [1.99]. Considering the fact that in the present sample the interface between Ni and Co has been found to contribute a high positive MAE [1.93], the value of +47 μeV/atom is amazingly close to the expected anisotropy energy of Co/Ni/Cu(001).

In this example of Co/Ni/Cu(001) XMCD-PEEM has been used for a quantitative analysis of the Ni spin moment projections, the characterization of local magnetization directions and the identification of a spin reorientation transition between in-plane and out-of-plane easy axes in the sample. The observed local moments' projections are consistent with an absolute value of the effective spin moment which is constant across the imaged area of the sample, and domains with either <110> in-plane magnetization or ±[001] out-of-plane magnetization. The connection of orbital moments and magnetic anisotropy adds an important feature to XMCD-PEEM microspectroscopy, which makes it an ideal tool for the study of local magnetic anisotropies in small magnetic structures.

1.5 Summary and outlook

XMCD in x-ray absorption and PEEM can be combined to imaging XMCD microspectroscopy measurements at a reasonable experimental effort. The PEEM is thereby used as a parallel detector for local electron yield with microscopic spatial

28

resolution. Scanning the photon energy of the incident x-ray beam and recording PEEM images at each energy step allows to extract the full spectroscopic information inherent to XMCD from every position in the images, if some experimental requirements concerning evenness of illumination, flux normalization, as well as linearity and stability of the image detection system can be fulfilled. Quantitative information about the element-resolved magnetic moments, separated into spin and orbital contributions, can be extracted from a full image XMCD microspectrum by the use of sum-rules. In cases where no special microscopic resolution is needed this can be used for a quick but detailed map of the thickness dependence of thin film samples by microspectroscopy of wedge shaped samples. This was illustrated by the example of Ni/Fe/Co ultrathin films on Cu(001), where the Ni and Fe layers were grown as crossed double-wedges.

The method can also be used to investigate micromagnetic phenomena by XMCD. The example of XMCD-PEEM microspectroscopy at the spin-reorientation transition between out-of-plane and in-plane easy magnetic axes in Co/Ni/Cu(001) showed how the correlation between the anisotropy of the orbital magnetic moment and the magnetocrystalline anisotropy can be used to obtain element-resolved information about local magnetic anisotropy from XMCD microspectra.

Future improvements concerning the brightness of the illumination and the efficiency of the detection system will reduce the noise level of the microspectra and allow to probe magnetic anisotropy at the microscopic level, for example in domain walls, or in technologically relevant magnetic microstructures. It will also enable one to choose a higher lateral resolution for microspectroscopy, maintaining reasonable acquisition times. The development of new PEEM instruments with aberration-correcting optics [1.59] will further push the limit for the attainable maximum resolution. Beamlines providing high brilliance circularly polarized radiation with the possibility of quick helicity reversal [1.103] will help to improve the accuracy of circular dichroism-based techniques.

The use of imaging energy filters [1.104-107] to select only electrons of a certain kinetic energy for the imaging process has interesting implications for magnetic microspectroscopy. On the one hand it allows to include magnetic dichroism effects that occur only in photoemission [1.108] in a microspectroscopic study. If the projective electron optics is tuned in order not to project the real space image plane onto the screen but the diffraction plane, on the other hand, photoelectron diffraction measurements [1.109-111] can be combined with XMCD. Positioning of the contrast aperture to certain features in the photoelectron diffraction pattern can then be used to obtain structure sensitive XMCD microspectroscopy data, and thus combine structural and magneto-spectroscopic information.

Finally the inclusion of time-resolved stroboscopic pump-probe experiments which exploit the pulsed time structure of synchrotron radiation [1.112] into XMCD-PEEM microspectroscopy opens the way for the quantitative investigation of magnetization dynamics on microscopic lengthscales. Snapshots of the spatial

29

spin and orbital magnetic moments' distribution in the course of reversible dynamic magnetization processes may be obtained in that way.

References

1.1. Tonner B. P., Dunham D., Droubay T., Kikuma J., Denlinger J., Rotenberg E., Warwick A. (1995): The development of electron spectromicroscopy. J. Electron Spectrosc. Relat. Phenom. **75**, 309

1.2. Casalis L., Jark W., Kiskinova M., Lonza D., Melpignano P., Morris D., Rosei R., Savoia A., Abrami A., Fava C., Furlan P., Pugliese R., Vivoda D., Sandrin G., Wei F.-Q., Contarini S., DeAngelis L., Gariazzo C., Natelli P., Morrison G. R. (1995): ESCA microscopy beamline at ELETTRA. Rev. Sci. Instrum. **66**, 4870

1.3. Voss J. (1997): The scanning soft x-ray microscope at Hasylab - imaging and spectroscopy of photoelectrons, photoluminescence, desorbed ions, reflected, scattered and transmitted light. J. Electron Spectrosc. Relat. Phenom. **84**, 29

1.4. Kiskinova M. (2000): Spectromicroscopy studies with high spatial resolution. Surf. Rev. Lett. **7**, 447

1.5. Baumgarten L., Schneider C. M., Petersen H., Schäfers F., Kirschner J. (1990): Magnetic x-ray dichroism in core-level photoemission from ferromagnets. Phys. Rev. Lett. **65**, 492

1.6. Kagoshima Y., Miyahara T., Ando M., Wang J., Aoki S. (1996): Magnetic domain-specific microspectroscopy with a scanning x-ray microscope using circularly polarized undulator radiation. J. Appl. Phys. **80**, 3124

1.7. Warwick T., Franck K., Kortright J. B., Meigs G., Morenne M., Myneni S., Rotenberg E., Seal S., Steele W. F., Ade H., Garcia A., Cerasari S., Denlinger J., Hayakawa S., Hitchcock A. P., Tyliszczak T., Kikuma J., Rightor E. G., Shin H.-J., Tonner B. P. (1998): A scanning transmission x-ray microscope for materials science spectromicroscopy at the advanced light source. Rev. Sci. Instrum. **69**, 2964

1.8. Pietzsch O., Kubetzka A., Bode M., Wiesendanger R. (2000): Real-space observation of dipolar antiferromagnetism in magnetic nanowires by spin-polarized scanning tunneling spectroscopy. Phys. Rev. Lett. **84**, 5212

1.9. Kleiber M., Bode M., Ravli´c R., Wiesendanger R. (2000): Topology-induced spin frustrations at th Cr(001) surface studied by spin-polarized scanning tunneling spectroscopy. Phys. Rev. Lett. **85**, 4606

1.10. Hubert A., Schäfer R. (1998): Magnetic domains. Springer, Berlin, and references therein

1.11. Weller D. (1996): Magneto-optical Kerr spectroscopy of transition metal alloy and compound films, in *Spin-Orbit-Influenced Spectroscopies of Magnetic Solids*, ed. by H. Ebert and G. Schütz, Springer, Berlin.

1.12. Ebert H. (1996): Magneto-optical effects in transition metal systems. Rep. Prog. Phys. **59**, 1665

1.13. Schneider C. M., Celinski Z., Neuber M., Wilde C., Grunze M., Meinel K., Kirschner J. (1994): Magneto-dichroic effects in energy- and angle-resolved photoemission: contrast mechanisms for the elementally sensitive imaging of magnetic domains. J. Phys.: Cond. Matt. **6**, 1177

1.14. Kinoshita T., Nath K. G., Haruyama Y., Watanabe M., Yagi M., Kimura S.-I., Fanelsa A. (1999): Photoelectron spectromicroscopy experiments at the UVSOR facility. J. Electron Spectrosc. Relat. Phenom. **92**, 165

1.15. Schneider C. M., Meinel K., Holldack K., Oepen H. P., Grunze M., Kirschner J. (1993): Magnetic spectro-microscopy using magneto-dichroic effects in photon-induced auger

30

electron emission, in *Magnetic Ultrathin Films*, ed. by B. T. J. e. al., Materials Research Society, Pittsburgh.

1.16. Schneider C. M., Holldack K., Kinzler M., Grunze M., Oepen H. P., Schäfers F., Petersen H., Meinel K., Kirschner J. (1993): Magnetic spectromicroscopy from Fe(100). Appl. Phys. Lett. **63**, 2432

1.17. Fischer P., Eimüller T., Schütz G., Guttmann P., Schmahl G., Prueg K., Bayreuther G. (1998): Imaging of magnetic domains by transmission x-ray microscopy. J. Phys. D: Appl. Phys. **31**, 649

1.18. Stöhr J., Wu Y., Samant M. G., Hermsmeier B. B., Harp G., Koranda S., Dunham D., Tonner B. P. (1993): Element-specific magnetic microscopy with circularly polarized x-rays. Science **259**, 658

1.19. Swiech W., Fecher G. H., Ziethen C., Schmidt O., Schönhense G., Grzelakowski K., Schneider C. M., Frömter R., Oepen H. P., Kirschner J. (1997): Recent progress in photoemission microscopy with emphasis on chemical and magnetic sensitivity. J. Electron Spectrosc. Relat. Phenom. **84**, 171

1.20. Hillebrecht F. U., Spanke D., Dresselhaus J., Solinus V. (1997): Imaging of magnetic domains by photoemission microscopy. J. Electron Spectrosc. Relat. Phenom. **84**, 189

1.21. Kuch W., Frömter R., Gilles J., Hartmann D., Ziethen C., Schneider C. M., Schönhense G., Swiech W., Kirschner J. (1998): Element-selective magnetic imaging in exchange-coupled systems by magnetic photoemission microscopy. Surf. Rev. Lett. **5**, 1241

1.22. Stöhr J., Padmore H. A., Anders S., Stammler T., Scheinfein M. R. (1998): Principles of x-ray magnetic dichroism spectromicroscopy. Surf. Rev. Lett. **5**, 1297

1.23. Anders S., Padmore H. A., Duarte R. M., Renner T., Stammler T., Scholl A., Scheinfein M. R., Stöhr J., Séve L., Sinkovic B. (1999): Photoemission electron microscope for the study of magnetic materials. Rev. Sci. Instrum. **70**, 3973

1.24. Kachel T., Gudat W., Koziol C., Schmidt T., Lilienkamp G., Bauer E., Altman M. (1997): Magnetic domain imaging with low energy electron microscopy. J. Appl. Phys. **81**, 5025

1.25. Bauer E. (1994): Low energy electron microscopy. Rep. Prog. Phys. **57**, 895

1.26. Bauer E. (1998): LEEM basics. Surf. Rev. Lett. **5**, 1275

1.27. Kuch W., Imada S., Gilles J., Offi F., Suga S., Kimura T., Yanagisawa J., Gamoh K., Kirschner J., unpublished

1.28. Scholl A., Stöhr J., Lüning J., Seo J. W., Fompeyrine J., Siegwart H., Locquet J.-P., Nolting F., Anders S., Fullerton E. E., Scheinfein M. R., Padmore H. A. (2000): Observation of antiferromagnetic domains in epitaxial thin films. Science **287**, 1014

1.29. Nolting F., Scholl A., Stöhr J., Seo J. W., Fompeyrine J., Siegwart H., Locquet J.-P., Anders S., Lüning J., Fullerton E. E., Toney M. F., Scheinfein M. R., Padmore H. A. (2000): Direct observation of the alignment of ferromagnetic spins by antiferromagnetic spins. Nature **405**, 767

1.30. Schütz G., Wagner W., Wilhelm W., Kienle P., Zeller R., Frahm R., Materlik G. (1987): Absorption of circularly polarized x rays in iron. Phys. Rev. Lett. **58**, 737

1.31. Thole B. T., Carra P., Sette F., van der Laan G. (1992): X-ray circular dichroism as a probe of orbital magnetization. Phys. Rev. Lett. **68**, 1943

1.32. Carra P., Thole B. T., Altarelli M., Wang X. (1993): X-ray circular dichroism and local magnetic fields. Phys. Rev. Lett. **70**, 694

1.33. Stöhr J. (1995): X-ray magnetic circular dichroism spectroscopy of transition metal thin films. J. Electron Spectrosc. Relat. Phenom. **75**, 253

1.34. Idzerda Y. U., Chen C. T., Lin H.-J., Tjeng H., Meigs G. (1995): Application of magnetic circular dichroism to magnetic thin films. Physica B **208-209**, 746

1.35. Ebert H. (1996): Circular magnetic x-ray dichroism in transition metal systems, in *Spin-Orbit-Influenced Spectroscopies of Magnetic Solids*, ed. by H. Ebert and G. Schütz, Springer, Berlin.

1.36. Stöhr J., Nakajima R. (1998): Magnetic properties of transition metal multilayers studied with x-ray magnetic circular dichroism spectroscopy. IBM J. Res. Develop. **42**, 73

31

1.37. Chen C. T., Idzerda Y. U., Lin H.-J., Smith N. V., Meigs G., Chaban E., Ho G. H., Pellegrin E., Sette F. (1995): Experimental confirmation of the x-ray magnetic circular dichroism sum rules for iron and cobalt. Phys. Rev. Lett. **75**, 152

1.38. Fano U. (1969): Spin orientation of photoelectrons ejected by circularly polarized light. Phys. Rev. A **178**, 131

1.39. Weller D., Stöhr J., Nakajima R., Carl A., Samant M. G., Chappert C., Mégy R., Beauvillain P., Veillet P., Held G. A. (1995): Microscopic origin of magnetic anisotropy in Au/Co/Au probed with x-ray magnetic circular dichroism. Phys. Rev. Lett. **75**, 3752

1.40. Wu R., Freeman A. J. (1994): Limitation of the magnetic-circular-dichroism spin sum rule for transition metals and importance of the magnetic dipole term. Phys. Rev. Lett. **73**, 1994

1.41. O'Brien W. L., Tonner B. P., Harp G. R., Parkin S. S. P. (1994): Experimental investigation of dichroism sum rules for V, Cr, Mn, Fe, Co, and Ni: influence of diffuse magnetism. J. Appl. Phys. **76**, 6462

1.42. Rioux D., Allen B., Höchst H., Zhao D., Huber D. L. (1997): Birefringence-induced interference effects in thin-film magnetic-circular-dichroism spectra. Phys. Rev. B **56**, 753

1.43. Schwitalla J., Ebert H. (1998): Electron core-hole interaction in the x-ray absorption spectroscopy of 3d transition metals. Phys. Rev. Lett. **80**, 4586

1.44. Vogel J., Sacchi M. (1994): Polarization and angular dependence of the $L_{2,3}$ absorption edges in Ni(110). Phys. Rev. B **49**, 3230

1.45. Le Cann X., Boeglin C., Carrière B., Hricovini K. (1996): Magnetic linear and circular dichroism in core-level photoemission and magnetic circular x-ray dichroism in absorption for ultrathin films Fe/Pd(100). Phys. Rev. B **54**, 373

1.46. Hunter Dunn J., Arvanitis D., Mårtensson N. (1996): Magnetism of thin Fe films on Cu(100). Phys. Rev. B **54**, R11157

1.47. Möllenstedt G., Lenz F. (1963): Electron emission microscopy, in *Advances in Electronics and Electron Physics*, ed. by L. Marton, Academic Press, London.

1.48. Bethke H., Klaua M. (1983): Photo-electron microscopy of work function changes. Ultramicroscopy **11**, 207

1.49. Engel W., Kordesch M. E., Rotermund H. H., Kubala S., von Oertzen A. (1991): A UHV-compatible photoelectron emission microscope for application in surface science. Ultramicroscopy **36**, 148

1.50. Kordesch M. E., Engel W., Lapeyre G. J., Zeitler E., Bradshaw A. M. (1989): The application of photoemission microscopy to the study of heterogeneous reactions over metal single crystal surfaces. App. Phys. A **49**, 399

1.51. Mundschau M., Kordesch M. E., Rausenberger B., Engel W., Bradshaw A. M., Zeitler E. (1990): Real-time observation of the nucleation and propagation of reaction fronts on surfaces using photoemission electron microscopy. Surf. Sci. **227**, 246

1.52. Rotermund H. H., Nettesheim S., von Oertzen A., Ertl G. (1992): Observation of surface diffusion of adsorbates on metal surfaces by photoemission electron microscopy (PEEM). Surf. Sci. **275**, L645

1.53. Nettesheim S., von Oertzen A., Rotermund H. H., Ertl G. (1993): Reaction diffusion patterns in the catalytic CO-oxidation on Pt(110): front propagation and spiral waves. J. Chem. Phys. **98**, 9977

1.54. Telieps W., Bauer E. (1985): An analytical reflection and emission UHV surface electron microscope. Ultramicroscopy **17**, 57

1.55. Tonner B. P., Harp G. R. (1988): Photoelectron microscopy with synchrotron radiation. Rev. Sci. Instrum. **59**, 853

1.56. Ziethen C., Schmidt O., Fecher G. H., Schneider C. M., Schönhense G., Frömter R., Seider M., Grzelakowski K., Merkel M., Funnemann D., Swiech W., Gundlach H., Kirschner J. (1998): Fast elemental mapping and magnetic imaging with high lateral resolution using a novel photoemission microscope. J. Electron Spectrosc. Relat. Phenom. **88-91**, 983

32

1.57. De Stasio G., Perfetti L., Gilbert B., Fauchox O., Capozi M., Perfetti P., Margaritondo G., Tonner B. P. (1999): MEPHISTO spectromicroscope reaches 20 nm lateral resolution. Rev. Sci. Instrum. **70**, 1740

1.58. Bauer E. (1996): LEEM studies of the early stages of epitaxial growth. Appl. Surf. Sci. **92**, 20

1.59. Fink R., Weiss M. R., Umbach E., Preikszas D., Rose H., Spehr R., Hartel P., Engel W., Degenhardt R., Wichtendahl R., Kuhlenbeck H., Erlebach W., Ihmann K., Schlögl R., Freund H.-J., Bradshaw A. M., Lilienkamp G., Schmidt T., Bauer E., Benner G. (1997): SMART: a planned ultrahigh-resolution spectromicroscope for BESSY II. J. Electron Spectrosc. Relat. Phenom. **84**, 231

1.60. Kuch W., Gilles J., Offi F., Kang S. S., Imada S., Suga S., Kirschner J. Element-selective mapping of magnetic moments in ultrathin magnetic films using a photoemission microscope. Surf. Sci. in print

1.61. Thomassen J., May F., Feldmann B., Wuttig M., Ibach H. (1992): Magnetic live surface layers in Fe/Cu(100). Phys. Rev. Lett. **69**, 3831

1.62. Kief M. T., Egelhoff Jr., W. F. (1993): Growth and structure of Fe and Co thin films on Cu(111), Cu(100), and Cu(110): a comprehensive study of metastable film growth. Phys. Rev. B **47**, 10785

1.63. Heinz K., Müller S., Bayer P. (1995): Multilayer reconstruction of ultrathin expitaxial fcc Fe films. Surf. Sci. **337**, 215

1.64. Bayer P., Müller S., Schmailzl P., Heinz K. (1993): Non-pseudomorphic and surface-reconstructed ultrathin epitaxial fcc Fe-films on Cu(100). Phys. Rev. B **48**, 17611

1.65. Li D., Freitag M., Pearson J., Qiu Z. Q., Bader S. D. (1994): Magnetic phases of ultrathin Fe grown on Cu(100) as epitaxial wedges. Phys. Rev. Lett. **72**, 3112

1.66. Straub M., Vollmer R., Kirschner J. (1996): Surface magnetism of ultrathin γ-Fe films investigated by nonlinear magneto-optical Kerr effect. Phys. Rev. Lett. **77**, 743

1.67. Wuttig M., Feldmann B., Thomassen J., May F., Zillgen H., Brodde A., Hannemann H., Neddermayer H. (1993): Structural transformations of fcc iron films on Cu(100). Surf. Sci. **291**, 14

1.68. Giergiel J., Kirschner J., Landgraf J., Shen J., Woltersdorf J. (1994): Stages of structural transformation in iron thin film growth on copper (100). Surf. Sci. **310**, 1

1.69. Giergiel J., Shen J., Woltersdorf J., Kirilyuk A., Kirschner J. (1995): Growth and morphology of ultrathin Fe films on Cu(001). Phys. Rev. B **52**, 8528

1.70. Lin M.-T., Shen J., Kuch W., Jenniches H., Klaua M., Schneider C. M., Kirschner J. (1998): Growth, morphology, and crystalline structure of ultrathin Fe films on $Cu_3Au(100)$. Surf. Sci. **410**, 290

1.71. Kang S. S., Kuch W., Kirschner J. (2001): Structural and magnetic properties of Fe thin films on $Cu_{90}Au_{10}(001)$. Phys. Rev. B **63**, 024401

1.72. Moruzzi V. L., Marcus P. M., Schwarz K., Mohn P. (1986): Ferromagnetic phases of bcc and fcc Fe, Co, and Ni. Phys. Rev. B **34**, 1784

1.73. Moruzzi V. L., Marcus P. M., Kübler J. (1989): Magnetovolume instabilities and ferromagnetism versus antiferromagnetism in bulk fcc iron and manganesePhys. Rev. B **39**, 6957

1.74. Marcus P. M., Qiu S. L., Moruzzi V. L. (1999): The magnetic phases of face-centred-cubic iron. J. Phys.: Cond. Matt. **11**, 5709

1.75. Escorcia-Aparicio E. J., Kawakami R. K., Qiu Z. Q. (1996): fcc Fe films grown on a ferromagnetic fcc Co(100) substrate. Phys. Rev. B **54**, 4155

1.76. Kawakami R. K., Escorcia-Aparicio E. J., Qiu Z. Q. (1996): Magnetic coupling in Co/face-centered-cubic Fe/Co sandwiches. J. Appl. Phys. **79**, 4532

1.77. Kuch W., Parkin S. S. P. (1997): Fe structural and magnetic phases in $Fe/Ni_{81}Fe_{19}(001)$ multilayers. Europhys. Lett. **37**, 465

1.78. Kuch W., Parkin S. S. P. (1998): Structural and magnetic phases of Fe in Fe/Ni(001) and $Fe/Ni_{81}Fe_{19}(001)$ multilayers. J. Magn. Magn. Mater. **184**, 127

33

1.79. Kuch W., Gilles J., Offi F., Kang S. S., Imada S., Suga S., Kirschner J. (2000): Imaging microspectroscopy of Ni/Fe/Co/Cu(001) using a photoemission microscope. J. Electron Spectrosc. Relat. Phenom. **109**, 249

1.80. Schmitz D., Charton C., Scholl A., Carbone C., Eberhardt W. (1999): Magnetic moments of fcc Fe overlayers on Cu(100) and Co(100). Phys. Rev. B **59**, 4327

1.81. O'Brien W. L., Tonner B. P. (1995): Magnetic phases of ultrathin Fe films on fcc Co(001). Surf. Sci. **334**, 10

1.82. O'Brien W. L., Tonner B. P. (1995): Room-temperature magnetic phases of Fe on fcc Co(001) and Ni(001). Phys. Rev. B **52**, 15332

1.83. Gao X., Salvietti M., Kuch W., Schneider C. M., Kirschner J. (1998): Photoelectron diffraction in magnetic dichroism: Surface live magnetic layers in fcc Fe/Co(001). Phys. Rev. B **58**, 15426

1.84. Kläsges R., Schmitz D., Carbone C., Eberhardt W., Kachel T. (1998): Surface magnetism and electronic structure of ultrathin fcc Fe films. Solid State Commun. **107**, 13

1.85. Lorenz R., Hafner J. (1996): Magnetic structure and anisotropy of thin Fe films on Cu(001) substrates. Phys. Rev. B **54**, 15937

1.86. Asada T., Blügel S. (1997): Total energy spectra of complete sets of magnetic states for fcc-Fe films on Cu(100). Phys. Rev. Lett. **79**, 507

1.87. Moroni E. G., Kresse G., Hafner J. (1999): Coherent epitaxy and magnetism of face-centred cubic Fe films on Cu(100). J. Phys.: Cond. Matt. **11**, L35

1.88. Spi`sak D., Hafner J. (2000): Structure and magnetism of γ-Fe overlayers on face-centered-cubic Co(001) substrates. Phys. Rev. B **62**, 9575

1.89. Lorenz R., Hafner J. (1998): Noncollinear magnetism in rough ultrathin γ-Fe films. Phys. Rev. B **58**, 5197

1.90. Slonczewski J. C. (1991): Fluctuation mechanism for biquadratic exchange coupling in magnetic multilayers. Phys. Rev. Lett. **67**, 3172

1.91. Slonczewski J. C. (1995): Overview of interlayer exchange theory. J. Magn. Magn. Mater. **150**, 13

1.92. Bruno P. (1989): Tight-binding approach to the orbital magnetic moment and magnetocrystalline anisotropy of transition-metal monolayers. Phys. Rev. B **39**, 865

1.93. Kuch W., Gilles J., Kang S. S., Imada S., Suga S., Kirschner J. (2000): Magnetic-circular-dichroism microspectroscopy at the spin reorientation transition in Ni(001) films. Phys. Rev. B **62**, 3824

1.94. Krams P., Lauks F., Stamps R. L., Hillebrands B., Güntherodt G. (1992): Magnetic anisotropies of ultrathin Co(001) films on Cu(001). Phys. Rev. Lett. **69**, 3674

1.95. Kowalewski M., Schneider C. M., Heinrich B. (1993): Thickness and temperature dependence of magnetic anisotropies in ultrathin fcc Co(001) structures. Phys. Rev. B **47**, 8748

1.96. Huang F., Kief M. T., Mankey G. J., Willis R. F. (1994): Magnetism in the few-monolayers limit: a surface magneto-optic Kerr-effect study of the magnetic behavior of ultrathin films of Co, Ni, and Co-Ni alloys on Cu(100) and Cu(111). Phys. Rev. B **49**, 3962

1.97. O'Brien W. L., Tonner B. P. (1994): Transition to the perpendicular easy axis of magnetization in Ni ultrathin films found by x-ray magnetic circular dichroism. Phys. Rev. B **49**, 15370

1.98. Schulz B., Baberschke K. (1994): Crossover from in-plane to perpendicular magnetization in ultrathin Ni/Cu(001) films. Phys. Rev. B **50**, 13467

1.99. Farle M., Mirwald-Schulz B., Anisimov A. N., Platow W., Baberschke K. (1997): Higher-order magnetic anisotropies and the nature of the spin-reorientation transition in face-centered-tetragonal Ni(001)/Cu(001). Phys. Rev. B **55**, 3708

1.100. Yafet Y., Gyorgy E. M. (1988): Ferromagnetic strip domains in an atomic monolayer. Phys. Rev. B **38**, 9145

1.101. Speckmann M., Oepen H. P., Ibach H. (1995): Magnetic domain structures in ultrathin Co/Au(111): On the influence of film morphology. Phys. Rev. Lett. **75**, 2035

1.102. Wilhelm F., Poulopoulos P., Srivastava P., Wende H., Farle M., Baberschke K., Angelakeris M., Flevaris N. K., Grange W., Kappler J.-P., Ghiringhelli G., Brookes N. B. (2000): Magnetic

34

anisotropy energy and the anisotropy of the orbital moment of Ni in Ni/Pt multilayers. Phys. Rev. B **61**, 8647

1.103. Weiss M. R., Follath R., Sawhney K. J. S., Senf F., Bahrdt J., Frentrup W., Gaupp A., Sasaki S., Scheer M., Mertins H.-C., Abramsohn D., Schäfers F., Kuch W., Mahler W. The elliptically polarized undulator beamlines at BESSY II. Nucl. Instr. and Meth. A (in print)

1.104. Turner D. W., Plummer I. R., Porter H. Q. (1988): Image bandpass filter in photoelectron spectromicroscopy. Rev. Sci. Instrum. **59**, 45

1.105. Marx G. K. L., Gerheim V., Schönhense G. (1997): Multipole WIEN-filter for a high-resolution X-PEEM. J. Electron Spectrosc. Relat. Phenom. **84**, 251

1.106. Sakai Y., Kato M., Masuda S., Harada Y., Ichinokawa T. (1998): Development of a low energy electron microscope with an energy analyzer. Surf. Rev. Lett. **5**, 1199

1.107. Schmidt T., Heun S., Slezak J., Diaz J., Prince K. C., Lilienkamp G., Bauer E. (1998): SPELEEM: Combining LEEM and spectroscopic imaging. Surf. Rev. Lett. **5**, 1287

1.108. Rossi G., Panaccione G., Sirotti F., Cherepkov N. A. (1997): Magnetic-field-averaged photoemission experiments with variable chirality. Phys. Rev. B **55**, 11483

1.109. Fadley C. S. (1988): Recent developments in photoelectron diffraction, in *Core-Level Spectroscopy in Condensed Systems*, ed. by J. Kanamori and A. Kotani, Springer, Berlin.

1.110. Fadley C. S. (1993): Diffraction and holography with photoelectrons and Auger electrons: some new directions. Surf. Sci. Rep. **19**, 231

1.111. Daimon H., Nakatani T., Imada S., Suga S., Kagoshima Y., Miyahara T. (1995): Circularly polarized light-induced dichroism in photoelectron diffraction observed with display-type spherical mirror analyzer. Rev. Sci. Instrum. **66**, 1510

1.112. Bonfim M., Ghiringhelli G., Montaigne F., Pizzini S., Brookes N. B., Petroff F., Vogel J., Camarero J., Fontaine A. (2001): Element-selective nanosecond magnetization dynamics in magnetic heterostructures. Phys. Rev. Lett. **86**, 3646
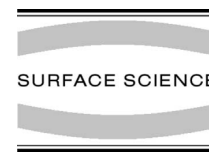
Element-selective mapping of magnetic moments in ultrathin magnetic films using a photoemission microscope

W. Kuch [a],[*], J. Gilles [a], F. Offi [a], S.S. Kang [a], S. Imada [b], S. Suga [b], J. Kirschner [a]

[a] *Max-Planck-Institut für Mikrostrukturphysik, Weinberg 2, D-06120 Halle, Germany*
[b] *Graduate School of Engineering Science, Osaka University, 1–3 Machikaneyama, Toyonaka 560-8531, Japan*

Abstract

We combine X-ray magnetic circular dichroism (XMCD) and photoelectron emission microscopy to obtain locally resolved magnetic information on a microscopic scale. Scanning the photon energy across elemental absorption edges and recording microscopic images of the local secondary electron intensity for both photon helicities at each photon energy step allows to analyze local XMCD spectra at any position of the imaged area of the sample. With the help of magnetic sum-rules local quantitative information about magnetic moments can be extracted from such microspectroscopic measurements. The full power of XMCD as a spectroscopic tool is so maintained, while microscopic spatial resolution is added. © 2001 Elsevier Science B.V. All rights reserved.

Keywords: Photoemission (total yield); Photoelectron emission; X-ray absorption spectroscopy; Iron; Nickel; Magnetic films

1. Introduction

The study of ultrathin magnetic structures and multilayers has recently attracted considerable interest, fueled by the prospect of technological applications in the fields of high density magnetic data recording, magnetic sensors, non-volatile magnetic random access memory, and spin electronics in general. The rapidly decreasing size of such magnetic structures calls for experimental techniques that allow the study of magnetic properties on a microscopic scale. Photoelectron emission microscopy (PEEM) is one such technique that has already proven its versatility for the imaging of magnetic domains in ultrathin films [1–3]. Magnetic circular dichroism in soft X-ray absorption (XMCD) serves as mechanism for magnetic contrast. The absorption of circularly polarized X-rays at elemental absorption edges depends on the relative orientation of sample magnetization and light helicity [4,5]. In PEEM a magnified image of the secondary electron intensity distribution at the sample surface is generated in a parallel way. The secondary electron intensity distribution under exposure to X-rays is a measure of the local X-ray absorption. In practice two images for opposite light helicity of the circularly polarized light at the maximum of the absorption edge are acquired and subtracted in order to separate magnetic from topographical contrast. This method has been successfully employed for the study of magnetic thin films, microstructures, and exchange coupled systems [2,3].

[*] Corresponding author. Tel.: +49-30-6392-4927; fax: +49-30-6392-4984.
E-mail address: kuch@bessy.de (W. Kuch).

The full power of XMCD lies in its spectroscopic information. Sum-rules [6,7] have been proposed to deduce quantitative magnetic information from the difference curve between photon energy scans for opposite light helicity. XMCD has since then developed into a widely used technique for the element-specific characterization of magnetic thin films and multilayers [8,9]. Although there has been some dispute about the applicability of these sum-rules [10,11], they seem to yield reasonable results for the 3d transition metals [8,9,12]. These sum-rules allow one to extract the spin and orbital magnetic moments from the evaluation of the integrated cross section at the L_3 and L_2 edges of transition metals for opposite light helicity, thereby enabling the separate determination of magnetic moments of different elements in the same sample.

A rather important point is the element-specificity of XMCD–PEEM, since in many materials for technological application the effects of magnetic coupling and/or electric transport between different magnetic layers are employed. By tuning the exciting X-ray radiation to the different absorption edges, a separate determination of the magnetically active layers is possible, if different elements are contained.

With the improved brilliance of radiation from third generation synchrotron light sources the acquisition times for PEEM images have become short enough to combine the microscopic information of PEEM and the spectroscopic information of XMCD in the most consequent way. This implies to scan the photon energy in small steps and record complete microscopic images of the secondary photoelectron intensity for both photon helicities at each step (full-image microspectroscopy), not only at the absorption maximum. From such a data set the analysis of local XMCD spectra at any position of the image is possible. The full quantitative information inherent to XMCD can thus be extracted with the spatial resolution given by the imaging process. Sum-rule analysis for every single pixel in the image does then result in microscopic maps of orbital and spin moments. This can be of the highest importance for the study and the understanding of micromagnetic aspects of magnetic anisotropy or magnetic interlayer coupling. Since the magnetocrystalline anisotropy manifests itself in an anisotropy of the orbital moment [13,14], even microscopic measurements of the angular dependence of magnetic anisotropies in an element-selective way may become possible.

In this contribution we demonstrate the practicability of this kind of microspectroscopy, and present examples of full-image XMCD–PEEM microspectroscopy. The setup and the carrying out of the experiments is described for the microscopic mapping of magnetic moments in microwedges of epitaxial magnetic films on a single crystal Cu(0 0 1) sample. Special emphasis is put on corrections to the data that are specific to imaging spectroscopy. A procedure for a simplified sum-rule analysis is presented that allows the automatic analysis of a large amount of XMCD data. Results for images of orbital and spin moments are shown for Fe in Ni/Fe/Co/Cu(0 0 1) and Ni in Co/Ni/Cu(0 0 1).

2. Experiment

The experiments were performed using circularly polarized synchrotron radiation emitted in the first harmonic from the twin-helical undulator beamline for soft X-ray spectroscopy BL25SU [15,16] of SPring-8 in Japan. After having set the two undulators to opposite helicity, helicity reversal was realized by closing one undulator and fully opening the other. The degree of circular polarization is >98%. The light was incident to the sample under a grazing angle of 30° from the sample surface.

The setup of the photoemission microscope (Focus IS-PEEM [17]) is identical to that described in previous publications [3]. In short, it consists of a three-lens electrostatic straight optical axis microscope with an integral sample stage and a variable contrast aperture. The magnified image is intensified by a two-stage microchannel plate, and converted into visible light by means of a scintillator crystal. The image is then computer-recorded with 12-bit resolution by a Peltier-cooled camera (PCO SensiCam [18]). The binning of camera pixels was adjusted to have exposure times of

single images of not more than 30 s, in order to achieve reasonable acquisition times for the complete spectral series of images. For the data presented here 4×4 and 8×8 binning was used. The width of the energy steps in the scans at the Ni $L_{2,3}$ edges was set to 0.65 eV before the L_3-edge and in between the L_3 and L_2 peaks, 0.26 eV near the L_3 peak, 0.34 eV near the L_2 peak, and 1.4 eV in the post-L_2 region. For the scans at the Fe $L_{2,3}$ edges a constant stepwidth of 0.22 eV was used.

Special attention has to be paid in microspectroscopy to the normalization of the local spectra to the incoming photon flux. In integral absorption spectroscopy this is usually easily achieved when simultaneously the absorption signal from the sample and the photoyield of a monitor is recorded. This can be a grid in the incoming photon beam, or an optical element such as a mirror. Since the entire photon beam is contributing to both the monitor signal and the signal from the sample, normalization is straightforward. In imaging microspectroscopy, however, the local, pixel-resolved, photon flux density cannot be measured, and may deviate significantly from the integral photon flux signal of such a monitor. An inhomogeneous distribution of the photon intensity within the imaged area on the sample invalidates the normalization to a conventional beam monitor. A further complication arises from the fact that the intensity distribution within the light beam from an undulator is also photon energy dependent.

In order to reduce the influence of these inhomogeneities, it is necessary to reduce the lateral extension of the light spot to not much more than the area imaged in the microspectroscopic measurement. This excludes portions of the X-ray beam that are irrelevant for the measurement from contributing to the monitor signal. It can be achieved by using appropriate apertures in the beamline. In beamline optics where the light spot is an image of the exit slit, reducing the exit slit width also reduces the illuminated area. Attention should also be paid to the adjustment of the imaged area to the center of the undulator radiation. After careful adjustment on BL25SU, the remaining deviation between the integral photon flux measured at the last optical element, a gold-coated refocusing mirror, and the local photon flux could

be reduced to less than 5–7%. It was determined from the correction procedure described in the next section.

Co, Ni, and Fe films were evaporated at room temperature by electron bombardment of high purity rods. Deposition rates were calibrated from the oscillations in specular medium energy electron scattering intensity during deposition. Typical deposition rates were between 0.3 and 0.7 ML/min. Wedge-shaped films were prepared by placing an aperture of 2×0.5 mm^2 in front of the sample. The distance to the sample surface could be varied between 1 and 1.5 mm. During deposition the sample-mask assembly was rocked by up to $\pm 7.5°$ about the long axis of the aperture. This results in stripes with a thickness plateau in the middle and wedges with a width in the range of 200–300 μm on both sides. After changing the sample azimuth by 90°, a second stripe could be prepared perpendicular to the first one, resulting in four regions of perpendicularly crossed wedges.

3. Data analysis

Fig. 1(a) shows raw Fe $L_{2,3}$ XMCD data of a single camera pixel in 8×8 binning mode, displaying the averaged information from a 3×3 μm^2 area of a bilayer of 10 atomic monolayers (ML) Fe and 6 ML Co on Cu(0 0 1). Spectra for positive and negative helicity are depicted by solid and dotted lines, respectively. The two peaks correspond to the Fe L_3 and L_2 absorption maxima. The acquisition time per image, i.e., per data point, was 10 s. The sample had been magnetized previously in the light incidence azimuth, which coincided with the substrate [1 1 0] crystallographic direction.

The corresponding monitor signal, representing the integral photon flux, is displayed in Fig. 1(b). The intensity for light of negative helicity, which was provided by the downstream undulator, is about 20–25% higher than that of the upstream undulator because of the shorter distance between source and pinhole aperture. It is also seen that the energetic position of the maxima of the harmonics are slightly different, with the maximum for negative helicity being about 4 eV higher in energy.
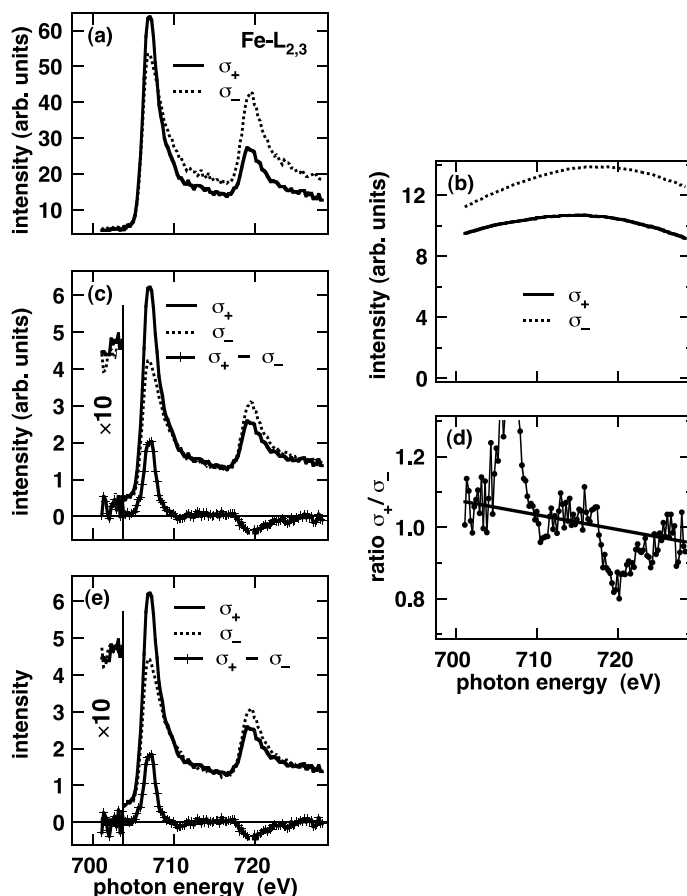
Fig. 1. Example for the correction of single pixel XMCD data of 10 ML Fe/6 ML Co/Cu(0 0 1). Curves for positive (negative) helicity are shown as solid (dotted) lines. (a) Raw data from a $3 \times 3 \ \mu m^2$ area of the sample. (b) Integral photon flux as measured from the photoyield of the last mirror. (c) Data of (a) corrected by the curves of (b). The difference between the two curves is also shown in the bottom. (d) Ratio of the two spectra of (c). The straight line is a linear fit to the data disregarding the peak regions. (e) Spectra from (c) after multiplying the curve for negative helicity by the straight line of (d). Also shown is the difference curve. The pre-edge region for photon energies below 704 eV is shown scaled by a factor of 10 in intensity in panels (c) and (e) for a better visualization of the alignment of the spectra.

Fig. 1(c) shows the spectra of panel (a) after normalization to the integral photon flux of panel (b). At the bottom of Fig. 1(c) the difference between the two spectra is presented. It shows the well-known magnetic circular dichroism with a positive difference at the L_3 edge, and a negative signal at the L_2 edge. The leftmost part of the figure (<704 eV) is magnified by a factor of 10 in intensity. Note that here the solid and dotted lines at ≈ 4.5 intensity units belong to the absorption curves, which display a pre-edge intensity of ≈ 0.45 intensity units, whereas the data points slightly above the zero line belong to the difference curve. The small residual differences between the two spectra in the pre-edge region seen in the magnified part of Fig. 1(c) are caused by differences between

the integral photon flux of panel (b) and the unknown local photon flux at the position in the image from where the spectra were taken. To correct these differences, the following procedure was adopted: First the ratio (intensity for positive helicity divided by intensity for negative helicity) of the normalized spectra of Fig. 1(c) was calculated. It is displayed in Fig. 1(d). Here it is seen that outside the absorption peaks the ratio between absorption of X-rays with positive and negative helicity is not exactly one, as it should be. The reason are inhomogeneities in local photon flux density, as described in the previous section. Because the energy relative to the respective maximum of the undulator harmonics is different in the two scans for opposite helicity, also the deviation from a ratio of one is energy-dependent. For the correction a linear energy dependence is assumed. It is obtained from a fit of a straight line to the ratio of Fig. 1(d). The peak regions exhibiting the magnetic dichroism are excluded before fitting. The result of the linear fit is then used to correct the single pixel spectra. In Fig. 1(d) this correction varies between $+7.0\%$ at the left-hand side, and -3.8% at the right-hand side. This energetic variation is caused by the energy dependence of the intensity distribution within the light spot of the undulator harmonics. It is narrower for higher energies relative to the peak maximum of the harmonics. In that case the photon flux density in the center of the light spot is higher. From Fig. 1(b) it is seen that the maximum of the undulator harmonics for positive helicity was at slightly lower energies than for negative helicities. The local intensity for positive helicity is consequently higher at the low energy side of the spectra of Fig. 1, since here the energy relative to the maximum is higher than for negative helicity.

The corrected spectra and corresponding difference curve are finally shown in Fig. 1(e). Again the region below 704 eV photon energy is shown magnified by a factor of 10 in intensity. Compared to the magnified part of Fig. 1(c), it is seen that now also in the pre-edge region the spectra overlap perfectly. The correction procedure as described above has been performed for all pixels in an image. Only a smooth variation of the fit parameters for the linear fits was observed within the imaged area. The maximum correction did not exceed 5–7% if care was taken for limiting the excess radiation outside the imaged area to a minimum. The small local variation of the correction can be due to slight deviations in the positions of the central undulator beam on the sample for the two helicities.

Sum-rule analysis can now be performed on the corrected single pixel data. Because of the high number of spectra that have to be analyzed in full-image microspectroscopy this has to be done automatically. A problem is that the data can sometimes be rather noisy, especially at positions where the dichroism is small. In most cases the result of interest in sum-rule analysis is two numbers, namely the spin and orbital moments. They are obtained from summing and subtracting the areas of the difference curve at the L_3 and the L_2 edges, respectively [6,7]. If the line shape of the helicity averaged absorption spectra is assumed to be constant over an image, then an analysis procedure that reduces the spectral information on two independent numbers is sufficient. The following fit procedure was therefore used: First a template XMCD spectrum with a sufficiently good statistics is generated by summing over a large area. This spectrum was then analyzed as described in more detail in Refs. [8,9,19]. All the corrected single pixel spectra are normalized on a per-atom basis by setting the intensity axis to zero before the $L_{2,3}$ edge, and to one above the edge. The template difference curve was then fitted to the single pixel difference curves. For this it was separated into two parts representing the dichroism at the L_3 and the L_2 edge. If the dichroism spectra at the L_3 and the L_2 edges individually keep their shape and only vary in size, a perfect fit is obtained by just independently scaling the two parts of the template difference curve. This was checked to be the case for the spectra presented here. The result of the fit are the two scaling factors that are needed to fit these two parts of the template difference curve to the single pixel difference curve. These two numbers can be directly converted into numbers for the spin and orbital moments of the single pixel XMCD spectrum, using the information from the analysis of the template spectrum. By

using only two fit parameters connected to the dichroism intensity at the L_3 and L_2 edge, the fit procedure is very stable, which is a prerequisite for obtaining meaningful information from noisy or scattered single pixel data. In addition, it is also easily programmed to run automatically over a large number of spectra.

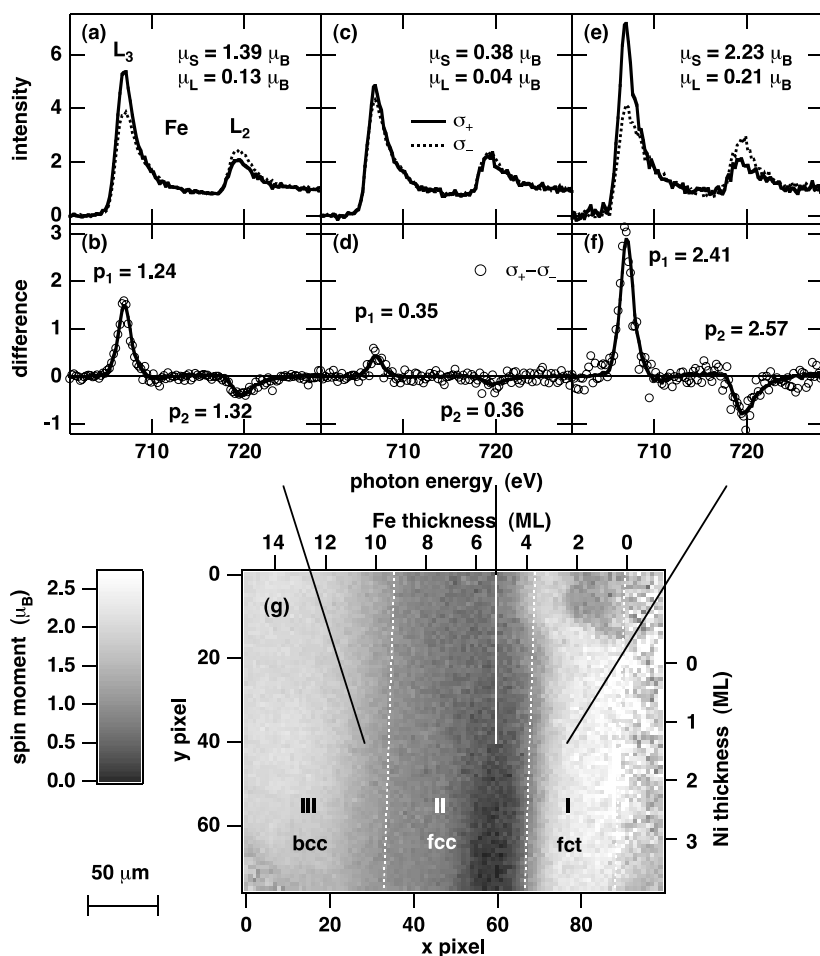Fig. 2(a)–(f) show examples of such a template fit procedure for three single pixel spectra of the Fe $L_{2,3}$ edges in Ni/Fe/Co/Cu(0 0 1). The Co thickness

Fig. 2. Example for the sum rule analysis of single pixel XMCD spectra. (a), (c), (e): Corrected single pixel absorption spectra at the Fe $L_{2,3}$ edges in 1.2 ML Ni/x ML Fe/6 ML Co/Cu(0 0 1) for positive (solid lines) and negative helicity (dotted lines). (b), (d), (f): Difference between spectra for opposite helicity of panels (a), (c), and (e) (open symbols). The Fe thickness x is $\approx$10 ML for (a) and (b), $\approx$5 ML for (c) and (d), and $\approx$2 ML for (e) and (f). The solid lines in panels (b), (d), and (f) are portions of a template difference curve, obtained from averaging over a larger area, scaled by the fit parameters p_1 and p_2 at the L_3 and L_2 edges, respectively, to match the single pixel difference data. The spin and orbital moments, calculated from p_1, p_2, and the spin and orbital moments of the template spectrum, are listed in panels (a), (c), and (e). (g): Grayscale map of Fe spin moments as explained on the left hand side of a 0–3.9 ML Ni/0–14 ML Fe crossed double-wedge on 6 ML Co/Cu(0 0 1), composed of pixels of 3×3 μm^2 size. The Fe thickness is given at the top axis, the Ni thickness at the right axis. Three regions with different structural and magnetic properties of Fe are labeled I, II, and III.

was 6 ML, the Ni thickness for the selected pixels ≈ 1.2 ML, and the Fe thickness ≈ 10 ML ((a), (b)), ≈ 5 ML ((c), (d)), and ≈ 2 ML ((e), (f)). The top panels show the corrected and scaled single pixel absorption spectra for positive helicity (solid lines) and negative helicity (dotted lines). In the lower panels the corresponding difference curves are depicted (open symbols). The solid lines in panels (b), (d), and (f) are the result of fits of the template difference curve to the single pixel difference curves. The scaling factors p_1 for scaling the L_3 dichroism and p_2 for scaling the L_2 dichroism of the template difference curve to the single pixel data are also given. The spin and orbital moments of the image pixels are calculated from p_1, p_2, and the sum-rule analysis of the template spectrum (spin moment 1.1 μ_B, orbital moment 0.1 μ_B). The moments found at the three pixels of Fig. 2 are listed in panels (a), (c), and (e).

4. Results and discussion

The strong variation of the resulting magnetic moments in Fig. 2 can be attributed to different magnetic and structural phases of iron in the Ni/Fe/Co trilayer. Fig. 2(g) shows a complete grayscale map of the Fe spin moments of a Ni (0–3.9 ML)/Fe (0–14 ML)/Co (6 ML)/Cu(0 0 1) crossed double-wedge sample. It is composed of 7600 pixels of 3×3 μm^2 size. The positions where the three example single pixel spectra of panels (a)–(f) have been taken are marked by the ends of the three straight lines. The legend for the conversion of the grayscale to magnetic moments is given on the left-hand side. The image shows a section of the double-wedge of Ni and Fe that includes the onset of both wedges. The Fe thickness increases from right to left as indicated at the top axis, the Ni thickness increases from top to bottom as indicated at the right-hand axis. It is seen that the three example single pixel spectra of the top panels have been chosen to represent three regions with rather different Fe spin moments. These regions are separated by white dotted lines, and labeled I, II, and III. Whereas region I exhibits Fe spin moments of $\approx 2.5\mu_B$, the moments in region II are significantly lower. In region III the spin moment

increases again from right to left to $\approx 2\mu_B$. In accordance with previous studies of Fe/Co/Cu(0 0 1) [20–22] and Fe/Cu(0 0 1) [23–25], the lower moments in region II are interpreted with a relaxed fcc phase of Fe containing non-ferromagnetic layers [26]. In region I tetragonally expanded fcc-like Fe (fct) with spin moments of about $2.5\mu_B$ is present, whereas at Fe thicknesses between 9 and 12 ML the Fe is converted into the bcc phase, showing spin moments of $\approx 2\mu_B$.

The two-dimensional mapping of magnetic moments in this Ni/Fe double-wedge on Co/Cu(0 0 1) also allows to observe changes in the Fe spin moment as a function of the Ni overlayer thickness. Such a change is recognized at Fe thicknesses between 4 and 6 ML. Here, the Fe spin moment is dropping to values of nearly zero for Ni thicknesses above ≈ 1.5 ML. This could be caused by an opposite magnetic orientation of the Fe top and bottom interface layers with non-ferromagnetic layers in between. An antiferromagnetic orientation of the Co and Ni layers in Ni/Fe/Co around 5.5 ML Fe thickness has been observed indeed [26]. The observed spin moments have to be interpreted as the depth-weighted average of all Fe layers, where the probing depth over which the secondary electron signal is reduced by a factor of $1/e$ is ≈ 17 Å [27]. Therefore a non-uniform depth distribution of magnetic moments, which most likely is present in region II, cannot be unambiguously determined from the present data. A simple model assuming a constant amount of ferromagnetic Fe at both interfaces plus non-ferromagnetic Fe in between would lead to a decreasing apparent magnetic moment with increasing Fe film thickness, which is not observed here. The situation is therefore probably more complicated, and the influence of surface and interface roughnesses as well as non-collinear moments may have to be considered.

In the previous example a high spatial resolution was not required, since only the distribution of magnetic properties along the wedges was measured. The PEEM was therefore operated at a low extractor voltage (about 200 V) to yield a large field of view. Fig. 3 shows an example of microspectroscopy with a higher resolution. Here the extractor voltage was 10 kV; together with a
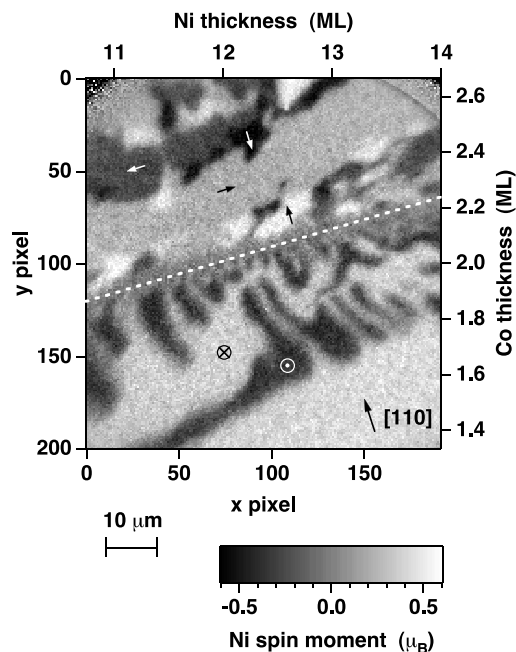
Fig. 3. Map of Ni spin moment projections onto the light incidence direction (from bottom to top, with an angle of 30° to the sample surface) as example for high resolution microspectroscopy. The image is the result of 76 800 single pixel XMCD spectra of 370×370 nm^2, the total data acquisition time of which was about 2 h 20 min. The sample is a Co/Ni/Cu(0 0 1) crossed double wedge. The Ni thickness is indicated at the top axis, the Co thickness at the right axis. The grayscale to magnetic moment conversion is given in the legend at the bottom. The white dotted line separates regions with in-plane magnetization (top) from regions with out-of-plane magnetization (bottom). The magnetization directions are indicated by arrows in some domains.

70 μm contrast aperture this resulted in a resolution of about 500 nm, as determined from linescans across domain boundaries. The pixel size was adjusted to 370×370 nm^2 by using a 4×4 binning of camera pixels. The exposure time per image was 30 s. Fig. 3 displays a section of a Co/Ni crossed double wedge on Cu(0 0 1). In the displayed area the Ni thickness increases from 10.7 to 14 ML from left to right, as indicated at the top axis, and the Co thickness increases from 1.35 to 2.65 ML from bottom to top, as indicated at the right-hand axis. The Ni spin moment as the result of 76800 single pixel XMCD spectra is presented

in a grayscale plot. The grayscale to magnetic moment conversion can be seen from the legend at the bottom. Note that here the grayscale is symmetric around zero. Unlike the previous example this sample was not magnetized by an external magnetic field before imaging. The resulting moments from the sum-rule analysis include therefore the cosine of the angle between local magnetization and the helicity of the incident X-rays, which is different for domains of different magnetization direction. It is thus not the absolute value of the spin moment that is obtained from the microspectroscopic analysis, but the projection onto the direction of the incoming light. The light incidence was from bottom to top of Fig. 3, with an angle of 30° to the sample surface.

Two regions with qualitatively different domain structure can be recognized. They are separated in Fig. 3 by the white dotted line. In the upper part of the image four different shades of gray are recognized, namely black, dark gray, light gray, and white. In the lower part only two different shades of gray are found, and the domain boundaries are more rounded. Quantitative analysis of the values of the Ni spin moment projection in the single domains leads to the interpretation that in the upper part of the image the magnetization direction is along the four $\langle 1\,1\,0 \rangle$ in-plane crystallographic directions, as indicated by arrows. The Cu(0 0 1) single crystal substrate was deliberately mounted under an azimuthal angle of 18° between light incidence and the $[1\,1\,0]$ axis, so that the four $\langle 1\,1\,0 \rangle$ directions all have different projections onto the light incidence direction. In the lower part of the image the values of the spin moment projection and the shape of the domains are consistent with an out-of-plane magnetization. Here the angle between the magnetization axis and the light helicity is 60°. The absolute value of the Ni spin moment is $0.65\mu_B$ over the entire image.

The dotted line in Fig. 3 represents a spin reorientation transition between in-plane and out-of-plane easy axes of magnetization. The spin reorientation transition occurs both as a function of Ni and Co layer thickness. Single films of Ni on Cu(0 0 1) exhibit an out-of-plane anisotropy over an extended thickness range [28–30], whereas Co/Cu(0 0 1) is always in-plane [31,32]. The observed

spin reorientation transition in Co/Ni/Cu(0 0 1) is thus the result of the interplay of Co and Ni anisotropies [33]: for high Ni thickness and low Co thickness the out-of-plane Ni anisotropy dominates, increasing the Co thickness and lowering the Ni thickness the in-plane contribution of the Co film wins.

Interesting is the domain shape in the out-of-plane region close to the spin reorientation transition: As the spin reorientation transition is approached, more and more oppositely magnetized domains are formed. This can be explained by the competition between the magnetostatic energy on the one hand, and the energy cost for creating domain walls on the other hand. Closely spaced alternatingly up and down magnetized perpendicular domains have a lower magnetostatic energy than a single out-of-plane domain due to partial flux closure [34]. The formation of such domains can be energetically favorable close to the spin reorientation transition [35] because at that point the anisotropy energy and hence the energy for the formation of domain walls (in which an in-plane component of the magnetization is present) is low.

5. Summary and conclusion

A practical method for element-selective microscopic mapping of magnetic moments by full-image XMCD microspectroscopy using a PEEM has been described. Spin and orbital moments are obtained from sum-rule analysis of single pixel XMCD spectra of a photon energy series of microscopic PEEM images. This has been applied to Ni/Fe/Co trilayers and Co/Ni bilayers, grown epitaxially on Cu(0 0 1). In the former system three different Fe thickness regions with different magnetic properties of the Fe layer have been observed. The Fe spin moment as a function of Fe and Ni layer thickness has been quantitatively evaluated. Below 4 ML and above ≈ 12 ML Fe thickness ferromagnetic phases with Fe spin moments of ≈ 2.5 and $\approx 2.0 \mu_B$, respectively, are found. Between 4 and ≈ 10 ML, a reduced net magnetic moment is observed, which between 4 and 6 ML Fe thickness depends also on Ni thickness. It may be due to a non-ferromagnetic configuration of fcc

Fe and an antiferromagnetic coupling between Co and Ni layers with magnetically live Fe interface layers. In Co/Ni/Cu(0 0 1) a spin-reorientation transition from in-plane to out-of-plane could be quantitatively followed in two-dimensional (Co and Ni) thickness space. The easy axis of magnetization switches from in-plane at lower Ni thicknesses or higher Co thicknesses to out-of-plane at higher Ni thicknesses or lower Co thicknesses. The formation of perpendicularly magnetized domains with decreasing size upon approaching the spin reorientation transition is explained by magnetostatic stray field energy minimization for decreasing domain wall energy.

In conclusion, microspectroscopy of wedges or crossed double wedges can help significantly in the magnetic characterization of layered systems. The microscopic spatial resolution of the quantitative magnetic information opens the way for the investigation of magnetic microstructures and microscopic domain structures by XMCD. The microspectroscopic evaluation of not only the spin moments but also the orbital moments [33] can help to characterize magnetic anisotropies on a microscopic scale, taking advantage of the relation between magnetocrystalline anisotropy and the anisotropy of the orbital moment [13,14].

References

[1] J. Stöhr, Y. Wu, M.G. Samant, B.B. Hermsmeier, G. Harp, S. Koranda, D. Dunham, B.P. Tonner, Science 259 (1993) 658.
[2] W. Swiech, G.H. Fecher, Ch. Ziethen, O. Schmidt, G. Schönhense, K. Grzelakowski, C.M. Schneider, R. Frömter,

H.P. Oepen, J. Kirschner, J. Electron Spectrosc. Relat. Phenom. 84 (1997) 171.

[3] W. Kuch, R. Frömter, J. Gilles, D. Hartmann, Ch. Ziethen, C.M. Schneider, G. Schönhense, W. Swiech, J. Kirschner, Surf. Rev. Lett. 5 (1998) 1241.

[4] J.L. Erskine, E.A. Stern, Phys. Rev. B 12 (1975) 5016.

[5] G. Schütz, W. Wagner, W. Wilhelm, P. Kienle, R. Zeller, R. Frahm, G. Materlik, Phys. Rev. Lett. 58 (1987) 737.

[6] B.T. Thole, P. Carra, F. Sette, G. van der Laan, Phys. Rev. Lett. 68 (1992) 1943.

[7] P. Carra, B.T. Thole, M. Altarelli, X. Wang, Phys. Rev. Lett. 70 (1993) 694.

[8] C.T. Chen, Y.U. Idzerda, H.-J. Lin, N.V. Smith, G. Meigs, E. Chaban, G.H. Ho, E. Pellegrin, F. Sette, Phys. Rev. Lett. 75 (1995) 152.

[9] J. Stöhr, J. Electron Spectrosc. Relat. Phenom. 75 (1995) 253.

[10] R. Wu, A.J. Freeman, Phys. Rev. Lett. 73 (1994) 1994.

[11] W.L. O'Brien, B.P. Tonner, G.R. Harp, S.S.P. Parkin, J. Appl. Phys. 76 (1994) 6462.

[12] Y.U. Idzerda, C.T. Chen, H.-J. Lin, H. Tjeng, G. Meigs, Physica B 208–209 (1995) 746.

[13] P. Bruno, Phys. Rev. B 39 (1989) 865.

[14] G. van der Laan, J. Phys.: Cond. Matt. 10 (1998) 3239.

[15] Y. Saitoh, T. Nakatani, T. Matsushita, T. Miyahara, M. Fujisawa, K. Soda, T. Muro, S. Ueda, H. Harada, A. Sekiyama, S. Imada, H. Daimon, S. Suga, J. Synchrotron Rad. 5 (1998) 542.

[16] Y. Saitoh, H. Kimura, Y. Suzuki, T. Nakatani, T. Matsushita, T. Muro, T. Miyahara, M. Fujisawa, K. Soda, S. Ueda, H. Harada, M. Kotsugi, A. Sekiyama, S. Suga, Rev. Sci. Instrum. 71 (2000) 3254.

[17] FOCUS GmbH, http://www.focus-gmbh.com.

[18] PCO Computer Optics GmbH, http://www.pco.de.

[19] W. Kuch, M. Salvietti, X. Gao, M.-T. Lin, M. Klaua, J. Barthel, C.V. Mohan, J. Kirschner, Phys. Rev. B 58 (1998) 8556.

[20] W.L. O'Brien, B.P. Tonner, Surf. Sci. 334 (1995) 10.

[21] W.L. O'Brien, B.P. Tonner, Phys. Rev. B 52 (1995) 15332.

[22] E.J. Escorcia-Aparicio, R.K. Kawakami, Z.Q. Qiu, Phys. Rev. B 54 (1996) 4155.

[23] J. Thomassen, F. May, B. Feldmann, M. Wuttig, H. Ibach, Phys. Rev. Lett. 69 (1992) 3831.

[24] D. Li, M. Freitag, J. Pearson, Z.Q. Qiu, S.D. Bader, Phys. Rev. Lett. 72 (1994) 3112.

[25] M. Straub, R. Vollmer, J. Kirschner, Phys. Rev. Lett. 77 (1996) 743.

[26] W. Kuch, J. Gilles, F. Offi, S. S. Kang, S. Imada, S. Suga, J. Kirschner, J. Electron Spectrosc. Relat. Phenom. 109 (2000) 249.

[27] R. Nakajima, J. Stöhr, Y.U. Idzerda, Phys. Rev. B 59 (1999) 6421.

[28] F. Huang, M.T. Kief, G.J. Mankey, R.F. Willis, Phys. Rev. B 49 (1994) 3962.

[29] W.L. O'Brien, B.P. Tonner, Phys. Rev. B 49 (1994) 15370.

[30] B. Schulz, K. Baberschke, Phys. Rev. B 50 (1994) 13467.

[31] P. Krams, F. Lauks, R.L. Stamps, B. Hillebrands, G. Güntherodt, Phys. Rev. Lett. 69 (1992) 3674.

[32] M. Kowalewski, C.M. Schneider, B. Heinrich, Phys. Rev. B 47 (1993) 8748.

[33] W. Kuch, J. Gilles, S.S. Kang, S. Imada, S. Suga, J. Kirschner, Phys. Rev. B 62 (2000) 3824.

[34] Y. Yafet, E.M. Gyorgy, Phys. Rev. B 38 (1988) 9145.

[35] M. Speckmann, H.P. Oepen, H. Ibach, Phys. Rev. Lett. 75 (1995) 2035.

Multilayers I: Coupling and Anisotropy   Andreas Schreyer, Chairman

Quantitative x-ray magnetic circular dichroism microspectroscopy of Fe/Co/Cu(001) using a photoemission microscope

W. Kuch,[a)] J. Gilles, S. S. Kang, F. Offi, and J. Kirschner
Max-Planck-Institut für Mikrostrukturphysik, Weinberg 2, D-06120 Halle, Germany

S. Imada and S. Suga
Osaka University, Graduate School of Engineering Science, 1-3 Machikaneyama,
Toyonaka 560-8531, Japan

Photoelectron emission microscopy is combined with soft x-ray magnetic circular dichroism (XMCD) absorption spectroscopy to obtain local element-resolved quantitative magnetic properties with microscopic resolution. This is applied to study 0–14 ML Fe wedges with a slope of 0.055 ML/μm on 6 ML Co/Cu(001). Local XMCD spectra at the Fe $L_{2,3}$ edge confirm the presence of three magnetically different thickness regions of Fe with effective spin moments of $2.5\mu_B$ (0–4.5 ML), $0.7\mu_B$ (4.5–11 ML), and $1.8\mu_B$ (>11 ML). The value of $0.7\mu_B$ in the second phase is consistent with an fcc Fe phase containing nonferromagnetic layers underneath a ferromagnetic surface. © *2000 American Institute of Physics.* [S0021-8979(00)44908-X]

Photoelectron emission microscopy (PEEM) in connection with resonant excitation by circularly polarized light has proven its usefulness for the study of magnetic microstructures and multilayers.[1,2] The lateral intensity distribution of emitted low energy secondary electrons is thereby magnified by an electron optics. The effect of soft x-ray magnetic circular dichroism (XMCD) provides the magnetic contrast. The absorption of circularly polarized photons at elemental absorption edges differs for different alignment of light helicity and magnetization direction,[3] leading to a difference in secondary electron intensity. Sum rules[4] allow one to extract spin and orbital magnetic moments from integrals in the difference curve of two absorption spectra for opposite light helicity.[5,6]

The combination of the principles of microscopy (PEEM) and spectroscopy (XMCD) unites the advantages of both methods, namely the element-selective quantitative information of electronic and magnetic properties of XMCD, and the lateral resolution of PEEM. It is what we call ''microspectroscopy,'' and results in images displaying quantitative magnetic properties on an element-resolved basis. Practically, this implies to scan the photon energy and record microscopic images of the secondary electron intensity for both helicities at each energy step. From such a set of images local XMCD spectra at any position in the image can be analyzed.

In this article we demonstrate the application of this PEEM–XMCD microspectroscopy to study the magnetic phases of Fe on fcc Co/Cu(001). A common means of efficiently studying the thickness dependence of thin film prop-

erties is to image their spatial distribution on wedge-shaped samples. For that purpose we deposited Fe as 0–14 ML microwedges on 6 ML Co/Cu(001), and obtained the full spectroscopic XMCD information of that wedge from the analysis of PEEM images.

Ultrathin epitaxial Fe films, grown at room temperature on Cu(001), are one of the most interesting systems with respect to the interplay between structural and magnetic properties.[7–11] For film thicknesses below ≈4 atomic monolayers (ML) a fully ferromagnetic fcc-like structure is present.[8] In the thickness range between 4 and 11 ML, a second phase, a relaxed fcc structure, is found with a nonferromagnetic behavior of the inner film layers, but ferromagnetism at the surface.[9] For thicknesses above ≈11 ML, a third phase appears, a ferromagnetic (011) oriented bcc phase.[10] Fe films grown on Co/Cu(001) exhibit a very similar sequence of structural and magnetic phases.[12–14] The main difference from Fe/Cu(001) concerns the direction of the easy magnetic axis, which is in-plane in the case of Fe/Co/Cu(001). As for the presence of the ferromagnetic surface layer in the second phase, controversial experimental evidence has been reported. While from oxygen adsorption[13] and XMCD experiments[12] it has been concluded that the surface is not ferromagnetic, other XMCD measurements[14] as well as measurements of photoelectron diffraction in magnetic dichroism[15] and spin-resolved valence band photoemission,[16] provided evidence for the presence of ferromagnetic surface layers on top of nonferromagnetic underlayers.

Co and Fe films were evaporated at room temperature by thermal evaporation. Before depositing the Fe wedge, the Co film was remanently magnetized by a field of 500 Oe in the [110] direction. The wedge-shaped Fe films were prepared by placing an aperture of 2×0.5 mm^2 in front of the sample,

---

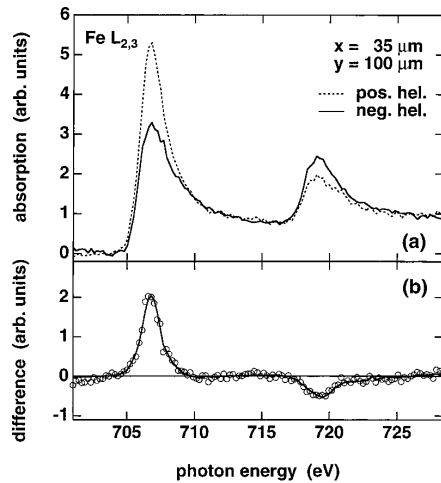[a)]Author to whom correspondence should be addressed; electronic mail: kuch@port.exp.bessy.de

FIG. 1. (a) Fe $L_{2,3}$ absorption spectra of a single 1.5×3 μm^2 pixel at coordinates $x = 35$ μm, $y = 100$ μm. The dashed (solid) line depicts absorption for positive (negative) helicity. (b) Markers: Difference between the two curves of (a). Line: Template difference curve, obtained from averaging 1500 pixels in the region of bcc Fe, presented here with different scaling at the L_3 and L_2 edge to fit the single pixel data.

FIG. 2. Result of the pixel-by-pixel sum-rule analysis of the imaged area in Fe/6 ML Co/Cu(001): (a) Fe effective spin moment μ_S, (b) Fe orbital moment μ_L. Different levels of gray correspond to different values of μ_S and μ_L, as explained in the respective legend. Three different phases as schematically shown are characterized by different moments.

with a distance of 1 mm to the sample surface. During deposition the sample was rocked by $\pm 7.5°$ about the long axis of the aperture. This results in a rectangle with two 255 μm broad wedges at the long sides, exhibiting slopes of 0.055 ML/μm.

The PEEM measurements were performed at beamline BL25SU of SPring-8 in Japan, which provides >95% circularly polarized light.[17] The light was incident under an angle of 30° to the sample surface, with an azimuthal angle of 18° to the [110] axis of the Cu substrate. The local photon energy resolution in the images is better than 150 meV. All images were normalized to the photoyield of the gold-coated refocusing mirror in front of the experimental chamber.

The setup of the photoemission microscope (Focus IS-PEEM)[18] is identical to that described in previous publications.[2] The contrast aperture was set to 70 μm for the present measurements. To obtain a large field of view, a low extraction voltage of about 200 V was used. This results in a lateral resolution of about 1 μm, and a field of view of about 380 μm. The magnified image is intensified by a two-stage multichannel plate, and converted into visible light by means of a scintillator crystal. The image is then computer-recorded with 12-bit resolution by a Peltier-cooled camera (PCO SensiCam).[19] Exposure time was 20 s/image, the total time for the acquisition of the over 3 million data points was about 1 h 50 min. The helicity was reversed once after completion of a full energy scan.

Figure 1(a) shows typical Fe $L_{2,3}$ absorption spectra of a single pixel of 1.5×3 μm^2 on the sample surface at 14 ML Fe thickness. The spectra are composed of information of that particular pixel from 242 different images. Dashed (solid) lines depict absorption for positive (negative) helicity. In panel (b) the corresponding difference is shown (open circles). The solid line gives the fit of a difference curve
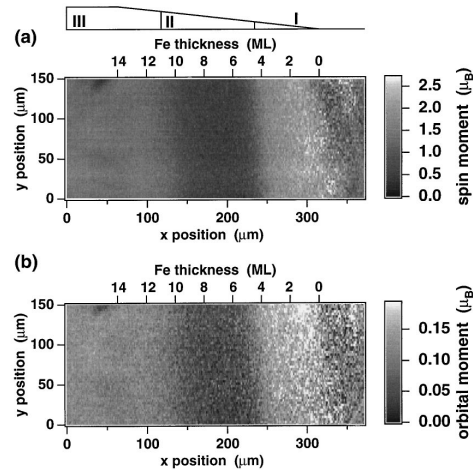
averaged from 1500 pixels at the thick end of the Fe wedge (bcc Fe). It serves as a template for the automated analysis of the 12 648 single pixel spectra. Only two parameters were used to fit that template difference curve to the single pixel difference curves. They describe the separate scaling of the L_3 and L_2 regions. Having analyzed the template XMCD spectra beforehand by means of the sum rules, sum-rule analysis of the single pixel data is obtained from these two fit parameters. This analysis is valid if the shape of the absorption spectra does not change over the imaged area. This was determined to be the case for the present Fe and Co images. The analysis of the template data was done as described elsewhere.[20] The data were corrected for the angle of incidence with respect to the [110] magnetization direction, and for the degree of light polarization. The number of Fe d holes was taken as 3.34.[21] For the analysis of the single pixel data the white line intensity was assumed to be proportional to the L_3 peak height. Only a smooth spatial variation of the white line intensity of less than 15% was present in the spectra over the imaged area. To avoid unreasonably long data acquisition times and contamination of the surface, the energy scans were taken only up to an energy of 728 eV. Part of the tail of the L_2 dichroism at higher photon energies is therefore not included in the analysis. This leads to systematic deviations of the magnetic moments as determined by the sum rules, predominantly of the orbital moment. A cutoff in the integration on the high energy side of the spectra leads to a higher apparent orbital moment.[22] From comparison with the curves for bulk Fe of Ref. 5 we estimate that the orbital moments will be affected by a factor of 2.6 ± 0.2, while the result for the effective spin moment is correct within 5%. To account for that, the orbital moments' values were corrected by a factor of 1/2.6.

Figure 2(a) shows the result of the pixel-by-pixel sum-rule analysis for the Fe effective spin moment μ_S. The Fe

thickness increases from right to left, as indicated. Different levels of gray correspond to different values of μ_S, as explained in the legend. The three different phases at Fe thicknesses of 0–4.5, 4.5–11, and >11 ML are clearly recognized by their different moments. The averaged values are $2.5\mu_B$ at 1.5–2 ML, $0.7\mu_B$ at 6–7 ML, and $1.8\mu_B$ above 14 ML. Analysis of Co $L_{2,3}$ microspectroscopy, seen through the Fe overlayer, revealed a constant value of $1.6\mu_B$ over the whole image.

In panel (b) the pixel-by-pixel analysis for the Fe orbital moment μ_L is shown. Compared to the spin moment [panel (a)] the noise is higher because μ_L is obtained from the difference between the areas of L_3 and L_2 dichroism, whereas they are summed for μ_S. The orbital moment qualitatively follows the spin moment through the sequence of the three different phases in the Fe wedge. The ratio of orbital to spin moment is roughly constant, with a slight change from 0.08 ± 0.01 in region I to 0.10 ± 0.01 in region III.

The Fe spin magnetic moments observed here agree qualitatively well with those found by Schmitz *et al.* ($3.0\mu_B$ in phase I, $1.1\mu_B$ in phase II),[14] although our values are systematically lower. The value of $0.7\mu_B$ in region II has to be interpreted as the depth-weighted average of all Fe layers. It is consistent with ferromagnetic Fe at the surface, for example, 2 ML ferromagnetic Fe ($2.2\mu_B$) on top of 6 ML nonferromagnetic Fe and a probing depth of 17 Å.[23] This contrasts with the result of Ref. 12, where a drop in the dichroism by a factor of about 10 between phase I and II was observed. $1.8\mu_B$ for bcc Fe is lower than the expected bulk value of $2.2\mu_B$. It is conceivable that the Fe films are even at 14 ML not yet entirely converted to the fully ferromagnetic bcc structure.

In conclusion, we have demonstrated how the combination of PEEM microscopy and XMCD spectroscopy can be used to obtain spectroscopic information on a microscopic scale. It allows the imaging of element-resolved local quantitative magnetic properties. Microspectroscopy of wedges or crossed double wedges can help significantly in the magnetic characterization of layered systems. Operating the photoemission microscope in high-resolution mode will open the way for the investigation of magnetic microstructures and microscopic domain structures by XMCD.

[1] J. Stöhr, Y. Wu, M. G. Samant, B. B. Hermsmeier, G. Harp, S. Koranda, D. Dunham, and B. P. Tonner, Science **259**, 658 (1993).

[2] W. Kuch, R. Frömter, J. Gilles, D. Hartmann, Ch. Ziethen, C. M. Schneider, G. Schönhense, W. Swiech, and J. Kirschner, Surf. Rev. Lett. **5**, 1241 (1998); W. Swiech *et al.*, J. Electron Spectrosc. Relat. Phenom. **84**, 171 (1997); C. M. Schneider, J. Magn. Magn. Mater. **175**, 160 (1997).

[3] J. L. Erskine and E. A. Stern, Phys. Rev. B **12**, 5016 (1975); G. Schütz, W. Wagner, W. Wilhelm, P. Kienle, R. Zeller, R. Frahm, and G. Materlik, Phys. Rev. Lett. **58**, 737 (1987).

[4] B. T. Thole, P. Carra, F. Sette, and G. van der Laan, Phys. Rev. Lett. **68**, 1943 (1992); P. Carra, B. T. Thole, M. Altarelli, and X. Wang, *ibid.* **70**, 694 (1993).

[5] C. T. Chen, Y. U. Idzerda, H.-J. Lin, N. V. Smith, G. Meigs, E. Chaban, G. H. Ho, E. Pellegrin, and F. Sette, Phys. Rev. Lett. **75**, 152 (1995).

[6] J. Stöhr, J. Electron Spectrosc. Relat. Phenom. **75**, 253 (1995).

[7] J. Thomassen, F. May, B. Feldmann, M. Wuttig, and H. Ibach, Phys. Rev. Lett. **69**, 3831 (1992).

[8] M. T. Kief and W. F. Egelhoff, Jr., Phys. Rev. B **47**, 10785 (1993); K. Heinz, S. Müller, and P. Bayer, Surf. Sci. **337**, 215 (1995).

[9] P. Bayer, S. Müller, P. Schmailzl, and K. Heinz, Phys. Rev. B **48**, 17611 (1993); D. Li, M. Freitag, J. Pearson, Z. Q. Qiu, and S. D. Bader, Phys. Rev. Lett. **72**, 3112 (1994); S. Müller, P. Bayer, A. Kinne, P. Schmailzl, and K. Heinz, Surf. Sci. **322**, 21 (1995); M. Straub, R. Vollmer, and J. Kirschner, Phys. Rev. Lett. **77**, 743 (1996).

[10] M. Wuttig, B. Feldmann, J. Thomassen, F. May, H. Zillgen, A. Brodde, H. Hannemann, and H. Neddermayer, Surf. Sci. **291**, 14 (1993); J. Giergiel, J. Kirschner, J. Landgraf, J. Shen, and J. Woltersdorf, *ibid.* **310**, 1 (1994); J. Giergiel, J. Shen, J. Woltersdorf, A. Kirilyuk, and J. Kirschner, Phys. Rev. B **52**, 8528 (1995).

[11] M. Zharnikov, A. Dittschar, W. Kuch, C. M. Schneider, and J. Kirschner, Phys. Rev. Lett. **76**, 4620 (1996); J. Magn. Magn. Mater. **174**, 40 (1997).

[12] W. L. O'Brien and B. P. Tonner, Surf. Sci. **334**, 10 (1995); Phys. Rev. B **52**, 15332 (1995).

[13] E. J. Escorcia-Aparicio, R. K. Kawakami, and Z. Q. Qiu, Phys. Rev. B **54**, 4155 (1996).

[14] D. Schmitz, C. Charton, A. Scholl, C. Carbone, and W. Eberhardt, Phys. Rev. B **59**, 4327 (1999).

[15] X. Gao, M. Salvietti, W. Kuch, C. M. Schneider, and J. Kirschner, Phys. Rev. B **58**, 15426 (1998).

[16] R. Kläsges, D. Schmitz, C. Carbone, W. Eberhardt, and T. Kachel, Solid State Commun. **107**, 13 (1998).

[17] Y. Saitoh *et al.*, J. Synchrotron Radiat. **5**, 542 (1998).

[18] FOCUS GmbH, Am Birkhecker Berg 20, D-65510 Hünstetten, Germany.

[19] PCO Computer Optics GmbH, Ludwigsplatz 4, D-93309 Kelheim, Germany.

[20] W. Kuch, M. Salvietti, X. Gao, M.-T. Lin, M. Klaua, J. Barthel, C. V. Mohan, and J. Kirschner, Phys. Rev. B **58**, 8556 (1998); W. Kuch, M. Salvietti, X. Gao, M. Klaua, J. Barthel, C. V. Mohan, and J. Kirschner, J. Appl. Phys. **83**, 7019 (1998).

[21] R. Wu and A. J. Freeman, Phys. Rev. Lett. **73**, 1994 (1994).

[22] S. Imada, T. Muro, T. Shishidou, S. Suga, H. Maruyama, K. Kobayashi, H. Yamazaki, and T. Kanomata, Phys. Rev. B **59**, 8752 (1999).

[23] R. Nakajima, J. Stöhr, and Y. U. Idzerda, Phys. Rev. B **59**, 6421 (1999).

Imaging microspectroscopy of Ni/Fe/Co/Cu(001) using a photoemission microscope

W. Kuch[a,*], J. Gilles[a], F. Offi[a], S.S. Kang[a], S. Imada[b], S. Suga[b], J. Kirschner[a]

[a]*Max-Planck-Institut für Mikrostrukturphysik, Weinberg 2, D-06120 Halle, Germany*
[b]*Graduate School of Engineering Science, Osaka University, 1–3 Machikaneyama, Toyonaka 560-8531, Japan*

Abstract

The magnetic phases of 0–6 atomic monolayers (ML) Ni/0–14 ML Fe/6 ML Co/Cu(001) trilayer crossed double wedges are studied by the combination of photoelectron emission microscopy and X-ray magnetic circular dichroism spectroscopy at the Fe $L_{2,3}$ edges. This microspectroscopic technique allows the extraction of local quantitative magnetic information. The presence of three magnetically different thickness regions of Fe with effective spin moments per atom of 2.5 μ_B (below ≈ 3.5 ML), 0.7 μ_B (≈ 3.5–11 ML), and 2.0 μ_B (above ≈ 11 ML) is confirmed. At 7–9 ML thickness, the value of 0.7 μ_B is consistent with a ferromagnetic Fe surface layer on top of non-ferromagnetic layers. The ratio of orbital to effective spin moment varies between 0.05 for very thin Fe films and 0.15 for thicker films, if correction of saturation effects is taken into account. Images of the magnetic circular dichroism asymmetry at the Ni and Co L_3 edges show that at 5.5 ML Fe thickness the Ni and Co magnetizations have opposite orientations, pointing towards antiferromagnetic coupling across the Fe layer. © 2000 Elsevier Science B.V. All rights reserved.

Keywords: Photoelectron emission microscopy; X-ray magnetic circular dichroism; Fcc Fe; Thin films; Magnetic moment

1. Introduction

Since its experimental discovery [1], magnetic circular dichroism in soft X-ray absorption (XMCD) spectroscopy has developed into a widely used technique for the element-specific characterization of magnetic thin films and multilayers [2,3]. The absorption of circularly polarized photons at elemental absorption edges differs for different alignment of light helicity and magnetization direction [4], leading to a difference in secondary electron intensity. Sum-rules have been proposed to deduce quantitative information from the difference curve between absorption spectra for opposite light helicity [5,6]. Although there has been some dispute about the applicability of these rules [2,7–11], they seem to yield reasonable results for the 3*d* transition metals [2,3,10,12–15]. These sum-rules allow one to extract numbers for the spin and orbital magnetic moments from the comparison of the integrated absorption cross section at the L_3 and L_2 edges of transition metals for opposite light helicity, thereby enabling the separate determination of magnetic properties of different elements in the same sample.

The rapidly decreasing size of technologically employed magnetic structures calls for techniques

*Corresponding author. Tel.: +49-30-6392-4927; fax: +49-30-6392-4984.

E-mail address: kuch@exp.bessy.de (W. Kuch).

that allow quantitative magnetic characterization on a microscopic scale. One way to add spatial resolution to the advantages of magnetic circular dichroism spectroscopy is the use of a photoelectron emission microscope (PEEM). In PEEM imaging, the lateral intensity distribution of emitted low energy secondary electrons is magnified by an electron optics. The intensity of secondary electrons can be used as a surface sensitive measure of the absorption of soft X-rays. It is therefore straightforward to combine the principles of microscopy (PEEM) and spectroscopy (XMCD) in order to unite the advantages of both methods, namely the element-selective quantitative information of electronic and magnetic properties of XMCD, and the lateral resolution of PEEM. This is called microspectroscopy, and can supply images displaying local electronic and magnetic properties of a sample as determined from the analysis of local XMCD spectra.

The effect of XMCD, i.e., the dependence of the absorption of circularly polarized photons at elemental absorption edges on the alignment of the magnetization direction and the light helicity, has in fact been employed as a contrast mechanism for the imaging of magnetic domains with PEEM [16–19]. Domains on the sample that have different geometrical projections of the magnetization direction onto the direction of the incoming X-rays show a different absorption cross section for circularly polarized photons at the absorption resonance. Imaged with PEEM, these domains can be distinguished by their different intensity of secondary electron emission. To obtain furthermore the *full* spectroscopic information inherent to XMCD requires the recording of microscopic images of the secondary electron intensity at many different photon energies for both helicities, not only at the absorption maximum. These images then constitute a set of local XMCD spectra for any position of the imaged sample area. Standard sum-rule analysis may then be performed for all pixels constituting the image in order to obtain images showing the absolute numbers of the components of spin and orbital magnetic moments along the light direction. The acquisition of such a spectral series of absorption images, or, in other words, the parallel recording of local XMCD spectra in a reasonable time became feasible with the availability of powerful third generation synchrotron light sources.

In this contribution we use PEEM–XMCD microspectroscopy to investigate the magnetic phases and the coupling behavior of ultrathin Fe films sandwiched between Ni and Co films on Cu(001). A common means of effectively studying the thickness dependence of thin film properties is to image their spatial distribution in wedge-shaped samples. The two-dimensional information present in plane images can be used to study the dependence of these properties on two independent parameters, for example the thicknesses of two of the constituting films. For the present study we prepared Ni/Fe/Co/Cu(001) films in which the Co thickness was constant at 6 atomic monolayers (ML), and in which both the Fe and the Ni layer were deposited as wedges, rotated by 90° in the film plane with respect to each other. To be able to image such wedge-shaped samples with PEEM, microscopic dimension wedges of 255-μm size were used.

Ultrathin epitaxial Fe films, grown at room temperature on Cu(001), are one of the most interesting systems with respect to the interplay between structural and magnetic properties [20–38]. For film thicknesses below ≈ 4 atomic monolayers (ML) a fully ferromagnetic tetragonally expanded fcc-like structure is present [20,21]. In the thickness range between 4 and 11 ML, a second phase with a relaxed fcc structure is found, in which one observes a non-ferromagnetic behavior of the inner film layers and ferromagnetism at the surface [22–25]. For thicknesses above ≈ 11 ML appears a third phase, a ferromagnetic (011) oriented bcc phase [26–28]. Fe films grown on Co/Cu(001) exhibit a very similar sequence of structural and magnetic phases [39–44]. The main difference with respect to Fe/Cu(001) concerns the direction of the easy magnetic axis in phases I and II, which is out-of-plane in the case of Fe/Cu(001) [29–32], and in-plane for Fe/Co/Cu(001). As for the presence of the ferromagnetic surface layer in the second phase, controversial experimental evidence has been reported. While from oxygen adsorption [41,42] and XMCD experiments [39,40] it has been concluded that the surface is not ferromagnetic, other XMCD measurements [43] as well as measurements of photoelectron diffraction in magnetic dichroism [45] and spin-resolved valence band photoemission [46] provided evidence for the presence of a ferromagnetic surface layer on top of

non-ferromagnetic underlayers. Our own previous PEEM–XMCD microspectroscopy experiments of Fe/Co/Cu(001) gave a spin moment of ≈ 0.7 μ_B in the second phase, which also supports the conclusion of a ferromagnetic Fe surface [44].

In Fe/$Ni_{81}Fe_{19}$ multilayers, it has been observed that non-ferromagnetic fcc Fe layers similar to the ones that exist in the second phase of Fe/Cu(001) or Fe/Co/Cu(001) can give rise to an antiferromagnetic coupling between the $Ni_{81}Fe_{19}$ layers at certain Fe layer thicknesses [47]. Using the magneto-optic Kerr effect, Escorcia-Aparicio et al. found that Co/Fe/ Co/Cu(001) films could not be saturated around 8 Å Fe film thickness in 1.9 kOe magnetic fields, which is a hint towards antiferromagnetic coupling of the two Co layers [41,42]. Except for Refs. [41,42] no other reports concerning antiferromagnetic interlayer coupling across fcc Fe films on Cu(001) substrates came to our knowledge. In this contribution, we study Ni/Fe/Co trilayers, in which the Ni and Fe layers are deposited as crossed wedges. This allows the imaging of the dependence of the magnetic properties on the thickness of both Ni and Fe layers. The use of Ni instead of Co as the top magnetic layer has the advantage that the magnetic signal of each layer, Co, Fe, and Ni, can be determined separately by virtue of the element-selectivity of XMCD, allowing the layer resolved characterization of the entire system. By imaging the onset of the Ni wedge, it is possible to compare the uncovered Fe/Co film with the Ni/Fe/Co trilayer. We find, indeed, that in the Ni/Fe/Co trilayers, antiferromagnetic coupling of the Ni and Co layers across the non-ferromagnetic Fe occurs at an Fe layer thickness of about 5.5 ML. In the Fe/Co bilayers, on the other hand, no indication for antiferromagnetic alignment between the Co magnetic layer and the Fe surface layer could be observed.

2. Experimental

The experiments were performed at room temperature in an ultrahigh vacuum chamber (base pressure 1×10^{-8} Pa in the sample preparation chamber, and 2×10^{-8} Pa in the PEEM chamber) equipped with standard facilities for sample preparation and surface characterization. Co, Ni, and Fe films were evapo-

rated at room temperature by electron bombardment of high purity rods. Deposition rates were about 0.4 ML/min for Co and Ni, and 0.6 ML/min for Fe. The evaporation rates were calibrated before preparation of the wedges for continuous films evaporated under identical conditions by means of the oscillations in medium energy electron diffraction intensity recorded during the growth. The accuracy of the film thicknesses cited here is estimated as 10%. The wedge-shaped films were prepared by placing an aperture of 2×0.5 mm^2 in front of the sample, with a distance to the sample surface of 1 mm. During deposition, the sample was rocked by $\pm 7.5°$ about the long axis of the aperture, which was set at a 90° different sample azimuth for Fe and Ni deposition. The total evaporation time corresponded to 6 ML for Co and Ni, and 14 ML for Fe. This results in four 255×255 μm^2 regions of crossed wedges with slopes of 0.055 and 0.023 ML/μm for Fe and Ni, respectively. A sketch of the crossed wedges is shown in Fig. 1. The circle highlights the approximate region in which the measurements were carried out. The samples were magnetized after the deposition of the continuous Co film by a field of 500 Oe along the [110] direction of the Cu substrate, and again immediately before the measurements in the photoemission microscope by a pulsed field of 310 Oe.

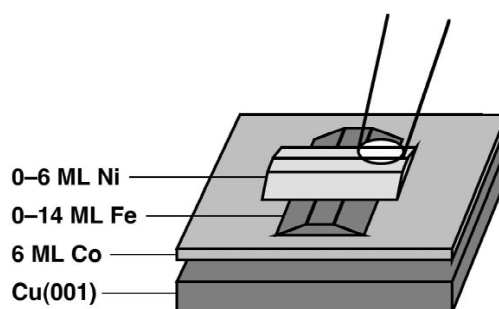Synchrotron radiation from the twin helical undulator beamline for soft X-ray spectroscopy

Fig. 1. Sketch of the sample. The wedge-shaped Fe and Ni films were prepared by evaporation through apertures of 2×0.5 mm^2 placed 1 mm in front of the sample, and rocking the sample about the long axis of the aperture. The circle highlights one of the four areas of crossed Ni–Fe double wedges in which the measurements were carried out.

BL25SU of SPring-8 in Japan was used. Circularly polarized light emitted in the first harmonic from one of two undulators is monochromatized by a varied spacing plane grating monochromator [48]. After having set the two undulators to opposite helicity, helicity reversal was realized by closing one undulator and fully opening the other, which took about 10 min. The degree of circular polarization is $> 98\%$. The light was incident to the sample under a grazing angle of 30° from the surface, with an azimuthal angle of 18° to the [110] axis of the Cu substrate. The entrance and exit slits of the monochromator were set to 290 μm for the measurements presented here. Since the light spot on the sample is an image of the exit slit, the local energy resolution at a certain spot on the sample does not depend on the slit size. It is estimated to be better than 150 meV, so that the spectra can be regarded as representing mainly the intrinsic lineshape of the Fe $L_{2,3}$ absorption edges. All images were normalized to the electron current measured at the last optical element, a gold-coated refocusing mirror. In order to minimize deviations in the ratio between the integral photon flux measured in that way and the local flux density in the imaged area, apertures behind the exit slit of the monochromator were adjusted to reduce the excess illuminated area at the sample surface outside the field of view of the microscope

The set-up of the photoemission microscope (Focus IS-PEEM; FOCUS GmbH, Hünstetten, Germany) is identical to that described in previous publications [17–19]. In short, it consists of a three-lens electrostatic straight optical axis microscope with an integral sample stage and a variable contrast aperture. To obtain a large field of view, a low extraction voltage of about 200 V was used. This results in a lateral resolution of about 1 μm and a field of view of about 380 μm. The magnified image is intensified by a two-stage microchannel plate, and converted into visible light by means of a scintillator crystal. The image is then computer-recorded with 12-bit resolution by a Peltier-cooled camera (PCO SensiCam; PCO Computer Optics GmbH, Kelheim, Germany). An 8×8 binning of camera pixels was used for the images presented here. One pixel then corresponded to 3×3 μm^2 of the sample surface. To reduce the amount of data, the region of interest was limited to a rectangle of 100×76 pixels, or $300 \times$

228 μm^2. The exposure time per image was 10 s. A total of 121 images for each helicity were recorded as a function of photon energy in the interval between 701 and 728 eV. The helicity was reversed only once after completion of a full energy scan. The total acquisition time was about 1 h 15 min, which included the moving time of the monochromator for wavelength scanning and the time needed to reverse the helicity.

3. Data analysis

For the computerized automatic sum-rule analysis of all of the 7600 XMCD spectra, a template spectrum fit similar to that described in more detail in Ref. [49] was used. Before fitting the single pixel data, a correction concerning deviations between the local photon flux at the position of each pixel and the integral photon flux from the mirror current caused by the angular distribution of the intensity in the undulator radiation had to be performed. After normalizing all images to the mirror current, images taken with light from the downstream undulator, which was set to deliver light of positive helicity, were scaled down by a factor that depended linearly on energy. This energy dependent correction factor was determined from fitting a straight line to the ratio of two absorption spectra for opposite helicity after normalization, thereby excluding the peak regions from the fit in which the dichroism occurs. This was done separately for all pixels in the image. The correction determined in that way did not exceed 5%. The spectra were then normalized to unity edge jump by adjusting the intensity axes of the spectra to zero in the pre-edge region, and to one in the post-edge region.

A template XMCD spectrum for the fits was obtained from summing up the spectra of 5644 pixels over the full range of the Fe wedge for Ni thicknesses from 0 to 3.5 ML. The sum-rule analysis of the template curve was done as in Refs. [50,51], thereby following the procedure described in Refs. [2,3]. In particular, a background consisting of two step functions of 0.5 eV width and relative statistical heights of 2/3 and 1/3 at the positions of the L_3 and L_2 absorption maxima, respectively, was subtracted from the spectra in order to obtain the white line

intensity. We assumed that the resulting integral of the helicity-averaged absorption spectra corresponded to 3.34 Fe 3d holes [7]. The difference between the absorption spectra for opposite light helicity were corrected for the angle of incidence with respect to the [110] magnetization direction, and for the degree of light polarization, which was taken as 98%. Evaluating the Fe spin and orbital magnetic moments by applying the sum rules [5,6] to the integral of the difference spectrum of measurements with opposite helicity, and normalizing to the white line intensity gives then an effective spin magnetic moment of the template spectrum $\mu_{S,eff} = (1.09\pm0.06)$ μ_B and an orbital magnetic moment $\mu_L = (0.28\pm0.06)$ μ_B. The effective spin magnetic moment is the quantity that is obtained from the application of the spin sum rule [6], and includes besides the spin magnetic moment μ_S also a contribution from the magnetic dipole term $\frac{7}{2}T_z$. The latter is zero in the bulk of cubic crystals, but can be of the same magnitude as the orbital moment in ultrathin films [52–56]. The above values represent a spatial average over the imaged area of the Ni/Fe double wedge, weighted by the local intensity. The errors quoted here represent the accuracy of the data. An additional systematic error that can be up to 20% may be present due to the details of background subtraction, the number of 3d holes, saturation effects [15,57–59], the degree of circular polarization, or the overlap between $2p_{3/2}$ and $2p_{1/2}$ final states [11].

We have to consider that the energy scans presented here were taken only up to an energy of 728 eV in order to keep data acquisition times short, and to avoid contamination of the surface. Part of the tail of the L_2 dichroism at higher photon energies is therefore not included in the analysis. This leads to systematic deviations of the magnetic moments as determined by the sum-rules, predominantly of the orbital moment. A cut-off in the integration on the high energy side of the spectra leads to a higher apparent orbital moment [60]. To quantify this effect we have re-analyzed the bulk Fe data of Ref. [2] after cutting off the high photon energy tail at 728 eV in the same way we analyzed our own data, in particular, after applying the local flux correction procedure described above. From that we obtained an orbital moment which is a factor of 2.6±0.2

higher, whereas the effective spin moment is affected by less than 5%. To account for that, we corrected our orbital moments' values by a factor of 1/2.6. The template curve orbital moment is thus $\mu_L = (0.11\pm0.02)$ μ_B. The reason for the stronger correction of the orbital moment is that the small missing dichroism signal from the high energy tail has a relatively higher influence on the smaller orbital moment, which is calculated from the difference of the L_3 and L_2 dichroism, than on the larger spin moment, where they are summed. As will be seen in Section 5, the corrected values of the Fe orbital moments are in reasonable agreement with values from literature, whereas without the correction the quantitative agreement would be lacking.

The pixel-by-pixel analysis could be done afterwards by fitting that template difference curve separately to all of the single pixel difference curves. Only two parameters were used for that, which describe the individual scaling of the difference curve in the L_3 and L_2 regions. The white line intensity was assumed to be proportional to the helicity averaged L_3 peak height. Only a smooth spatial variation of the white line intensity of less than 20% was present in the spectra over the full imaged area. Sum-rule analysis of the single pixel data is obtained from the two fit parameters, based on the analysis of the template spectra. The two degrees of freedom of the fit to the template curve are thus easily converted into numbers for the Fe spin and orbital moment for every pixel in the image. By using only two-fit parameters connected to the dichroism intensity at the L_3 and L_2 edge, the fit procedure is very stable, which is a prerequisite for obtaining meaningful information from noisy or scattered single pixel data. This analysis is valid if the shape of the absorption spectra does not change over the imaged area. This was checked to be the case for the Fe spectra presented here.

To illustrate the template fit procedure, three typical single pixel XMCD spectra from 3×3 μm^2 areas of the sample surface are shown in Fig. 2. The pixels denoted (a), (b), and (c) correspond to Fe thicknesses of ≈ 2, 5, and 10 ML, respectively, capped by ≈ 1.2 ML Ni. These pixels have been chosen to show strongly different Fe magnetic moments; the Fe thickness of (a) corresponds to phase I, that of (b) to phase II, and that of (c) to the
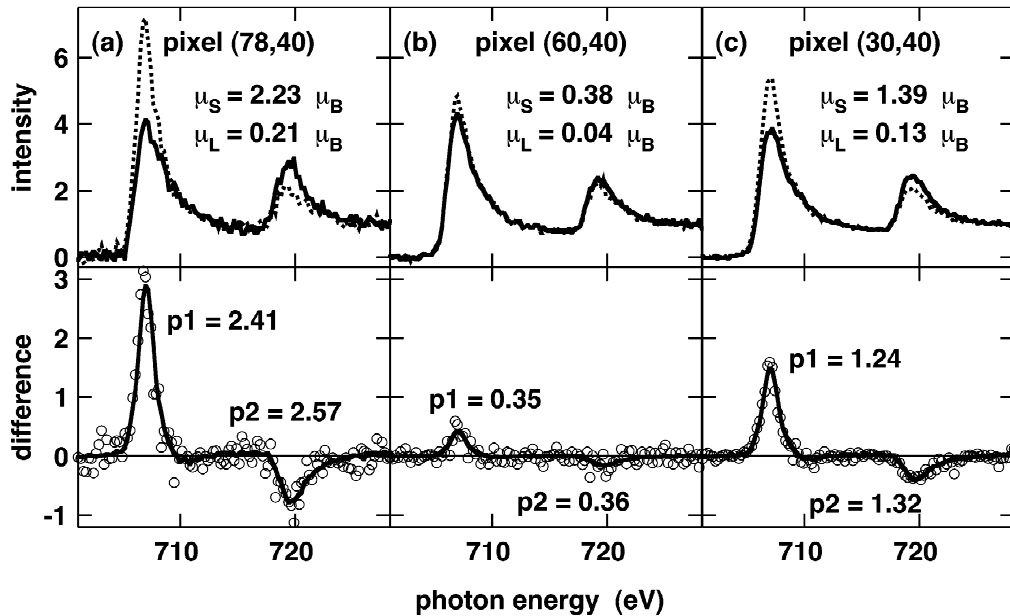
Fig. 2. Single pixel XMCD spectra from three different 3×3 μm^2 spots on the sample surface. (a) Data of pixel (78,40) ($x - y$ coordinates (234, 120 μm), ≈ 2 ML Fe thickness), (b) data of pixel (60,40) ($x - y$ coordinates (180, 120 μm), ≈ 5 ML Fe thickness), (c) data of pixel (30,40) ($x - y$ coordinates (90, 120 μm), ≈ 10 ML Fe thickness). Top: single pixel absorption spectra for positive (dotted lines) and negative helicity (solid lines). Bottom: corresponding difference curves (solid symbols) and fit using a template difference spectrum (lines), scaled by the fit parameter p_1 (p_2) at the L_3 (L_2) edge, as indicated, in order to fit the respective single-pixel difference curves. The results of the fits in terms of spin and orbital moments are given in the top panel. Note the different vertical scale in the top and bottom panels.

transition region between phases II and III. In the top panel, the absorption spectra of each of the three pixels for positive and negative helicity are reproduced as dotted and solid lines, respectively. The corresponding dichroism curves are shown underneath as the difference between these two curves (solid symbols). The lines in the difference spectra represent the template difference spectrum, scaled by the fit parameters $p1$ at the L_3 edge, and $p2$ at the L_2 edge to fit the respective single pixel difference data. The results of the fits for these pixels in terms of spin and orbital moments are given in the top panel. Note how the noise, as seen from the scatter in the difference data, is reduced for thicker Fe films.

4. Results

The result of the pixel-by-pixel sum-rule analysis for the Fe effective spin moment $\mu_{S,eff}$ is presented

in Fig. 3a. Different levels of gray correspond to different values of $\mu_{S,eff}$, as explained in the legend on the left hand side. The Fe and Ni thicknesses of the crossed double wedge are given at the top and right axes, respectively. The behavior of the Fe spin moment in the crossed double wedge is dominated by a strong dependence on the Fe film thickness. Three different regions labeled I, II, and III in Fig. 3 at approximately 0–3.5 ML, 3.5–11 ML, and > 11 ML Fe thickness are clearly recognized by their different moments. They can be correlated to the three different magnetic phases of Fe, as outlined in Section 1. A black stripe indicating a strongly reduced Fe spin moment is recognized around 5.5 ML Fe thickness and Ni coverages of more than 1.5 ML. Another effect of the Ni cap layer seems to be a small shift of the transition from phase I to phase II towards lower Fe thicknesses starting just at the onset of the Ni wedge. The reduced moment in the upper right corner at Fe thicknesses below 2 ML, in
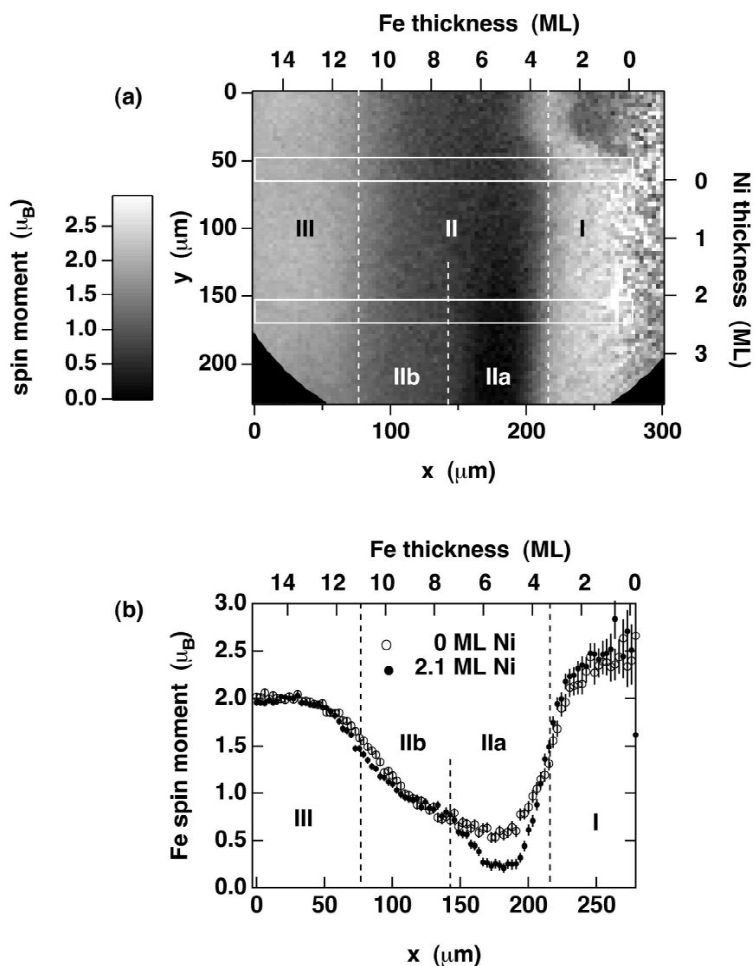
Fig. 3. (a) Result of the pixel-by-pixel sum-rule analysis for the Fe effective spin moment $\mu_{S,eff}$. Different levels of gray correspond to different values of $\mu_{S,eff}$, as explained in the legend. The thickness of the Fe wedge increases from right to left, the thickness of the Ni wedge from top to bottom, as indicated at the top and right axes. Regions with different values of $\mu_{S,eff}$ are separated by dashed vertical lines and labeled I through III, IIa, IIb. The white rectangles indicate the positions at which linescans are presented in panel (b). (b) Horizontal linescans of $\mu_{S,eff}$ of the uncovered Fe/6 ML Co/Cu(001) layer (open symbols) and of ≈ 2.1 ML Ni/Fe/6 ML Co/Cu(001) (solid symbols) at the positions indicated in panel (a). The linescans result from a seven-pixel vertical average across the width of the rectangles shown in (a).

contrast, is due to a domain in the Fe/Co film with a different component of magnetization in the detection direction, as will be seen from the Co asymmetry image.

Fig. 3b shows horizontal linescans of the Fe effective spin moment for the uncovered Fe/Co/Cu(001) layer (open symbols) and centered around 2.1 ML Ni/Fe/Co/Cu(001) (solid symbols), averaged over seven vertical pixels. The linescans are done in the regions indicated in Fig. 3a by white rectangles (solid lines). In phase I for Fe thicknesses below 2 ML moments of 2.5 μ_B are observed for both films with and without Ni overlayer. Between 2 and 3 ML, already a certain reduction of the spin

moment to ≈ 2.2 μ_B is present. Between 3 and 4.5 ML the moments drop strongly. Values of 0.7 μ_B are reached without a Ni cap layer between 4.5 and 8 ML (phase II). The main difference between the linescan of the uncapped Fe/Co film and the Ni/Fe/ Co film is observed around 5.5 ML Fe thickness, which we will call phase IIa in the following. Underneath the Ni layer, a value of only 0.25 μ_B is found in that region, compared to 0.7 μ_B in the uncapped Fe film. The latter value is the same as that encountered in Ni/Fe/Co for slightly higher Fe thicknesses between 6 and 8 ML (phase IIb). For thicker Fe films, the moments eventually increase to reach a value of 2.0 μ_B in phase III at around 12 ML Fe thickness.

To see the coupling behavior between the Co and Ni layers across the Fe film, images at the Co and Ni L_3 peak maximum as well as for 6-eV lower photon energy were acquired for both helicities, and normalized to the integral photon flux. From that the asymmetry of the L_3 peak heights for opposite helicity $I(\sigma_+)$ and $I(\sigma_-)$ is formed as $(I(\sigma_+) - I(\sigma_-))/(I(\sigma_+) + I(\sigma_-))$. $I(\sigma_+)$ and $I(\sigma_-)$ are thereby calculated from the difference between peak and pre-edge intensities. The resulting asymmetries at the Co and Ni edges are shown in Fig. 4. The Co layer (Fig. 4a) shows a uniform magnetization over nearly the entire range of the image. Towards higher Fe thicknesses a higher noise and maybe also a slight increase of the Co asymmetry are observed. The latter, however, could be an artifact introduced by the increasing influence of Fe absorption background at the energy of the Co L_3 absorption. Microspectroscopy measurements of Co $L_{2,3}$ absorption spectra at a different position of the same film, where the same asymmetry was found, gave a Co effective spin moment of 1.6 μ_B, and an orbital moment of 0.13 μ_B. We conclude from the similarity to the Co bulk magnetic moment that the Co film over most of the imaged area is in a saturated single domain state with the magnetization along [110]. Only in the upper right corner is a reduced asymmetry of roughly 1/2 compared to the rest of the image observed. Here the Co film is obviously not saturated. This is reflected also in the plot of the Fe spin moment (Fig. 3a), as already mentioned. It can be explained by a domain with a different magnetization direction, for example along [010], which means a projection onto the light propagation direction of $\cos(18° + 45°)$ instead of

$\cos 18°$. The presence of very small domains that are not resolved here can also not be ruled out. In any case, a macroscopic structural peculiarity of the substrate at that position, as for example locally higher roughness or higher step density, is probably the cause for the lower asymmetry. We will restrict ourselves in the following on the results from the area in which the Co film is a single domain.

Fig. 4b shows the dichroic asymmetry at the Ni L_3 edge. Pay attention to the grayscale, which is symmetric around zero in contrast to Fig. 4a. A negative Ni L_3 asymmetry of -0.09 is present around 5.5 ML Fe thickness and >3 ML Ni thickness, whereas the rest of the Ni film shows an almost constant positive value of $+0.09$. Bright contrast consequently indicates a magnetization direction parallel to that of the Co magnetization, dark contrast a magnetization direction opposite to that of the Co magnetization. Comparison of Figs. 4b and 3a reveals that the region of reversed Ni magnetization coincides exactly with the region in which the low Fe spin moment (phase IIa) is observed. Clearly no differences are seen in the Co asymmetry at that position. Altogether, antiparallel alignment of the Ni and Co magnetization is found around 5.5 ML Fe thickness in Ni/Fe/Co/Cu(001), which is correlated with an additional reduction of the apparent Fe spin moment.

The orbital moment μ_L is the second quantity that can be extracted from the pixel-by-pixel sum-rule analysis. It is found that the general behavior of μ_L is quite similar to that of the effective spin moment $\mu_{S,eff}$. It is therefore more interesting to see the behavior of the ratio of μ_L and $\mu_{S,eff}$. This is presented in Fig. 5a in a grayscale plot of the same sample area as before. Especially in the regions of low magnetic moment, the noise in $\mu_L/\mu_{S,eff}$ is rather high. In Fig. 5b linescans of the ratio of orbital to spin moment as a function of Fe thickness for 0 and 2.1 ML Ni overlayer are shown, obtained at the same positions in an identical way as the linescans shown in Fig. 3b (white rectangles in Fig. 5a). The values for $\mu_L/\mu_{S,eff}$ are mostly between 0.05 and 0.10 for both Fe/Co/Cu(001) and ≈ 2.1 ML Ni/Fe/ Co/Cu(001). Between 4 and 7 ML Fe, the statistical error is too high to state a clear trend, especially when there is Ni on top of the film. A decrease of the orbital moment when reducing the Fe thickness below 2 ML is seen from Fig. 5b. Though not so
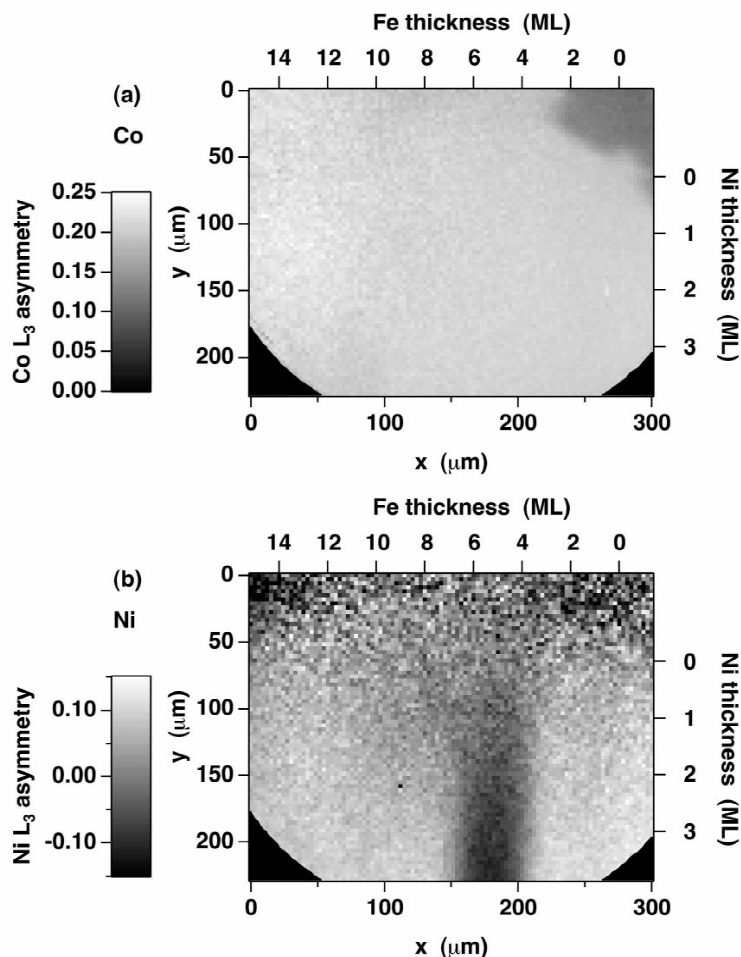
Fig. 4. (a) Co L_3 absorption asymmetry image of the difference between peak and pre-edge intensities for opposite helicities. Different levels of gray correspond to different values of the asymmetry, as explained in the legend. The imaged area is the same as in Fig. 3a. (b) Ni L_3 absorption asymmetry image. Different levels of gray correspond to different values of the asymmetry, as explained in the legend. Note that here, in contrast to panel (a), the grayscale is symmetric around zero. Around the x coordinate 180 μm, the Ni magnetization is antiparallel to the Co magnetization.

significant, another reduction of $\mu_L/\mu_{S,\text{eff}}$ may be present for increasing the Fe film thickness above 10 ML.

5. Discussion

The Fe effective spin magnetic moments observed here for uncovered Fe/Co/Cu(001) agree qualita-

tively well with those found by Schmitz et al. (3.0 μ_B in phase I, 1.1 μ_B in phase II) [43], although our values are systematically lower. The value of 0.7 μ_B at 8 ML Fe thickness (region II) contrasts the result of Refs. [39,40], where a drop in the dichroism by a factor of about ten between phase I and phase II was observed. The spin moment of 0.7 μ_B has to be interpreted as the depth-weighted average of all Fe layers. We assume here a probing depth of 17 Å [59]
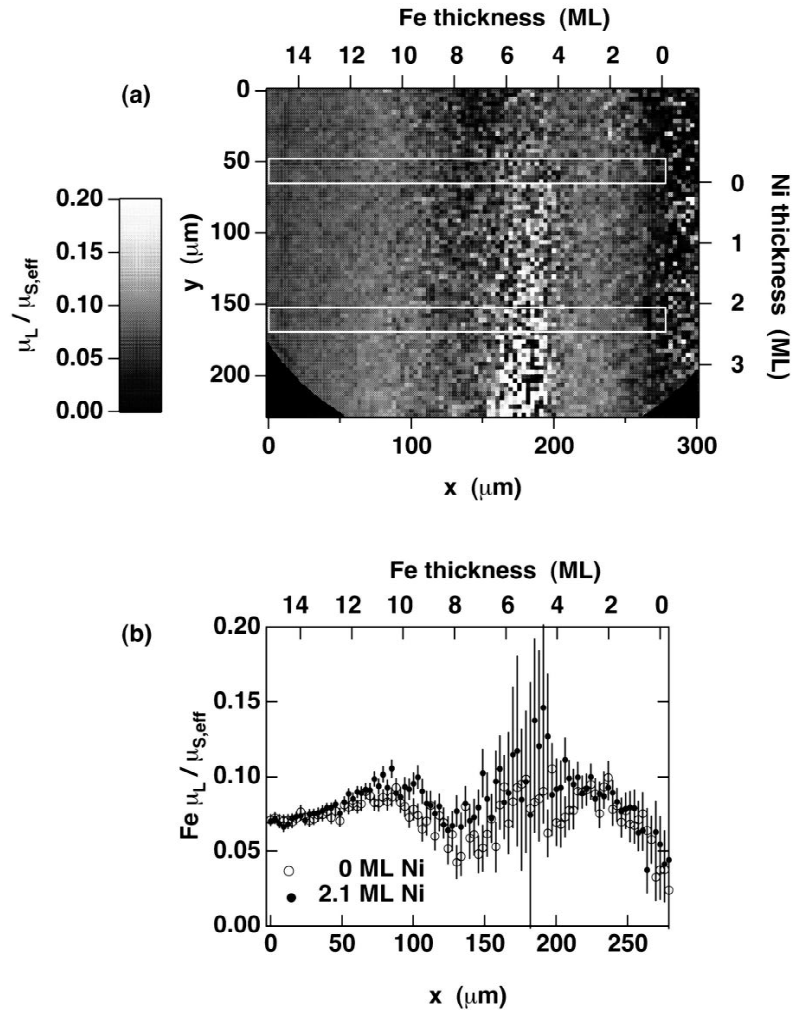
Fig. 5. (a) Result of the pixel-by-pixel sum-rule analysis for the ratio of Fe orbital to effective spin moment $\mu_L/\mu_{S,eff}$. Different levels of gray correspond to different values of $\mu_L/\mu_{S,eff}$, as explained in the legend. The white rectangles indicate the positions at which linescans are presented in panel (b). (b) Horizontal linescans of $\mu_L/\mu_{S,eff}$ of the uncovered Fe/6 ML Co/Cu(001) layer (open symbols) and of ≈ 2.1 ML Ni/Fe/6 ML Co/Cu(001) (solid symbols) at the positions indicated in panel (a). The linescans result from a seven-pixel vertical average across the width of the rectangles shown in (a).

in which the secondary electron signal is reduced by a factor of $1/e$, and an average Fe layer spacing of 1.77 Å [22,23]. A value of 0.7 μ_B would then be consistent with, for example, 2 ML ferromagnetic Fe (2.2 μ_B) on top of 6 ML non-ferromagnetic Fe, or with 1 ML ferromagnetic Fe at the surface, 5 ML non-ferromagnetic Fe in the interior, and 2 ML ferromagnetic Fe at the Fe–Co interface. Our result thus supports the conclusion from photoelectron diffraction in magnetic dichroism of 8 ML Fe/Co/Cu(001) [45] and spin-resolved valence band photo-emission [46] that ferromagnetism is present at the

surface of Fe/Co/Cu(001). It has to be noted though that a constant amount of ferromagnetic Fe at both interfaces plus non-ferromagnetic Fe in between would lead to a decreasing apparent magnetic moment with increasing Fe film thickness. This is obviously not what we observe here (cf. Fig. 3b). The situation is therefore probably more complicated. There exist several theoretical studies about the magnetic structure of fcc Fe on Cu(001) [61–68] or on Co(001) [69] which result in a layered antiferromagnetic arrangement of either monoatomic or biatomic Fe layers of different moments. The actual magnetic configuration depends sensitively on the Fe film thickness. In a real system consequently the influence of surface and interface roughness can not be neglected, and the magnetic structure of the Fe films in phase II is probably not just described in terms of magnetic and non-magnetic Fe layers. We will come back to that point later when we discuss the coupling behavior across the Fe films in phase II.

The value of 2.0 μ_B for the spin moment of bcc Fe is slightly lower than the expected Fe bulk moment of 2.2 μ_B [70], but it agrees well with XMCD measurements of thicker bcc Fe films [2]. Hunter Dunn et al. obtained values of 3.4 and 2.25 μ_B for Fe/Cu(001) in region I and III, respectively, using XMCD [14]. We believe that the discrepancy between our values of Fe/Co/Cu(001) and their values for Fe/Cu(001) could be again mainly explained by systematic errors in the sum-rule analysis, and may not be significant enough to conclude a different magnetic behavior of Fe related to the presence of the Co layer. In Ref. [43], in contrast, the Fe spin moment was even found to be about 0.2–0.3 μ_B lower in Fe/Cu(001) compared to Fe/Co/Cu(001).

An important issue for measurements of the absorption by total or partial electron yield is saturation effects [15,57–59]. Saturation effects arise when the penetration depth of the X-rays in the film for a given angle of incidence becomes comparable to the electron escape depth. They can be especially serious for Fe because of the high absorption at the Fe L_3 edge. The X-ray penetration depth, which is several thousands of Å below the Fe $L_{2,3}$ edge, is reduced to the order of only 100 Å at the L_3 absorption maximum [59]. These effects can normally only be accounted for if a series of measurements for varying angle of incidence is performed. Nakajima et al.

extracted quantitative information from comparison of absorption measurements carried out in transmission, and absorption measurements using the total electron yield [59]. From the information given in Ref. [59] we can judge the influence of saturation effects on the present measurements. Whereas for very thin Fe films no saturation effects occur, at 14 ML Fe they can result in an underestimation of the effective spin moment of about 8%, and of the orbital moment of up to 50%. Thus in Fig. 6, a tentative correction of the linescan data of Fig. 5b is shown, where the correction factor varied linearly from one at 0 ML Fe to two at 14 ML Fe. The most prominent difference with respect to Fig. 5b is consequently seen at Fe thicknesses above 8 ML. Considering the error bars in Figs. 5b and 6, the numbers derived here for the ratio of orbital to spin moment are in agreement with those of Ref. [43] for Fe/Co/Cu(001) (0.06 and 0.07 in phases I and II, respectively), and with those of Ref. [14] for Fe/Cu(001) (0.07 in phases I and III). In thicker Fe films, however, a value of only 0.043 has been measured in transmission [2].

A somewhat surprising result is the decreasing trend of the orbital moment for the very thin Fe
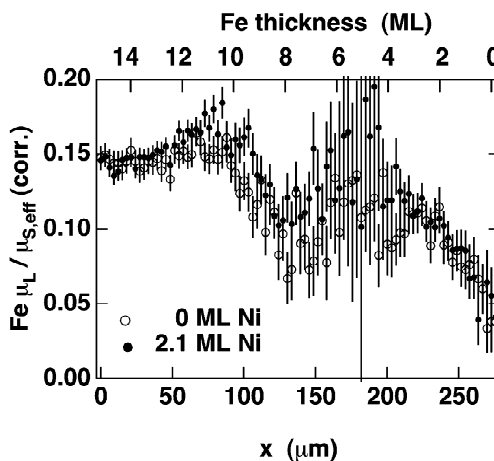

Fig. 6. Horizontal linescans of Fe $\mu_L/\mu_{S,eff}$ of the uncovered Fe/6 ML Co/Cu(001) layer (open symbols) and of ≈ 2.1 ML Ni/Fe/6 ML Co/Cu(001) (solid symbols) like in Fig. 5b, corrected for saturation effects. A factor that varied linearly in Fe thickness from one at 0 ML Fe to two at 14 ML Fe was assumed for the correction.

films. Usually it is assumed that a reduction of atomic coordination and dimensionality in the sub-monolayer thickness range leads to an increasing orbital contribution to the magnetic moment [71,72]. Such a tendency has been observed experimentally for decreasing thickness of Co films on Cu(001) [73] and Fe atomic monolayers in $L1_0$ FeCu layered compounds [50,51]. The answer for the opposite thickness behavior of the Fe orbital moment in Fe/Co/Cu(001) may be found in the details of the hybridization between Fe and Co electronic states. Theoretical calculations could help to check for such an influence of the Co underlayer on the Fe orbital moment. Another point that should be considered in the discussion of orbital moments is the connection to magnetic anisotropy. In a simple perturbation model the anisotropy of the orbital moment is linked to the magnetocrystalline anisotropy [74]. This leads to higher orbital moments in samples magnetized along the preferred magnetization axis compared to a magnetization direction along a hard axis [49,52,53,75–78]. For increased strength of the anisotropy, the orbital moment difference between measurements with saturation along the easy and hard axes is increased in a way that the hard axis orbital moment is reduced, and the easy axis orbital moment enhanced [52,53,78].

Fe films on Cu(001) show a perpendicular aniso-tropy in the thickness range 0–11 ML [29–32]. From the structural similarity of Fe/Cu(001) and Fe/Co/Cu(001) [39–42] it would be plausible that the intrinsic spin–orbit-derived anisotropy of Fe in Fe/Co/Cu(001) is also perpendicular, and that it is the in-plane anisotropy contribution of the Co layer that forces the Fe/Co bilayer magnetization into the film plane. A higher perpendicular magnetocrystalline anisotropy of the thinner Fe film would thus be correlated with a lower orbital moment, measured in the in-plane magnetized Fe/Co film. This could be a reason for the observed reduction of the Fe orbital moment at very low Fe thicknesses (cf. Fig. 6). Following Ref. [74] there should be a linear relation-ship between the magnetocrystalline anisotropy and the orbital moment difference, with the propor-tionality constant being the spin–orbit coupling parameter times a prefactor that depends on the band structure. This factor should be between 2.5 and 5 meV/μ_B for 3d transition metals [52,53]. Experimen-

tally, for Co/Au a factor as low as 0.8 meV/μ_B was found [78], whereas a factor of roughly 4 meV/μ_B could explain observations made in Ni films [49]. The thickness dependence of the magnetocrystalline anisotropy of Fe/Cu(001) follows approximately a 240 μeV/t + const. behavior [31,32], where t is the Fe thickness in ML. This converts into an estimate of the expected Fe orbital moment anisotropy of rough-ly 0.05 μ_B /t + const., or $0.02\mu_{S,eff}$ /t + const., with $\mu_{S,eff} = 2.5$ μ_B. The observed reduction of the orbital moment at low Fe thicknesses is thus of the same order of magnitude as the expected influence of the magnetocrystalline anisotropy. The enhancement at Fe thicknesses above 10 ML could be analogously explained by the lower perpendicular anisotropy in phase III [32].

We now turn our attention to the antiferromagnetic alignment of the Ni layer with respect to the Co layer around 5.5 ML Fe thickness (Fig. 4), and its influence on the Fe spin moment (Fig. 3). If we assume ferromagnetic Fe layers at both interfaces, then these layers would experience a strong direct ferromagnetic coupling to the respective neighboring magnetic layers (Co or Ni). In the case of anti-ferromagnetic alignment of Co and Ni, the Fe layers at both interfaces should consequently be aligned oppositely to each other. This leads to a lower apparent moment compared to a ferromagnetic align-ment. The small positive net Fe moment seen experimentally in that case (≈ 0.25 μ_B) could thus be due to the (incomplete) cancellation of these interface contributions. As a model, a 5 ML Fe film composed of two ferromagnetic layers at the Fe–Co interface, two non-ferromagnetic layers above, and one oppositely magnetized atomic layer at the Ni–Fe interface will provide about 0.2 μ_B when measured by XMCD. This is close to the experimental value. It could, however, also be explained by a model in which just the interface layer at the Co–Fe interface contributes to ferromagnetism.

The question remains why a higher moment is observed in the uncovered Fe/Co film around 5.5 ML Fe thickness. One could think of relating this to ferromagnetic contributions from Fe interface layers from both interfaces as in the case of Ni/Fe/Co, but this time aligned parallel. Quantitatively, however, this does not give exactly the experimental observa-tion. Assuming the same model as before but with a

parallel alignment of all contributing layers (i.e., one Fe layer at the Fe–Ni interface and two Fe layers at the Co–Fe interface being ferromagnetic with the magnetization pointing all in the same direction) a value of 1.3 μ_B is expected by XMCD. This is about a factor of two higher than what is observed. The reason for the different Fe moment with and without the Ni overlayer can thus not just be the presence and absence of antiferromagnetic alignment of magnetic Fe interface layers within the Fe film. As mentioned before, the very simple model where we assume ferromagnetic and non-ferromagnetic layers does not adequately describe the thickness dependence of the Fe spin moment in phase II. Although the value of 0.7 μ_B at 8 ML is a clear hint for a ferromagnetic surface layer magnetically aligned with the Co film, a much higher value would be expected at 5 ML, where the contribution of the non-ferromagnetic layers is relatively decreased. It is thus feasible that there is a partial antiferromagnetic alignment of the Fe surface with respect to the Co at the uncapped 5 ML Fe/Co film. The experimental observations could be explained as the result of the influence of interface roughness and magnetic frustrations with and without Ni overlayer. A more realistic model with layerwise or bilayerwise antiferromagnetism will have to be taken into account. There is also the possibility that without Ni a 90° orientation of the magnetization of the Fe surface layer around 5 ML Fe thickness is present after the application of the external field, similar to the 'spin-flop' state in antiferromagnets. One has also to consider the presence of non-collinear moments induced by frustrations at step edges, as proposed by Lorenz and Hafner [66], which might further complicate the interpretation, or the existence of a non-collinear spin-spiral phase in the Fe layer [67,68].

In (001)-oriented Fe/$Ni_{81}Fe_{19}$ multilayers, antiferromagnetic coupling between the $Ni_{81}Fe_{19}$ layers has been observed around 9 Å Fe layer thickness [47]. This Fe layer thickness coincides quite well with the thickness of 5.5 ML, at which we observe the antiferromagnetic coupling between the Ni and Co films. Escorcia-Aparicio et al. concluded from a magneto-optical Kerr-effect study of Co/Fe/Co/Cu(001) that antiferromagnetic coupling between the two Co layers is present in the entire thickness range of phase II, namely from 7.4 to 16.4 Å [41,42]. They

distinguished between 'weak' and 'strong' antiferromagnetic coupling. Whereas split hysteresis loops were observed in the former regime, no saturation was possible in fields up to 1.9 kOe in the latter regime [41,42]. 'Strong' antiferromagnetism was found around 7 Å Fe thickness. This corresponds to slightly less than 4 ML, and is thus somewhat lower than the value we find in the Ni/Fe/Co trilayers. We nevertheless think that it is the same underlying mechanism that is responsible for both. Having Ni instead of Co as one of the sandwiching layers could account for the difference in Fe film thickness for the antiferromagnetic interlayer coupling.

In contrast to Refs. [41,42] we do not observe antiferromagnetic coupling other than around 5.5 ML Fe thickness. In studies of interlayer exchange coupling [79] it was never observed that antiferromagnetic coupling occurred over an extended thickness range as it was claimed for the 'weak' antiferromagnetic coupling in Co/Fe/Co in Refs. [41,42]. We therefore believe that the split magnetization loops in phase II of Refs. [41,42] have other reasons. It is conceivable that the influence of step-induced uniaxial in-plane anisotropies becomes dominant in the case of small (ferromagnetic) interlayer coupling, leading to a two-step magnetization reversal process with reduced remanence. Another explanation could be a biquadratic (90°) coupling of the two Co layers caused by a higher substrate roughness than in our case. In that case, though, one would expect to observe also a region of ferromagnetic coupling, since biquadratic coupling is thought to be the consequence of competing ferromagnetic and antiferromagnetic contributions mixed by film morphology [80,81].

In Refs. [41,42] two different regions of 'strong' antiferromagnetic coupling have been observed, which could suggest some kind of oscillatory exchange coupling across the Fe layer. The second region of 'strong' antiferromagnetic coupling was found just at the Fe thicknesses where the films convert to bcc Fe (phase III), and thus was obscured by the reappearance of ferromagnetism. To test that point, the authors of Refs. [41,42] grew also a Co/Fe/Co trilayer on a deliberately contaminated Cu(001) substrate. It is known that carbon can extend the thickness range of phase II in Fe/Cu(001) [33–35]. A more pronounced region of 'strong'

antiferromagnetic coupling was then found in such films at around 18 Å Fe thickness [41,42]. In our films, we conclude from the behavior of the spin moment as a function of Fe thickness that the conversion of fcc to bcc Fe is getting significant already at 9–10 ML Fe thickness (cf. Fig. 3b). This is consistent with the observation from scanning tunnelling microscopy that small amounts of bcc precipitates in Fe/Cu(001) are present already at Fe thicknesses as low as 6 ML [27]. The complete absence of a second region of antiferromagnetic coupling in our Ni/Fe/Co films could thus just be the consequence of the occurrence of the bcc Fe phase, which gives rise to a direct strong ferromagnetic coupling between the Ni and Co layers.

Such a second region of possible antiferromagnetic coupling was indeed observed in a preliminary experiment on Ni/Fe/Co/Cu(001) that was carried out shortly after a bake-out of the chamber. Here the pressure during Fe evaporation rose to 2×10^{-7} Pa. The result is presented in Fig. 7. It shows, from left to right, the Co, Fe, and Ni L_3 asymmetry images of a crossed double wedge similar to the double wedge described above. Different shades of gray correspond to different (positive and negative) values of the asymmetry, as explained in the legend. The Fe and Ni thicknesses are given at the upper and right axes, respectively. Horizontal linescans of the asymmetry, taken at 4 ± 0.5 ML Ni thickness, are shown superimposed over the images. In the upper right corner of the images a region with incomplete or rotated magnetization can be recognized, which we ignore in the following. Comparing the Fe image of Fig. 7 to Fig. 3a, one can see that in the 'dirty' film the onset
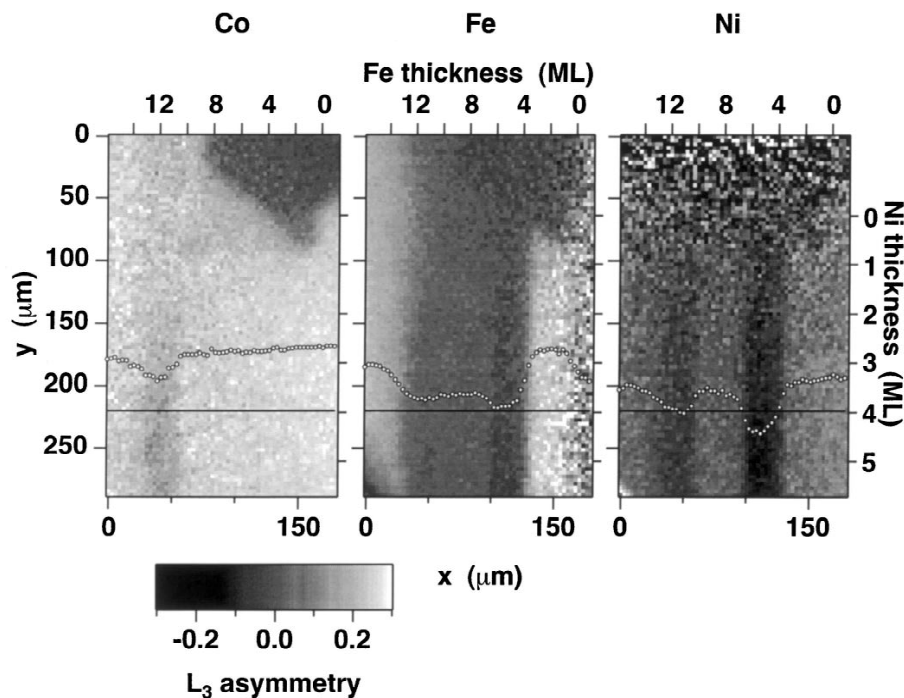
Fig. 7. Co, Fe, and Ni (from left to right) L_3 absorption asymmetry images of a crossed double wedge similar to the one shown in Figs. 3–5, but prepared under worse vacuum conditions (pressure during Fe evaporation $\approx 2 \times 10^{-7}$ Pa). Different shades of gray correspond to different (positive or negative) values of the asymmetry, as explained in the legend. The Fe and Ni thicknesses are given at the upper and right axes, respectively. Two distinct stripes of darker contrast are observed in the Fe and Ni asymmetry images at about 5 and 11 ML Fe thickness. Linescans of the asymmetry, taken at 4 ± 0.5 ML Ni thickness as 14-pixel vertical average, are shown superimposed.

of the bcc phase, characterized by the bright contrast, is located at 12–13 ML Fe thickness, about 1–2 ML higher thickness than in the clean film of Fig. 3a (11 ML). At 5.5 ML Fe, basically the same behavior as in the clean film is observed. At that Fe thickness the Ni magnetization is oriented antiparallel to the Co film, and the Fe asymmetry exhibits a distinctly lower asymmetry at the same position. The difference of the 'dirty' film with respect to the clean film is the observation of a second dark stripe in both the Fe and Ni asymmetry images at around 11 ML Fe thickness. Also in the Co image a slightly lower asymmetry is seen at that position. This second dark stripe could be a hint towards a second oscillation of antiferromagnetic interlayer coupling. The difference in thickness between the first and second region is about 6 ML (≈ 11 Å). This is the same as found between the regions of 'strong' antiferromagnetic coupling in Refs. [41,42], and also similar to the long period oscillations in most fcc transition metal systems [79]. Unlike the first dark stripe at 5.5 ML Fe thickness, however, the second stripe at 11 ML does not show negative asymmetry at the Ni L_3 edge, but just a value close to zero. This could of course be a consequence of the smaller coupling strength in the second antiferromagnetic maximum. Nevertheless, the present images do not strictly prove antiferromagnetic coupling in that region. Another explanation could, for example, be a greatly enhanced coercivity due to structural imperfections in the transition region from fcc to bcc. A non-collinear arrangement of Fe moments at that thickness, induced by an enhanced step density, could also be a possibility. On the other hand, the dark contrast in the Co image of Fig. 7 is not explained by just an enhanced coercivity in the Fe film, since the sample was already magnetized a first time after deposition of the Co layer. Altogether, we think that the present data show indications suggesting oscillatory exchange coupling through the Fe layer in the system Ni/Fe/Co/Cu(001).

6. Conclusions

We have used the combination of PEEM and XMCD spectroscopy in a study of the magnetic phases of Fe in Fe/Co/Cu(001) and Ni/Fe/Co/

Cu(001). This full-image microspectroscopic technique allows spectroscopic information to be obtained on a microscopic scale. It can be used to image element-resolved quantitative magnetic properties. Microspectroscopy of crossed double wedges greatly facilitates the magnetic characterization of layered systems, as shown in the present case.

The magnetic phases of Fe on Co/Cu(001) have been identified, and their magnetic properties (effective spin moment, orbital moment) could be determined simultaneously for any position in the double wedge. Below 4 ML Fe, a high moment ferromagnetic phase is found. The reduced net magnetic moment between 4 and ≈ 10 ML Fe thickness is due to a complicated non-ferromagnetic configuration of fcc Fe. From the size of the experimentally measured spin moment we conclude that at 7–9 ML Fe thickness, the Fe surface layer contributes to the ferromagnetic signal of the film. The antiparallel orientation of the Ni magnetization in Ni/5.5 ML Fe/Co/Cu(001) is most likely due to antiferromagnetic coupling across the Fe layer at that thickness. It is not entirely clear what happens without Ni layer at 5.5 ML Fe/Co/Cu(001). The observed net magnetization of the Fe layer at that thickness is probably also affected by antiferromagnetic coupling between the Co film and the Fe surface layer. Above ≈ 10 ML Fe thickness, the films are again ferromagnetic in both the Ni/Fe/Co and the Fe/Co systems, with a somewhat lower moment than in phase I. The Fe orbital to effective spin moment ratio does not show a distinctly different behavior in the three phases. We interpret the decrease towards small Fe thicknesses as an influence of Fe magnetocrystalline anisotropy on the orbital moment. Images taken from Ni/Fe/Co/Cu(001) trilayers prepared under enhanced residual gas supply indicate that the magnetic coupling across the phase II Fe film might be due to an oscillatory interlayer coupling. In addition to 5.5 ML Fe thickness, in these images, reduced Ni and Fe apparent moments were also observed around 11 ML Fe thickness, that is, at about 6 ML higher Fe thickness. This could be the signature of a second antiferromagnetic maximum. Detailed field-dependent studies should help to clarify the coupling behavior across fcc Fe, and to deduce quantitative information about the coupling strength.

Acknowledgements

References

[1] G. Schütz, W. Wagner, W. Wilhelm, P. Kienle, R. Zeller, R. Frahm et al., Phys. Rev. Lett. 58 (1987) 737.

[2] C.T. Chen, Y.U. Idzerda, H.-J. Lin, N.V. Smith, G. Meigs, E. Chaban et al., Phys. Rev. Lett. 75 (1995) 152.

[3] J. Stöhr, J. Electron Spectrosc. Relat. Phenom. 75 (1995) 253.

[4] J.L. Erskine, E.A. Stern, Phys. Rev. B 12 (1975) 5016.

[5] B.T. Thole, P. Carra, F. Sette, G. van der Laan, Phys. Rev. Lett. 68 (1992) 1943.

[6] P. Carra, B.T. Thole, M. Altarelli, X. Wang, Phys. Rev. Lett. 70 (1993) 694.

[7] R. Wu, A.J. Freeman, Phys. Rev. Lett. 73 (1994) 1994.

[8] W.L. O'Brien, B.P. Tonner, G.R. Harp, S.S.P. Parkin, J. Appl. Phys. 76 (1994) 6462.

[9] D. Rioux, B. Allen, H. Höchst, D. Zhao, D.L. Huber, Phys. Rev. B 56 (1997) 753.

[10] Y.U. Idzerda, C.T. Chen, H.-J. Lin, H. Tjeng, G. Meigs, Physica B 208–209 (1995) 746.

[11] Y. Teramura, A. Tanaka, T. Jo, J. Phys. Soc. Jpn. 65 (1996) 1053.

[12] J. Vogel, M. Sacchi, Phys. Rev. B 49 (1994) 3230.

[13] X. Le Cann, C. Boeglin, B. Carrière, K. Hricovini, Phys. Rev. B 54 (1996) 373.

[14] J. Hunter Dunn, D. Arvanitis, N. Mårtensson, Phys. Rev. B 54 (1996) R11157.

[15] V. Chakarian, Y.U. Idzerda, C.T. Chen, Phys. Rev. B 57 (1998) 5312.

[16] J. Stöhr, Y. Wu, M.G. Samant, B.B. Hermsmeier, G. Harp, S. Koranda et al., Science 259 (1993) 658.

[17] W. Kuch, R. Frömter, J. Gilles, D. Hartmann, Ch. Ziethen, C.M. Schneider et al., Surf. Rev. Lett. 5 (1998) 1241.

[18] W. Swiech, G.H. Fecher, Ch. Ziethen, O. Schmidt, G. Schönhense, K. Grzelakowski et al., J. Electron Spectrosc. Relat. Phenom. 84 (1997) 171.

[19] C.M. Schneider, J. Magn. Magn. Mater. 175 (1997) 160.

[20] M.T. Kief, W.F. Egelhoff Jr., Phys. Rev. B 47 (1993) 10785.

[21] K. Heinz, S. Müller, P. Bayer, Surf. Sci. 337 (1995) 215.

[22] P. Bayer, S. Müller, P. Schmailzl, K. Heinz, Phys. Rev. B 48 (1993) 17611.

[23] S. Müller, P. Bayer, A. Kinne, P. Schmailzl, K. Heinz, Surf. Sci. 322 (1995) 21.

[24] D. Li, M. Freitag, J. Pearson, Z.Q. Qiu, S.D. Bader, Phys. Rev. Lett. 72 (1994) 3112.

[25] M. Straub, R. Vollmer, J. Kirschner, Phys. Rev. B 77 (1996) 743.

[26] M. Wuttig, B. Feldmann, J. Thomassen, F. May, H. Zillgen, A. Brodde et al., Surf. Sci. 291 (1993) 14.

[27] J. Giergiel, J. Kirschner, J. Landgraf, J. Shen, J. Woltersdorf, Surf. Sci. 310 (1994) 1.

[28] J. Giergiel, J. Shen, J. Woltersdorf, A. Kirilyuk, J. Kirschner, Phys. Rev. B 52 (1995) 8528.

[29] J. Thomassen, F. May, B. Feldmann, M. Wuttig, H. Ibach, Phys. Rev. Lett. 69 (1992) 3831.

[30] P. Xhonneux, E. Courtens, Phys. Rev. B 46 (1992) 556.

[31] D.E. Fowler, J.V. Barth, Phys. Rev. B 53 (1996) 5563.

[32] W. Platow, A.N. Anisimov, M. Farle, K. Baberschke, Phys. Stat. Sol. (a) 173 (1999) 145.

[33] S.D. Bader, J. Appl. Phys. 76 (1994) 6425.

[34] A. Kirilyuk, J. Giergiel, J. Shen, J. Kirschner, Phys. Rev. B 52 (1995) R11672.

[35] A. Kirilyuk, J. Giergiel, J. Shen, M. Straub, J. Kirschner, Phys. Rev. B 54 (1996) 1050.

[36] M. Zharnikov, A. Dittschar, W. Kuch, C.M. Schneider, J. Kirschner, Phys. Rev. Lett. 76 (1996) 4620.

[37] M. Zharnikov, A. Dittschar, W. Kuch, C.M. Schneider, J. Kirschner, J. Magn. Magn. Mater. 174 (1997) 40.

[38] R. Vollmer, J. Kirschner, Phys. Rev. B 61 (2000) 4146.

[39] W.L. O'Brien, B.P. Tonner, Surf. Sci. 334 (1995) 10.

[40] W.L. O'Brien, B.P. Tonner, Phys. Rev. B 52 (1995) 15332.

[41] E.J. Escorcia-Aparicio, R.K. Kawakami, Z.Q. Qiu, Phys. Rev. B 54 (1996) 4155.

[42] R.K. Kawakami, E.J. Escorcia-Aparicio, Z.Q. Qiu, J. Appl. Phys. 79 (1996) 4532.

[43] D. Schmitz, C. Charton, A. Scholl, C. Carbone, W. Eberhardt, Phys. Rev. B 59 (1999) 4327.

[44] W. Kuch, J. Gilles, S.S. Kang, F. Offi, J. Kirschner, S. Imada, S. Suga, J. Appl. Phys. 87 (2000) 5747.

[45] X. Gao, M. Salvietti, W. Kuch, C.M. Schneider, J. Kirschner, Phys. Rev. B 58 (1998) 15426.

[46] R. Kläsges, D. Schmitz, C. Carbone, W. Eberhardt, T. Kachel, Solid State Commun. 107 (1998) 13.

[47] W. Kuch, S.S.P. Parkin, J. Magn. Magn. Mater. 184 (1998) 127.

[48] Y. Saitoh, T. Nakatani, T. Matsushita, T. Miyahara, M. Fujisawa, K. Soda et al., J. Synchrotron Rad. 5 (1998) 542.

[49] W. Kuch, J. Gilles, S.S. Kang, S. Imada, S. Suga, J. Kirschner, Phys. Rev. B (2000), in press.

[50] W. Kuch, M. Salvietti, X. Gao, M.-T. Lin, M. Klaua, J. Barthel et al., Phys. Rev. B 58 (1998) 8556.

[51] W. Kuch, M. Salvietti, X. Gao, M. Klaua, J. Barthel, C.V. Mohan et al., J. Appl. Phys. 83 (1998) 7019.

[52] D. Weller, J. Stöhr, R. Nakajima, A. Carl, M.G. Samant, C. Chappert et al., Phys. Rev. Lett. 75 (1995) 3752.

[53] H.A. Dürr, G. van der Laan, B.T. Thole, Phys. Rev. Lett. 76 (1996) 3464.

[54] C.F.J. Flipse, J.J. de Vries, G. van der Laan, M. Surman, A. Partridge et al., J. Magn. Magn. Mater. 148 (1995) 141.

[55] H.A. Dürr, G. van der Laan, Phys. Rev. B 54 (1996) R760.

[56] G. van der Laan, H.A. Dürr, Physica B 248 (1998) 121.

[57] W.L. O'Brien, B.P. Tonner, Phys. Rev. B 50 (1994) 2963.

[58] J. Hunter Dunn, D. Arvanitis, N. Mårtensson, M. Tischer, F. May, M. Russo et al., J. Phys.: Cond. Matt. 7 (1995) 1111.

[59] R. Nakajima, J. Stöhr, Y.U. Idzerda, Phys. Rev. B 59 (1999) 6421.

[60] S. Imada, T. Muro, T. Shishidou, S. Suga, H. Maruyama, K. Kobayashi et al., Phys. Rev. B 59 (1999) 8752.

[61] R. Lorenz, J. Hafner, Phys. Rev. B 54 (1996) 15937.

[62] L. Szunyogh, B. Újfalussy, P. Weinberger, Phys. Rev. B 55 (1997) 14392.

[63] T. Asada, S. Blügel, Phys. Rev. Lett. 79 (1997) 507.

[64] T. Asada, S. Blügel, J. Magn. Magn. Mater. 177–181 (1998) 1233.

[65] Y. Zhou, W. Zhang, L. Zhong, X. Nie, D.-S. Wang, J. Magn. Magn. Mater. 167 (1997) 136.

[66] R. Lorenz, J. Hafner, Phys. Rev. B 58 (1998) 5197.

[67] M. Uhl, L.M. Sandratski, J. Kübler, Phys. Rev. B 50 (1994) 291.

[68] P.M. Marcus, S.L. Qiu, V.L. Moruzzi, J. Phys. Cond. Matt. 11 (1999) 5709.

[69] A. Mokrani, O. Elmouhssine, G. Moraïtis, C. Demangeat, J. Magn. Magn. Mater. 198–199 (1999) 561.

[70] E.P. Wohlfahrt, in: E.P. Wohlfahrt (Ed.), Ferromagnetic Materials, Vol. 1, North Holland, Amsterdam, 1980.

[71] O. Eriksson, L. Nordström, A. Pohl, L. Severin, A.M. Boring, B. Johansson, Phys. Rev. B 41 (1990) 11807.

[72] H. Ebert, R. Zeller, B. Drittler, P.H. Dederichs, J. Appl. Phys. 67 (1990) 4576.

[73] M. Tischer, O. Hjortstam, D. Arvanitis, J. Hunter Dunn, F. May, K. Baberschke et al., Phys. Rev. Lett. 75 (1995) 1602.

[74] P. Bruno, Phys. Rev. B 39 (1989) 865.

[75] D. Weller, Y. Wu, J. Stöhr, M.G. Samant, B.D. Hermsmeier, C. Chappert, Phys. Rev. B 49 (1994) 12888.

[76] J. Stöhr, H. König, Phys. Rev. Lett. 75 (1995) 3748.

[77] H.A. Dürr, G.Y. Guo, G. van der Laan, J. Lee, G. Lauhoff, J.A.C. Bland, Science 277 (1997) 213.

[78] J. Stöhr, J. Magn. Magn. Mater. 200 (1999) 470.

[79] B. Heinrich, J.A.C. Bland (Eds.), Ultrathin Magnetic Structures, Vol. 2, Springer, Berlin, 1994, and references therein.

[80] J. Slonczewski, Phys. Rev. Lett. 67 (1991) 3172.

[81] J. Slonczewski, J. Magn. Magn. Mater. 150 (1995) 13.

Magnetic-circular-dichroism microspectroscopy at the spin reorientation transition in Ni(001) films

W. Kuch, J. Gilles, and S. S. Kang

Max-Planck-Institut für Mikrostrukturphysik, Weinberg 2, D-06120 Halle, Germany

S. Imada and S. Suga

Osaka University, Graduate School of Engineering Science, 1–3 Machikaneyama, Toyonaka 560-8531, Japan

J. Kirschner

Max-Planck-Institut für Mikrostrukturphysik, Weinberg 2, D-06120 Halle, Germany

(Received 10 November 1999)

The spin reorientation transition in fcc Co/Ni/Cu(001) epitaxial ultrathin films as a function of Co and Ni film thickness is studied by the combination of photoelectron emission microscopy and x-ray magnetic-circular-dichroism spectroscopy at the Ni $L_{2,3}$ edge. This microspectroscopic technique allows one to extract local quantitative information about the Ni magnetic properties on a submicrometer scale. Domain images in the thickness range of 1.4–2.6 atomic monolayers (ML) Co and 11–14 ML Ni show that the spin reorientation occurs as a function of both Co and Ni thicknesses. Increasing the Co thickness or decreasing the Ni thickness leads to a switching of the magnetic easy axis from [001] out-of-plane to ⟨110⟩ in-plane directions. A constant effective Ni spin moment similar to the bulk magnetic moment is observed. The Ni orbital to spin moment ratio shows distinctly different values for out-of-plane magnetization (0.080 ± 0.005) and in-plane magnetization (0.053 ± 0.005). This is discussed in terms of the connection to the Ni magnetocrystalline anisotropy. The domain density of the perpendicular magnetization increases towards the spin reorientation transition line.

I. INTRODUCTION

A considerable portion of current research on ultrathin magnetic films is focused on the direction of the easy axis of magnetization. It is determined by the magnetic anisotropy energy (MAE), which in epitaxial thin films contains important thickness-dependent contributions connected to the presence of a surface or interface, or to the elastic strain. The minimum of the sum of the MAE and the magnetostatic demagnetizing energy (shape anisotropy) defines the easy axis of magnetization. Spin reorientation transitions of the easy axis of magnetization in ultrathin films may occur as a function of film thickness, temperature, or composition. Both thin films with a magnetization in the film plane and perpendicular to it have important technological relevance. Therefore measurement and control of the MAE are important technical issues.

The MAE is related to the anisotropy of the orbital magnetic moment, as discussed by Bruno,[1] and later experimentally verified.[2–5] The orbital moment should be higher for a direction of magnetization preferred by the MAE.[6–8] This opens the possibility of determining the angular dependence of the MAE in an element-selective way by measuring the orbital magnetic moment by magnetic circular dichroism in soft x-ray absorption (XMCD). XMCD probes the spin and orbital asymmetry of the unoccupied part of the band structure just above the Fermi level.[9] Transitions of spin- and orbit-polarized core level electrons into the unoccupied part of the exchange split valence bands are excited by circularly polarized x rays. The dichroism, i.e., the difference in absorption intensity upon reversal of helicity, thereby depends on the projection of the direction of the incoming photons

onto the magnetization direction. The intensity of photoemitted electrons from a sample surface is most often used as a convenient measure for the absorption.

Sum rules have been proposed to deduce quantitative information from XMCD spectra.[10,11] Although there has been some dispute about the applicability of these rules,[12–15] they seem to yield reasonable results for the $3d$ transition metals.[14–16] These sum rules allow one to extract numbers for the spin and orbital magnetic moments from a comparison of the absorption cross section at the L_3 and L_2 edges of transition metals. They enable thus the separate determination of magnetic properties of different elements in the same sample.

This element specificity has been used by Dürr *et al.* to study element-resolved anisotropies of a stack of three atomic monolayer (ML) Co on top of 30 ML Ni on Cu(001).[4] Epitaxial Ni films on Cu(001) show a spin reorientation transition from an easy axis parallel to the film plane at film thicknesses below ≈8–10 ML to an easy axis perpendicular to the film plane at thicknesses between ≈8 ML and 56–75 ML.[17–25] The perpendicular magnetization is attributed to a magnetoelastic contribution to the MAE caused by substrate-induced strain in the epitaxial Ni film.[20–28] The MAE of Co/Cu(001), on the other hand, favors an in-plane easy axis.[29–32] Although the gross magnetization direction is in the plane of the film in 3 ML Co/30 ML Ni/Cu(001), it was possible by using XMCD to prove that the Ni film still maintains its perpendicular MAE.[4] The stronger in-plane anisotropy contribution of the (thinner) Co film, however, redirects the magnetization direction of the entire film to the in-plane direction.

From this competition of Ni perpendicular MAE, Co in-

plane MAE, and (in-plane) magnetostatic energy, it follows that spin reorientation transitions in Co/Ni/Cu(001) can be expected to take place at proper combinations of Ni and Co film thicknesses for which these energy contributions cancel out.[33] The total MAE of the Co/Ni stack may be designed to give a desired value by tuning the Co and Ni film thicknesses. The spin reorientation transitions in Co/Ni double layers are thus "enforced" in the sense that the elemental anisotropies of the single constituents do not change their sign between out-of-plane and in-plane magnetization of the entire bilayer. Therefore both the Ni and Co films experience transitions from their respective hard axis to the easy axis of magnetization at the spin reorientation transition and vice versa. The element-resolved MAEs probed by XMCD should consequently exhibit a distinct change in orbital moment at the spin reorientation transition.

The rapidly decreasing size of technologically employed magnetic structures fuels the development of techniques which allow the imaging of magnetic domains on a submicrometer scale. Photoelectron emission microscopy (PEEM) combined with resonant excitation by circularly polarized light is one that has already proved its feasibility for the study of magnetic microstructures and multilayers.[34,35] The lateral intensity distribution of emitted low-energy secondary electrons is magnified by electron lenses. Magnetic contrast is achieved by the XMCD effect: Circularly polarized radiation tuned to elemental absorption edges leads to dichroism in absorption and, hence, to a different secondary electron intensity for domains having different magnetization components along the direction of incoming light. Magnetic domains can then be distinguished in the images by different grayscales corresponding to the secondary electron intensity.

The consequent improvement is to take advantage of the *full* spectroscopic information inherent to XMCD without giving up the spatial resolution of PEEM. This implies scanning the photon energy and recording microscopic images of the secondary electron intensity for both photon helicities at each energy step, not only at the absorption maximum. Local XMCD spectra at any position can be analyzed from such a set of images. Instead of the qualitative information contained in images of magnetic domains obtained at one fixed photon energy, full quantitative information can be extracted from XMCD analysis of such a spectral series of images with the same spatial resolution. With the availability of powerful third-generation synchrotron light sources, the acquisition of such spectral series of absorption images became feasible in a reasonable time. The advantages of both methods, namely, the element-selective quantitative information on electronic and magnetic properties by means of XMCD, and the lateral resolution of PEEM, are combined in this way for performing microspectroscopy.

In this contribution we present an XMCD-PEEM microspectroscopic study of the spin reorientation transition in epitaxial Co/Ni/Cu(001) films. Both Co and Ni layers were prepared as crossed wedges with slopes rotated by 90° with respect to each other. In these samples the spin reorientation transition can be observed as a line separating the regions of in-plane and perpendicular magnetization, determined by the cancellation of Co and Ni MAE and shape anisotropy energy as a function of both layer thicknesses. XMCD spectra at the Ni $L_{2,3}$ edge were recorded for pixels corresponding to

370×370 nm^2 on the sample surface. Sum-rule analysis of these local XMCD spectra is used to present microscopic images of the effective Ni spin magnetic moment in the vicinity of the spin reorientation transition. Analysis with respect to the orbital moment reveals that a distinct jump of the Ni orbital magnetic moment occurs right at the spin reorientation transition, in accordance with an intrinsic Ni elemental MAE favoring out-of-plane magnetization irrespective of the magnetization direction of the whole Co/Ni stack.

II. EXPERIMENT

The measurements were performed at the twin helical undulator beamline for soft x-ray spectroscopy BL25SU of SPring-8 in Japan. Circularly polarized light emitted in the first harmonic from one of the two undulators is monochromatized by a varied spacing plane grating monochromator.[36] After having set the two undulators to opposite helicity, helicity reversal was realized by closing one undulator and fully opening the other, which took about 10 min. The degree of circular polarization is expected to be between 95% and 99%. The light was incident to the sample under a grazing angle of 30° from the surface, with an azimuthal angle of 23° to the [110] axis of the Cu substrate. The entrance and exit slits of the monochromator were set to 290 μm for the measurements presented here, which was enough to illuminate a sufficiently large area on the sample. Since the light spot on the sample is an image of the exit slit, the exit slit setting is not critical, and does not influence the photon flux density or the *local* photon energy resolution. The local energy resolution is estimated to be better than 150 meV, so that the spectra can be regarded as representing mainly the intrinsic line shape of the Ni $L_{2,3}$ absorption. The energy dispersion resulting from having an image of the exit slit on the sample surface was found to be only about 20 meV over the vertical dimension of the images taken here (74 μm). All images were normalized to the electron current measured at the last optical element, a gold-coated refocusing mirror.

The experiments were performed at room temperature in an ultrahigh-vacuum chamber (base pressure 1×10^{-8} Pa in the sample preparation chamber and 2×10^{-8} Pa in the PEEM chamber) equipped with standard facilities for sample preparation and surface characterization. The surface of the Cu(001) single-crystal substrate was prepared and checked by Ar ion bombardment, annealing, Auger electron spectroscopy, and low-energy electron diffraction. Nickel and cobalt films were evaporated at room temperature by electron bombardment from high-purity rods. Deposition rates were 0.3 ML/min for Ni and 0.7 ML/min for Co, while the overall pressure in the chamber did not exceed 2×10^{-8} Pa. The evaporation rates were calibrated before preparation of the wedges for continuous films evaporated under identical conditions by means of the oscillations in the medium-energy electron diffraction intensity recorded during the growth. The accuracy of the film thicknesses cited here is estimated as 10%. The wedge-shaped films were prepared by positioning apertures of 2×0.5 mm^2 in front of the sample, with a distance to the sample surface of 1.5 mm in the case of Ni and 1.1 mm in the case of Co. During deposition the sample and mask assembly was slowly (0.1°/s for Ni, and 0.2°/s for Co) rocked by $\pm 6°$ about the long axis of the aperture,

which was set at a 90° different sample azimuth for Ni and Co deposition. The total evaporation time corresponded to 14 ML for Ni and 4 ML for Co. This results in four 320×220 μm^2 (Ni$\times$Co) regions of crossed wedges with slopes of 46 and 18 ML/mm for Ni and Co, respectively.

The setup of the photoemission microscope (Focus IS-PEEM) is identical to that described in previous publications.[35] In short, it consists of a three-lens electrostatic straight optical axis microscope with an integral sample stage and a variable-contrast aperture. The extractor voltage was set to 10.0 kV and the aperture to 70 μm for the measurements presented here, which resulted in a resolution of about 0.5 μm. The projection lens voltages were adjusted to give a field of view of ≈ 95 μm. The magnified image is intensified by a two-stage microchannel plate, and converted into visible light by means of a scintillator crystal. The image is then computer recorded with 12-bit resolution by a Peltier-cooled camera (PCO SensiCam). A 4×4 binning of camera pixels was used for the images presented here. One pixel then corresponded to 0.37×0.37 μm^2 of the sample surface. To reduce the amount of data, the region of interest was limited to a rectangle of 192×200 pixel, or 71×74 μm^2. In this area, Ni and Co thicknesses varied in the ranges 10.7–14 ML and 1.33–2.67 ML, respectively.

Exposure times of 30 s per image were used for the energy scans. A total of 105 images for each helicity were recorded as a function of photon energy. The width of the energy steps in the scans was set to 0.65 eV before the L_3 edge and in between the L_3 and L_2 peaks, 0.26 eV near the L_3 peak, 0.34 eV near the L_2 peak, and 1.4 eV in the post-L_2 region. The helicity was reversed only once after completion of a full energy scan. The total time for acquisition of over 8×10^6 data points took about 2 h and 20 min, which included the moving time of the monochromator for wavelength scanning and the time needed to reverse the helicity. The scans were started 9 h after preparation of the films. Although a considerable contamination by residual gas can be expected at the Co surface after that time, we believe that the influence of gas adsorption on the magnetic and electronic properties of the Ni film capped by the Co layer is of minor importance. Possible impacts on the MAE of the Co/Ni double layer will be discussed in Sec. V.

III. DATA ANALYSIS

Sum-rule analysis of the 76 800 absorption spectra had to be automated. The procedure for that is described as follows: After subtraction of the camera offset, the data were normalized to the mirror current. This gives a normalization to the overall photon flux of the entire light spot. It turned out that an additional correction was necessary to account for differences between the *integral* and the *local* photon flux, caused by the angular distribution of the intensity in the undulator radiation, which is also energy dependent. This is different for the two helicities, since the source is located at different positions for the upstream and downstream undulator. For the measurements presented here the ratio of local to integral photon flux of the downstream undulator, which was set to deliver light of positive helicity (photon spin in light propagation direction), was found to be higher by about 18% than that of the upstream undulator. In addition, the difference

between the two undulators depended on the photon energy and the position within the light spot on the sample surface. A correction linear in energy was found to be sufficient to account for that.

This energy-dependent correction factor was determined from fitting a straight line to the ratio of two absorption spectra for opposite helicity while excluding from the fit the peak regions in which the dichroism occurs. This was done separately for all pixels in the image. The correction was found to vary smoothly over the image area. It was between 16% and 18% on the low-energy end of the spectra and between 16% and 21% at the high-energy end. The spectra were then normalized to unity edge jump by adjusting the intensity of the spectra to zero in the pre-edge region and to one in the post-edge region. Saturation effects arising from the finite penetration depth of the x rays at the Ni absorption maxima[37–40] are estimated to have only a minor influence of less than 2% for the spin moments and $<4\%$ for the orbital moments at the angle of light incidence and film thickness used here.[40]

To simplify the automated processing of the spectra, a complete sum-rule analysis, which was done as outlined in Ref. 14 or 41, was performed beforehand on the averaged spectra of 320 pixels, taken from a large domain in the lower half of the image. In particular, a background consisting of two step functions with relative statistical heights of 2/3 and 1/3 at the positions of the L_3 and L_2 absorption maxima, respectively, was subtracted from the spectra in order to obtain the white line intensity. The width of these step functions was chosen as 0.5 eV. We assumed the resulting integral of the helicity-averaged absorption spectra to correspond to 1.4 Ni $3d$ holes, rather than determining the number of holes from comparison to a sample with known moment as suggested in Ref. 41. This number enters linearly in both results for the spin and orbital magnetic moments, and thus cancels if we use their ratio. It was chosen to be the same as in Ref. 4; measurements of Srivastava *et al.* of the white line absorption intensity of Ni/Cu(001) as a function of Ni thickness also suggest a number close to 1.4 for Ni thicknesses above 10 ML.[42] The difference between the absorption spectra for opposite light helicities was corrected for the degree of polarization, which was taken as 97%. Evaluating the spin and orbital magnetic moments by applying the sum rules[10,11] to the proper integral of the difference spectrum and normalizing it to the white line intensity gives for Ni an effective spin magnetic moment $\mu_{S,eff} = (0.32 \pm 0.015) \mu_B$ and an orbital magnetic moment $\mu_L = (0.045 \pm 0.01) \mu_B$. The effective spin magnetic moment is the quantity that is obtained from application of the spin sum rule.[11] It includes the spin magnetic moment μ_S, plus a contribution from the magnetic dipole term $\frac{7}{2} T_z$. The latter is zero in the bulk of cubic crystals, but can be of the same magnitude as the orbital moment in ultrathin films.[2] If we identify these spectra as belonging to a perpendicularly magnetized domain, the effective spin moment of the film, corrected for the angle between magnetization direction and light incidence direction, would be $0.32 \mu_B / \cos 60° = (0.64 \pm 0.03) \mu_B$. This value is already slightly higher than the bulk value of the Ni magnetic moment $(0.62 \mu_B)$.[43] The errors quoted here represent the statistical significance of the data. An additional systematic error, possibly up to 20%, may be present according to
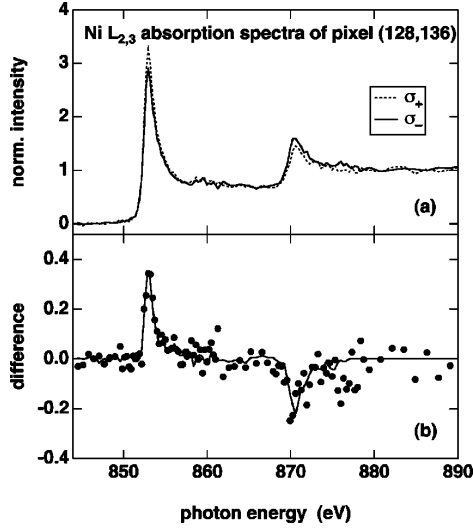
FIG. 1. (a) Ni $L_{2,3}$ absorption spectra of 370×370 nm^2 pixel (128,136). Spectra for positive (negative) helicity are reproduced by dotted (solid) lines. (b) Solid symbols: difference between the two curves of panel (a). Line: template difference spectrum obtained from averaging 320 pixels, shown here with different scaling at the L_3 and the L_2 edge to fit the single-pixel data of pixel (128,136).

the details of background subtraction, the contribution of the magnetic dipole term,[2,7,11,12,44] the number of $3d$ holes, saturation effects, the degree of circular polarization, or the overlap between $2p_{3/2}$ and $2p_{1/2}$ final states.[45] Since the variation of the Ni thickness in the present case is relatively small, we can safely assume that all of the above-mentioned sources of uncertainty in the determination of absolute numbers by the sum rules are virtually constant throughout the range of presented data. They thus do not affect the comparison of moments within the same sample, but have to be kept in mind when discussing the absolute values of the magnetic moments or comparing to literature values.

The XMCD spectra analyzed in this way served as a template for the automated analysis of the single-pixel spectra. The difference curve of the template XMCD spectra was cut into two parts mainly associated with the $2p_{3/2}$ and $2p_{1/2}$ cores, respectively, at 866 eV photon energy. The normalized difference spectra of each pixel were then fitted by that template curve, using only two scaling factors as parameters to fit the two parts. This method was checked to fit the spectra reasonably well over the whole imaged area. Thereby it is assumed that the shape or energetic position of the difference curves is constant. By using only two fit parameters connected to the dichroism intensity at the L_3 and L_2 edges, the fit procedure is very stable, which is a prerequisite for obtaining meaningful information from noisy or scattered single-pixel data. An example is shown in Fig. 1. It shows in the top panel (a) typical absorption spectra of a 0.37×0.37 μm^2 area of the sample for positive and negative helicity (σ_+ and σ_-, respectively). The corresponding dichroism is shown in the bottom panel (b) as the difference between these two curves (solid symbols). The line in Fig. 1(b) is the template difference spectrum, scaled at the L_3 edge by a factor of -0.92 and at the L_2 edge by a factor of
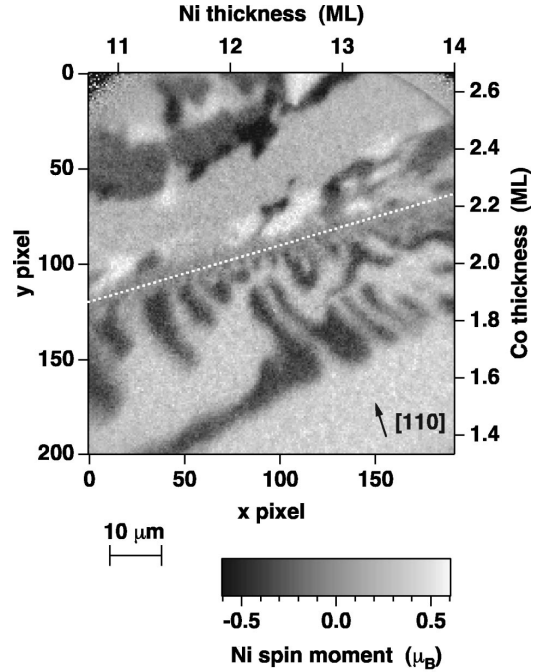
FIG. 2. Result of the pixel-by-pixel sum-rule analysis for the Ni effective spin moment $\mu_{S,eff}$. Different geometrical projections onto the direction of the incident light (from bottom to top, 30° above image plane) are represented by different grayscales, as defined in the legend. Ni and Co thicknesses are given at the top and right axes, respectively. The dotted white line highlights the spin reorientation line which separates regions with out-of-plane magnetization (bottom, two different grayscales) and in-plane magnetization (top, four different grayscales).

-1.60 to fit the single-pixel difference data.

Knowing the area under the L_3 and L_2 peaks of the template difference curve, the respective integrals of the single-pixel curve can be obtained by multiplication with the two fit parameters. It is assumed that the white line intensity of the spectra does not change within the images, being the same as in the template spectra. Some confidence into that assumption is established from checking the height at the L_3 maximum of all of the normalized single-pixel spectra. It varied by less than 5% over the entire image except for its upper edge, where deviations of up to 10% were found. The two degrees of freedom of the fit to the template curve are thus easily converted into the component of spin and orbital moments along the light incidence direction for each pixel of the image.

IV. RESULTS

Figure 2 shows the result for the Ni effective spin moment $\mu_{S,eff}$. The component of $\mu_{S,eff}$ along the direction of the incident light (from bottom to top) is represented in a grayscale, as defined in the legend at the bottom of the image. The Ni and Co thicknesses of the crossed double wedge are given at the top and right axes, respectively. Two distinct

regions with different domain structures are distinguished in Fig. 2, separated by a line that goes from approximately 1.9 ML Co thickness on the left hand side to about 2.2 ML on the right hand side (white dotted line in Fig. 2). Below that line only domains with two different shades of gray, light and dark gray, are found. The average values here are $\pm 0.32 \mu_B$. As mentioned before, this is attributed to perpendicularly magnetized domains, belonging to an absolute value of the spin moment of twice that number, $0.64 \mu_B$. In the top part of the image, domains with four different grayscales are present. They are seen in Fig. 2 as black, dark gray, bright gray, and white domains. The corresponding values of the effective spin moment are $\pm 0.52 \mu_B$ for the black and white and $\pm 0.22 \mu_B$ for the dark and bright gray domains. This can be attributed to an in-plane magnetization along four equivalent easy axes along the four $\langle 110 \rangle$ directions. To be able to distinguish all four in-plane magnetization directions, the crystal had been deliberately mounted with an oblique azimuthal incidence angle of $\approx 23°$ with respect to the $[110]$ direction. The projections of the $\pm [110]$ directions onto the incoming light are thus $\pm \cos 30° \cos 23° \approx \pm 0.80$; those of the $\pm [1\bar{1}0]$ are $\pm \cos 30° \cos 67° \approx \pm 0.34$. The image displays thus perpendicularly magnetized domains below the dotted line and domains that are magnetized along easy in-plane $\langle 110 \rangle$ directions on top of that line. The $\mu_{S,eff}$ values of the geometrical projections of the different in-plane and perpendicular domains correspond all to an absolute value of the effective spin moment of Ni of $\approx 0.65 \mu_B$. This is slightly higher than the Ni bulk moment of $0.62 \mu_B$. As mentioned in Sec. III, however, systematic errors of the order of 20% may be involved in the determination of absolute numbers by sum-rule analysis.

The two regions are separated by a stripe of about 4 μm width, in which the spin reorientation takes place. Its position depends both on the Ni and Co thickness. A spin reorientation from perpendicular to in-plane configuration takes place for decreasing Ni thickness d_{Ni} or increasing Co thickness d_{Co}. The position of the line of the spin reorientation transition can be approximated by $d_{Co} = 0.116 d_{Ni} + 0.62$ ML (d_{Co}, d_{Ni} in ML). The apparent average moment in that stripe is close to zero. Approaching the spin reorientation transition from the perpendicularly magnetized area in the bottom, the average domain size seems to be decreasing. Though it is hard to tell from the present image, the interior of the spin reorientation transition region probably consists of small unresolved domains.

Figure 3 shows, analogously to Fig. 2, the Ni orbital moment of the double wedge. The same domain pattern is recognized although the noise in that image is much higher, especially at the top, where the Ni signal is attenuated by a thicker Co overlayer than at the bottom. The reason for the higher noise in the image of the orbital moment distribution is that the absolute values of the integrals of the L_3 and L_2 dichroism are subtracted in the orbital moment sum-rule analysis, in contrast to the analysis of the spin moment, where they are summed. The worse statistics of the smaller signal and noisier dichroism of the L_2 edge compared to the L_3 edge has thus a much stronger influence on the statistics
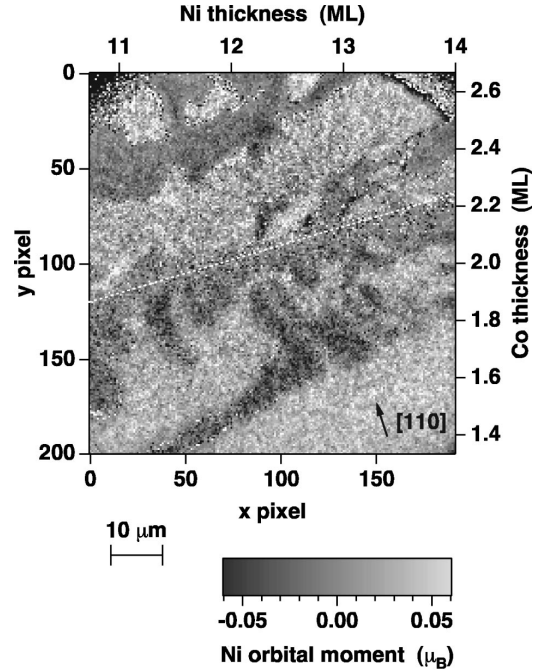

FIG. 3. As Fig. 2, but for the Ni orbital moment μ_L. Different geometrical projections onto the direction of the incident light (from bottom to top, 30° above image plane) are represented by different grayscales, as defined in the legend.

of the orbital moment, where it is close to canceling with the L_3 dichroism.

The interesting quantity for the interpretation of the orbital moment, independent of the magnetization direction, is the ratio of the orbital to spin moment, $\mu_L / \mu_{S,eff}$. Furthermore, assumptions made in the sum-rule analysis concerning the number of d holes, degree of circular polarization, and the determination of the white line intensity do not influence that ratio. However, it is clear from Fig. 3 that the statistics of the present single-pixel data do not allow the pixelwise interpretation in terms of orbital moments. To improve the statistical error in $\mu_L / \mu_{S,eff}$, the information from several pixels has therefore to be averaged. Since we are interested in the behavior of the orbital moment across the spin reorientation transition, averaging of pixels with a common distance from the dotted line has been employed. The result is shown in Fig. 4. Here the orbital to spin moment ratio $\mu_L / \mu_{S,eff}$ is plotted as a function of the distance from the spin reorientation line. The left hand side of Fig. 4 corresponds to the in-plane region of the image, the right hand side to the out-of-plane region. In the center (at the spin reorientation transition) several data points are outside the plot area of Fig. 4 because of division by zero. Each data point contains information of 192 pixels along a line parallel to the spin reorientation transition. $\mu_L / \mu_{S,eff}$ is obtained from the slope of a straight line fit through the origin to a plot of μ_L vs $\mu_{S,eff}$ of these 192 pixels. This way the relative weight of pixels with moments' projections close to zero is automatically reduced.

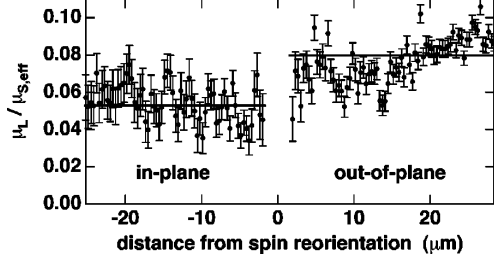Although there is considerable scatter, the orbital moment

FIG. 4. Orbital to spin moment ratio $\mu_L/\mu_{S,eff}$ as a function of the distance from the spin reorientation line. Each data point is an average of 192 pixels along a line parallel to the spin reorientation transition in Fig. 2. Solid lines mark the average $\mu_L/\mu_{S,eff}$ ratio in the in-plane region (left hand side) and in the out-of-plane region (right hand side).

in the out-of-plane region is seen to be distinctly higher than in the in-plane region by more than $0.02\mu_{S,eff}$. The thick horizontal solid lines in Fig. 4 mark the average $\mu_L/\mu_{S,eff}$ values of the data points that are within the extent of that line. On the in-plane side the average is 0.053 ± 0.005 and on the out-of-plane side 0.080 ± 0.005. In addition, from a look at the data of Fig. 4 one might infer a decreasing trend in the magnitude of the orbital to spin moment ratio towards the spin reorientation transition from both sides. Although the former finding—the sudden change in the orbital moment at the spin reorientation—can be clearly stated, the latter is close to the statistical error. Similar averaging line scans parallel to the spin reorientation line for both perpendicular and in-plane magnetization did not show any such systematic trend. We thus conclude that the orbital moment is approximately constant on both sides of the spin reorientation, but shows distinctly different values for in-plane and out-of-plane magnetization.

V. DISCUSSION

From the position of the spin reorientation line in the two-dimensional d_{Ni}, d_{Co} space of Fig. 2, several statements about the contributing anisotropy energy terms can be made. The energy difference of in-plane magnetization minus out-of-plane magnetization may be written as

$$E(d_{Ni},d_{Co}) = K_{Ni}(d_{Ni}) + K_{Co}(d_{Co})$$
$$-\frac{1}{2}\mu_0(M_{Ni}^2 d_{Ni} + M_{Co}^2 d_{Co}), \qquad (1)$$

where K_{Ni},K_{Co} denote the differences in the MAE between the in-plane and out-of-plane magnetization for the Ni and Co layer, respectively, with $\mu_0 = 4\pi\times10^{-7}$ V s A^{-1}m^{-1} and M_{Ni},M_{Co} saturation magnetizations per unit volume. The last two terms describe the magnetostatic demagnetizing energy. $E(d_{Ni},d_{Co}) = 0$ at the spin reorientation. It is obvious from the tilt of the reorientation line (dotted line in Fig. 2) that $K_{Ni}(d_{Ni})$ increases with increasing d_{Ni} and that $K_{Co}(d_{Co})$ decreases with increasing d_{Co}. A linear behavior is often assumed to simplify the thickness dependence of K_{Ni},K_{Co}:

$$K_{Ni}(d_{Ni}) = K_{Ni}^b d_{Ni} + K_{Ni}^s,$$

$$K_{Co}(d_{Co}) = K_{Co}^b d_{Co} + K_{Co}^s. \qquad (2)$$

In order to follow the usual interpretation of K^b and K^s as bulk and interface anisotropies, for each film the contributions from both interfaces have to be summed, and the common interface between Ni and Co has to be equally divided onto K_{Ni}^s and K_{Co}^s. Although the Co thicknesses in the present case are clearly too low for a separation into bulk and surface terms, we use the linear approximation of Eq. (2) for the sake of (limited) comparison with published literature values.

As mentioned in Sec. IV, the condition $E(d_{Ni},d_{Co}) = 0$ is approximately fulfilled for $d_{Co} = \alpha d_{Ni} + d_0$, where $\alpha = 0.115\pm0.015$ and $d_0 = (0.62\pm0.18)$ ML. Inserting that into Eq. (1), both of the coefficients for the thickness-dependent and the thickness-independent parts of E have to be zero. From the thickness-dependent coefficients, a relationship between K_{Ni}^b and K_{Co}^b is established:

$$-\frac{K_{Ni}^b - \frac{1}{2}\mu_0 M_{Ni}^2}{K_{Co}^b - \frac{1}{2}\mu_0 M_{Co}^2} = \alpha. \qquad (3)$$

Using bulk moments[43] and atomic volumes for epitaxial Co/Cu(001) (Ref. 46) and Ni/Cu(001) (Refs. 47 and 48) films, one gets $\frac{1}{2}\mu_0 M_{Co}^2 = 87.0$ μeV/atom and $\frac{1}{2}\mu_0 M_{Ni}^2 = 11.6$ μeV/atom. Putting these values into Eq. (3), one obtains the result $K_{Co}^b = (190\pm25)$ μeV$-(8.6\pm1.1)K_{Ni}^b$. This links the thickness-dependent part of the Ni MAE to the thickness-dependent part of the Co MAE in order to reproduce the experimentally observed slope of the reorientation line.

It has been discussed in the literature that the perpendicular anisotropy of Ni films on Cu(001) arises from a thickness-dependent magnetoelastic contribution to the MAE,[20,21,23–25,27,28] i.e., $K_{Ni}^b > 0$. The MAEs of both pure Ni and Co films on Cu(001) have been measured already previously by conventional techniques. Values of $K_{Ni}^b = +24$ μeV/atom,[21] $+30$ μeV/atom,[20] $+34$ μeV/atom,[23] and $+38$ μeV/atom (Ref. 26) are reported in the literature, obtained from ferromagnetic resonance measurements[20,21,23] and magnetic Kerr effect measurements.[26] The corresponding values for K_{Co}^b using Eq. (3) are then calculated to lie between ≈-20 and -140 μeV/atom. This agrees well with values found in literature, which range from -16 μeV/atom (Ref. 29) over -77 μeV/atom (Ref. 31) to -320 μeV/atom.[30] The slope α of the transition line in Fig. 2 is thus explained by the ratio of Co and Ni effective anisotropies [Eq. (3)].

The extrapolated intersection d_0 of the spin reorientation line with the $d_{Ni} = 0$ line is somewhat more difficult to discuss, not only because the error related to d_0 is much bigger than the error in α, but also because the separation into bulk and interface properties for Co is problematic at very low thicknesses, where the Co films may not even be completely closed. From the thickness-independent coefficients of Eq. (1) follows

$$K_{Ni}^s + K_{Co}^s = \left(\frac{1}{2} \mu_0 M_{Co}^2 - K_{Co}^b \right) d_0. \qquad (4)$$

This allows one to estimate the thickness-independent part of the MAE, $K_{Ni}^s + K_{Co}^s$, to be between $+50$ and $+150$ μeV/(surface atom). Negative interface anisotropies have been reported in the literature for the Ni-Cu interface [-163 μeV/(surface atom),[26] -65 μeV/(surface atom),[18] or -83 μeV/(surface atom) (Ref. 19)] and the vacuum-Co interface [-420 μeV/(surface atom) (Ref. 29)]. Under the assumption that the vacuum-Co and Ni-Cu interface contributions in Co/Ni/Cu(001) are the same as the above-mentioned literature values of Co/Cu(001) and Cu/Ni/Cu(001), respectively, the MAE connected to the Co-Ni interface has to be relatively high and positive. A previously published value is $+94$ μeV/(surface atom).[30] If we assume the above-mentioned literature values to be relevant in our film, the Co-Ni interface contribution would have to be of the order of $+500$ μeV/(surface atom) to lead to a positive value of $K_{Ni}^s + K_{Co}^s$.

It is known from scanning tunneling microscopy that room-temperature-grown Ni/Cu(001) films become increasingly rough with thickness.[49] However, only a small effect of roughness on the Ni-vacuum interface anisotropy has been found.[50] We have to recall at that point that the measurements were made more than 9 h after the preparation of the Co/Ni layer. Contamination by residual gas adsorption is most likely to influence the vacuum-Co interface. Surface contamination can be expected to drastically decrease the absolute value of the vacuum-Co interface contribution to the MAE, and could also lower M_{Co} to some extent for the Co film thicknesses imaged here. Both terms energetically favor the out-of-plane magnetization. We have indeed observed in Co/Ni crossed wedges that the spin reorientation line moved towards higher Co thicknesses as a function of time; i.e., $E(d_{Ni}, d_{Co})$ is becoming more positive with time, namely, with increasing contamination. This could also account for a discrepancy between the present data and those of Ref. 18. There, 2 ML Co has been found to be sufficient to pull the magnetization of an underlying Ni film into the film plane in the complete thickness range between 0 and 18 ML, whereas out-of-plane magnetization is observed in our data between ≈ 13 and 14 ML Ni and 2 ML Co (cf. Fig. 2).

Taking the large scatter in published anisotropy values and the relatively large error into account in the determination of d_0, it is wise to draw only qualitative conclusions about the surface and interface contributions to the total MAE from the present data. Altogether, the positive value of the sum of the thickness-independent terms ($K_{Ni}^s + K_{Co}^s$) is probably the result of a large positive Co-Ni interface contribution. It overcompensates the negative contribution from the Ni-Cu interface and the possibly remaining small negative anisotropy from the Co surface. The ratio between the thickness-dependent MAEs of Ni and Co is in good agreement with values for other epitaxial Co and Ni ultrathin film systems on Cu(001) from the literature.

Besides the above statements about the magnetic anisotropy energies, quantitative PEEM-XMCD microspectroscopy at the Ni $L_{2,3}$ edge allows one to extract position-dependent element-resolved magnetic information concerning spin and orbital moments. The absolute value of the Ni effective spin moment is found to be about constant over the whole image, with roughly the value of the Ni bulk moment. This is in agreement with Ref. 51, where a Ni spin moment of $0.6\mu_B$ in the center layers of Ni/Cu(001) was calculated, while an enhanced moment of $0.73\mu_B$ was predicted for the surface layer. A strongly reduced moment, as found in Cu/Ni/Cu/Si(001) ($0.1\mu_B$ at 30 Å Ni film thickness),[52] can be excluded. This could be an effect related to the different substrate. Previous XMCD measurements of 28 ML Ni/Cu(001), by contrast, yielded even a spin moment as large as $1.2\mu_B$.[38]

The behavior of the ratio of orbital to spin moment across the spin reorientation transition (Fig. 4) is most interesting. It is very likely connected to the Ni magnetocrystalline anisotropy K_{Ni}, which according to the above discussion is positive over the whole range of the image. That means that for the Ni layer the easy axis of magnetization is out of plane. In the upper part of the image the magnetization direction is consequently along hard in-plane directions with respect to the Ni MAE, in the lower part along easy out-of-plane directions. The latter seems to be connected to a distinctly higher orbital to spin moment ratio. This confirms the connection of orbital moment anisotropy and magnetocrystalline anisotropy. According to Bruno[1] there should be a proportionality between the orbital moment difference $\Delta\mu_L$ for out-of-plane and in-plane magnetization and the MAE:

$$K_{Ni} = -\frac{\xi}{4} \frac{G}{H} \frac{\Delta\mu_L}{\mu_B}. \qquad (5)$$

ξ is the spin-orbit coupling parameter, which for Ni is about 50 (Ref. 47) to 100 meV (Ref. 53), and G and H are density-of-states integrals.[1] $G/H = 1$ only if the exchange splitting is larger than the bandwidth. For transition metals, a rough estimate for G/H is 0.2 or smaller,[2] leading to a proportionality factor between $\Delta\mu_L$ and the MAE of about -2.5–5 meV/μ_B. It was pointed out later by van der Laan that Eq. (5) is only approximately true for the case of a completely filled majority spin band.[8] For Ni, though, this can be assumed to be the case. In Ref. 4 a much higher proportionality factor of ≈ -17 meV/μ_B was calculated for Ni. Another calculation of Hjortstam *et al.* yielded a factor of ≈ -18 or ≈ -26 meV/μ_B, depending on whether the orbital polarization correction is included or not.[27] According to the value we use, the difference between our measured orbital moments for out-of-plane and in-plane magnetization $\Delta\mu_L = (\mu_{L,\perp}/\mu_{S,eff} - \mu_{L,\parallel}/\mu_{S,eff}) \mu_{S,eff} = (0.080 - 0.053) \times 0.65\mu_B = (0.018 \pm 0.004)\mu_B$ corresponds to an MAE of either ≈ 60 μeV/atom (for -3 meV/μ_B) or ≈ 300 μeV/atom (for -17 meV/μ_B).

For the interpretation of our data we have assumed here that the influence of changes in the magnetic dipole term T_z on the effective spin moment $\mu_{S,eff} = \mu_S - \frac{7}{2}T_z$ is small. In fact it has been observed that the magnetic dipole term $\frac{7}{2}T_z$ is of the same magnitude as the orbital moment,[2] so that the observed changes in $\mu_L/\mu_{S,eff}$ (cf. Fig. 4) can be considered as mainly representing the changes in μ_L. For $3d$ metals like Ni it is furthermore expected that MAE contributions related to T_z are much weaker than contributions due to the

orbital moment.[8] Experimentally we did not observe a significant difference in $\mu_{S,eff}$ between in-plane and out-of-plane magnetization.

The value of 60 μeV/atom for the MAE agrees in magnitude with the above-discussed thickness-dependent literature MAE values for Ni/Cu(001) films.[20,21,23,26] Here 300 μeV/atom, though, would be a factor of 5 too high. In comparing to anisotropy energies, however, one has to keep in mind that the orbital moments measured by XMCD represent a depth-weighted average over the probing depth of the secondary electrons (about 25 Å for Ni).[40] The highly positive contribution to the MAE of the Co-Ni interface could lead to a higher orbital moment anisotropy in the top Ni layers with respect to lower layers and, consequently, to a higher value of $\Delta\mu_L$. In 13 ML Ni, the exponential attenuation of the secondary electron signal leads to a contribution of 1.45/13 from the topmost atomic layer and to a contribution of 0.65/13 from the bottommost layer. Thus, for example, a $+200$ μeV/surface atom Co-Ni interface anisotropy confined to the top layer and a 30-μeV/atom-volume MAE distributed evenly over the film would be observed as 70 μeV/atom. Moreover, the depth distribution of magnetic anisotropy, which is phenomenologically described by a linear dependence on thickness, is not known.

In an XMCD study of 3 ML Co/33 ML Ni/Cu(001), Dürr *et al.* found an even higher orbital moment anisotropy for Ni.[4] Their value, measured in a transverse geometry, corresponds to an orbital moment difference of $(0.028 \pm 0.014)\mu_B$.[7] Calculations of Hjortstam *et al.*, by contrast, gave orbital moment differences of $0.006\mu_B$ or $0.004\mu_B$ for calculations with and without an orbital polarization correction, respectively,[27] taking a tetragonal distortion of $c/a = 0.94$. Their absolute value for the angle-averaged orbital moment $(\mu_L^\perp + 2\mu_L^\parallel)/3$ at that distortion without orbital polarization is $0.047\mu_B$, which is quite close to our experimental value $(0.08 + 2 \times 0.053) \times 0.65\mu_B/3 = 0.04\mu_B$. Including orbital polarization they arrive at $0.064\mu_B$.[27]

All in all, a low proportionality constant $K_{Ni}/\Delta\mu_L$ of about -4 meV/μ_B is required for an agreement of our experimental data with the expected Ni MAE. It is clear that the uncertainties in this constant do at present not allow conclusions on the exact size of the MAE from XMCD measurements. Ultimate quantitative insight into the relation between magnetocrystalline anisotropy and orbital moment anisotropy will depend on further detailed theoretical studies. However, the measured anisotropy of the orbital moment is qualitatively well accounted for by the behavior of the magnetic anisotropy.

As the last point to discuss, the domain configuration close to the spin reorientation transition is left. The basic features seen in Fig. 2, i.e., a decreasing domain size on the perpendicular side of the reorientation and a distinct stripe in which no clear in-plane or out-of-plane magnetization is visible, resemble those of spin reorientations imaged in Co/Au(111) wedges.[54,55] (Note that in our study the spin reorientation happens as a function of two independent parameters, the Ni and Co film thicknesses in the crossed double wedge, in contrast to these earlier reports.) Films exhibiting a perpendicular anisotropy can lower the magnetostatic energy by the formation of alternatingly up and down magnetized domains.[56] Analytic calculations for the average

domain size in such systems revealed a dependence on the film thickness and, more prominently, on the domain wall energy.[57,58] As the latter is reduced by the reduction of the effective anisotropy energy $E(d_{Ni}, d_{Co})$ upon approaching the spin reorientation transition, smaller domains become energetically more favorable. This explains well the experimentally observed decrease of domain size as approaching the spin reorientation transition.[54,59] In our study on Co/Ni/Cu(001) we also see this striking dependence of domain size of the perpendicularly magnetized domains on the distance from the spin reorientation line (lower part of Fig. 2). Alternatingly up and down magnetized stripe domains, oriented perpendicularly to this line, are formed. Closer to the spin reorientation transition they split into smaller stripes, thus reducing the average domain width. We interpret this behavior in accordance with the above-mentioned studies by the balance of magnetostatic energy reduction by stripe domain formation and the cost of domain wall energy necessary to create these domains.

VI. SUMMARY

We have used the combination of XMCD and PEEM in a study of the thickness-dependent spin reorientation transition in ultrathin epitaxial Co/Ni/Cu(001) films. This full-image microspectroscopic technique allows one to obtain quantitative magnetic information with microscopic spatial resolution at any position of an image. Looking at the spin reorientation transition in crossed double wedges of Co and Ni results in images where the transition from in plane to out of plane magnetization direction can be followed in two-dimensional thickness space. The easy axis of magnetization switches from in plane at lower Ni thicknesses or higher Co thicknesses to out of plane at higher Ni thicknesses or lower Co thicknesses. The condition for zero MAE difference between in-plane and out-of-plane magnetization can be approximated by a linear dependence on both thicknesses. From this we deduce the relative size of the Co and Ni thickness-dependent (''bulk'') MAE and the double-layer thickness-independent (''surface'') MAE. Both are in good agreement with values found in literature.

Pixel-by-pixel sum-rule analysis of the images results in images displaying the Ni spin and orbital magnetic moments, projected onto the propagation direction of the illuminating x rays. The Ni effective spin moment is constant with an absolute value of $\approx 0.65\mu_B$. The orbital moment is distinctly higher for out-of-plane magnetization than for in-plane magnetization. We interpret this difference as reflecting the Ni MAE, which leads to an anisotropy in the orbital moment with respect to the magnetization direction. The Ni MAE favors perpendicular magnetization for all thicknesses, so that in-plane and out-of-plane magnetization directions of the Co/Ni bilayer represent hard and easy axes for the Ni layer, respectively.

The formation of perpendicularly magnetized domains with decreasing size upon approaching the spin reorientation transition can be explained by magnetostatic stray field energy minimization for decreasing domain wall energy. XMCD-PEEM microspectroscopic studies with improved lateral resolution will have the potential to investigate magnetic moments in very small domains and even in domain

walls. Such experiments will help us to elucidate the detailed mechanism of the spin reorientation transition in the Co/Ni/Cu(001) system and deliver valuable experimental information in the field of micromagnetics.

Note added in proof. Recently, an article by F. Wilhelm *et al.* was published [Phys. Rev. B **61**, 8647 (2000)] in which the proportionality constant of our Eq. (5), $K_{Ni}/\Delta\mu_L$, was experimentally determined for Ni in Ni/Pt multilayers as 2.6 meV/μ_B. This value fully supports our discussion.

[1] P. Bruno, Phys. Rev. B **39**, 865 (1989).

[2] D. Weller, J. Stöhr, R. Nakajima, A. Carl, M. G. Samant, C. Chappert, R. Mégy, P. Beauvillain, P. Veillet, and G. A. Held, Phys. Rev. Lett. **75**, 3752 (1995).

[3] H. A. Dürr and G. van der Laan, J. Appl. Phys. **81**, 5355 (1997).

[4] H. A. Dürr, G. Y. Guo, G. van der Laan, J. Lee, G. Lauhoff, and J. A. C. Bland, Science **277**, 213 (1997).

[5] D. Weller, Y. Wu, J. Stöhr, M. G. Samant, B. D. Hermsmeier, and C. Chappert, Phys. Rev. B **49**, 12 888 (1994); H. A. Dürr, G. van der Laan, J. Vogel, M. Finazzi, and J. B. Goedkoop, IEEE Trans. Magn. **MAG-34**, 1201 (1998).

[6] J. Stöhr and H. König, Phys. Rev. Lett. **75**, 3748 (1995).

[7] H. A. Dürr and G. van der Laan, Phys. Rev. B **54**, R760 (1996).

[8] G. van der Laan, J. Phys.: Condens. Matter **10**, 3239 (1998).

[9] J. L. Erskine and E. A. Stern, Phys. Rev. B **12**, 5016 (1975); G. Schütz, W. Wagner, W. Wilhelm, P. Kienle, R. Zeller, R. Frahm, and G. Materlik, Phys. Rev. Lett. **58**, 737 (1987).

[10] B. T. Thole, P. Carra, F. Sette, and G. van der Laan, Phys. Rev. Lett. **68**, 1943 (1992).

[11] P. Carra, B. T. Thole, M. Altarelli, and X. Wang, Phys. Rev. Lett. **70**, 694 (1993).

[12] R. Wu and A. J. Freeman, Phys. Rev. Lett. **73**, 1994 (1994).

[13] W. L. O'Brien, B. P. Tonner, G. R. Harp, and S. S. P. Parkin, J. Appl. Phys. **76**, 6462 (1994); D. Rioux, B. Allen, H. Höchst, D. Zhao, and D. L. Huber, Phys. Rev. B **56**, 753 (1997).

[14] C. T. Chen, Y. U. Idzerda, H.-J. Lin, N. V. Smith, G. Meigs, E. Chaban, G. H. Ho, E. Pellegrin, and F. Sette, Phys. Rev. Lett. **75**, 152 (1995).

[15] Y. U. Idzerda, C. T. Chen, H.-J. Lin, H. Tjeng, and G. Meigs, Physica B **208−209**, 746 (1995).

[16] J. Vogel and M. Sacchi, Phys. Rev. B **49**, 3230 (1994); X. Le Cann, C. Boeglin, B. Carrière, and K. Hricovini, *ibid.* **54**, 373 (1996); J. Hunter Dunn, D. Arvanitis, and N. Mårtensson, *ibid.* **54**, R11 157 (1996).

[17] F. Huang, M. T. Kief, G. J. Mankey, and R. F. Willis, Phys. Rev. B **49**, 3962 (1994); W. L. O'Brien and B. P. Tonner, *ibid.* **49**, 15 370 (1994).

[18] W. L. O'Brien, T. Droubay, and B. P. Tonner, Phys. Rev. B **54**, 9297 (1996).

[19] R. Vollmer, T. Gutjahr-Löser, J. Kirschner, S. van Dijken, and B. Poelsema, Phys. Rev. B **60**, 6277 (1999).

[20] B. Schulz and K. Baberschke, Phys. Rev. B **50**, 13 467 (1994).

[21] B. Schulz, R. Schwarzwald, and K. Baberschke, Surf. Sci. **307−309**, 1102 (1994).

[22] G. Bochi, C. A. Ballentine, H. E. Inglefield, C. V. Thompson, R. C. O'Handley, H. J. Hug, B. Stiefel, A. Moser, and H.-J. Güntherodt, Phys. Rev. B **52**, 7311 (1995).

[23] M. Farle, B. Mirwald-Schulz, A. N. Anisimov, W. Platow, and K. Baberschke, Phys. Rev. B **55**, 3708 (1997).

[24] M. Farle, W. Platow, A. N. Anisimov, P. Poulopoulos, and K. Baberschke, Phys. Rev. B **56**, 5100 (1997).

[25] M. Farle, A. N. Anisimov, W. Platow, P. Poulopoulos, and K. Baberschke, J. Magn. Magn. Mater. **198−199**, 325 (1999).

[26] R. Jungblut, M. T. Johnson, J. aan de Stegge, A. Reinders, and F. J. A. den Broeder, J. Appl. Phys. **75**, 6424 (1994).

[27] O. Hjortstam, K. Baberschke, J. M. Wills, B. Johansson, and O. Eriksson, Phys. Rev. B **55**, 15 026 (1997).

[28] C. Uiberacker, J. Zabloudil, P. Weinberger, L. Szunyogh, and C. Sommers, Phys. Rev. Lett. **82**, 1289 (1999); G. Y. Guo, J. Magn. Magn. Mater. **176**, 97 (1997).

[29] P. Krams, F. Lauks, R. L. Stamps, B. Hillebrands, and G. Güntherodt, Phys. Rev. Lett. **69**, 3674 (1992).

[30] M. T. Johnson, J. J. de Vries, N. W. E. McGee, J. aan de Stegge, and F. J. A. den Broeder, Phys. Rev. Lett. **69**, 3575 (1992).

[31] M. Kowalewski, C. M. Schneider, and B. Heinrich, Phys. Rev. B **47**, 8748 (1993).

[32] C. M. Schneider, A. K. Schmid, P. Schuster, H. P. Oepen, and J. Kirschner, in *Magnetism and Structure in Systems of Reduced Dimension*, edited by R. F. C. Farrow, B. Dieny, M. Donath, A. Fert, and B. D. Hermsmeier (Plenum, New York, 1993); E. Navas, P. Schuster, C. M. Schneider, J. Kirschner, A. Cebollada, C. Ocal, R. Miranda, J. Cerdá, and P. de Andrés, J. Magn. Magn. Mater. **121**, 65 (1993); W. Weber, A. Bischof, R. Allenspach, C. H. Back, J. Fassbender, U. May, B. Schirmer, R. M. Jungblut, G. Güntherodt, and B. Hillebrands, Phys. Rev. B **54**, 4075 (1996); W. Weber, R. Allenspach, and A. Bischof, Appl. Phys. Lett. **70**, 520 (1997).

[33] J. Lee, G. Lauhoff, and J. A. C. Bland, Phys. Rev. B **56**, R5728 (1997); G. Lauhoff, J. Lee, J. A. C. Bland, J. P. Schillé, and G. van der Laan, J. Magn. Magn. Mater. **177-181**, 1253 (1998).

[34] J. Stöhr, Y. Wu, M. G. Samant, B. B. Hermsmeier, G. Harp, S. Koranda, D. Dunham, and B. P. Tonner, Science **259**, 658 (1993); J. Stöhr, H. A. Padmore, S. Anders, T. Stammler, and M. R. Scheinfein, Surf. Rev. Lett. **5**, 1297 (1998).

[35] W. Swiech, G. H. Fecher, Ch. Ziethen, O. Schmidt, G. Schönhense, K. Grzelakowski, C. M. Schneider, R. Frömter, H. P. Oepen, and J. Kirschner, J. Electron Spectrosc. Relat. Phenom. **84**, 171 (1997); C. M. Schneider, J. Magn. Magn. Mater. **175**, 160 (1997); W. Kuch, R. Frömter, J. Gilles, D. Hartmann, Ch. Ziethen, C. M. Schneider, G. Schönhense, W. Swiech, and J. Kirschner, Surf. Rev. Lett. **5**, 1241 (1998).

[36] Y. Saitoh, T. Nakatani, T. Matsushita, T. Miyahara, M. Fujisawa, K. Soda, T. Muro, S. Ueda, H. Harada, A. Sekiyama, S. Imada, H. Daimon, and S. Suga, J. Synchrotron Radiat. **5**, 542 (1998).

[37] W. L. O'Brien and B. P. Tonner, Phys. Rev. B **50**, 2963 (1994).

[38] J. Hunter Dunn, D. Arvanitis, N. Mårtensson, M. Tischer, F. May, M. Russo, and K. Baberschke, J. Phys.: Condens. Matter **7**, 1111 (1995).

[39] V. Chakarian, Y. U. Idzerda, and C. T. Chen, Phys. Rev. B **57**, 5312 (1998).

[40] R. Nakajima, J. Stöhr, and Y. U. Idzerda, Phys. Rev. B **59**, 6421 (1999).

[41] J. Stöhr, J. Electron Spectrosc. Relat. Phenom. **75**, 253 (1995).

[42] P. Srivastava, N. Haack, H. Wende, R. Chauvistré, and K. Baberschke, Phys. Rev. B **56**, R4398 (1997).

[43] E. P. Wohlfahrt, in *Ferromagnetic Materials*, edited by E. P. Wohlfahrt (North-Holland, Amsterdam, 1980), Vol. 1.

[44] C. F. J. Flipse, J. J. de Vries, G. van der Laan, M. Surman, A. Partridge, and W. J. M. de Jonge, J. Magn. Magn. Mater. **148**, 141 (1995); G. van der Laan and H. A. Dürr, Physica B **248**, 121 (1998).

[45] Y. Teramura, A. Tanaka, and T. Jo, J. Phys. Soc. Jpn. **65**, 1053 (1996).

[46] J. R. Cerdá, P. L. de Andres, A. Cebollada, R. Miranda, E. Navas, P. Schuster, C. M. Schneider, and J. Kirschner, J. Phys.: Condens. Matter **5**, 2055 (1993).

[47] W. Kuch, A. Dittschar, K. Meinel, M. Zharnikov, C. M. Schneider, J. Kirschner, J. Henk, and R. Feder, Phys. Rev. B **53**, 11 621 (1996).

[48] W. Platow, U. Bovensiepen, P. Poulopoulos, M. Farle, K. Baberschke, L. Hammer, S. Walter, S. Müller, and K. Heinz, Phys. Rev. B **59**, 12 641 (1999).

[49] J. Shen, J. Giergiel, and J. Kirschner, Phys. Rev. B **52**, 8454 (1995).

[50] P. Poulopoulos, J. Lindner, M. Farle, and K. Baberschke, Surf. Sci. **437**, 277 (1999).

[51] O. Hjortstam, J. Trygg, J. M. Wills, B. Johansson, and O. Eriksson, Phys. Rev. B **53**, 9204 (1996).

[52] S. Hope, J. Lee, P. Rosenbusch, G. Lauhoff, J. A. C. Bland, A. Ercole, D. Bucknall, J. Penfold, H. J. Lauter, V. Lauter, and R. Cubitt, Phys. Rev. B **55**, 11 422 (1997).

[53] A. R. Mackintosh and O. K. Anderson, in *Electrons at the Fermi Surface*, edited by M. Springford (Cambridge University Press, Cambridge, England, 1980).

[54] M. Speckmann, H. P. Oepen, and H. Ibach, Phys. Rev. Lett. **75**, 2035 (1995).

[55] H. P. Oepen, M. Speckmann, Y. Millev, and J. Kirschner, Phys. Rev. B **55**, 2752 (1997).

[56] Y. Yafet and E. M. Gyorgy, Phys. Rev. B **38**, 9145 (1988).

[57] A. B. Kashuba and V. L. Pokrovsky, Phys. Rev. B **70**, 3155 (1993); Phys. Rev. B **48**, 10 335 (1993); B. Kaplan and G. A. Gehring, J. Magn. Magn. Mater. **128**, 111 (1993).

[58] Y. Millev, J. Phys.: Condens. Matter **8**, 3671 (1996).

[59] R. Allenspach and A. Bischof, Phys. Rev. Lett. **69**, 3385 (1992).

Lebenslauf

Persönliche Daten:

Name:	Wolfgang Kuch
geboren am:	07. Januar 1964
in:	Boston, U.S.A.
Staatsangehörigkeit:	deutsch und U.S.
Familienstand:	verheiratet, ein Kind

Schulausbildung:

1970 – 1974	Karl-von-Ibell-Schule (Grundschule) in Frankfurt a. M.
1974 – 1980	Leibnizschule (Gymnasium) in Frankfurt a. M.
1980 – 1983	Friedrich-Dessauer-Gymnasium (gymnasiale Oberstufe) in Frankfurt a. M.

Grundwehrdienst:

Juli 1983 – Sept. 1984

Wissenschaftlicher Werdegang:

Okt. 1984 – Mai 1989	Studium der Physik an der Johann Wolfgang Goethe-Universität in Frankfurt a. M., am 18.05.1989 Diplom, Thema der Diplomarbeit: „Sauerstoffadsorption und Oxidbildung auf Nickel(111)"
Juli 1989 – März 1993	Doktorarbeit bei der Deutschen Forschungsanstalt für Luft- und Raumfahrt (DLR) in Stuttgart, am 12.07.1993 Promotion an der Universität Stuttgart, Thema der Dissertation: „Adsorption von Wasser auf reinen und vorbelegten Nickel(111)-Oberflächen"
seit 01.04.1993	Wissenschaftlicher Mitarbeiter am Max-Planck-Institut für Mikrostrukturphysik, Halle/Saale
Feb. – Juli 1996	Forschungsaufenthalt am IBM Almaden Research Center, San Jose, U.S.A.

Halle, 29. November 2001

Erklärung an Eides statt

Ich erkläre hiermit, die vorliegende Habilitationsschrift

Abbildende magnetische Mikrospektroskopie

selbständig und ohne fremde Hilfe verfasst und keine anderen als die von mir angegebenen Quellen und Hilfsmittel benutzt zu haben. Die den benutzten Werken wörtlich oder inhaltlich entnommenen Stellen sind als solche kenntlich gemacht.

Halle, 29. November 2001

Danksagung

An erster Stelle möchte ich Herrn Prof. J. Kirschner für sein kontinuierliches Interesse und die wohlwollende Förderung der vorliegenden Arbeiten danken. Es war nicht zuletzt seine konstruktive Kritik während zahlreicher Diskussionen, die meinen Ehrgeiz immer wieder aufs neue anstachelte.

Um aufzulisten, für was ich Frau B. Zada danke, müsste hier ein separates Kapitel eingefügt werden. Ihrer unschätzbare Hilfe bei allen technischen und administrativen Dingen wie zum Beispiel dem Durchführen der Zollabwicklung bei den Transporten nach Japan und vielem mehr ist es zu verdanken, dass auch in arbeitsintensiven Zeiten der Blick für das Wesentliche nicht verloren ging.

Besonderer Dank gebührt den Kollegen und Mitarbeitern, die bei der Durchführung der Strahlzeiten beteiligt waren. Aufgrund der tatkräftigen Mithilfe von F. Offi, Dr. S. Kang, J. Gilles, Dr. S. Imada und Prof. S. Suga während Tag- und Nachtschichten konnten die Messungen effektiv und erfolgreich durchgeführt werden.

Den weiteren gegenwärtigen und früheren Mitgliedern der Arbeitsgruppe für Synchrotronstrahlung, L. Chelaru, Dr. J. Wang, F. Helbig, Dr. M. Kotsugi, K. Fukumoto, Dr. C. M. Schneider, Dr. R. Frömter, Dr. M. Seider, Dr. X. Gao, Dr. M. Salvietti, Dr. A. Dittschar, Dr. M. Zharnikov, Prof. M.-T. Lin, U. Pracht, Dr. K. Meinel und Dr. F. Baudelet danke ich für ihre Unterstützung, die gute Zusammenarbeit und den gemeinsamen Spaß bei der Arbeit und bei vielen Freizeitaktivitäten.

Ich danke meinen Kollegen im Max-Planck-Institut für Mikrostrukturphysik, Dr. D. Sander, Dr. W. Wulfhekel, Dr. G. Steierl, Dr. R. Hertel, Dr. U. Hillebrecht, Dr. H. Schwabe, Dr. R. Vollmer, Dr. H. L. Meyerheim, Dr. J. Barthel, Dr. M. Klaua, Dr. Shah, F. Porratti, F. Zavaliche,